UNIVERSITÀ
DEGLI STUDI
DI PADOVA

Università degli studi di Padova
Dipartimento di Scienze Chimiche

CORSO DI DOTTORATO in SCIENZA E INGEGNERIA
DEI MATERIALI E DELLE NANOSTRUTTURE
XXX CICL0

SILK BASED NANOCOMPOSITES FOR BIOPHOTONIC AND OPTICAL DEVICES

Coordinatore: Ch.mo Prof. Giovanni Mattei
Supervisore: Prof. Alessandro Martucci

Dottorando : Elena Colusso

ANNO ACCADEMICO 2017-2018

To my family

"I don't know anything,
but I do know that everything is interesting
If you go into it deeply enough. "
Richard Feynman

Abstract

In the last decade silk fibroin (SF), the protein extracted from the silk fibers, emerged as an attractive material for biophotonic applications due to its biocompatibility combined with unique mechanical and optical properties. A strategy to enhance the optical properties of silk, and to simultaneously introduce specific functionalities, is to combine silk with some specific inorganic, organic or biological compounds.

The work here presented reports the results achievable by combining silk with two different inorganic nanoparticles for the fabrication of optical nanostructured devices.

The first strategy investigated was to combine silk with titanate nanosheets (TNSs), a 2D precursor of TiO2, in order to significantly increase the refractive index of silk while preserving all its specific properties. The structural and functional characterizations of the SF-TNSs composites were performed to correlate the material structure with its properties. In particular, the ion exchange process was investigated as a strategy to easy functionalize post-process the material.

A second strategy that was investigated exploits the combination of gold nanoparticles within the silk matrix in order to introduce plasmonic functionalities in the material. Specifically, in this first phase, the inclusion of gold nanoparticles was exploited to induce localized heating thanks to the excitation of the nanoparticles plasmon resonance, an effect that can be potentially used in biomedical applications in the treatment of bacterial infections.

Finally, the fabrication of simple optical and photonic devices with the nanocomposites, such as multilayer Bragg reflectors and inverse opals, was demonstrated. In particular, a bioinspired multilayer optical structured was fabricated with the SF-TNSs material, showing a stimuli-responsive behavior, which results in a reversible change of structural coloration in response to humidity.

Sommario

Nell'ultimo decennio la fibroina di seta (SF), la proteina estratta dalle fibre prodotte dal baco, è emersa come candidato ideale per applicazioni biofotoniche grazie alla sua biocompatibilità combinata con proprietà meccaniche ed ottiche uniche. Una strategia per migliorare le proprietà ottiche della seta e per introdurre contemporaneamente funzionalità specifiche è quella di combinare tale materiale con composti inorganici, organici o biologici specifici.

Il lavoro qui presentato riporta i risultati ottenuti dalla combinazione della fibroina con due diverse nanoparticelle inorganiche per la fabbricazione di dispositivi ottici nanostrutturati.

La prima strategia proposta ha previsto la combinazione della seta con *nanosheets* di titanato (TNSs), un precursore 2D di TiO_2, al fine di aumentarne significativamente l'indice di rifrazione pur conservandone tutte le proprietà specifiche. Si sono eseguite caratterizzazioni strutturali e funzionali del nanocomposito SF-TNSs al fine di correlare la struttura del materiale con le sue proprietà. In particolare, si è studiato il processo di scambio ionico come metodo per la funzionalizzazione post fabbricazione del materiale.

Una seconda strategia investigata sfrutta invece la combinazione di nanoparticelle d'oro con la matrice di seta per introdurre funzionalità plasmoniche nel materiale. In particolare, in questa prima fase, l'inclusione di nanoparticelle d'oro è stata sfruttata per indurre riscaldamento localizzato grazie all'eccitazione della risonanza plasmonica, un effetto potenzialmente utilizzato nelle applicazioni biomediche nel trattamento delle infezioni batteriche.

Infine, sono state realizzate semplici strutture ottiche e fotoniche con i nanocompositi sintetizzati, quali riflettori Bragg multistrato e opali inversi.

Acknowledgements

First, I would like to thank my supervisor, Professor Alessandro Martucci, without which all this work would not have been possible. Thank you for being always available to answer all of my questions, for the patience, for the support, and for always encouraging me to do my best even when the results were late to come.
Thanks also to Professor Guglielmi for the interesting scientific discussions and professional suggestions.

The work presented in this thesis is the result, for a large part, of collaborations with excellent researchers whom I would like to express my gratitude. In particular, I want to thank Dott. Giovanni Perotto for giving me the opportunity to continue his work on the silk-titanates material, for the many suggestions and tips provided, and for all the TEM images present in this manuscript.

A grateful acknowledgment goes to Prof. Fiorenzo Omenetto, for giving me the opportunity to spend two periods in his group at Tufts University and for the useful discussions and precious suggestions. Thank to all the researchers and students of SilkLab for welcoming me and making me feel at home during my stay in Boston, for sharing with me not only scientific ideas but even funny moments (like cooking competitions).
I am grateful to Dott. Yu Wang for teaching me how to fabricate the inverse opals, for the precious suggestions and for the SEM characterizations. Thanks to Weyn Li for the help in the gold nanorods synthesis and Meng Li for the help in the optical characterizations. A special thank goes to Fabio de Ferrari for the simulations of the opals, but also for the continuous support and the fruitful discussions.
A further acknowledgment goes to Prof. Paolo Minzioni for the photodynamic characterizations and for introducing me to the world of lasers.

I also want to give my acknowledgements to Dott. Joseph Arsecularatne (UNSW) for the indentation tests and Dott. Gabrio Vallotto and Prof. Elti Cattaruzza for the ICP measurements and for the helpful discussions on ion exchange.

I am grateful to my colleagues in the Industrial Engineering Department at the University of Padua for a unique research atmosphere. Sincere thanks go in particular to my research group, NanoEng: Gianmarco Giordano, Marco Sturaro, Marco Angiola e Andrea Paduano, Prof. A. Martucci and Prof. Massimo Guglielmi.

Finally, I want to thank my family and all the friends around the world who have been there for me through this incredible adventure over the years.

Contents

List of Figures

List of Tables

Introduction

In the last decades, the increasing research work in the nanotechnology field associated with the request to develop a more sustainable industry, have moved the interest of the material scientist community to the study of a new class of nanostructured materials that involve a naturally occurring polymer (biopolymer) in combination with an inorganic moiety, and showing at least one dimension in the nanoscale. These hybrids materials, commonly designated as "bionanocomposites", combine the advantages of the biopolymeric matrix, such as biocompatibility and biodegradability, with the functional properties provided by the inorganic fillers (often in the form of nanoparticles), and present interesting application in, among others, optical and photoelectrical devices, biomedical engineering, sensing.[1]

Two main reasons moved the choice to replace the common petroleum-derived polymers with biopolymers in the synthesis of the nanocomposites. The first one is related with the biodegradability and sustainability of the obtained materials, derived by the use of a natural polymer, which offer the opportunity to develop environmentally friendly materials. The second one is instead related with the biocompatibility, an important property for the use of these biohybrids in food packaging or in medicine.

Poly(lactic acid), cellulose, collagen, chitosan, chitin, keratin and silk are common examples of biopolymers derived by natural sources. Among them silk, a traditional material used for centuries in clothing, is currently discovering new applications in medicine and in the development of a "green" hi-technology. This protein based polymer, produced by different organisms such as spiders, worms and butterflies, presents the typical properties of a biopolymers, such as biocompatibility and biodegradability, associated with good mechanical performances. The most diffused silk, derived from the *Bombyx mori* silkworm, offer the advantage of a wide

availability due to a consolidate production for the textile industry, associated with the possibility to be processed in a wide range of formats in its "regenerated" form, derived by an all water-based process. Recently, this material has also been proposed as platform for the fabrication of resorbable and implantable electronic devices, sensors and for optical and biophotonic applications. Thanks to its refractive index (1.54 at 633 nm), high transparency, low surface roughness of silk derived films, possibility to fabricate devices on the micro- and nanoscale, this material is an ideal candidate for the fabrication of photonic crystals, waveguides and others optical devices, able to interact with the natural environment (including the human body).[2]

The aim of the present thesis work is the fabrication and characterization of silk-based nanocomposites that combine the intrinsic properties of the silk fibroin (SF) with the functionalities typical of the selected nanoparticles for application in optical and photonic-based devices. Two different types of nanoparticles were investigated, a titanium oxide based particles called titanates nanosheets (TNSs) and gold nanorods (AuNRs).

Titanates are 2D-layered materials, with a very small size, good dispersibility in polymer matrices and high refractive index. Moreover, because of their layered structure, they present interesting ion exchange properties that allow introduction of new functionalities to the nanocomposite. The choice of these nanoparticles was dictated by the interest in development of an high refractive index material to improve the optical performances of the silk-based devices.[3,4] In the course of my Ph.D. work, great effort was devoted to the characterization of the material (in particular for what concern the ion exchange properties) and to the development of new optical devices, such as multilayer Bragg reflector and inverse opals.

Gold nanoparticles were also investigated for the fabrication of a material suitable for laser-heating application in medicine. In fact, gold nanoparticles are inert in vivo, non-toxic, and easy to synthesize. In particular, nanorods were explored because of the presence of a surface plasmon resonance peak in the NIR region, in the so called "biological window".[5,6] The study of this second material started only

during the last year of my PhD activity, and has been focused in particular on the synthesis and preliminary physio-chemical characterization of the material.

My research work was developed in the framework of a collaboration with the group of Prof. Omenetto at Tufts University, pioneer in the use of silk for optics and hi-tech applications, and dott. Giovanni Perotto at ITT Genova, who first proposed the combination of silk with TNSs for the fabrication of a high refractive index material.

The thesis is divided in six chapters. In *Chapter 1* an overview of the literature on the silk-based materials is presented, focusing on the description of the structural-related properties of the silks, the processing methods of silk and its main applications. A section is also dedicated to review the works already present in literature on silk-based nanocomposites.

In *Chapter 2* the two nanocomposites materials studied during the PhD activity are introduced. A first part is focus on the SF-TNSs nanocomposite, with particular attention on the effect of the methanol annealing and on the optical and structural properties of thin films made with such material. A brief review of the previous published work is reported at the beginning of the section. In the second part the second nanocomposite is described, with particular attention on the synthesis, structural characterization and photo-thermal properties of the SF-AuNRs composite.

In *Chapter 3*, the ion exchange properties of the SF-TNSs nanocomposite are investigated as a strategy for post-synthetic functionalization. In particular, the process is explored for the introduction of plasmonic and fluorescent functionalities.

Chapter 4 and *Chapter 5* deal with optical application of the two nanocomposites. In *Chapter 4*, a bio-inspired multilayer structure made with the SF-TNSs material is described and characterized as platform for optical sensing of humidity. *Chapter 5* collects the main results obtained on the fabrication of silk-nanocomposites based inverse opal structures.

Finally, the conclusions and future perspectives of the PhD activity will be discussed in *Chapter 6*.

References

[1] M. Darder, P. Aranda, E. Ruiz-Hitzky, *Adv. Mater.* **2007**, *19*, 1309.

[2] F. G. Omenetto, D. L. Kaplan, *Nat. Photonics* **2008**, *2*, 641.

[3] A. Antonello, M. Guglielmi, V. Bello, G. Mattei, A. Chiasera, M. Ferrari, A. Martucci, *J. Phys. Chem. C* **2010**, *114*, 18423.

[4] G. Perotto, M. Cittadini, H. Tao, S. Kim, M. Yang, D. L. Kaplan, A. Martucci, F. G. Omenetto, *Adv. Mater.* **2015**, *27*, 6728.

[5] H. Chen, L. Shao, Q. Li, J. Wang, H. Misawa, P. van Dorpe, P. Nordlander, S. A. Maier, S. Wolff, M. Fischer, S. Gsell, M. Schreck, C. Becher, U. Sennhauser, B. Hecht, *Chem. Soc. Rev.* **2013**, *42*, 2679.

[6] N. G. Khlebtsov, L. A. Dykman, Optical properties and biomedical applications of plasmonic nanoparticles. *J. Quant. Spectrosc. Radiat. Transf.* **2010**, *111*, 1–35.

Chapter 1.

Overview on silk materials

1.1. Introduction

Silks are a class of biopolymers fibrous materials produced by a number of animals (best known as anthropods), such as spiders, worms and butterflies. These natural fibers present incredible mechanical properties, with performance comparable to synthetic materials like kevlar and nylon. Among silk variants, particular interest is devoted to the silkworm silk of *Bombyx mori* for the greatest economic importance and to the dragline silks of spiders such as *Nephila clavipes,* because of the unique mechanical properties.[1] A great effort was made in the last decades to study the mechanism of natural spinning through a reverse engineering process and to replicate synthetically these materials. Recent progress in understanding the relationship between structure and processing have led to the transformation of this ancient and commodity material, in particular silkworm silk, into a variety of new material formats. [2]

Silkworm silk is the most diffused and studied and its use extends from industrial textiles to medicine. The fibers are composed of two protein microfilaments of fibroin, brought together by a glue-like glycoprotein called sericin. Sericin is usually removed to isolate the fibroin trough a dissolution in a sodium carbonate solution, a process called “degumming”. The degummed fibers present themselves interesting properties and for centuries they were used as sutures by physicians, thanks to their mechanical properties and biocompatibility. The possibility to dissolve the fibers and obtain a water based solution (regenerated silk)

gave the opportunity to expand the use of silk to a fabrication of a wide range of structures, from films and sponges, to more complex nano- and micro-structures. The sustainability, biocompatibility and biodegradability of this material make the silk an ideal platform that can replace the petrol-derived plastics in the fabrication of bio-derived materials for a variety of technological and biomedical applications.[1,3–5]

1.2. Structure of silk proteins

Silks are protein-based polymer and as a protein, they present a primary chemical structure characterized by a sequence of amino acids, that are classified based on the type of side chains (R groups) that are attached to a certain protein backbone. Silk fibroin from silkworm is composed by two protein chains, the heavy chain and the light chain, linked together via a single disulfide bonds. The amino acid composition consists primarily of glycine (43%), alanine (30%) and serine (12%), tyrosine (5.3%), valine (1.8%), and only 4.7% of the other 15 amino acid types. In the heavy chain of the silk fiber, the crystalline domains are characterized of glycine-X repeats, where X is alanine, serine, threonine and valine. Each domain consists of subdomains hexapeptides (as GAGAGS, GAGAGY, GAGAGA with G is glycine, A alanine, S serine and Y tyrosine), that end with tetrapeptides (like GAAS or GAGS). The non-repetitive regions (linkers) are characterized by charged residual aminoacidic not present in the crystalline regions. [6–8] The primary sequence of these domains results in a hydrophobic protein with a natural co-block polymer design.

This primary structure is arranged in a secondary structure through intramolecular forces between amino acid residues of the polypeptide chain. The principal arrangements of the silk fibroin are α-helix, β-sheets, turns and random coils. The helixes are stabilized by intra-chains hydrogen bonds that are formed between the carbonyl groups and the hydrogen atoms of the amine group. The R-chains of any residue are located outside the spiral due to their steric size inside the chain. Sheets are folded structures formed by two or more polypeptide chains, among which an inter-chains hydrogen bond is formed. The -R groups are positioned

perpendicular to the plane of the peptide bonds, alternately above and below the sheet. Crystalline β-sheets can be arranged in different arrangements, among them three have been suggested as being the crystal structure of the fibroin: polar-antiparallel, polar-parallel and antipolar-antiparallel arrangements. The arrangement strongly affects the mechanical properties of the silk structure.[9] In **Figure 1.1** it is visible the structural representation of the different arrangements.

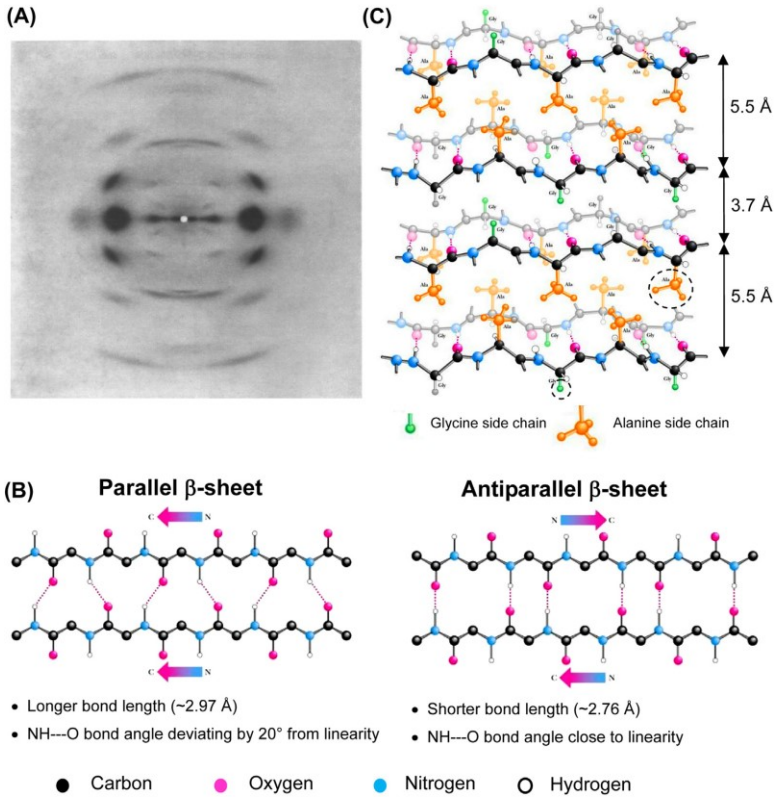

Figure 1.1. (A) X-ray diffraction (XRD) pattern for silk fibroin fibers. (B) Bond length and bond angle in parallel and antiparallel fibroin sheets. (C) Widely accepted polar-stacking of antiparallel sheets, with the surface of one sheet projecting entirely methyl groups (side chains) of alanine residues and the other surface of the same sheet projecting only hydrogen atoms (sidechains) of glycine residues. The intersheet distances alternate at 5.5 Å and 3.7 Å respectively. Reproduced from Koh et al. [9]

Based on the different secondary structure, three main polymorphisms have been identified for the silk fibroin in the solid state, called silk I, silk II and silk III. The first form (silk I) refers to the water-soluble state characterized by a predominance of random coils.[10] This structure easily converts to silk II upon exposure to heat, physical spinning or alcohol (methanol). Silk II is instead an insoluble conformation

reach in β-sheets. The β-sheets are arranged so that the methyl groups and hydrogen groups of opposing sheets interact to form the intersheet stacking in the crystal. Van der Waals forces and hydrogen bonds generate a thermodynamic stable form which is water stable and insoluble in several solvents including mild acid and alkaline conditions. The third form (silk III) is represented by an unstable structure observed at the water/air interface, characterized by a predominance of helixes.[7,11]

1.2.1. Control of the structural conformation

The control of the silk conformation represents an important task during the processing of the silk fibroin (especially in the case of the regenerated one), because strongly determines the physical properties (mechanical, thermal, optical and dielectric) and the stability of the final silk-based structures. Common methods to induce a structural change involve the use of post-treatments of processed silk. A transition from helix and random coil structures to sheets can be induced by temperature,[12] alcohols (methanol, ethanol, 2-propanol),[13–15] humidity and water vapor,[16,17] high pressure,[18] mechanical stretching[19] and salt solutions.[20,21]

An important role in the conformation transition is played by water. Water molecules plasticize the protein structures with hydrogen bonds and promote the solvent-induced crystallization (e.g., methanol). Water enhance chain mobility of non-crystalline domains, by disrupting intramolecular cohesive forces between the protein chains and reducing the steric hindrance.[17,22] In the case of methanol treatment, the crystallization is related with a mechanism of dehydration. The presence of water induces the swelling of the protein, promoting the penetration on the polar alcohol molecules.[23] Water-vapor annealing can be also used to promote the formation of β-sheets. The presence of water reduces the glass transition temperature of the protein (e.g. from 180° C for dried silk protein to <25° C with 25% moisture content),[24] making possible to obtain a molecular motion of the protein chains with annealing under this temperature. The final content of sheets is controllable by acting on the temperature and the time of the treatment. **Figure 1.2**

schematizes the silk film secondary structure organization for both water annealed and methanol immersed methods.

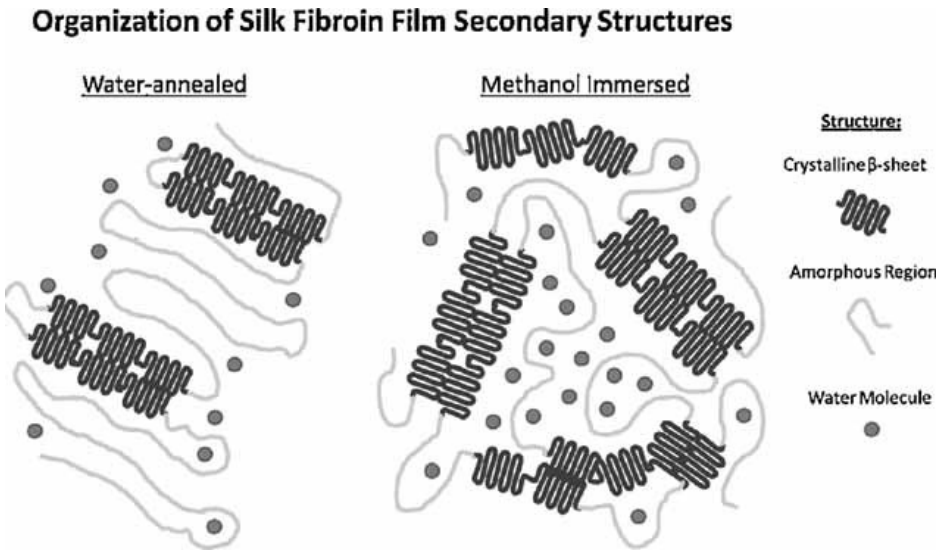

Figure 1.2. Schematic rapresentation of silk film secondasry structure organization for amourphous, β-sheets crystalline region and water molecules for both water-annealed and methanol immersed methods.[22]

An alternative method is to control the self-assembly of the protein during the processing, by acting on environmental conditions or by applying a stress (e.g. spinning). In the case of the drying process of silk films, three main factors influence the conformation of the fibroin: concentration, humidity and temperature. The self-assembly process of fibroin molecules results directly affected by the volatilization rate of water molecules in aqueous solution at constant environmental conditions. As reported in the phase diagram in **Figure 1.3**, in a particular range of conditions it is possible to have the coexistence of silk I and silk II structure.[10] Compared to the post-process treatments, this method often lack of reproducibility of the final material structural features.

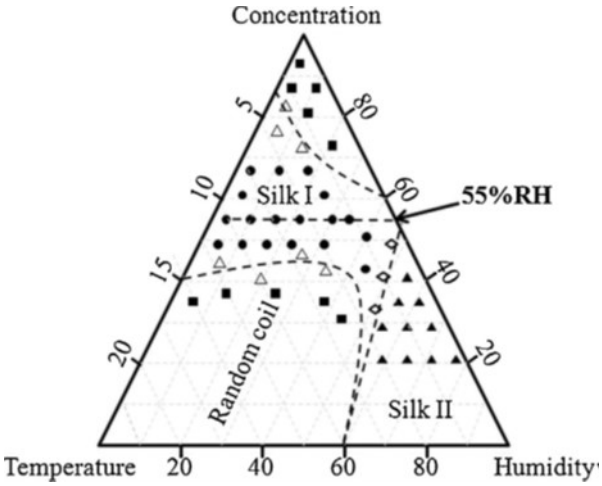

Figure 1.3. Partial ternary phase diagram of silk I structure formation.[10]

All these factors have to be taken into account during the process of the silk fibroin and the fabrication of devices, to optimize and control the final properties of the structures.

1.3. Properties of silk materials

1.3.1. Biocompatibility and biodegradability

Silk have been investigated for centuries as biomaterial due to the successful use of the silk fibers as suture material.[7] The biocompatibility of silk materials is a processing-dependent property. Problems of hypersensitivity and inflammatory processes were observed in the case of the virgin fibers. However, in the absence of the silk sericin component (degummed silk fiber), it was obtained a reduction of these issues and successful implantation and cell culture. Interesting, sericin by itself exhibits minimal macrophage response, suggesting that it may be the co-existence of the two protein (fibroin and sericin) that causes inflammatory responses. Regenerated fibroin, obtained from dissolution of degummed fibers, does not cause significant thrombogenic reactions, but also stimulates cell adhesion on its surface by promoting tissue growth.[25] From 1993 silk fibroin is recognized by the US Food and Drug Administration as biomaterial.[26]

Another feature of biomaterials, related to their in vivo application, is the degradation capacity. According to the definition of US Pharmacopoeia, fibroin is considered a non-degradable biomaterial, as fibers retain more than 50% of their tensile resistance after two months from their implantation. However, the studies reported in the literature demonstrate the degradability of the regenerated fibroin protein but at an average longer time. Fibroin is a polymer subjected to enzymatic degradation (through the action of the protease) whose degradation products are the amino acids that make up the protein itself. The rate of degradation of the fibroin substrates depends on the structure, morphology, and the mechanical and biological conditions of the site of implant. It is possible to control the degradation times by acting on the crystallinity and distribution of the molecular weight of the fibroin, as well as on the morphology of the substrate to be implanted.[7]

Thanks to these characteristics, fibroin is an ideal candidate for the fabrication of biomedical devices. The native form can be processed using textiles technique in wires, non-woven fabrics, and mats. Thanks to the versatile processability, various morphologies can be regenerated from dissolved fibers such as films, membranes, hydrogels and sponges. In addition, fibroin scaffolds (compared to other protein such as collagen) have the ability to be easily sterilized without denaturation of the protein (by using ethylene oxide, radiation γ, autoclave or ethanol).[25]

1.3.2. Mechanical properties

Natural silks (in particular spider silk) are known to present impressive mechanical properties, comparable to synthetic polymers such as Kevlar.[27] *B. mori* silk fibers have an ultimate tensile strength of 300-750 MPa and elastic modulus of 17 GPa, while *Nephila* silk can achieved 1100 MPa as ultimate strength. The mechanical properties of silks are listed in **Table 1.1** and compared with other synthetic fibers.[9]

Table 1.1. Mechanical data of silk-worms silk along with other fibrous materials.[9]

Material	Young's modulus (GPa)	Ultimate strength (MPa)	Breaking Strain (%)	Toughness (MJm^{-3})
Silkworm silk fibroin (Bombyx mori)	10-17	300-740	4-26	70-78
B-sheet crystallites (Bombyx mori)	16-18	-	-	-
Spider silk (Nephila clavipes)	10.9	875	16.7	
Spider silk (Nephila edults)	-	1300	38	200
Spider silk (Araneus)	10	1100	27	160
Collagen	0.0018-0.0046	0.9-7.4	24-68	-
Wool	0.5	200	50	60
Nylon	1.8-5	430-95	18	80
Kevlar	130	3600	2.7	50
Propylene	4.6	490	23	-

These impressive mechanical properties are closely related with the hierarchical structure of the silk. The strength and the stiffness are dictated mainly by the β-sheets crystallites, while the elongation and the toughness are governed by the semi-amorphous regions. Silk fibroin can form intramolecular/intermolecular β-sheets, parallel/antiparallel β-sheets, as well as crystallites of different sizes and orientations. All these factors influence the mechanical behavior of the final structure. Intramolecular β-sheets increase the strength of the fibers compared to the intermolecular ones, and this explains why spider silk presents an higher ultimate modulus compared to the worm silk. Recently, it was found that crystallites confined to a few nanometers can achieve higher strength, stiffness and toughness compared to large crystallites. On the other hand, the orientation of this crystallite plays an important role: naturally spun silkworm silk has been reported to have an orientation function.[9]

The mechanical properties of the silkworm silk are not limited to the natural fibers. It is possible to enhance the properties of both natural and regenerated silk by acting on the fabrication process, by changing morphologies and by functionalization.[9]

1.3.3. Electronic properties

Silk is a natural insulator in the net state, with a relatively high dielectric constant (~7).[28] Silk films were used as gate dielectric materials of organic thin-films transistor (OTFT), because they present several advantageous features, such as solution-processability, flexibility, optical transparency (ca. > 90%), and great resistance to organic solvents.[29] Wang et al. fabricated a pentacene OTFT using a 420 nm thick silk film (capacitance of 30 $nFcm^{-2}$) as the gate dielectric material, which exhibits high field-effect mobility and at a low operating voltage.[30] Shi et al. have employed 337 nm thick silk film (capacitance of 10.8 $nFcm^{-2}$) as the gate dielectric material in the fabrication of a poly(3-hexylthiophene) based OTFT , which operates in devices driven by low voltage.[31] More recently Park et al. demonstrate that the dielectric performances of silk fibroin as gate in OTFT are strictly dependent of the secondary structure of the protein.[32] In particular, inter-chain hydrogen bonding in β-sheet structure plays a key role in both insulating properties of gate-dielectric and electrical properties. Silk fibroin can contain free -CO and -NH groups, which are not restricted to inter-chain hydrogen bonding in β-sheet structure. Under negative gate-bias, these mobile groups increase dipole of the gate-dielectric, inducing slow polarization. Instead, in the case of methanol treated films, the same groups are strongly restricted by hydrogen bonding and not polarization effects were observed.[32]

Despite these works, recently it was demonstrated that silk membranes deriving from natural cocoons can generate electrical current in particular condition of temperature and moisture.[33] Even the mechanism is not very clear, researchers observed that the electrical behaviors are strongly dependent on the wet state and the presence of elements such as Na, K, Cl, S, Mg in the membranes. This suggests that the generation of observed current was caused by ionic conduction. A probable explanation is that, in presence of moisture and water vapor, the water molecules diffuses into the porous matrix, become mobile, and interact with elements like Na, K,

Cl as well as with the protein matrix, resulting in the generation of charged ionic species.

1.3.4. Thermal properties

The thermal properties of silk protein materials are strongly influenced by the hydration conditions. Silk protein has a compact crystal structure, resistant to interaction with water molecules. Instead, the amorphous regions of the chains are accessible to water molecules. The interaction of the amorphous regions with water disrupt the hydrogen bonds between the amides, improving the mobility of the protein chains. This results in a lower glass transition temperature (T_g) of the protein. This thermal behavior was investigated by using differential scanning calorimetry (DSC) and thermogravimetric analysis (TG).[13,16,34–36] In the case of *Bombyx mori,* it was found that a film obtained by regenerated silk fibroin solution containing 5% of moisture showed a T_g at around 60° C, while in the dry state it was around 178° C. [24] The heat capacity of the solid silk-water system, below T_g, was estimated from a sum of linear combinations of the molar fractions of the vibrational heat capacities of dry silk and glassy water. Below T_g, contributions to the heat capacity of solid silk and the silk-water system was found related only with the vibrational motions. In the case of amorphous films, the heat capacity increases beyond the vibrational limit when approaching T_g due to a large-amplitude motion.[37]

For a random coil silk fibroin, intra- and inter-molecular hydrogen bonds are broken between 150 and 180° C. The glass transition is observed at 175° C. The random-coil to β-form transition accompanied by reformation of hydrogen bonds occurs above 180° C, while crystallization to the β-form crystals starts at above 190° C. The α-form and β-form fibroins lose water up to 100° C on heating, and molecular motions in the crystalline regions starts at 175° C. The α-form to β-form transition is induced thermally at 270° C. [34] **Figure 1.4** shows typical DSC curves for silkworm silk fibroin films.

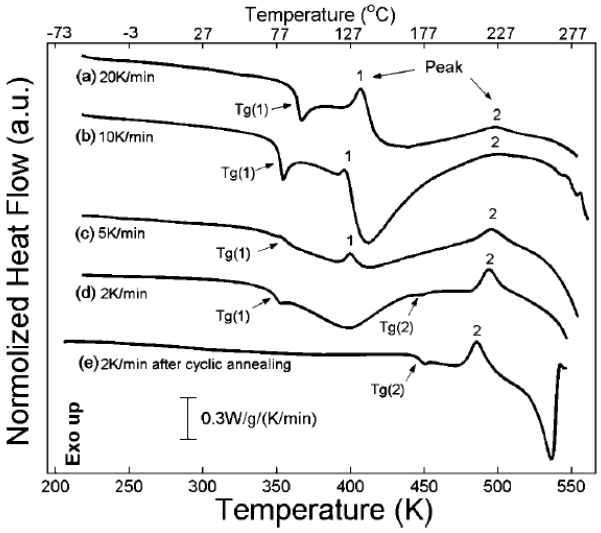

Figure 1.4. Standard DSC scans of silk fibroin films from -65 to 280 °C with the heating rates (a) 20, (b) 10, (c) 5, (d) 2, and (e) 2 K/min. The samples from (a) to (d) are silk fibroin films containing 5.5 wt % bound water molecules before heating. The sample in (e) is a totally pure silk fibroin sample after water removal. The heat flow has been normalized for sample mass and for heating rate.[12]

Silk fibroin shows a thermal behavior stable until 150° C. In presence of water instead, an endothermic peak ranging from 80 to 150° C is commonly detectable and related to water evaporation associated with a weight loss (from TG analysis). In these samples it is also possible to observe a first glass transition in the range between 60°C to 160° C, as previously anticipated. At 178° C, they go through the same glass transition reported in previous study. The thermal degradation associated happens around 280° C.[12]

1.3.5. Optical properties

Thanks to the transparency, mechanical robustness, biocompatibility, easy surface-patterning and degradability, silk has attracted attention as material for optical application. Silk materials are transparent in a wide range (300-2000 nm) with a characteristic absorption in the wavelength range 270-300 nm, assigned to π->π* transition of the Tyr, Phe and Try residues aminoacidic in the molecular chain.[38] From an optical point of view, the performances of silk are dictated by the refractive index and in particular by the refractive index contrast between silk and

the environment. Compared to other polymer and protein based materials, silk present an high refractive index (1.54 at 633 nm).[39]

Recently, Perotto et al. (2017) published a work where they extensively investigated the optical properties of regenerated silk fibroin extracted from *Bombyx mori*, *Antheraea mylitta*, *Samia ricini* and *Anthanaraea assamensis*.[40] They found that the refractive index of the regenerated *B. mori* silk was found to be 1.543±0.001 at 630nm, in agreement with the result previously reported. *A. mylitta* silk has a refractive index similar to the *Bombyx mori* silk (1.539 @500 nm), while *A. assamensis* and *S. ricini* had significantly lower refractive indices at 500 nm: 1.521 and 1.499 respectively. Interesting, the refractive index and the absorption of the silk extracted from the gland of the *Bombyx mori* silkworm were higher (n= 1.566±0.001) compared to the regenerated one, probably due to a slightly more dense packing of the secondary structure. In **Table 1.2** the optical constant obtained from the ellipsometry characterization are reported for the different types of silk.

Table 1.2. Values of the refractive index at 500 nm, Cauchy parameters, and Urbach absorption amplitude for the different types of silks.[40]

		Uncryst. *B. mori*	**Cryst. *B. mori***	**Native *B. mori***	***A. mylitta***	***S. ricini***	***A. assamensis***
n (@ 500 nm)		1.554	1.558	1.566	1.539	1.499	1.524
Cauchy	A	1.5231 ± 0.0004	1.5303 ± 0.0003	1.551± 0.001	1.5204 ± 0.004	1.475 ± 0.004	1.504 ± 0.001
	B	0.0079 ± 0.0001	0.0066 ± 0.0001	0.0026± 0.0003	0.0036 ± 0.0011	0.0057 ± 0.0009	0.0047 ± 0.0004
	C	$6{\cdot}10^{-6}$ ± $1{\cdot}10^{-6}$	110 10^{-6} ± $10{\cdot}10^{-6}$	240 10^{-6} ± $30{\cdot}10^{-6}$	$290{\cdot}10^{-6}$ ± $100{\cdot}10^{-6}$	$50{\cdot}10^{-6}$ ± $100{\cdot}10^{-6}$	$120{\cdot}10^{-6}$ ± $40{\cdot}10^{-6}$
Uerbauch	A	0.0028 ± 0.0006	0.003 ± 0.001	0.029± 0.001	0.005 ± 0.009	0.043 ± 0.008	0.024 ± 0.002

In another recent work, Asha et al. (2015) reported the tuning of the refractive index and the optical band gap of silk fibroin films by electron irradiation.[38] They observed that the absorption band of the silk films changed with the increase of the irradiation dose, while its position slightly shifted to higher wavelength. The Band gap energy of virgin silk was measured 4.18 eV, while the Urbach energy 0.524 eV.

Both the values decreased in the irradiated samples probably because of the decreased in the crystalline nature of the silk. On the other side, they found an increase of the refractive index with irradiation doses.

Finally, the non-linear optical properties of silk fibroin fibers were recently characterized. In their work Kuiala et al.,[41] observed a second harmonic generation and a third harmonic generation signals originated from configurational defects such as torsional twisting. They also characterized the waveguiding properties of *B. mori* silkworm silk fibers, observing a value of propagation loss coefficient of about 2.8 $dBmm^{-1}$ on average, which decreased with longer wavelength. This loss coefficient was correlated to two primary effects: material and waveguide properties, and localized scatters (such as debris on fiber surface and helical twisting of the fibers).

1.4. Processing methods

The processing of the silk materials starts from the preparation of the silk solutions from dissolution of the natural sources. The regenerated silk fibroin solution (RSF) can be easily arranged in different forms like films, fibers, powder, hydrogels, mat, sponges and coatings, by using different techniques on both the micro- and the nano-scale. A schematic overview of the process used to obtain the solution from the fibers and of the different final forms is reported in **Figure 1.5**.

As first step, silk fibers are dissolved in a denaturating agent to prepare a processable aqueous based solution. Different denaturating agents can be used, such as chaotropic salts solution like lithium bromide (LiBr).[42,43] The salts can be easily exchanged by dialysis to obtain a final water based solution. Alternatively, silk proteins can be dissolved in fluorinated organic solvents such as hexafluoroisopropanol (HFIP) or acid like formic acid (FA).[44,45] For the *Bombyx mori* silk the most diffused method to obtain the silk protein solution involved the degumming of the fibers to remove the sericin, followed by dissolution in a concentrate LiBr solution. A final dialysis process in DI water provides a pure aqueous

solution of silk fibroin. The reader can find all the details in the protocol published by Rockwood et al. [42]

After preparing the silk solution, additional substances can be added before or during the processing, such as plasticizers (e.g., glycerol),[46] other synthetic polymer or biopolymer,[1,25,47] inorganic (such as quantum dots, metal nanoparticles) [48–52] or organic dopant (cells, enzymes, proteins).[53]

Silk fibroin (SF) can be assembled in micro- and nanoparticles by using several methods. SF molecules can be arranged in a particle shape through interaction between the hydrophilic and hydrophobic chain segments. The self-assembly can be promoted by the addition of organic solvent (such as ethanol),[54] poly vinyl alcohol (PVA)[55] or phosphate buffer solution,[56] or by quenching below the freezing point[57] or by milling.[58] Various other methods have been reported, including desolvation, spray drying, laminar jet break-up, capillary microdot and electrospray techniques.[11]

The principal application of the SF particles is in drug delivery, thanks to the possibility to easy incorporate small drugs without retention of their function and to control the release by acting on the degradation of the SF through control of the secondary structure. Other applications are in wound healing and bioimaging.[59]

SF fibrously structures such as fibers and mats are obtained by spinning processes. One of the most common is the electrospinning because of its flexibility and versatility. The morphology and the structure of SF can be tune by acting on the concentration, flow rate, voltage and receive distance. The electrospun mats can be spinned by using solvents such as polyethylene oxide (PEO), hexafluoroisopropanol (HFIP), formic acid, hexafluoroacetone (HFA) or using high concentrated SF all-aqueous solution. Inorganic dopants can be easily added to fabricate composite mats.[60–63]

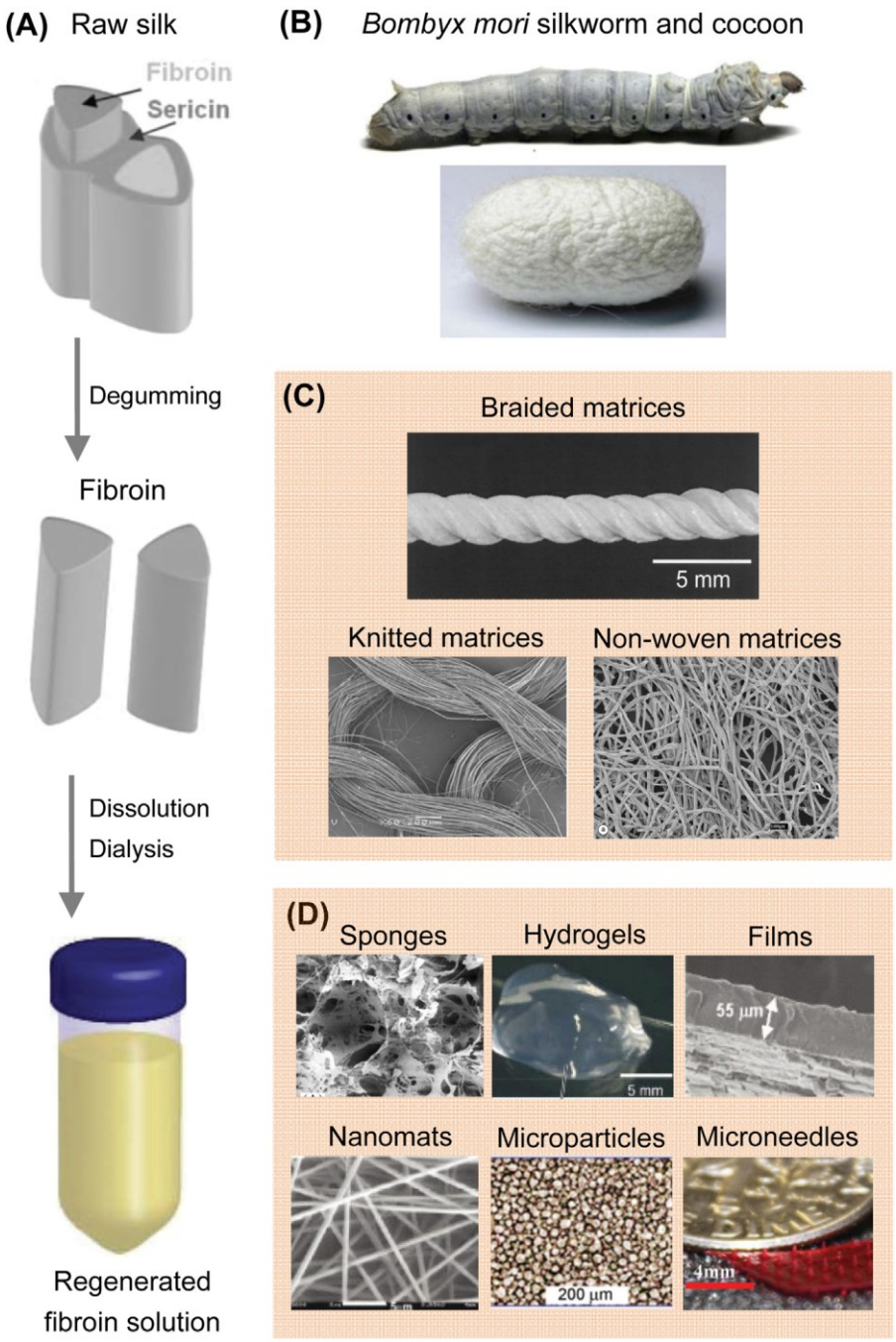

Figure 1.5. Bombyx mori silkworm silk in various morphologies. (A) The raw silk consists of two fibroin fibers held together with a layer of sericin on theirsurfaces. After degumming to remove sericin, the fibroin fibers are dissolved in lithium bromide solution followed by dialyzing against ultrapure wateror polyethylene glycol to obtain regenerated fibroin solution. (B) Mature silkworm and produced cocoon. (C) Silk braided, knitted, andnon-woven matrices constructed from the fibroin fibers. (D) Silk sponges, hydrogels, films, nanofibrous mats, microparticles, and microneedles constructed from the regenerated fibroin solution.[9]

Fibroin hydrogels are formed via sol-gel transition trough the aggregation of the fibroin molecules into β-sheets or cross-linking of fibroin molecules to form an interconnected network with high water content. The gelation of SF can be promoted by sonication, vortex, heating, solvent treatment, photo-crosslinking and electrogelation.[64–69] Recently, a new method has been proposed by Partlow et al. to fabricate highly tunable elastic SF hydrogels via crosslinking of Tyrosine residues in SF generated by horseradish peroxidase (HRP) and hydrogen peroxide.[70]

Three-dimensional SF scaffold and sponges can be obtained by salt leaching, gas foaming, freeze-drying or by 3D printing techniques. For the salt leaching technique, NaCl particles are usually used as porogens.[7,42,71] On the other hand, lyophilized SF sponges with a controlled porosity can be fabricated by controlling freeze temperature and concentration. More recently, the rapid prototyping technologies has been used to create three-dimensional scaffold by using silk based solution as ink for direct writing.[72–75] The use of 3D techniques allows the fabrication of SF predesigned structures that can meet requirements for tissue engineering application.[11]

The silk water solution can be then processed into films and coatings using various processing techniques such as casting, spin coating, vertical deposition and spin assisted layer-by-layer assembly. Mechanically robust films can be obtained by simple casting of the solution on a smooth and clean plate with natural evaporation or drying under a certain temperature, with the ability to control the thickness from ten nanometers to hundred micrometers.[76,77] Thin films can be prepared by using spin-coating or dip-coating.[2,78] Spin-assisted layer-by-layer assembly method is able to produce ultrathin (ten nanometers) and mechanically robust free-standing silk fibroin films, resulted by physical formation of β-sheets during the spin coating process without the use of cross-linking reactions.[79] SF fibroin films with controlled architecture can be also obtained by electrogelation.[80]The stability of the films can be also improved by acting on the secondary structure of the protein using water-annealing,[17] alcohol immersion,[81] stretching[82] or slow-drying.[83]

As anticipated, silk films can be formed even on the micro- and nano-scale. Simple casting on patterned surfaces can be used to replicate nanostructures with feature sizes less than 10 nanometers.[77] Photolithography is a widely used method to fabricate micropatterned SF materials.[84] Park et. al reported the use of SF as a positive-tone photoresist in lithography, using water as chemical develop without the necessity to introduce photo-initiators or to use harsh solvent.[85] Soft-lithography is another technique used to produce optical-grade micro and nanopatterns on SF films, based on molding and printing with an elastomeric stamp, highly effective, convenient and inexpensive.[86] Electron beam lithography was also successfully employed to produce nanometer scale patterns using all water based silk solution as resist. Thanks to its polymorphic crystalline structure, silk was used either as a positive or negative resist through interactions with an electron beam.[87] The silk solution can also be used to direct write microstructures using the inject printing technique. The incorporation of nanoparticles, enzymes, antibiotics, growth factors opens the possibility of generating a portfolio of functional inks that can be used to print forms with extended and useful functions.[39,88]

1.5. Silk-based nanocomposites

Silk is a unique material because of its mechanical properties associated with biocompatibility and biodegradability. A new approach to improve the properties of the silk is the development of multifunctional composites through the combination of active organic or inorganic counterparts, which provide new properties to the hybrid systems.[89] A wide range of composite materials were developed combining silk proteins with polymer (both synthetic and natural), proteins and polysaccharides, organic and inorganic particles. Here a brief review of the silk-nanoparticles composites materials will be presented, with a particular attention for the metal and metal oxide nanoparticles (NPs).

Metal NPs can be conjugated to many proteins by simple mixing the proteins solution with a metal colloidal solution and the protein typically bonds to the metal

trough the amines or thiols groups. Alternatively, metal NPs can be grown inside the protein matrix by reducing the precursors using redacting agents or UV irradiations. Silk fibroin has already been combined with metal NPs, in particular silver and gold.[89]

Silver (Ag) nanoparticles have antibacterial and electronic properties, that make them interesting for applications in coatings and textiles. SF fibers have been coated with Ag NPs by simply immersing the fibers in a solution of NPs or in a precursor solution (silver salt), inducing the formation of the metallic silver by photochemical reduction or by tyrosine mediated reduction in basic condition.[90–92] Ag NPs were easily synthesized using SF as biotemplate with a green process based on the photoreduction of silver nitrate salt promoted by a lamp or sunlight, where silk had the double function of stabilizer and dispersing agent. The nanocomposite material was then used as film for antibacterial application.[93] Da Silva et al. reported the incorporation of Ag NPs in a SF film for the development of a distributed feedback (DFB) laser.[52]

Gold (Au) NPs are extensively study for biomedical and sensing application because of their optical properties associated with low cytotoxicity. Au NPs were grown on silk fibers via an in-situ redox reduction between the tyrosine residues on the silk protein and the gold ions.[94,95] Naturally spun spider silk fibers have been coated with gold NPs via incubation in aqueous solution of chloroauric acid.[96] Recently, silk-gold NPs composites were easily synthesized by simple mixing silk solution and Au NPs solution and used as substrate for surface enhancement Raman spectroscopy (SERS) application[97] or deposited as thin films for broadband absorber.[98] Gold NPs were also incorporated in silk inverse opals or hydrogel for photo-dynamic application.[99,100] In another work, Das et al. report the use of a silk-gold nanocomposites for the fabrication of a conduit for functional peripheral nerve regeneration.[101] Gogurla et al. combined gold NPs and SF for the fabrication of a flexible resistive switching memory device.[102] In another recent work, they instead demonstrated negative photoconductivity in gold-silk hydrogel exposed to UV light.[103]

Silk proteins were also combined with transition metal oxides or sulfides. Natural spider silk fibers were dip-coated with such NPs to obtain magnetic fibers without detrimental effects on the mechanical properties.[96] Silkworm silk fibers were also decorated with magnetite NPs by grafting with electrostatic interaction.[104] Core–shell magnetite/SF NPs were successfully prepared via a one-step solvothermal process and their biocompatibility was demonstrated for biomedical application as MRI contrast agents and drug carriers.[105] More recently, magnetite NPs were incorporated in silk scaffolds for wound healing application.[106]

Films composed of SF and titanium dioxide NPs were prepared by sol-gel method using ultrasonication. Compared to the pure SF films, the mechanical and thermal properties of SF/nano-TiO2 composite films were improved, and the solubility in water was decreased due to the formation of structural transition from Silk I to Silk II during the preparation of SF composite film.[107] Membrane prepared using the same approach showed also higher crystallinity and better antibacterial activity.[108] Recently, Cai et al. demonstrated the *in vivo* incorporation of nano-TiO_2 in silkworm silk by introduction of the particles in the worms diet. The produced silk showed improved mechanical properties and ultraviolet resistance.[109]

SF was also combined with luminescent quantum dots (QDs). For example, cadmium telluride (CdTe) nanocrystals were chosen to impart luminescence to silk fibers by electrostatic grafting.[110] Cadmium sulphide QDs were successfully synthesized on the surface of silk fibers via γ-ray irradiation.[111] 2-mercaptoethylamine- (MEA-) and mercaptopropionic acid- (MPA-) capped CdTe-QDs were physically incorporated in silk films and the films were used as optical sensor for detection of hydrogen peroxide in solution.[49] Li et al. incorporated functionalized blue-light ZnSe and the yellow-light CdTe QDs in silk films and characterized the white-light-emitting properties.[112]

Beside the metal and metal oxide NPs, a wide range of minerals and biominerals were introduced in silk matrix to improve the mechanical properties and promote biomineralization process. Among them, we can count calcium carbonate, calcium phosphate (hydroxyapatite),[89] silica[48] and hydrotalcite.[113]

Finally, it is also important to mention the silk-based nanocomposite obtain by the combination of silk with carbon-based NPs and graphene. Chakravarty et al. fabricated a silk-carbon NPs scaffold for chemiresistive sensing of nitroaromatic compound.[51] Silk-carbon nanotube composites were used as electrode for flexible biocatalytic fuel-cell[114] or as substrate to induce human stem cell neuronal differentiation.[5,115] Ultra-robust graphene oxide-silk fibroin nanocomposites membranes were fabricated by using a layer by layer approach.[116] Alternatively, silk fibroin-graphene oxide films with high tensile strength were obtained by casting composite hydrogels.[117] Hybrid nanocomposites were also obtained by direct growth of silk nanofibrils on graphene sheets.[118]

1.6. Application of silk materials

The first application of the silk-based materials is in the biomedical field. Silk shows interesting features such as biodegradability and biocompatibility that make it ideal for the development of scaffolds, wound dressing as well as drug delivery system.[7,25] Silk fibers both natural and spinned are used as sutures. Non-woven mats prepared via electrospinning are currently investigated as antibacterial wound dressing, while silk-based hydrogels were demonstrated to promote wound healing. Electrospun fibers, 3D printing scaffold and coating are also investigated for application in tissue engineering and to promote cell growth. Silk based particles are instead studied for drug-delivery applications.[11,89,119] Recently, silk was also employed for the fabrication of an organic retina[120] or in nerve regeneration.[101]

B. mory silk fibers have been used for century in textile industry due to their strength and luster. One of the problem is that they are subject to phototendering and phtoyellowing.[121] The fabrication of a new class of silk-based fibers composed of regenerated fibroin and other components can reduced this problem. The addition of polyacrylonitrile for example, improve the stability to photo-oxidation, while the incorporation of silver adds to the fabric antibacterial properties.[61,89,122] A new

approach for intrinsic functionalization and coloration can be also provide a greener and cost effective solution for dyeing industry.[123]

Thanks to the barrier properties and the capability to preserve the functionality of complex molecules,[53] recently silk was proposed as "packaging" material for stabilize and preserve at room temperature drugs and antibiotic,[124] or as edible coating for perishable food preservation.[125] Zhang et al. demonstrated that self- standing silk protein biomaterial matrices were capable of stabilizing labile vaccines and antibiotics, even at temperatures up to 60° C over more than 6 months.[124] On the other hand, Marelli et al. created dip-coated film on fruits and demonstrated that, thanks to the water-based post-processing control of the protein polymorphism, the diffusion of gases through the silk fibroin thin membranes (e.g. O_2 and CO_2 diffusion, water vapour permeability) was reduced, enhancing the fruits' shelf life at room conditions.[125]

The ability to reform the material into thick films enables the use of silk as a substrate for microfluidic devices. Silk-based microfluidic devices were fabricated by using a water-based soft-lithography technique for cells culture applications.[126] Tsioris et al. reported silk based pH sensor (optofluidic device) by combining optically active and chemically modified (with carboxylic acid) silk film with PDMS microfluidic platform.[127] More recently, Zhao et al. fabricated a bio-functionalized microfluidic system using an elastomeric silk hydrogel as substrate material.[128]

Silk fibroin is being actively investigated for use as supporting or substrates in optics and sensors. As anticipated, thanks to its refractive index higher than air and water, silk can be used for light-guiding or light-confinement. Fibroin as been developed as waveguides and implantable optical fibers,[39,129] gratings,[130] lens,[4] holograms[131] and microprism arrays.[132] 2D and 3D photonic structures were fabricated with silk by using different techniques. Structural color based on periodic nanopatterned 2D lattices in silk protein films were demonstrated by imprinting periodic lattices of nanoscale holes and use as substrates for refractive index sensing of liquid and for glucose monitoring.[133,134] Kim at al. demonstrated the fabrication of

silk inverse opals structures by direct replica of an opal template.[99] Thanks to a specific functionalization, silk inverse opals were studied as sensing platform for colorimetric immunosensing[135] or tissue culture.[136] More recently, deformable silk hydrogel inverse opals were fabricated via photo-crosslinking of stilbene chromophore with silk molecules for application as an artificial tapetum, to help improve human night vision to see as nocturnal animals do.[69] Not only photonic sensors, but even plasmonic or hybrid systems were fabricated by combining silk with gold and silver for sensing and bio-sensing applications [137–139] or as insulator-metal resonator.[140]

Silk was also proposed as substrates for metamaterials,[141] resorbable and degradable electronics,[142,143] conformal implantable and dissolvable electrodes,[144] optical antenna for food sensing [145] or detection of tooth enamel. [146] As previously explained, silk is also used as dielectric for the fabrication of OTFT [30] or as substrate for the fabrication of flexible organic solar cells.[147]

An overview of all the possible applications of silk based materials is illustrated in **Figure 1.6**.

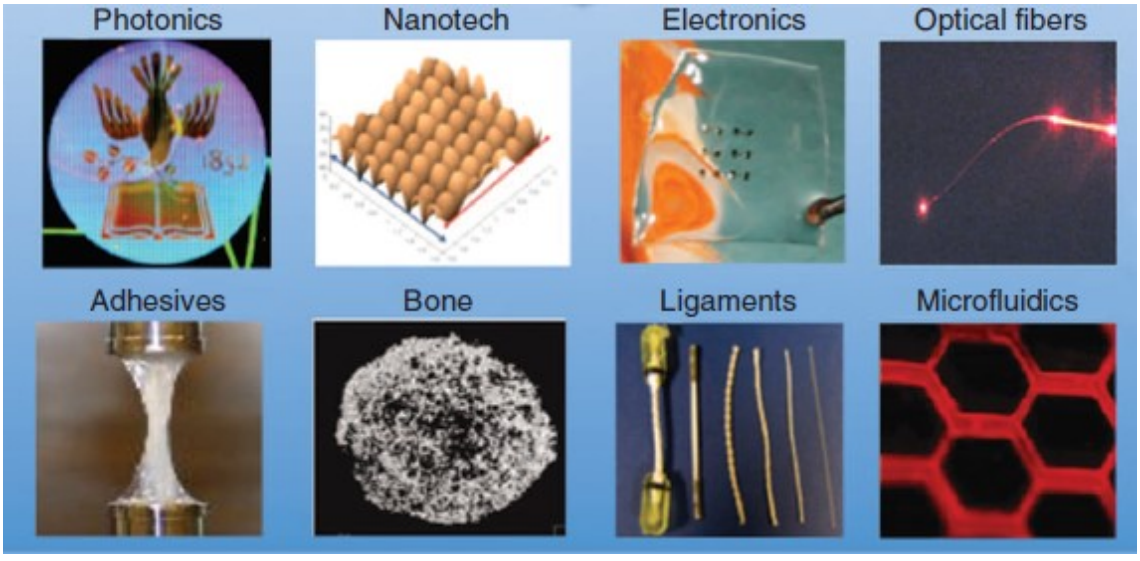

Figure 1.6. Schematic illustration of all the main applications of the silk-based materials, ranging from medicine (e.g, scaffolds for bone regeneration or ligaments) to optics, photonics, microfluidics and electronics.[1]

References

[1] F. G. Omenetto, D. L. Kaplan, *Science (80).* **2010**, *329*, 528.

[2] H. Tao, D. L. Kaplan, F. G. Omenetto, *Adv. Mater.* **2012**, *24*, 2824.

[3] F. G. Omenetto, D. L. Kaplan, *Nat. Photonics* **2008**, *2*, 641.

[4] H. Tao, D. L. Kaplan, F. G. Omenetto, *Adv. Mater.* **2012**, *24*, 2824.

[5] C. Dionigi, T. Posati, V. Benfenati, A. Sagnella, A. Pistone, S. Bonetti, G. Ruani, F. Dinelli, G. Padeletti, R. Zamboni, M. Muccini, *J. Mater. Chem. B* **2014**, *2*, 1424.

[6] C.-Z. Zhou, F. Confalonieri, M. Jacquet, R. Perasso, Z.-G. Li, J. Janin, *Proteins Struct. Funct. Genet.* **2001**, *44*, 119.

[7] C. Vepari, D. L. Kaplan, *Prog. Polym. Sci.* **2007**, *32*, 991.

[8] C. Z. Zhou, F. Confalonieri, N. Medina, Y. Zivanovic, C. Esnault, T. Yang, M. Jacquet, J. Janin, M. Duguet, R. Perasso, Z. G. Li, *Nucleic Acids Res.* **2000**, *28*, 2413.

[9] L. D. Koh, Y. Cheng, C. P. Teng, Y. W. Khin, X. J. Loh, S. Y. Tee, M. Low, E. Ye, H. D. Yu, Y. W. Zhang, M. Y. Han, Structures, mechanical properties and applications of silk fibroin materials. *Prog. Polym. Sci.* **2015**, *46*, 86–110.

[10] J. Ming, F. Pan, B. Zuo, *Int. J. Biol. Macromol.* **2015**, *75*, 398.

[11] Y. Qi, H. Wang, K. Wei, Y. Yang, R.-Y. Zheng, I. Kim, K.-Q. Zhang, *Int. J. Mol. Sci.* **2017**, *18*, 237.

[12] X. Hu, D. Kaplan, P. Cebe, *Macromolecules* **2008**, *41*, 3939.

[13] M. Tsukada, Y. Gotoh, M. Nagura, N. Minoura, N. Kasai, G. Freddi, *J. Polym. Sci. Part B Polym. Phys.* **1994**, *32*, 961.

[14] D. Wilson, R. Valluzzi, D. Kaplan, *Biophys. J.* **2000**, *78*, 2690.

[15] H. Y. Kweon, Y. H. Park, *J. Appl. Polym. Sci.* **1999**, *73*, 2887.

[16] H.-J. Jin, J. Park, V. Karageorgiou, U.-J. Kim, R. Valluzzi, P. Cebe, D. L. Kaplan, *Adv. Funct. Mater.* **2005**, *15*, 1241.

[17] X. Hu, K. Shmelev, L. Sun, E.-S. Gil, S.-H. Park, P. Cebe, D. L. Kaplan, *Biomacromolecules* **2011**, *12*, 1686.

[18] H. Peng, S. Zhou, J. Jiang, T. Guo, X. Zheng, X. Yu, *J. Phys. Chem. B* **2009**, *113*, 4636.

[19] H.-J. Jin, D. L. Kaplan, *Nature* **2003**, *424*, 1057.

[20] X. Chen, D. P. Knight, Z. Shao, F. Vollrath, *Biochemistry* **2002**, *41*, 14944.

[21] C. B. Borkner, M. B. Elsner, T. Scheibel, *ACS Appl. Mater. Interfaces* **2014**, *6*, 15611.

[22] B. D. Lawrence, S. Wharram, J. A. Kluge, G. G. Leisk, F. G. Omenetto, M. I. Rosenblatt, D. L. Kaplan, *Macromol. Biosci.* **2010**, *10*, 393.

[23] J. Magoshi, M. Mizuide, Y. Magoshi, K. Takahashi, M. Kubo, S. Nakamura, *J. Polym. Sci. Polym. Phys. Ed.* **1979**, *17*, 515.

[24] X. Hu, D. Kaplan, P. Cebe, *Thermochim. Acta* **2007**, *461*, 137.

[25] B. Kundu, N. E. Kurland, S. Bano, C. Patra, F. B. Engel, V. K. Yadavalli, S. C. Kundu, *Prog. Polym. Sci.* **2014**, *39*, 251.

[26] J. Melke, S. Midha, S. Ghosh, K. Ito, S. Hofmann, Silk fibroin as biomaterial for bone tissue engineering. *Acta Biomater.* **2016**, *31*, 1–16.

[27] D. Porter, F. Vollrath, *Adv. Mater.* **2009**, *21*, 487.

[28] J. Veres, S. Ogier, G. Lloyd, D. De Leeuw, Gate insulators in organic field-effect transistors. *Chem. Mater.* **2004**, *16*, 4543–4555.

[29] B. Zhu, H. Wang, W. R. Leow, Y. Cai, X. J. Loh, M.-Y. Han, X. Chen, *Adv. Mater.* **2016**, *28*, 4250.

[30] C.-H. Wang, C.-Y. Hsieh, J.-C. Hwang, *Adv. Mater.* **2011**, *23*, 1630.

[31] L. Shi, X. Xu, M. Ma, L. Li, *Appl. Phys. Lett.* **2014**, *104*, 23302.

[32] M. H. Park, J. Kim, S. C. Lee, S. Y. Cho, N. R. Kim, B. Kang, E. Song, K. Cho, H.-J. Jin, W. H. Lee, *RSC Adv.* **2016**, *6*, 5907.

[33] B. Tulachan, S. K. Meena, R. K. Rai, C. Mallick, T. S. Kusurkar, A. K. Teotia, N. K. Sethy, K. Bhargava, S. Bhattacharya, A. Kumar, R. K. Sharma, N. Sinha, S. K. Singh, M. Das, *Sci. Rep.* **2015**, *4*, 5434.

[34] Shigeo Nakamura, J. Magoshi, Y. Magoshi, In *Silk Polymers: Materials Science and Biotechnology*; American Chemical Society: Washington DC, 1994; pp. 211–221.

[35] J. Guan, Y. Wang, B. Mortimer, C. Holland, Z. Shao, D. Porter, F. Vollrath, *Soft Matter*

2016, *12*, 5926.

[36] J. E. Brown, S. K. Davidowski, D. Xu, P. Cebe, D. Onofrei, G. P. Holland, D. L. Kaplan, *Biomacromolecules* **2016**, *17*, 3911.

[37] M. Pyda, X. Hu, P. Cebe, *Macromolecules* **2008**, *41*, 4786.

[38] S. Asha, Y. Sangappa, S. Ganesh, *J. Spectrosc.* **2015**, *2015*, 1.

[39] S. T. Parker, P. Domachuk, J. Amsden, J. Bressner, J. A. Lewis, D. L. Kaplan, F. C. Omenetto, *Adv. Mater.* **2009**, *21*, 2411.

[40] G. Perotto, Y. Zhang, D. Naskar, N. Patel, D. L. Kaplan, S. C. Kundu, F. G. Omenetto, *Appl. Phys. Lett.* **2017**, *111*, 103702.

[41] S. Kujala, A. Mannila, L. Karvonen, K. Kieu, Z. Sun, *Sci. Rep.* **2016**, *6*, 22358.

[42] D. N. Rockwood, R. C. Preda, T. Yücel, X. Wang, M. L. Lovett, D. L. Kaplan, *Nat. Protoc.* **2011**, *6*, 1612.

[43] D. M. Phillips, L. F. Drummy, D. G. Conrady, D. M. Fox, R. R. Naik, M. O. Stone, P. C. Trulove, H. C. De Long, R. A. Mantz, *J. Am. Chem. Soc.* **2004**, *126*, 14350.

[44] K. Makaya, S. Terada, K. Ohgo, T. Asakura, *J. Biosci. Bioeng.* **2009**, *108*, 68.

[45] I. C. Um, H. Kweon, Y. H. Park, S. Hudson, *Int. J. Biol. Macromol.* **2001**, *29*, 91.

[46] S. Lu, X. Wang, Q. Lu, X. Zhang, J. A. Kluge, N. Uppal, F. Omenetto, D. L. Kaplan, *Biomacromolecules* **2010**, *11*, 143.

[47] V. Gupta, A. Aseh, C. N. Ríos, B. B. Aggarwal, A. B. Mathur, *Int. J. Nanomedicine* **2009**, *4*, 115.

[48] A. Hou, H. Chen, *Mater. Sci. Eng. B Solid-State Mater. Adv. Technol.* **2010**, *167*, 124.

[49] D. Lu, Z. Zheng, S. Guo, C. Wang, D. L. Kaplan, X. Wang, *J. Sensors* **2015**, *2015*.

[50] L. Jia, L. Guo, J. Zhu, Y. Ma, *Mater. Sci. Eng. C* **2014**, *43*, 231.

[51] S. Chakravarty, N. Bhardwaj, B. B. Mandal, N. Sen Sarma, *J. Mater. Chem. C* **2016**, *4*, 8920.

[52] R. R. da Silva, C. T. Dominguez, M. V. dos Santos, R. Barbosa-Silva, M. Cavicchioli, L. M. Christovan, L. S. a. de Melo, A. S. L. Gomes, C. B. de Araújo, S. J. L. Ribeiro, *J. Mater. Chem. C* **2013**, *1*, 7181.

[53] A. B. Li, J. A. Kluge, N. A. Guziewicz, F. G. Omenetto, D. L. Kaplan, *J. Control. Release* **2015**, *219*, 416.

[54] Y. Q. Zhang, W. De Shen, R. L. Xiang, L. J. Zhuge, W. J. Gao, W. B. Wang, *J. Nanoparticle Res.* **2007**, *9*, 885.

[55] X. Wang, T. Yucel, Q. Lu, X. Hu, D. L. Kaplan, *Biomaterials* **2010**, *31*, 1025.

[56] A. S. Lammel, X. Hu, S.-H. Park, D. L. Kaplan, T. R. Scheibel, *Biomaterials* **2010**, *31*, 4583.

[57] P. C. Bessa, E. R. Balmayor, H. S. Azevedo, S. Nürnberger, M. Casal, M. van Griensven, R. L. Reis, H. Redl, *J. Tissue Eng. Regen. Med.* **2010**, *4*, 349.

[58] R. Rajkhowa, X. Hu, T. Tsuzuki, D. L. Kaplan, X. Wang, *Biomacromolecules* **2012**, *13*, 2503.

[59] A. B. Mathur, V. Gupta, *Nanomedicine (Lond).* **2010**, *5*, 807.

[60] T. Hodgkinson, Y. Chen, A. Bayat, X.-F. Yuan, *Biomacromolecules* **2014**, *15*, 1288.

[61] S. Sukigara, M. Gandhi, J. Ayutsede, M. Micklus, F. Ko, *Polymer (Guildf).* **2003**, *44*, 5721.

[62] H.-J. Jin, S. V Fridrikh, G. C. Rutledge, D. L. Kaplan, *Biomacromolecules* **2002**, *3*, 1233.

[63] M. L. Lovett, C. M. Cannizzaro, G. Vunjak-Novakovic, D. L. Kaplan, *Biomaterials* **2008**, *29*, 4650.

[64] X. Wang, J. A. Kluge, G. G. Leisk, D. L. Kaplan, *Biomaterials* **2008**, *29*, 1054.

[65] M. B. Applegate, B. P. Partlow, J. Coburn, B. Marelli, C. Pirie, R. Pineda, D. L. Kaplan, F. G. Omenetto, *Adv. Mater.* **2016**, *28*, 2417.

[66] J. Kundu, L. A. Poole-Warren, P. Martens, S. C. Kundu, *Acta Biomater.* **2012**, *8*, 1720.

[67] R. R. Mallepally, M. A. Marin, M. A. McHugh, *Acta Biomater.* **2014**, *10*, 4419.

[68] F. P. Seib, E. M. Pritchard, D. L. Kaplan, *Adv. Funct. Mater.* **2013**, *23*, 58.

[69] K. Min, S. Kim, S. Kim, *Proc. Natl. Acad. Sci. U. S. A.* **2017**, *114*, 6185.

[70] B. P. Partlow, C. W. Hanna, J. Rnjak-Kovacina, J. E. Moreau, M. B. Applegate, K. A. Burke, B. Marelli, A. N. Mitropoulos, F. G. Omenetto, D. L. Kaplan, *Adv. Funct. Mater.* **2014**, *24*, 4615.

[71] M. Li, W. Tao, S. Lu, C. Zhao, *Polym. Adv. Technol.* **2008**, *19*, 207.

[72] R. R. Jose, J. E. Brown, K. E. Polido, F. G. Omenetto, D. L. Kaplan, *ACS Biomater. Sci. Eng.* **2015**, *1*, 780.

[73] M. R. Sommer, M. Schaffner, D. Carnelli, A. R. Studart, *ACS Appl. Mater. Interfaces* **2016**, acsami.6b11440.

[74] L. Sun, D. L. Kaplan, *Adv. Healthc. Mater.* **2012**, *1*, 729.

[75] M. J. Rodriguez, J. Brown, J. Giordano, S. J. Lin, F. G. Omenetto, D. L. Kaplan, *Biomaterials* **2017**, *117*, 105.

[76] O. N. Tretinnikov, Y. Tamada, *Langmuir* **2001**, *17*, 7406.

[77] B. D. Lawrence, F. Omenetto, K. Chui, D. L. Kaplan, *J. Mater. Sci.* **2008**, *43*, 6967.

[78] A. Sagnella, A. Pistone, S. Bonetti, A. Donnadio, E. Saracino, M. Nocchetti, C. Dionigi, G. Ruani, M. Muccini, T. Posati, V. Benfenati, R. Zamboni, *RSC Adv.* **2016**, *6*, 9304.

[79] C. Jiang, X. Wang, R. Gunawidjaja, Y. H. Lin, M. K. Gupta, D. L. Kaplan, R. R. Naik, V. V. Tsukruk, *Adv. Funct. Mater.* **2007**, *17*, 2229.

[80] J. E. Bressner, B. Marelli, G. Qin, L. E. Klinker, Y. Zhang, D. L. Kaplan, F. G. Omenetto, *J. Mater. Chem. B* **2014**, *2*, 4983.

[81] N. Minoura, M. Tsukada, M. Nagura, *Polymer (Guildf).* **1990**, *31*, 265.

[82] M. Demura, T. Asakura, *Biotechnol. Bioeng.* **1989**, *33*, 598.

[83] Q. Lu, X. Hu, X. Wang, J. A. Kluge, S. Lu, P. Cebe, D. L. Kaplan, *Acta Biomater.* **2010**, *6*, 1380.

[84] R. K. Pal, N. E. Kurland, C. Wang, S. C. Kundu, V. K. Yadavalli, *ACS Appl. Mater. Interfaces* **2015**, *7*, 8809.

[85] J. Park, S.-G. Lee, B. Marelli, M. Lee, T. Kim, H.-K. Oh, H. Jeon, F. G. Omenetto, S. Kim, *RSC Adv.* **2016**, *6*, 39330.

[86] H. Perry, A. Gopinath, D. L. Kaplan, L. D. Negro, F. G. Omenetto, *Adv. Mater.* **2008**, *20*, 3070.

[87] S. Kim, B. Marelli, M. A. Brenckle, A. N. Mitropoulos, E. S. Gil, K. Tsioris, H. Tao, D. L. Kaplan, F. G. Omenetto, *Nat. Nanotechnol.* **2014**, *9*, 306.

[88] H. Tao, B. Marelli, M. Yang, B. An, M. S. Onses, J. A. Rogers, D. L. Kaplan, F. G. Omenetto,

Adv. Mater. **2015**, *27*, 4273.

[89] J. G. Hardy, T. R. Scheibel, *Prog. Polym. Sci.* **2010**, *35*, 1093.

[90] Q. Dong, H. Su, D. Zhang, *J. Phys. Chem. B* **2005**, *109*, 17429.

[91] M. Kang, R. Jung, H.-S. Kim, J. H. Youk, H.-J. Jin, *J. Nanosci. Nanotechnol.* **2007**, *7*, 3888.

[92] A. Shi-yun, G. Ji-gang, Z. Lu-sheng, M. Zhi-jun, L. Xiao-chen, *Spectrosc. Spectr. Anal.* **2008**, *28*, 2126.

[93] X. Fei, M. Jia, X. Du, Y. Yang, R. Zhang, Z. Shao, X. Zhao, X. Chen, *Biomacromolecules* **2013**, *14*, 4483.

[94] H. Yin, S. Ai, W. Shi, L. Zhu, *Sensors Actuators, B Chem.* **2009**, *137*, 747.

[95] Y. Zhou, W. Chen, H. Itoh, K. Naka, Q. Ni, H. Yamane, Y. Chujo, *Chem. Commun.* **2001**, *0*, 2518.

[96] E. L. Mayes, F. Vollrath, S. Mann, *Adv. Mater.* **1998**, *10*, 801.

[97] C. Guo, G. N. Hall, J. B. Addison, J. L. Yarger, *RSC Adv.* **2015**, *5*, 1937.

[98] S. H. Tsao, D. Wan, Y. S. Lai, H. M. Chang, C. C. Yu, K. Te Lin, H. L. Chen, *ACS Nano* **2015**, *9*, 12045.

[99] S. Kim, A. N. Mitropoulos, J. D. Spitzberg, H. Tao, D. L. Kaplan, F. G. Omenetto, *Nat. Photonics* **2012**, *6*, 818.

[100] N. Kojic, E. M. Pritchard, H. Tao, M. A. Brenckle, J. P. Mondia, B. Panilaitis, F. Omenetto, D. L. Kaplan, *Adv. Funct. Mater.* **2012**, *22*, 3793.

[101] S. Das, M. Sharma, D. Saharia, K. K. Sarma, M. G. Sarma, B. B. Borthakur, U. Bora, *Biomaterials* **2015**, *62*, 66.

[102] N. Gogurla, S. P. Mondal, A. K. Sinha, A. K. Katiyar, W. Banerjee, S. C. Kundu, S. K. Ray, *Nanotechnology* **2013**, *24*, 345202.

[103] N. Gogurla, A. K. Sinha, D. Naskar, S. C. Kundu, S. K. Ray, *Nanoscale* **2016**, *8*.

[104] S. Xu, J. Song, H. Morikawa, Y. Chen, H. Lin, *Mater. Lett.* **2015**, *164*, 274.

[105] W. Sheng, J. Liu, S. Liu, Q. Lu, D. L. Kaplan, H. Zhu, *J. Mater. Chem. B* **2014**, *2*, 7394.

[106] M. C. Bunea, E. Vasile, B. Galateanu, A. Hudita, M. Serban, C. Zaharia, *Mater. Plast.* **2017**, *54*, 83.

[107] X.-X. Feng, L.-L. Zhang, J.-Y. Chen, Y.-H. Guo, H.-P. Zhang, C.-I. Jia, *Int. J. Biol. Macromol.* **2007**, *40*, 105.

[108] Y. Xia, G. Gao, Y. Li, *J. Biomed. Mater. Res. Part B Appl. Biomater.* **2009**, *90B*, 653.

[109] L. Cai, H. Shao, X. Hu, Y. Zhang, *ACS Sustain. Chem. Eng.* **2015**, *3*, 2551.

[110] M. Chu, G. Liu, *IEEE Trans. Nanotechnol.* **2008**, *7*, 308.

[111] S. Chang, B. Kang, Y. Dai, D. Chen, *Mater. Lett.* **2008**, *62*, 3447.

[112] N. Lin, F. Hu, Y. Sun, C. Wu, H. Xu, X. Y. Liu, *Adv. Funct. Mater.* **2014**, *24*, 5284.

[113] T. Posati, V. Benfenati, A. Sagnella, A. Pistone, M. Nocchetti, A. Donnadio, G. Ruani, R. Zamboni, M. Muccini, *Biomacromolecules* **2014**, *15*, 158.

[114] P. Tseng, G. Perotto, B. Napier, P. Riahi, W. Li, E. Shirman, D. L. Kaplan, I. V. Zenyuk, F. G. Omenetto, *Adv. Electron. Mater.* **2016**, *2*, 1600190.

[115] C.-S. Chen, S. Soni, C. Le, M. Biasca, E. Farr, E. Y.-T. Chen, W.-C. Chin, *Nanoscale Res. Lett.* **2012**, *7*, 126.

[116] K. Hu, M. K. Gupta, D. D. Kulkarni, V. V. Tsukruk, *Adv. Mater.* **2013**, *25*, 2301.

[117] L. Huang, C. Li, W. Yuan, G. Shi, *Nanoscale* **2013**, *5*, 3780.

[118] S. Ling, C. Li, J. Adamcik, S. Wang, Z. Shao, X. Chen, R. Mezzenga, *ACS Macro Lett.* **2014**, *3*, 146.

[119] A. S. Lammel, X. Hu, S. H. Park, D. L. Kaplan, T. R. Scheibel, *Biomaterials* **2010**, *31*, 4583.

[120] J. F. Maya-Vetencourt, D. Ghezzi, M. R. Antognazza, E. Colombo, M. Mete, P. Feyen, A. Desii, A. Buschiazzo, M. Di Paolo, S. Di Marco, F. Ticconi, L. Emionite, D. Shmal, C. Marini, I. Donelli, G. Freddi, R. Maccarone, S. Bisti, G. Sambuceti, G. Pertile, G. Lanzani, F. Benfenati, *Nat. Mater.* **2017**, *16*, 681.

[121] A. Sionkowska, A. Planecka, *Polym. Degrad. Stab.* **2011**, *96*, 523.

[122] A. Sagnella, C. Chieco, V. Benfenati, N. Di Virgilio, S. Toffanin, S. Cavallini, T. Posati, A. Pistone, G. Varchi, G. Ruani, M. Muccini, F. Rossi, R. Zamboni, *Compos. Part B Eng.* **2015**, *68*, 281.

[123] N. C. Tansil, L. D. Koh, M. Y. Han, *Adv. Mater.* **2012**, *24*, 1388.

[124] J. Zhang, E. Pritchard, X. Hu, T. Valentin, B. Panilaitis, F. G. Omenetto, D. L. Kaplan, *Proc.*

Natl. Acad. Sci. U. S. A. **2012**, *109*, 11981.

[125] B. Marelli, M. A. Brenckle, D. L. Kaplan, F. G. Omenetto, *Sci. Rep.* **2016**, *6*, 25263.

[126] C. J. Bettinger, K. M. Cyr, A. Matsumoto, R. Langer, J. T. Borenstein, D. L. Kaplan, *Adv. Mater.* **2007**, *19*, 2847.

[127] K. Tsioris, G. E. Tilburey, A. R. Murphy, P. Domachuk, D. L. Kaplan, F. G. Omenetto, *Adv. Funct. Mater.* **2010**, *20*, 1083.

[128] S. Zhao, Y. Chen, B. P. Partlow, A. S. Golding, P. Tseng, J. Coburn, M. B. Applegate, J. E. Moreau, F. G. Omenetto, D. L. Kaplan, *Biomaterials* **2016**, *93*, 60.

[129] M. Applegate, A. Mitropoulos, G. Perotto, D. Kaplan, F. Omenetto, *Adv. Photonics 2015* **2015**, NT1B.4.

[130] B. D. Lawrence, M. Cronin-Golomb, I. Georgakoudi, D. L. Kaplan, F. G. Omenetto, *Biomacromolecules* **2008**, *9*, 1214.

[131] M. Cronin-Golomb, A. R. Murphy, J. P. Mondia, D. L. Kaplan, F. G. Omenetto, *J. Polym. Sci. Part B Polym. Phys.* **2012**, *50*, 257.

[132] H. Tao, J. M. Kainerstorfer, S. M. Siebert, E. M. Pritchard, A. Sassaroli, B. J. B. Panilaitis, M. A. Brenckle, J. J. Amsden, J. Levitt, S. Fantini, D. L. Kaplan, F. G. Omenetto, *Proc. Natl. Acad. Sci.* **2012**, *109*, 19584.

[133] J. J. Amsden, P. Domachuk, A. Gopinath, R. D. White, L. D. Negro, D. L. Kaplan, F. G. Omenetto, *Adv. Mater.* **2010**, *22*, 1746.

[134] J. J. Amsden, H. Perry, S. V. Boriskina, A. Gopinath, D. L. Kaplan, L. Dal Negro, F. G. Omenetto, *Opt. Express* **2009**, *17*, 21271.

[135] K. A. Burke, M. A. Brenckle, D. L. Kaplan, F. G. Omenetto, *ACS Appl. Mater. Interfaces* **2016**, *8*, 16218.

[136] P. Tseng, S. Zhao, A. Golding, M. B. Applegate, A. N. Mitropoulos, D. L. Kaplan, F. G. Omenetto, *ACS Omega* **2017**, *2*, 470.

[137] M. Lee, H. Jeon, S. Kim, *Nano Lett.* **2015**, *15*, 3358.

[138] S. Kim, A. N. Mitropoulos, J. D. Spitzberg, D. L. Kaplan, F. G. Omenetto, *Opt. Express* **2013**, *21*, 8897.

[139] J. Park, Y. Choi, M. Lee, H. Jeon, S. Kim, *Nanoscale* **2015**, *7*, 426.

[140] H. Kwon, S. Kim, *ACS Photonics* **2015**, *2*, 1675.

[141] H. Tao, J. J. Amsden, A. C. Strikwerda, K. Fan, D. L. Kaplan, X. Zhang, R. D. Avertit, F. G. Omenetto, *Adv. Mater.* **2010**, *22*, 3527.

[142] D. H. Kim, Y. S. Kim, J. Amsden, B. Panilaitis, D. L. Kaplan, F. G. Omenetto, M. R. Zakin, J. A. Rogers, *Appl. Phys. Lett.* **2009**, *95*, 2.

[143] M. A. Brenckle, H. Cheng, S. Hwang, H. Tao, M. Paquette, D. L. Kaplan, J. A. Rogers, Y. Huang, F. G. Omenetto, *ACS Appl. Mater. Interfaces* **2015**, *7*, 19870.

[144] D.-H. Kim, J. Viventi, J. J. Amsden, J. Xiao, L. Vigeland, Y.-S. Kim, J. A. Blanco, B. Panilaitis, E. S. Frechette, D. Contreras, D. L. Kaplan, F. G. Omenetto, Y. Huang, K.-C. Hwang, M. R. Zakin, B. Litt, J. A. Rogers, *Nat. Mater.* **2010**, *9*, 511.

[145] H. Tao, M. A. Brenckle, M. Yang, J. Zhang, M. Liu, S. M. Siebert, R. D. Averitt, M. S. Mannoor, M. C. McAlpine, J. A. Rogers, D. L. Kaplan, F. G. Omenetto, *Adv. Mater.* **2012**, *24*, 1067.

[146] M. S. Mannoor, H. Tao, J. D. Clayton, A. Sengupta, D. L. Kaplan, R. R. Naik, N. Verma, F. G. Omenetto, M. C. McAlpine, *Nat. Commun.* **2012**, *3*, 763.

[147] Y. Liu, N. Qi, T. Song, M. Jia, Z. Xia, Z. Yuan, W. Yuan, K.-Q. Zhang, B. Sun, *ACS Appl. Mater. Interfaces* **2014**, *6*, 20670.

Chapter 2.

Synthesis and characterization of silk-nanoparticles composite materials

2.1. Introduction

Natural silk materials produced by silkworms and spiders have been used by humans for centuries. Recently, researchers have moved from focusing on pure silk materials to the develop of silk-based composites with a number of exciting applications.[1] Among them, bio-nanocomposites, which combine a biopolymer matrix (as silk fibroin) with an inorganic moieties showing at least one dimension at nanoscale, are promising materials for applications in optical, optoelectronic and biomedical devices. As anticipated in the *Introduction*, this new generation of materials offers the advantages of the biopolymer (such as biocompatibility and biodegradability) with the functional properties derived by the nanoparticles.

In this chapter two different "bio-nanocomposites" will be presented, obtained by the combination of silk fibroin (SF) with titanates nanosheets (TNSs) and gold nanorods (AuNRs). The chapter is divided into two main parts, the first is dedicated to SF-TNSs nanocomposite and the second to the SF-AuNRs. A large space will be reserved at the beginning of each section to review the literature, to provide a clear background and clarify the hypotheses of work. Afterword, the synthesis and some characterizations of the materials will be presented.

It should be emphasized that, despite the fact that this chapter is at the beginning, some characterizations have been made only in the last period of the

doctoral studies and therefore some results require further experimental evidences to be confirmed (as will be adequately explained). The purpose of this chapter is to provide to the reader a preliminary characterization of the materials studied, which will then be investigated in the following chapters for specific applications or for the development of more complex nanostructures.

2.2. High refractive index silk-TNSs nanocomposite

Because of its excellent mechanical and optical properties, associated with biocompatibility and biodegradability, silk is an excellent material for the development of biocompatible optical sensors. Many studies have been made on the development of optical and photonic applications based on silk, as microlenses, waveguides, diffraction grating and inverse opals,[2–5] while in literature there is little documentation on improving the optical and electrical properties of the silk. Recently, it was demonstrated the possibility to fabricate a new nanocomposite based on silk and titanates nanosheets (TNSs) with a high and tunable refractive index, preserving the processability of the silk material.[6]

TNSs are 2D layers materials made of sheets with a composition of $[Ti_nO_{2n+1}]^{2-}$ arranged in a layered fashion with intercalated cations between the layers. They present a very small size (one-unit cell in thickness and 3-5 nm in length), high refractive index, simple synthesis and good processability. Because of their 2D structure and the small size, these compounds exhibit distinctive chemical, electronic and optical properties in comparison with the bulk forms, which make them attractive for a wide range of application, from optolectronic, to photocatalysis and sensing.[7] These nanoparticles can be synthesized using both top-down and bottom-up approaches. Single nanosheets with a lepidocrocite structure can be prepared by a bottom-up approach via wet-chemical one-pot synthesis. For example, A. Antonello proposed a sol-gel based synthesis to obtained TNSs from titanium isopropoxide, which can be easily exfoliated in a water based solution of tetramethylammonium hydroxide (TMAH), where the colloidal stability is preserved, thanks to the electrostatic interaction between the sheets and the TMA^+ cations.[8,9] **Figure 2.1**(b)

shows a TEM mage of the TNSs produced according to this synthesis. A schematic representation of the single sheet structure is also reported.

These nanoparticles have very high refractive index (1.83 at 630 nm), which can be increased by post-processing treatments such as UV irradiation and thermal annealing (see **Figure 2.1**(c)). The increase of the refractive index is due to the decomposition of the organic cations intercalated, with a consequent collapse of the layered structure, which can be detected by the variation of the diffraction pattern (see **Figure 2.1**(d)).

(a)

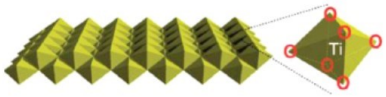

(c)

sample	refractive index	thickness contraction (%)	*d* (nm)
100	1.83	0	1.14
UV	2.15	39	0.93
200	2.03	24	1.14
UV+200	2.28	57	0.69
UV+200b	2.26	54	0.71[a]
500	2.30	59	—[b]

(b)

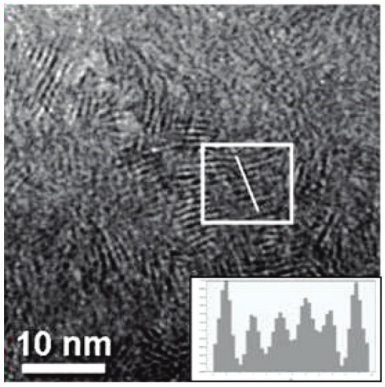

(d)

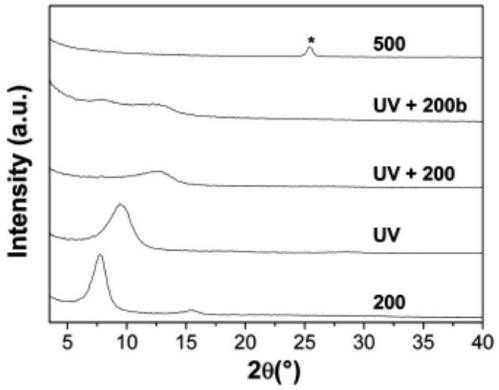

Figure 2.1. (a) Schematic illustration of the crystalline structure of a TNS sheet.[7] (b) TEM image of TNSs nanosheets dispersed in methanol and deposited on a copper grid. (c) Refractive index, interlayer distance and thickness contraction of TNSs thin films after different treatments. (d) XRD pattern of the TNSs after the treatments.[9]

Thanks to their small size and water solubility, TNSs were successfully used to synthesize SF composite with high refractive index and high optical transparency. SF-TNSs nanocomposite with high TNSs content (up to 90% in weight) were easily fabricated by simple mixing the two water based solutions. Several deposition methods were used, like spin coating and drop casting, to produce supported thin films or free-standing membranes, and several curing treatments were investigated

to control and tune the properties of the nanocomposite (such as UV and temperature to increase the refractive index, or methanol annealing to crystallize the fibroin and make the material water insoluble).

Figure 2.2(a) shows free-standing films with a thickness of 30 μm fabricated by casting. The films were transparent even at very high concentration of TNSs (**Figure 2.2**(b)), with low absorbance in the 400-1300 nm range (scuttering effects were detected only for the 10:90 SF-TNSs compositions), high flexibility when hydrated and without cracks **Figure 2.2**(c)).

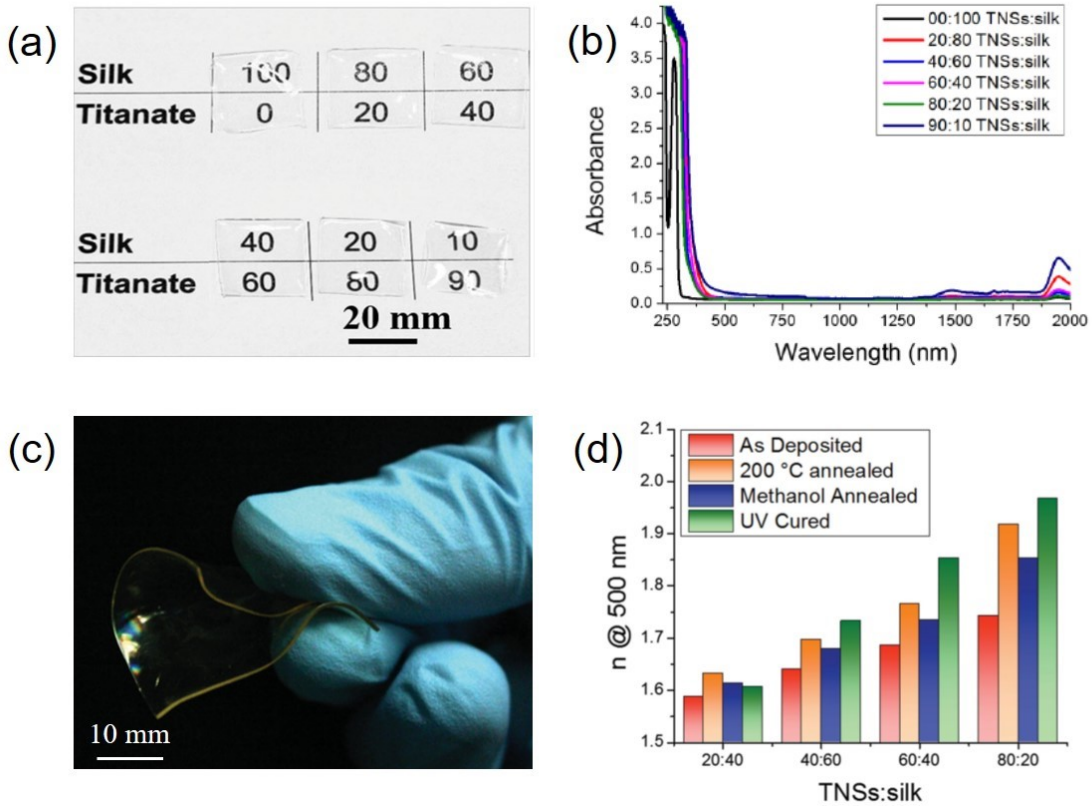

Figure 2.2. (a) Free-standing films of SF-TNSs nanocomposites with different silk and TNSs concentartions. (b) UV-VIS-NIR absorbance spectra of the samples reported in (a). (c) Free-standing film made with 50:50 SF-TNSs, made flexible by simple hydration with water after methanol annealing. (d) Refractive index of the nanocomposites at 500nm for different concentrations of TNSs and for different tretaments.[6]

Acting on the concentration of the particles and on the curing treatments, the refractive index of the SF-TNSs material was tuned from 1.55 to 1.97. UV radiation

was found the most efficient way of curing TNSs, giving the highest refractive index achieved among the different annealings, as reported in the histogram in **Figure 2.2**(d).

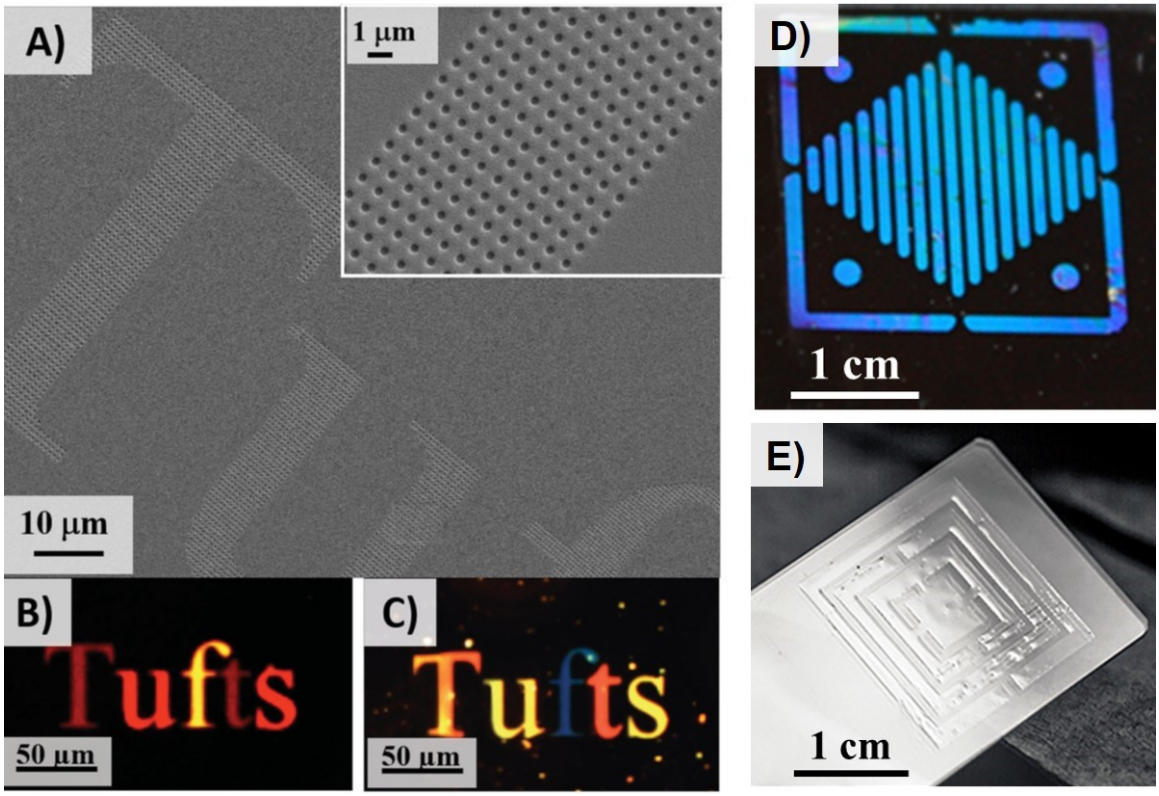

Figure 2.3. A) SEM picture of 200nm holes e-beam lithographed with different lattices on a SF-TNSs nanocomposite with 25:75 SF-TNSs ratio. B) Structural colors of the nanocomposite thin films (n=1.8) and C) pure silk (n=1.55). D) A 200 nm thick 20:80 SF-TNSs nanocomposite thin films patterned using UV lithography. E) SF-TNSs nanocomposite ink jet printed on a glass slide.[6]

This new nanocomposite not only showed the good optical properties derived by the TNSs, but even preserved the processability typical of the silk matrix. Different fabrication techniques already used for the pure silk where applied to the nanocomposite to generate structure in the micro and nano-scale. As shows in **Figure 2.3**, it was possible to fabricate nanostructures using e-beam lithography, UV lithography and ink-jet printing, even for high TNSs filling factors. This enable the unique opportunity to shape the TNSs into devices of interest, not possible without the integration in the SF matrix.

One of the advantage of this new high refractive index (HRI) material is the possibility to increase the optical performances of the silk-based devices, especially in application where silk is interfaced with fluids (such as biological environment). A key point for the use of this devices in a real scenario, it is the control of the water-stability and biodegradability. One of the easy way to control the stability of the silk-based structure is acting on secondary structure of the protein by post-processing, such as methanol or water annealing. Taking into count these considerations, we decided to examine in depth the effect of the methanol annealing on the structural properties of the SF-TNSs nanocomposites. The results obtained will be presented in the *Section 2.2.2* of this chapter. A second study was instead focus of the mechanical properties of SF-TNSs coatings, characterized through nanoindentation tests (*Section 2.2.3*). All the results here presented are complementary to the work previously published by Perotto et al,[6] and preliminary for the studies presented in the following chapters.

2.2.1. Synthesis

The synthesis of the nanocomposite started from the preparation of two water solution, the silk fibroin (SF) solution and the titanates nanosheets (TNSs) dispersion.[6] SF solution was extracted from the silk cocoons with the process previously reported.[10] Briefly: silk cocoons were cut in small pieces and boiled in a 0.02 M Na_2CO_3 solution to remove sericin. After rinsing with distilled water (DI), dried fibers were dissolved in a 9.6M LiBr solution at 60° C for 4 hours. The solution was then dialyzed in water to remove the salt, to obtain a 6% SF solution in water. The solution was then diluted with DI water to 5% w/v for the following preparations.

TNSs were synthesized using a sol-gel process previously reported.[9] Briefly: titanium tetraisopropoxide were added to warm (110° C), degassed and dehydrated ethylene glycol. A second injection of tetramethylammonium hydroxide dissolved in water was performed quickly to induce the formation of the sheets. After 4 hours of reaction, the solution was cooled down and flocculation was promoted by adding acetone. The particulate was then washed with acetone and methanol to remove the

unreacted reagents and the residual solvent and dried in vacuum. A stock solution of 20% w/v of TNSs was prepared by dissolving the powder in 1 M TMAH aqueous solution.

High refractive index SF-TNSs nanocomposite was synthesized by gently mixing the stock TNSs solution with the SF solution in an appropriate ratio. Different formulations were tested, between them the 50:50 in weight SF-TNSs was selected as representative to study the properties of the nanocomposite. Free-standing films were fabricated by casting the solution on a PDMS mold, while thin films were deposited on different substrates by spin-coating (see *Appendix A2.2*). **Figure 2.4** shows an example of a free-standing film realized with a composition of 50:50 SF-TNSs (30 μm thick), showing high transparency, flexibility and even reflectivity due to the high refractive index of the TNSs.

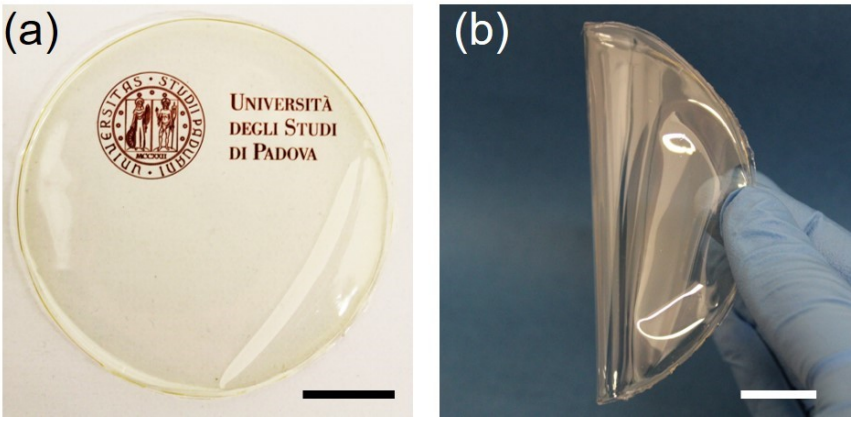

Figure 2.4. Free standing film made with 50:50 SF-TNSs formulation (as prepared). The film shows high transparency (a) and flexibility (b). The scale bars are 2cm.

Different post-deposition annealing processes were performed on the samples: methanol, temperature, ion exchange and UV light. Methanol annealing was performed by dipping the samples in methanol for 30 min. Temperature annealing was effectuated by treated the sample in a hoven at 200° C for 1h in air. Ion exchange was performed by dipping the methanol annealed samples in a 0.1 M $AgNO_3$ aqueous solution for 6 min, followed by UV irradiation for 30 min with (UVL-56 365 nm UV

lamp, Upland, CA91786 USA), to reduce the silver (this process will be extensively investigated in *Chapter 3*).

2.2.2. Methanol annealing

It is well known that methanol annealing is an efficient way to crystallize fibroin proteins making water stable the silk structure (see *Chapter 1*). It is clear that this insolubilization is a result of the crystallization of the fibroin to *β-sheet*, following the *random coil* to *β-form* transition.[11] Systematic studies on the mechanism of methanol crystallization are reported in literature, focused on the effect of the solvent concentration and time of immersion. As demonstrated by Magoshi,[12] the conformational transition is related with a mechanism of dehydration. In solution, when a hydrophilic alcohol such as methanol and ethanol is added to the silk fibroin, the molecular chains of the fibroin interacted quickly and strongly with one another. This induces a rearrangement of the protein chains, which changes the conformation from a random coil to a *β-sheet* structure.[13] A similar effect can be obtained on SF membranes, especially in presence of residual water in the films, which acted as swelling agent toward silk membrane, thus promoting penetration of methanol.[11]

The treatment was found to be an efficient way to cure SF-TNSs as well.[6] In this case, the molecular weight of the protein played a critical role in the stability of the composite films. Only in the case of high molecular weight (boiling time <45 min), the SF-TNSs membranes resulted insoluble in water, probably because the process is related with the cross-link of the protein network. As reported in the previous paragraph, the effect of this treatment is an increase of the refractive index of the material. The hypothesis suggested by Perotto is that the methanol cures the TNSs in a same way of the temperature and UV irradiation, through a dehydration and deintercalation of the TMA^+.

We confirmed this hypothesis through a further study on the crystalline structure of the nanocomposite through circular dichroism (CD) and XRD analysis, associated with TEM and FTIR characterizations. The study was conducted on films

deposited on substrates (quartz or silicon) by spin coating, to obtain indications about the thin films formation for the following study on the coatings (*Section 2.2.3*) and on the multilayer structure reported in *Chapter 4*.

CD was used for solid-state conformation study of fibroin protein to evaluate the effect of spin coating deposition, TNSs and methanol effect on the secondary structure. The analysis was effectuated on thin films deposited on a quartz substrate, using spin coatings. The concentration of the solutions was set to 5% w/v and the spin parameters were 3000 rpm x 60 s (final thickness determined by ellipsometry around of 150 nm).

CD spectroscopy is based on the different absorption of the circular polarized light by the chiral molecules. The secondary structures of the proteins (α-helix, β-turns, β-sheets and random coils) show a characteristics absorption in the far UV range (178-250 nm). For example, a pronounced negative peak (*negative cotton effect*) at 195 nm is characteristic of a random coil, a wide negative peak at 216 nm and a pronounced positive peak (*positive cotton effect*) at 185-200 nm are instead indicative of a β-sheets structure, while the peaks at 192 nm (positive), 208 nm (negative) and 222 nm (negative) are due to the absorption of the α-helix conformation.[14]

Figure 2.5(a) shows the CD spectra of the SF films as prepared (black) and after methanol annealing (red). The spectrum of the as-prepared film shows a wide negative band between 208 and 220 nm, ascribable to a random coil structure that present a small percentage of β-sheets and helix.[15,16] The presence of a small amount of sheets and helix can be related with the gelation process during the formation of the films, which involves the formation of small crystalline nuclei for the interaction between the protein chains (hydrophobic interaction and hydrogen bonds).[14,17] After the methanol annealing the structure results complete dominate by the β-sheets conformation, as visible from the presence of a negative peak at 216 nm and a second positive peak between 190 and 210 nm (the spectrum is not complete because of the saturation of the signal). This conformation confirms the effect of this treatment on the secondary structure, as previously explained.

In the case of the SF-TNSs film with the formulation 50:50 %w/v, the spectra are less defined because of the strong saturation of the signal under 200 nm probably caused by the presence of the TNSs. As reported in **Figure 2.5**(b), the as prepared film presents the incipit of a negative peak around 200 nm, probably related with a random coil structure. The methanol annealed instead shows a marked negative peak at 216-217 nm, indicative of a β-sheets structure.

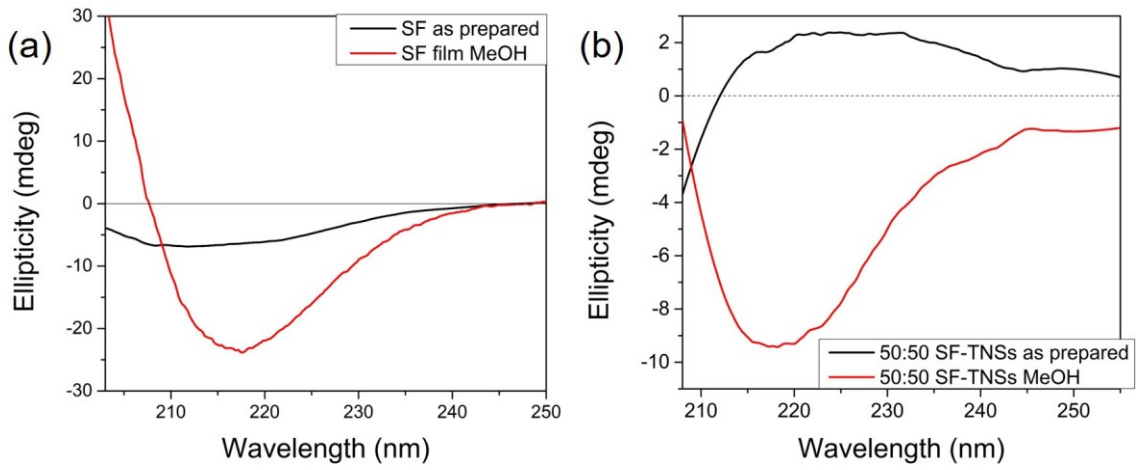

Figure 2.5. CD spectra of SF (a) and 50:50: SF-TNSs (b) thin films before (black) and after methanol annealing (red).

Unfortunately, the saturation of the signal under 200 nm caused by the high absorption of the TNSs and of the protein (as visible from the absorbance spectra of the same sample reported in **Figure 2.6**) did not permit a complete characterization of the films. Probably, it could be possible to obtain better results by depositing a thinner layer. It is in any case confirm the effect of the methanol annealing on the fibroin structure even in the case of the thin films.

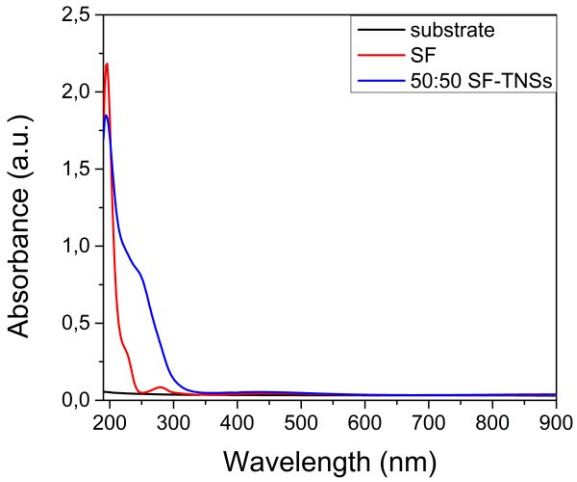

Figure 2.6. Absorbance spectra of SF (red), 50:50 SF-TNSs (blue) thin films deposited on quartz used for the CD characterizations. In the same image is reported also the spectrum of the substrate (black).

To further characterize the films, FTIR spectra were collected on thin films deposited on silicon substrates in the same conditions. The spectrum of the as prepared SF film presents an amorphous structure characterized by random coils (1640-1649 cm^{-1}) and helix (1650 cm^{-1}) conformations, as visible from the absorbance of the Amide I band (see **Figure 2.7**(a)). After the methanol annealing, the peak related with the random coil decreased and increased the peak of the β-sheets crystalline structure at 1626 cm^{-1}. The tyrosine absorbance in the Amide II region also shifted to 1515 cm^{-1}, indicating the packing of the dense β-sheets crystals.[18] The result was similar in the case of the nanocomposite film, even if in this case the structure of the as prepared film resulted dominated by random coils, with lower absorbance due to the helix forms. After the methanol treatment, the absorption due to the sheets increases, indicating the crystallization of the structure. In the case of the nanocomposite it was also visible the absorbance peak at 1487cm^{-1} corresponding to asymmetrical C-H bending of methyl group of the TMA^+.[19] The peak intensity decreases after the treatment, indicating a partial deintercalation of the ions from the structure. This results confirm the effect previously reported for the free-standing films.[6]

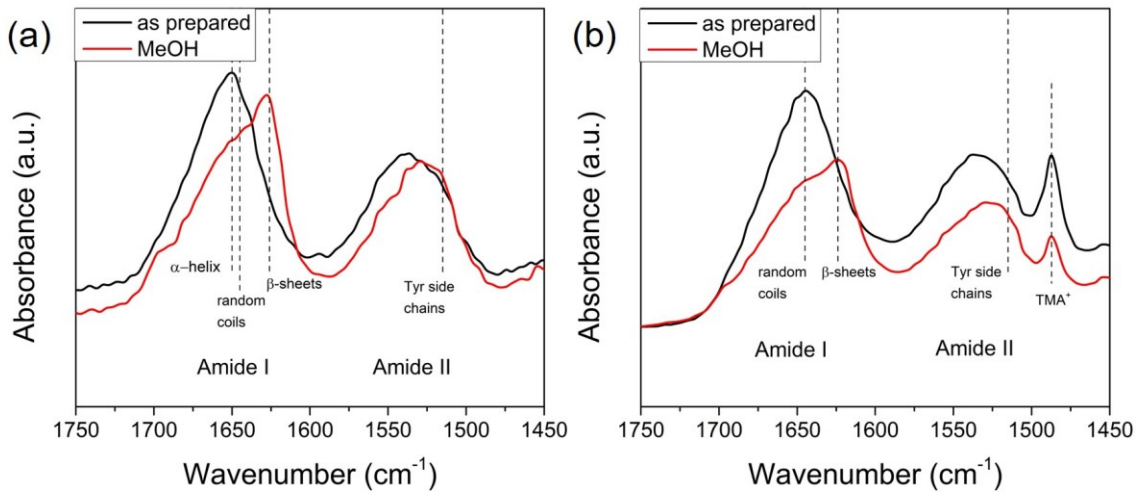

Figure 2.7. FTIR spectra of thin films deposited on silicon substrate before (black) and after (red) methanol annealing: (a) pure silk fibroin and (b) 50:50 SF-TNSs nanocomposite.

The crystallization of the SF was also confirmed by TEM images. **Figure 2.8**(a) shows the formation of the β-sheets in a SF matrix after methanol annealing. The crystalline nature of the sample was determined from the examination of a localized region in high resolution TEM images using a Fast Fourier Transform (FFT).

Figure 2.8(c) gives the corresponding diffraction pattern (reciprocal space) of the selected region of interest in **Figure 2.8**(a). From the profile extracted (**Figure 2.8**(b)) we calculated a plane distance between the sheets equal to 0.33 nm after the annealing. The result is comparable with the expected plane distance obtained by the Bragg law from XRD patterns. **Table 2.1** summarizes the values obtained by TEM images and compared with the distances reported in literature obtained by XRD analysis.[13]

Table 2.1. Plane distance calculated from the profiles extracted from TEM images compared with the value obtained by the Bragg Law.

Sample	TEM	Bragg Law (XRD)[13]	
As prepared	0.40 ± 0.04 nm	2θ = 20º	0.44 nm
MeOH annealed	0.33 ± 0.04 nm	2θ = 24º	0.37 nm

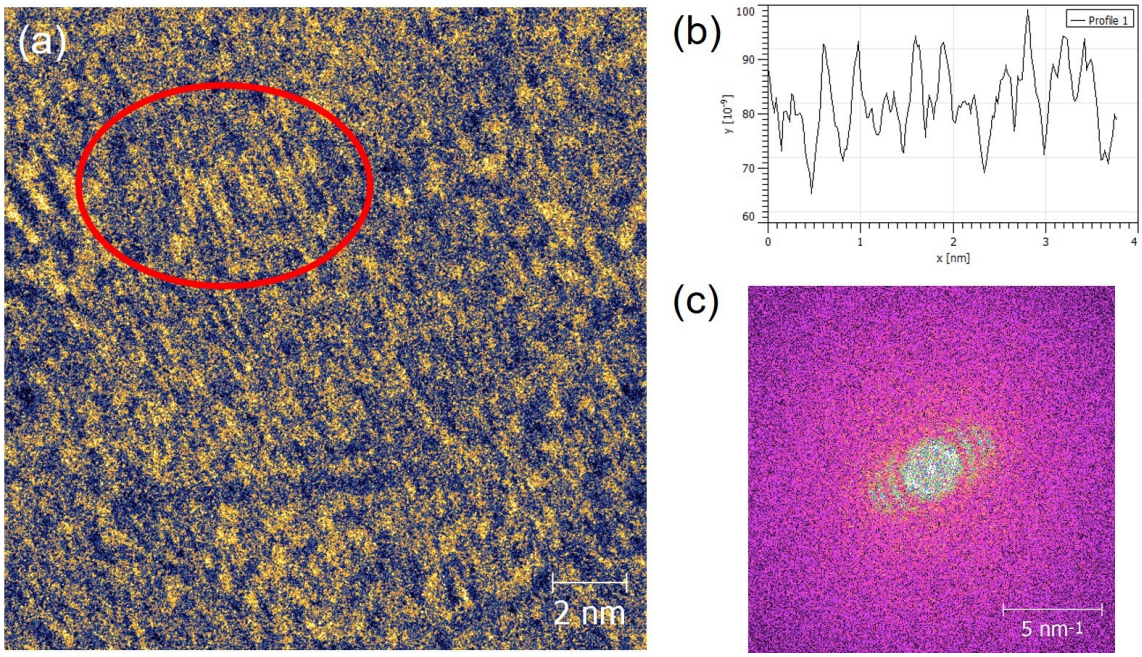

Figure 2.8. HR-TEM image of a SF film deposited on a copper grid after methanol annealing. (b) Profile extrapolated from the region circled in red. (c) FFT diffraction of interest circled in (a).

As anticipated in the introduction of the section, it was found that the methanol annealing acts on the TNSs with a curing effect as well, by dehydration and densification. From TEM analysis it was determined a distance between the TNS sheets of 1.00±0.11 nm which decreases to 0.80±0.08 nm after the annealing. These results were compared with the distances calculated with the Bragg Law from the XRD patterns on films reported in **Figure 2.9**. From the XRD analysis we calculated an interlayer distance of 1.70 nm, higher compared to the value obtained from the TEM images. This is probably due to the contributions of a wide range of TNSs crystals in the XRD patterns, which present a different intercalation of the SF chains and a different stacking, as already observed from TEM images.[6] Also in this case the contraction of the interlayer distance caused by the annealing is confirmed (see **Table 2.2**).

Table 2.2. Interlayer distance between the TNS sheets obtained by TEM images and calculated from XRD patterns by the Bragg Law.

Sample	TEM[6]	Bragg Law (XRD)	
As prepared	1.00 ± 0.11 nm	2θ = 5.2º	1.70 nm
MeOH annealed	0.80 ± 0.08 nm	2θ = 5.6º	1.58 nm

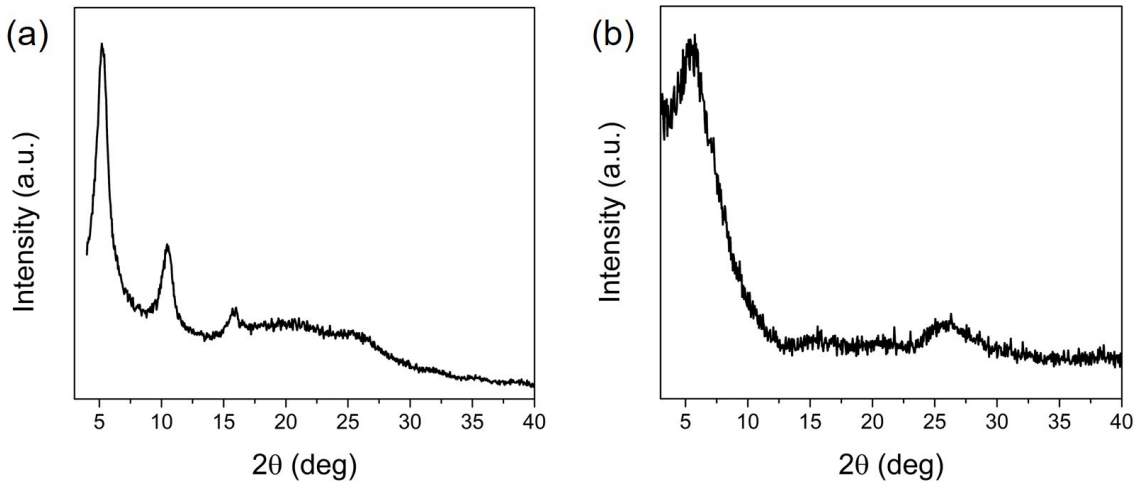

Figure 2.9. XRD pattern of a 50:50 SF-TNSs nanocomposite film deposited on a glass slide before (a) and after methanol annealing (b).

In conclusion, we can confirm that the methanol annealing affects the structure of both SF and SF-TNSs nanocomposite thin films by inducing a transition to the crystalline conformation of the protein and a densification of the TNSs layered structure.

2.2.3. Nanoindentation study on SF-TNSs composite thin films

Albeit the enormous work on films and coatings made with silk proteins,[20,21] there is a little documentation on the characterization of the mechanical properties of silk-NPs based coatings.[22,23] Mechanical properties of nanocomposites provide interesting indications about the interaction between the nanoparticles (NPs) and the silk matrix. With the change of the SF/NPs ratio, the interaction between the particles and the fibroin chains can change and alter the mechanical properties of the material.

A similar effect can be induced by the conformational transition in the secondary structure of the protein promoted by post-treatment.[24]

In this section, we will present the fabrication and characterizations of silk-TNSs nanocomposites thin-films and the characterization of their mechanical properties trough nanoindentation test. The films were deposited by spin coating on alumina and silicon substrates (previously treated to obtain an hydrophilic surface). Three different formulations were selected: 100:0 (SF), 80:20 and 50:50 %w/v SF-TNSs. All the samples were first treated with methanol to crystallize the SF and make water insoluble and then treated with temperature (TT) or exposed to ion exchange with silver ions followed by UV irradiation (Ag+UV) (see *Section 2.2.2*).

As anticipated, the addition of TNSs to the silk matrix as well as the post-fabrication treatments increase the refractive index of the materials, improving the optical performances of the silk. The addition of fillers in the polymer fibroin matrix and the crystallization of the protein could also affect the mechanical properties of the material. We tried to investigate this phenomenon by combining the results obtained by ellipsometer spectroscopy, with nanoindentation tests and AFM characterizations.

In **Table 2.1** the optical constants of the films measured by ellipsometry on samples deposited on silicon substrate are summarized. The data are obtained by fitting of the experimental data using a Cauchy layer with Urbach absorption to model the refractive index (see *Appendix A3.11*). The results confirm what previously observed: the increase of the TNSs content and the post-deposition treatments, increase the refractive index of the materials.[6] This characterization gives a qualitative indication about the effect of the treatments that promote the crystallization of the SF and the densification of the films.

Table 2.3. Refractive index of SF and SF-TNSs nanocomposite as a function of TNSs concentration and treatments obtained by ellipsometry.

Sample	Treatment	n (@500nm)	thickness (nm)
SF	MeOH	1.560	148
	Ag+UV	1.566	149
	TT	1.573	149
80:20 SF-TNSs	MeOH	1.621	116
	Ag+UV	1.679	73
	TT	1.632	112
50:50 SF-TNSs	MeOH	1.783	45
	Ag+UV	1.752	132
	TT	1.802	77

To test the mechanical properties of the SF-TNSs films, nanoindentation test were carried out on thin films deposited on an alumina substrate. The measurements were effectuated at the University of New South Wales (UNSW, Sydney) by Dr Joseph Arsecularatne. The characterizations were performed according to the protocol reported in *Appendix A3.6*, on coatings with a thickness of about 200 nm. For each sample, at least ten nanoindentations were effectuated at different locations of the surface, using two different loads (100 μN and 50 μN). It was observed a larger variability of the reduced elastic modulus (E_r) and hardness (H) under lower load, likely due to surface irregularities. **Table 2.4** summarized the value of modulus and hardness obtained by the combinations of the different measurements.

Table 2.4. Summary of the average values of elastic modulus and hardness of the SF and SF-TNSs nanocomposite as a function of TNSs concentration and post-deposition treatments.

Sample	Treatment	E_r (GPa)	H (GPa)
SF	MeOH	22 ±5	0.58 ±0.05
	Ag+UV	25 ±5	0.6 ±0.05
	TT	26 ±6	0.75 ±0.07
80:20 SF-TNSs	MeOH	22 ±5	0.58 ±0.02
	Ag+UV	26 ±6	0.7 ±0.06
	TT	32 ±7	0.9 ±0.1
50:50 SF-TNSs	MeOH	33 ±8	0.92 ±0.12
	Ag+UV	56 ±9	1.15 ±0.12
	TT	49 ±9	1.3 ±0.1

In general, increasing the TNSs concentration in the nanocomposite improves both the stiffness and the hardness of the material, especially in the case of combined treatments, as shown in the plots in **Figure 2.10**(a) and (b). It is interesting to note that the addition of 20% in weight of TNSs did not improve the mechanical properties of the crystallized SF, while for 50% of TNSs we observed an increase of E_r of 50% and of H of 58.6%, compared to the reference SF MeOH.

This can be related with the composite structure obtained during the self assembly of the material, which is strictly related with the concentration of the nanofillers. According to the classical polymer nano-composite model,[25,26] three types of structures based on 2D nanomaterials and a polymer matrix can be self-assembled in the micro/nano- scale: (a) disordered nanocomposite (low concentration of fillers randomly distributed); (b) ordered-intercalated nanocomposites (polymer chains intercalated between the layers, forming a "crosslinked" network); and (c) micro-composites (high concentration of fillers stacked together and not perfectly intercalated). The obtained structure depends on the nature of the components and the method of preparation. Considering the XRD results presented in the previous paragraph and the TEM analysis reported in literature,[6] we can suppose that in the case of the 50:50 SF-TNSs composition it was

probably obtained an intercalation of the polymer between the TNSs layers, able to enhance the mechanical properties.[22,27]

Concerning the effect of the treatments, it was observed that both the combined Ag exchange + UV reduction and the thermal annealing induce a significative increase of the properties with a linear trend as a function of the TNSs concentration. This is likely related with the increase of densification of the material induced by the treatments (as confirmed by the ellipsometry) combined with the possible nucleation of Ag particles after the photoreduction (see *Chapter 3*). The maximum increase was observed for the 50:50 SF-TNSs nanocomposite: reduced elastic modulus increased of about 154% in the case of 50:50 SF-TNSs Ag+UV compared to the value of the SF films (only MeOH annealed), while hardness increased of 124% for 50:50 SF-TNSs TT compared to the reference SF MeOH.

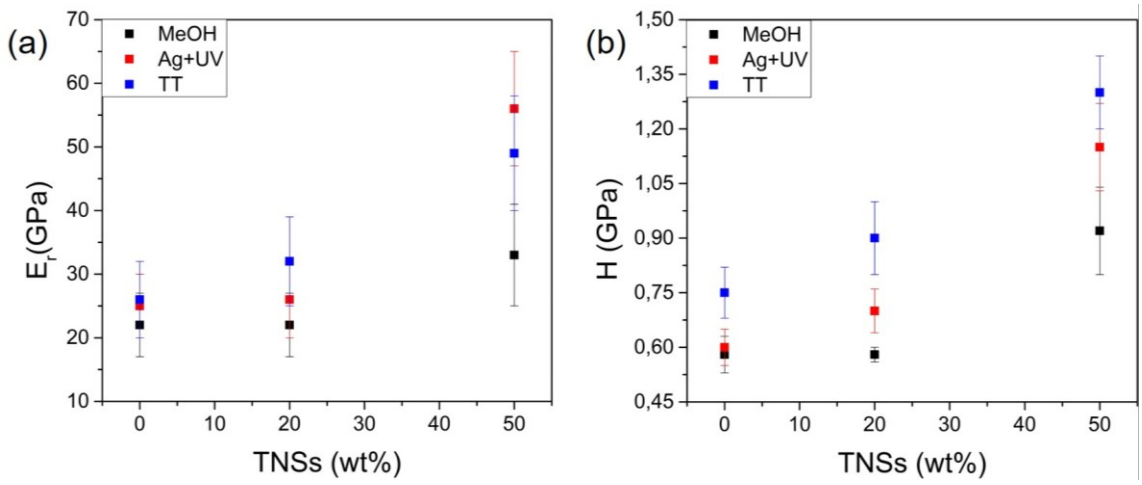

Figure 2.10. Trend of reduced elastic modulus (a) and hardness (b) of SF-TNSs nanocomposite thin films as a fucntion of the TNSs concentration, for different post-deposition treatments.

Comparing the modulus and the hardness values obtained in this study with the properties reported for other biopolymer based nanocomposites (measured using the nanoindentation technique), we observed that the SF-TNSs nanocomposite present an incredible performance (**Table 2.5**.). We supposed that this improvement is due to the high filling fraction obtainable thanks to the good dispersibility of the

TNSs in the silk fibroin matrix, compared for example to other silk-graphene composites.[22]

Table 2.5. Comparison of elastic modulus and hardness obtained by nanoindentation studies for different biopolymer based composite materials.

Material	E (GPa)	H (GPa)	Reference
50:50 SF-TNSs MeOH	33	0.92	Present study
50:50 SF-TNSs Ag+UV	56	1.15	Present study
50:50 SF-TNSs TT	49	1.3	Present study
Collagen + Nano HA (20wt%)	0.6	0.1	[28]
Chitosan N-doped graphene sheets (2.3wt%)	6.7	0.4	[28]
Chitosan Functionalized carbon nanotubes (0.5wt%)	3.5	0.223	[28]
Chitosan/Montmorillonite (10%)	4.92	0.199	[29]
Silk-graphene sheets (0.5wt%)	1.9	0.12	[22]

As already anticipated, we observed a large variability of the modulus and hardness for different locations of measurement, especially in the case of the 50:50 SF-TNSs material. This variability was caused by surface irregularities and disuniformity. The samples, in fact, presented some defects related with the spin coating process (comets and thickness variations along the surface). To better investigate the influence of the surface properties, atomic force microscopy measurements were conducted on samples prepared deposited on silicon substrates. As reported in **Table 2.6**, an increase of the surface roughness was measured for all the compositions in the case of the Ag+UV treatments.

Table 2.6 Roughness average (Ra) and root-mean-square roughness (rms) of the SF-TNSs thin films deposited on silicon calcultaed from the AFM micrographs reported in Figure 2.11.

Sample	Treatment	R_a [nm]	rms [nm]
SF	MeOH	0.372	0.472
	Ag+UV	3.23	4.35
	TT	0.292	0.357
80:20 SF-TNSs	MeOH	0.660	0.832
	Ag+UV	1.38	1.705
	TT	0.590	0.743
50:50 SF-TNSs	MeOH	0.627	0.791
	Ag+UV	8.06	9.854
	TT	0.430	0.541

Figure 2.11 shows the AFM micrographs obtained for all the samples. In general, the average roughness (R_a) measured on small scale increases with the TNSs concentration. The values are in every case law (<1 nm), excepted for the Ag+UV treatment. For this combination, it was measured an increase of R_a of about 7 nm, associated with a morphology characterized by the presence of "particles" on the surface (see (d), (e) and (f)).

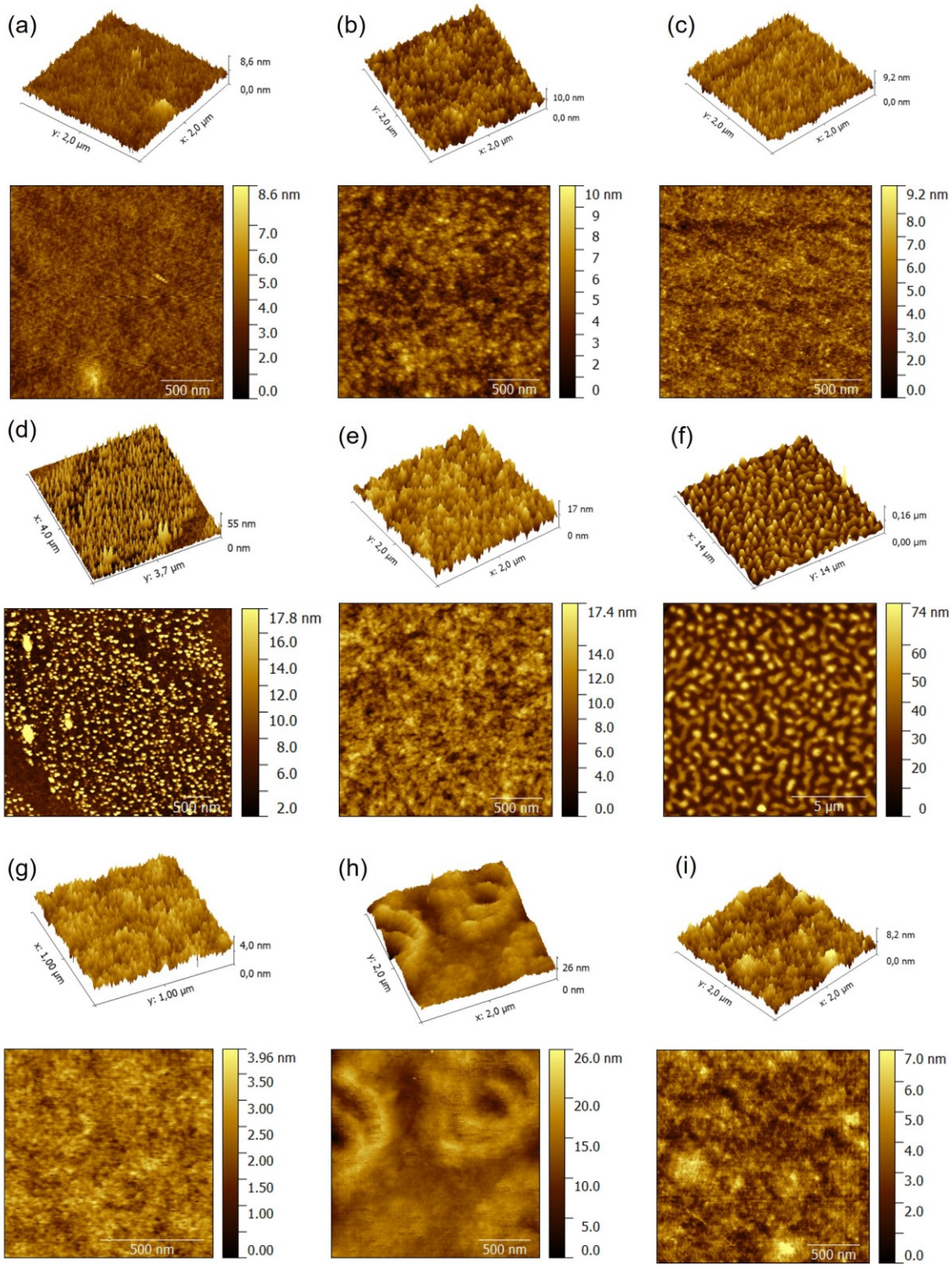

Figure 2.11. AFM micropgraphs of the SF-TNSs nanocomposite for different concentration and tretaments : (a) SF MeOH, (b) 80:20 SF-TNSs MeOH, (c) 50:50 SF-TNSs MeOH: (d) SF Ag+UV, (e) 80:20 SF-TNSs Ag+UV, (f) 50:50 SF-TNSs Ag+UV; (g) SF TT, (h) 80:20 SF-TNSs TT, (i) 50:50 SF-TNSs TT.

This is clearly visible in **Figure 2.12**, showing as an example the AFM micrograph of a larger area of the 80:20 SF-TNSs sample (Ag+UV), which present a random distribution of particles on the surface. We supposed that the particles are silver agglomerates nucleated on the surface after the UV irradiation, but further investigations should be necessary to confirm this hypothesis.

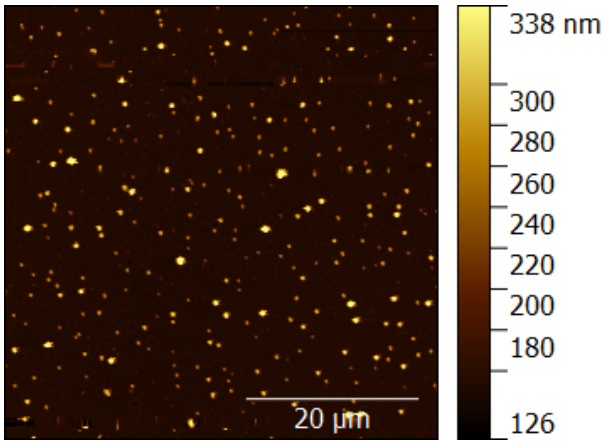

Figure 2.12. AFM micrograph of the 80:20 SF-TNSs nanocomposite film after ion exchange with silver and UV irradiation.

Another interesting observation is related to the surface of the sample in **Figure 2.11**(h), which shows a singular nanostructure, characterized by a "hill and valley" morphology. We observed a similar structure for other samples with a different concentration of TNSs deposited on silicon by spin-coating. Even if the number of experimental observation is small to clearly explain this phenomenon, we could suppose that the shear forces applied during the spin process and the particles concentration have an influence on the assembly process of the protein, as already reported in the case of silk fibroin films.[30,31]

In conclusion, we can affirm that the TNSs concentration as well as the post-deposition treatments affect the morphology and the mechanical properties of SF-TNSs nanocomposite films, with a general improvement of both elasticity and hardness. The enhancement of the properties and the singular nanostructures observed for some composition suggest that there is an influence of the TNSs

concentration in the assembly process of the material. Further investigations are necessary to determine the mechanism of assembly, considering also the influence of the substrate and the presence of shear forces during the formation of the films. The comparison with the as deposited SF films (not subjected to methanol annealing) and with the free-standing films could also be helpful to completely characterize the assembly mechanism.

2.3. Thermally-responsive silk-AuNRs composite

Metal nanoparticles (in particular gold) are extensive studied for a wide range of application (energy, sensing, biomedical) because of their localized surface plasmon resonance (LSPR) properties.[32–39] One of the interesting phenomena related with the LSPR is the photothermal effect. When a metal nanoparticle is irradiated with a light source matching the LSPR absorption, the optical energy can efficiently be convert to local heat through the plasmonic optical energy, rapidly increasing the temperature of the surrounding medium.[38] This light-induced temperature increase can activate biological processes,[40] induce phase changes of surrounding matrices,[41] or change the shape/morphology of the nanoparticles.[42] This photothermal process has been studied in medicine for the treatment of bacterial infection, photodynamic therapy, cancer therapy.[43–50]

Light activated AuNPs embedded in polymer matrices have been used widely in materials, sensing, biomedical and photonic applications.[41,51–54] The polymer scaffold in AuNP–polymer composites can serve three purposes: (1) assembling the NPs into composite material, (2) serving as a matrix that induces ordering and anisotropic orientation in clusters and on surfaces, (3) acting as a functional element and (4) providing flexibility and possibility to be shaped in different forms.[55]

For heating-mediated application, an important factor to consider is the thermal behavior of the matrix. In a polymer matrix the increase in the equilibrium temperature is strictly correlated with the glass transition temperature (T_g) and the melting point (T_m) of the polymer, because phase changes of the polymer can induce

heat dissipation. Here gold nanoparticles were embedded in a silk fibroin matrix. Silk fibroin presents a high Tg (~180° C [56,57]) that suggests the possibility to operate in a wide range of temperature with reduced heat loss.

Gold NPs/silk composites have been already proposed for different types of applications. Tsao *et al.*[58] studied a gold nanocomposite/silk thin films with ultrahigh broadband absorbance for photo-thermo-electronic application, using a white-light source to induce photo-heating of the material. Guo and coworkers[59] developed a method for making gold nanoparticle-embedded silk nanocomposite films as substrates for Surface-enhanced Raman scattering (SERS) spectroscopy. The silk-based AuNPs composite was also proposed for focal infection treatment using laser-mediated heating by Kojic *et. al*.[60] In this work gold nanoparticles were embedded in an injectable and degradable silk hydrogel. The bactericidal effect of the nanoheater was then studied in vivo and in vitro by using a green laser source (532 nm) at a laser power comparable to the power provided by a laser pointer.

All these works used gold nanoparticles as LSPR source. Recently, research in the biomedical field is focused on particles that present LSPR in the NIR region. The NIR range (700-900 nm) is above the absorption of biological molecules such as hemoglobin and below the range absorbed by water. In this wavelength the light can penetrate the biological tissue with relatively light attenuation and tissue damage.[46]

Moved by this reason, we decided to focalize our study on the combination of silk fibroin with gold nanorods. Gold nanorods are anisotropic nanoparticles that present two plasmon resonances, one in the visible range similar to AuNPs, and the stronger one at longer wavelength related with the longitudinal resonance and dependent on the particle aspect ratio (i.e. the ratio between length and thickness of the rod). Compared to other type of nanostructures, AuNRs have larger extinction coefficient (108-1010 $M^{-1}cm^{-1}$) and narrower line-widths, with consequently higher photothermal conversion efficiencies and higher sensitivity to changes in the local dielectric constant.[61] One of the limit for their use in biomedical application is the presence of residual surfactant derived from the synthesis, which are toxic (cetyltrimethylammonium bromide, CTAB). To avoid this problem, different surface

modifications were proposed.[47] In this case, CTAB was replaced with thiolated polyethyleneglycol (PEG).[62,63] On the other hand, the incorporation in the SF matrix could solve the limitations related with the safety concerns, poor biocompatibility and limited tunability.[60]

In the following section of the chapter, I will report the fabrication and characterization of nanocomposite films embedded gold nanorods and the first results obtained by laser-mediated heating experiments.

2.3.1. Synthesis

SF-AuNRs nanocomposites were prepared by starting from the SF and AuNRs solution. SF was extracted from the *bombyx mory* fibers according to the protocol reported in literature[10] and extensively explained in the *Appendix A1.1*. The final concentration of SF in solution was 6% w/v.

AuNRs were synthesized by following the seed-mediated growth method and stabilized in aqueous solutions by cetyltrimethylammonium bromide (CTAB) [64]. To prevent the aggregation of the particles, facilitate the dispersion in the silk matrix and remove the toxic CTAB, AuNRs were capped with thiol-terminated methoxy poly(ethylene glycol) (mPEG-SH).[47] After the functionalization, the solution was concentrated to have a final concentration of particles in solution of 2 mg/ml. All the details are reported in *Appendix A1.3.*

The SF-AuNRs nanocomposites were prepared by mixing the two solutions in different ratio. Free-standing membrane were prepared by drop casting on a PDMS surface under hood in a controlled environment (30%RH, room temperature), to reduce the formation of coffee rings and avoid problem of agglomeration of the particles during the self assembly of the protein. The samples were dried overnight until the complete formation of the films.

2.3.2. Results and discussion

Figure 2.13(a) shows a TEM image of the as-synthesized AuNRs. The particles present an aspect ratio of about 3. The UV-VIS-NIR spectrum of the PEGylated AuNRs water solution is showed in **Figure 2.13**(b). The spectrum is characterized by the presence of two characteristics absorption peaks due by the plasmonic oscillations along the two directions of the rods. The main peak is centered in the NIR range at 765 nm, in the as-called biological window and suitable for laser-mediated photodynamic therapy applications, while the second peak is centered at 530 nm.

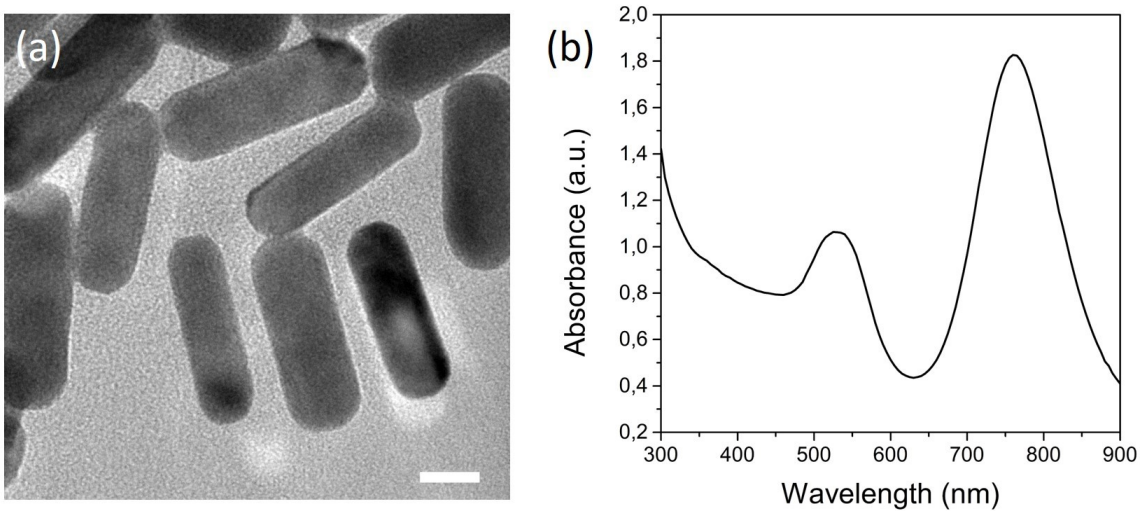

Figure 2.13. (a) TEM image of AuNRs (scale bar 10 nm). (b) UV-VIS-NIR absorbance spectrum of the PEG-capped AuNRs solution.

The AuNRs solution was then mixed with the SF solution to obtain the nanocomposite free standing films. The final free-standing films appeared uniformly red colored and transparent. The final thickness of the sample was measured to be ~40 μm. After the incorporation of the AuNRs in the silk matrix, the plasmonic peaks shift to longer wavelength. This redshift is clearly visible in the transmittance spectra of the film reported in **Figure 2.14**. Compared to the SF film, the increase of the NPs concentration induces a general decrease of the transmittance, with two marked peaks in correspondence of the LSPR peaks of the rods. The LSPR wavelengths are

redshift of about 10 nm (540 nm and 575 nm) and the two peaks results broader than those of the AuNRs in aqueous solution.

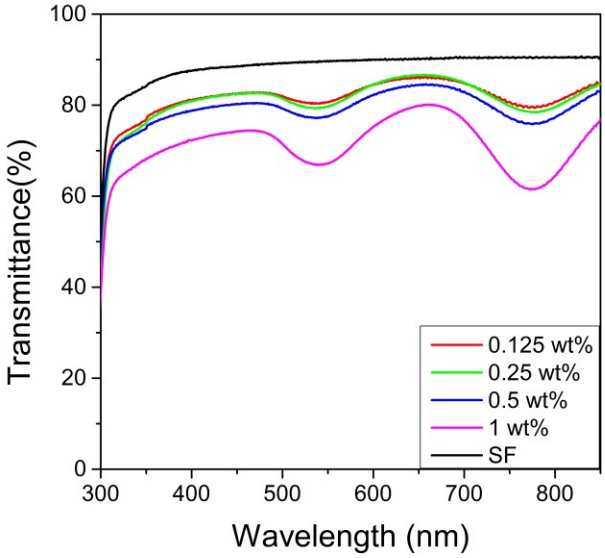

Figure 2.14. Transmittance spectra of the SF-AuNRs composite films with different nominal concentration of nanoparticles. For comparison is reported the spectrum of a SF film prepared in the same condition.

The red-shift is probably due to the difference in the refractive indices of the surrounding media, since the silk fibroin presents a refractive index higher than water.[65] Instead, the broadening can be correlated to the spatial and random distribution of the particles inside the SF matrix.

We also investigated the structure of the silk fibroin films with different nominal concentration of AuNRs. In **Figure 2.15** the FTIR spectra of the samples with different nominal concentration of AuNRs are reported. No variation in the secondary structure of the protein were detected by observation of the Amide I and II bands (1700- 1500 cm^{-1}). The Amide I band presents a predominant of random coils (1640-1649 cm^{-1}) and α-helix conformation, while no variation of the characteristic peak of the β-sheet is observed at 1626 cm^{-1}.[18] The results are similar for all the spectra.

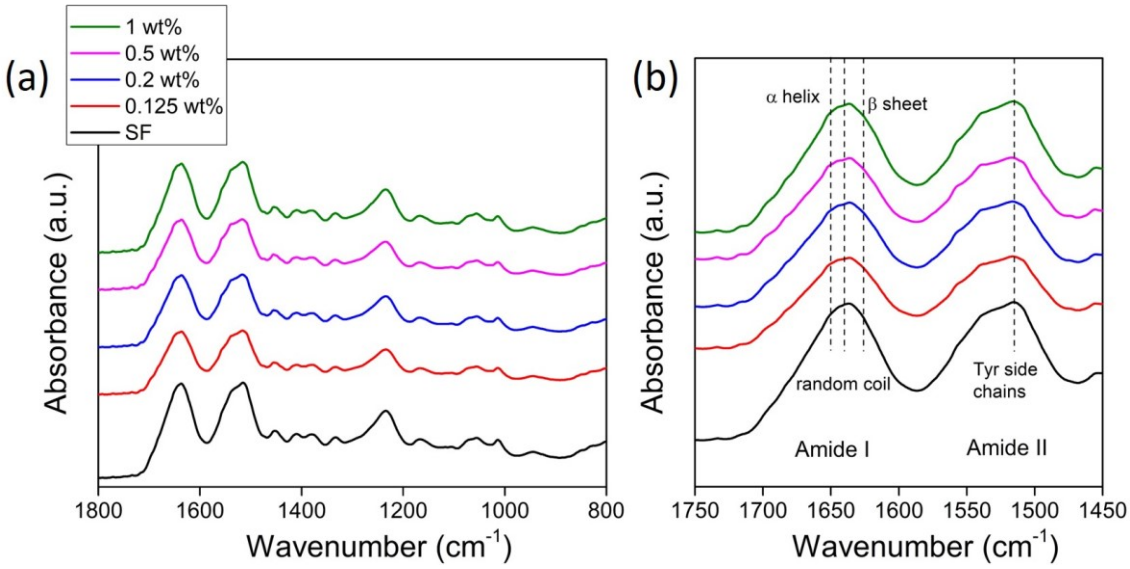

Figure 2.15. (a) Typical FTIR spectra of SF films with different nominal concentration in weight of AuNRs. (b) Particular of the FTIR spectra showing the Amide I and Amide II bands of the protein.

The temperature stability of a AuNRs-SF composite was investigated by DSC-TG analysis. In **Figure 2.16**(a) it is reported the weight loss of a film conataining 1% in weight of gold NRs. The samples lose about of 10% in weight between 25° to 300° C, corresponding to the loss of the adsorbed water. The trend is similar with the results obtained for SF films.[66] In **Figure 2.16**(b) it is instead reported the DSC curve. The analysis was conducted following the procedure reported in *Appendix A3.8*. The first heating cycle from -80° C to 230° C (before the degradation temperature of SF) shows a large endothermic peak at 100° C corresponding to the evaporation of the water present in the film. After cooling down, the second heating step reveals the thermal behavior of the pure material. The composite presents a high stability from room temperature up to 150° C (same behavior of the SF matrix).[67] The T_g was estimated at 178° C as for the pure SF.[56,58,68] No crystallization peaks of the protein induced by temperature were detected, because the crystallization process happens at about 220-250° C during the degradation.[69]

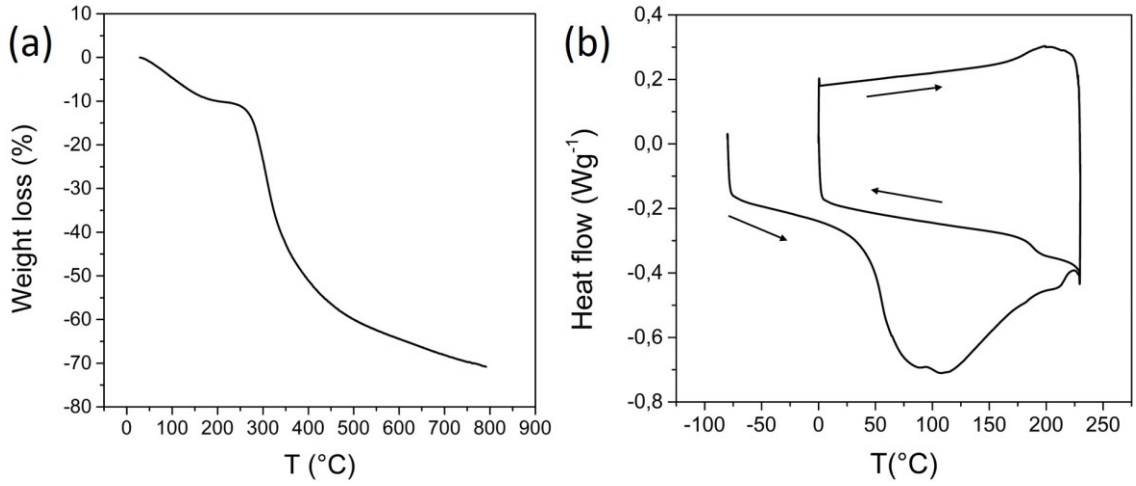

Figure 2.16. TGA (a) and DSC (b) curves of AuNRs-SF composite film with a concentration of 1% in wight of Au particles.

The photothermal conversion capability of the AuNRs-SF composite films were investigated by measuring the temperature increase of the material when irradiated with 808 nm laser light source closed to the LSPR (at 775 nm) of the AuNRs. A thermal IR camera was employed to measure in situ the temperature changes of the composite films. Considering the hygroscopic behavior of the silk, all the experiments were conducted in condition of 40% RH. Further details are reported in *Appendix A3.17*.

Figure 2.17(b) and (c) display typical thermal images recorded from a SF film and a sample containing 1 wt% of gold, respectively, after 5 minutes of exposition to the laser source at 4 Wcm^{-2}. As expected, we observed significant temperature increase in the case of the nanocomposite with a homogeneous distribution in the irradiated area of the sample, accompanied by a slight heat dissipation along the edges of the film. Instead, no significant increase of temperature from the room temperature (25° C) was detected in the case of the SF film.

The average temperature within the irradiated sample area was used to represent the global temperature of the composite film. With this thermal measurement, it was possible to determine the photo-thermal behavior of the material in different condition.

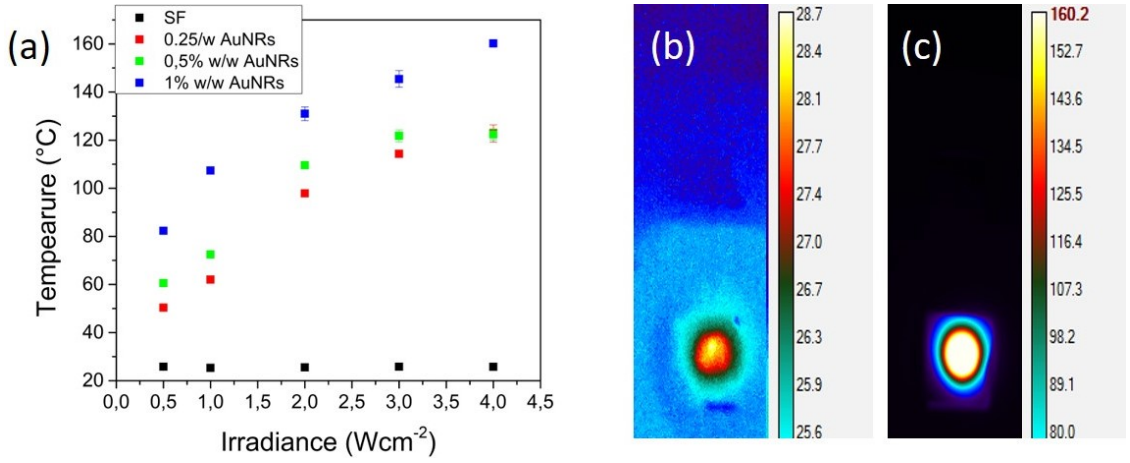

Figure 2.17. (a) Plot of the temperature changes for the nanocomposite films in the presence of different gold concentration at various laser irradiance. (b) and (c) Thermal images of a SF and nanocomposite (1 wt% gold) film after 5 minutes of esposition to a 808 nm laser source with an irradiance of 4 Wcm^{-2}.

In **Figure 2.17**(a) the equilibrium temperature reached by the nanocomposite films in the presence of different gold amount is plotted as function of the laser intensity. As expected, by increasing the gold concentration there is an increase of the equilibrium temperature. The relation between temperature and intensity is linear for all the sample below ~100° C, while above this temperature there is a change of slop. In the case of 0.25 wt% and 0.5 wt% samples, it is visible a sort of plateau, while for the highest concentration the temperature still increases with a different slop. The variations in the final temperature of the samples with respect to the amount of AuNRs can be explained by their optical behavior, especially the different absorbance. Most of the light is converted to heat by the composite films and, consequently, the final temperature is increased. We supposed that the absorbance at 808 nm had almost reached the saturation in the case of the law concentration of particles.[58] In the case of 1 wt% sample it was not possible to evaluate the maximum temperature reachable because of the operation range of the IR camera (limit of detection for the IR camera was 160° C).

It is also important to underline that above this temperature the photothermally deposited energy can couple to the cooperative segmental motions now available because the temperature is closed to the T_g of the SF matrix (especially in the case of presence of residual water in the film).

Another mechanism to consider is the reshaping of the gold nanorods. It is well known that a rod-to-sphere shape transition can be induced by photo-annealing and thermo-annealing below the melting points driven by surface diffusion.[70] In the case of the photo-annealing it depends on time of irradiation, type of laser source (pulse or continuum, femtosecond or nanosecond), power.[42,71]

Possible conformation transitions in the matrix were investigated also by FTIR. As reported in **Figure 2.18**(a), no changes were detected in all the compositions irradiated at the maximum intensity. The structure of the fibroin is still dominated by the random coils. In **Figure 2.18**(b) it is also reported the comparison with the untreated sample for one composition.

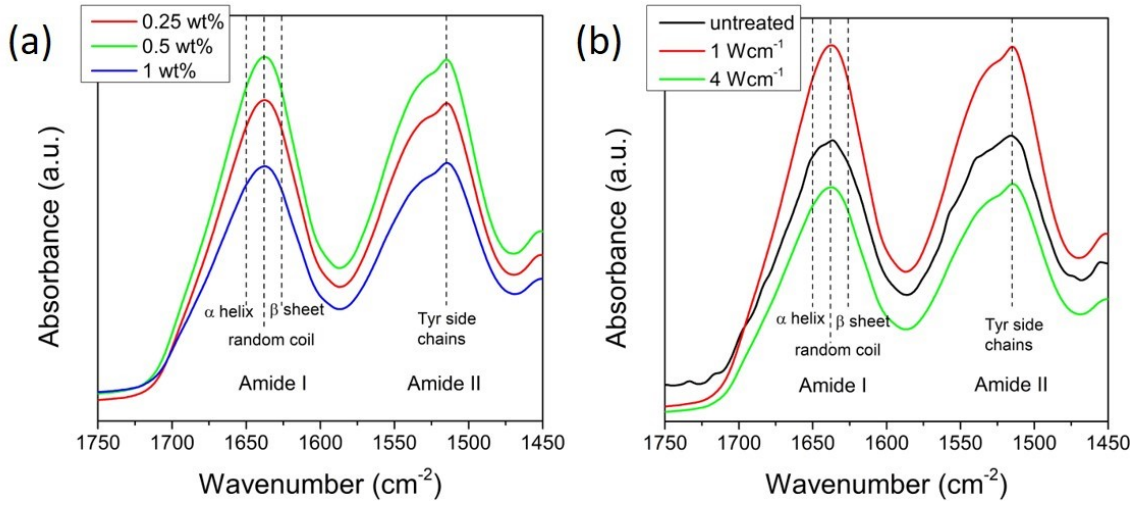

Figure 2.18. (a) FTIR spectra of SF-AuNRs with different composition after irradiation with a 808 nm laser source at 4 Wcm^{-1}. (b) FTIR spectra of SF-AuNRs (1 wt% NPs) untreated and after irradiation at different laser intensity.

Taking into account all these considerations and the temperature range of interest for the biomedical application, we further exploited the thermal response below 100° C. **Figure 2.19**(a) displays the relation between the laser intensity and the temperature for a maximum irradiance of 2 Wcm^{-2} in the case of 0.25wt% composite.

We confirmed the linear relation in all the considered temperature range and the equilibrium temperature is reached in only 5sec (**Figure 2.19**(b)).

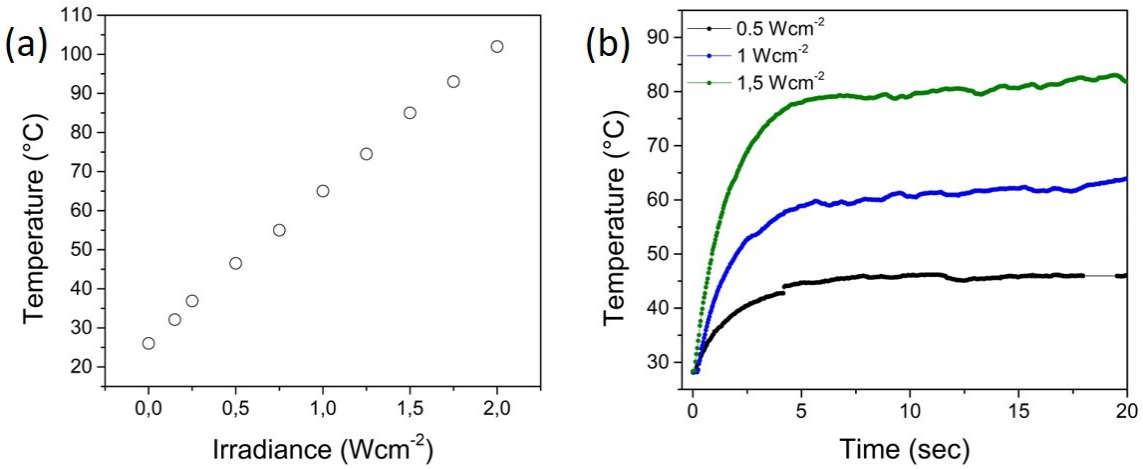

Figure 2.19. (a) Maximum temperature achieved as a funtion of irradiance for a SF-AuNRs composite film (0.25 wt%) when irradiated with a 808 nm laser source. (b) Temperature attained as a function of time when varying the 808 nm laser intensity for SF-AuNRs (0.25 wt%) nanocomposite films in ambient.

Finally, we evaluated the temperature decay after the laser had been turned off. As visible in **Figure 2.20**, the nanocomposite cools down in about 15 seconds reaching 90% of the initial temperature (60°C, for $1Wcm^{-2}$).

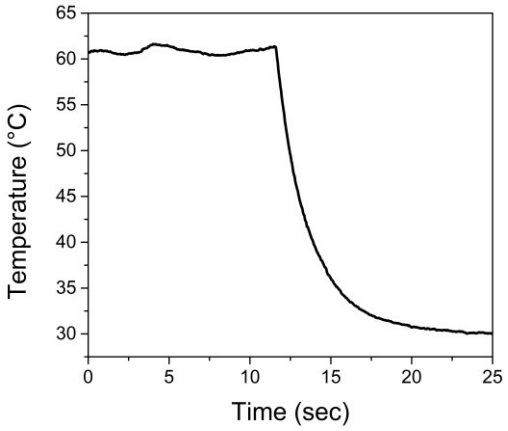

Figure 2.20. Temperature decay for a SF-AuNRs film (0.25 wt%) when the laser had been turned off (310 s).

In conclusion, we described the fabrication of SF-AuNRs composite films by a simple method based on the mixing of the two water-based solutions. We characterized the optical transmittance as a function of the particles concentration and we evaluated the effect of the AuNRs on the SF secondary structure and on the thermal stability. Finally, we characterized the photothermal behavior of the SF-AuNRs films when irradiated with a laser source matching the longitudinal LSPR peak of the rods. We demonstrated a good stability and a faster response of the material, and the possibility to tune the temperature achieved by acting on the NPs concentration and the laser intensity. Further studies are needed for elucidating the effects of the thickness of the film, the possible reshaping of the nanorods on the absorbance of the material and the thermal properties in a biological-like environment.

2.4. Conclusions

In this chapter we introduced two different SF-based nanocomposites combined the biopolymer matrix with TNSs and AuNRs.

The possibility to tune the refractive index of the silk by acting on the concentration of the TNSs was already demonstrated by Perotto et al.[6] Here we further investigated the effect of the methanol annealing on the structural properties of the materials and for the first time we characterized the mechanical properties of the nanocomposite by nanoindentation tests. Even if the results are only preliminary, the good mechanical behavior (in terms of modulus and hardness) suggests the possibility to investigate this nanocomposite not only for optical application but even for improving and controlling the mechanical properties of silk-based structure.

Secondary, we demonstrated the possibility to easy synthesize a SF-AuNRs composite materials with tunable optical properties (in terms of plasmon resonance of the particles) acting on the AuNRs concentration and by controlling the fabrication process. The preliminary results related with the thermo-response behavior confirm the potentiality of this material for photodynamic therapy applications. The material could also be suitable for the realization of flexible plasmonic devices for sensing or plasmonic heating.[52,53]

References

[1] J. G. Hardy, T. R. Scheibel, *Prog. Polym. Sci.* **2010**, *35*, 1093.

[2] F. G. Omenetto, D. L. Kaplan, *Nat. Photonics* **2008**, *2*, 641.

[3] H. Tao, D. L. Kaplan, F. G. Omenetto, *Adv. Mater.* **2012**, *24*, 2824.

[4] S. T. Parker, P. Domachuk, J. Amsden, J. Bressner, J. A. Lewis, D. L. Kaplan, F. C. Omenetto, *Adv. Mater.* **2009**, *21*, 2411.

[5] S. Kim, A. N. Mitropoulos, J. D. Spitzberg, H. Tao, D. L. Kaplan, F. G. Omenetto, *Nat. Photonics* **2012**, *6*, 818.

[6] G. Perotto, M. Cittadini, H. Tao, S. Kim, M. Yang, D. L. Kaplan, A. Martucci, F. G. Omenetto, *Adv. Mater.* **2015**, *27*, 6728.

[7] L. Wang, T. Sasaki, *Chem. Rev.* **2014**, *114*, 9455.

[8] A. Antonello, **2009**, 1.

[9] A. Antonello, M. Guglielmi, V. Bello, G. Mattei, A. Chiasera, M. Ferrari, A. Martucci, *J. Phys. Chem. C* **2010**, *114*, 18423.

[10] D. N. Rockwood, R. C. Preda, T. Yücel, X. Wang, M. L. Lovett, D. L. Kaplan, *Nat. Protoc.* **2011**, *6*, 1612.

[11] M. Tsukada, Y. Gotoh, M. Nagura, N. Minoura, N. Kasai, G. Freddi, *J. Polym. Sci. Part B Polym. Phys.* **1994**, *32*, 961.

[12] J. Magoshi, M. Mizuide, Y. Magoshi, K. Takahashi, M. Kubo, S. Nakamura, *J. Polym. Sci. Polym. Phys. Ed.* **1979**, *17*, 515.

[13] J. Nam, Y. H. Park, *J. Appl. Polym. Sci.* **2001**, *81*, 3008.

[14] W. Tao, M. Li, C. Zhao, *Int. J. Biol. Macromol.* **2007**, *40*, 472.

[15] Y. Gotoh, M. T. A, N. M. B, *Int. J. Biol. Macromol.* **1996**, *19*, 41.

[16] N. Greenfield, G. D. Fasman, *Biochemistry* **1969**, *8*, 4108.

[17] Z. Ayub Haider, M. Arai, K. Hirabayashi, *Biosci. Biotechnol. Biochem.* **1993**, *57*, 1910.

[18] X. Hu, K. Shmelev, L. Sun, E.-S. Gil, S.-H. Park, P. Cebe, D. L. Kaplan, *Biomacromolecules*

2011, *12*, 1686.

[19] P. Čapková, M. Pospíšil, J. Miehé-Brendlé, M. Trchová, Z. Weiss, R. Le Dred, *J. Mol. Model.* **2000**, *6*, 600.

[20] C. B. Borkner, M. B. Elsner, T. Scheibel, *ACS Appl. Mater. Interfaces* **2014**, *6*, 15611.

[21] S. Lu, X. Wang, Q. Lu, X. Zhang, J. A. Kluge, N. Uppal, F. Omenetto, D. L. Kaplan, *Biomacromolecules* **2010**, *11*, 143.

[22] F. Wang, S. S. Jyothirmayee Aravind, H. Wu, J. Forys, V. Venkataraman, K. Ramanujachary, X. Hu, *Mater. Sci. Eng. C* **2017**, *79*, 728.

[23] C. Jiang, X. Wang, R. Gunawidjaja, Y. H. Lin, M. K. Gupta, D. L. Kaplan, R. R. Naik, V. V. Tsukruk, *Adv. Funct. Mater.* **2007**, *17*, 2229.

[24] L. D. Koh, Y. Cheng, C. P. Teng, Y. W. Khin, X. J. Loh, S. Y. Tee, M. Low, E. Ye, H. D. Yu, Y. W. Zhang, M. Y. Han, *Prog. Polym. Sci.* **2015**, *46*, 86.

[25] L. Peponi, D. Puglia, L. Torre, L. Valentini, J. M. Kenny, Processing of nanostructured polymers and advanced polymeric based nanocomposites. *Mater. Sci. Eng. R Reports* **2014**, *85*, 1–46.

[26] E. P. Giannelis, *Appl. Organomet. Chem.* **1998**, *12*, 675.

[27] Q. Dang, S. Lu, S. Yu, P. Sun, Z. Yuan, *Biomacromolecules* **2010**, *11*, 1796.

[28] A. M. Díez-Pascual, M. A. Gómez-Fatou, F. Ania, A. Flores, *Prog. Mater. Sci.* **2015**, *67*, 1.

[29] S. F. Wang, L. Shen, Y. J. Tong, L. Chen, I. Y. Phang, P. Q. Lim, T. X. Liu, *Polym. Degrad. Stab.* **2005**, *90*, 123.

[30] N. E. Kurland, J. Kundu, S. Pal, S. C. Kundu, V. K. Yadavalli, *Soft Matter* **2012**, *8*, 4952.

[31] I. Greving, M. Cai, F. Vollrath, H. C. Schniepp, *Biomacromolecules* **2012**, *13*, 676.

[32] S. L. Dodson, C. Cao, H. Zaribafzadeh, S. Li, Q. Xiong, *Biosens. Bioelectron.* **2015**, *63*, 472.

[33] M. Maisonneuve, C. Valsecchi, C. Wang, A. G. Brolo, M. Meunier, *Biosens. Bioelectron.* **2015**, *63*, 80.

[34] N. Gogurla, A. K. Sinha, D. Naskar, S. C. Kundu, S. K. Ray, *Nanoscale* **2016**, *8*.

[35] J. Pérez-Juste, I. Pastoriza-Santos, L. M. Liz-Marzán, P. Mulvaney, In *Coordination Chemistry Reviews*; Elsevier, 2005; Vol. 249, pp. 1870–1901.

[36] J. R. Cole, N. J. Halas, *Appl. Phys. Lett.* **2006**, *89*, 153120.

[37] N. G. Khlebtsov, L. A. Dykman, Optical properties and biomedical applications of plasmonic nanoparticles. *J. Quant. Spectrosc. Radiat. Transf.* **2010**, *111*, 1–35.

[38] P. K. Jain, X. Huang, I. H. El-Sayed, M. A. El-Sayed, *Plasmonics* **2007**, *2*, 107.

[39] M. Hu, J. Chen, Z.-Y. Li, L. Au, G. V. Hartland, X. Li, M. Marquez, Y. Xia, *Chem. Soc. Rev.* **2006**, *35*, 1084.

[40] S. H. Yun, S. J. J. Kwok, *Nat. Biomed. Eng.* **2017**, *1*, 8.

[41] P. Zijlstra, J. W. M. Chon, M. Gu, 7 S S Chang, C. W. Shih, C. D. Chen, W. C. Lai, C. R. C. Wang, 10 H Petrova, J. Pérez-Juste, I. Pastoriza-Santos, G. V Hartland, L. M. Liz-Marzán, P. Mulvaney, *Phys. Opt. EXPRESS* **2001**, *114*, 2362.

[42] A. B. Taylor, A. M. Siddiquee, J. W. M. Chon, *ACS Nano* **2014**, *8*, 12071.

[43] A. M. Gobin, E. M. Watkins, E. Quevedo, V. L. Colvin, J. L. West, *Small* **2010**, *6*, 745.

[44] P. G., T. U., A. O., H. M., S. N., B. Y.Y., B. S., A.-B. R., K. a., H. H., *Nat. Nanotechnol.* **2009**, *4*, 669.

[45] J.-E. Park, M. Kim, J.-H. Hwang, J.-M. Nam, *Small Methods* **2017**, *1*, 1600032.

[46] L. E. Strong, J. L. West, *Wiley Interdiscip. Rev. Nanomedicine Nanobiotechnology* **2011**, *3*, 307.

[47] Z. Zhang, J. Wang, C. Chen, *Theranostics* **2013**, *3*, 223.

[48] N. Frazier, R. Robinson, A. Ray, H. Ghandehari, *Mol. Pharm.* **2015**, *12*, 1605.

[49] M. L. Brongersma, N. J. Halas, P. Nordlander, *Nat. Nanotechnol.* **2015**, *10*, 25.

[50] E. C. Dreaden, A. M. Alkilany, X. Huang, C. J. Murphy, M. A. El-Sayed, *Chem. Soc. Rev.* **2012**, *41*, 2740.

[51] C. Liu, K. Hayashi, K. Toko, *Sensors Actuators, B Chem.* **2012**, *161*, 504.

[52] P. Wang, L. Zhang, Y. Xia, L. Tong, X. Xu, Y. Ying, *Nano Lett.* **2012**, *12*, 3145.

[53] C. Fang, L. Shao, Y. Zhao, J. Wang, H. Wu, *Adv. Mater.* **2012**, *24*, 94.

[54] H. Zhang, H. Xia, Y. Zhao, *J. Mater. Chem.* **2012**, *22*, 845.

[55] Y. Ofir, B. Samanta, V. M. Rotello, *Chem. Soc. Rev.* **2008**, *37*, 1814.

[56] J. Magoshi, S. Nakamura, *J. Appl. Polym. Sci.* **1975**, *19*, 1013.

[57] J. Guan, Y. Wang, B. Mortimer, C. Holland, Z. Shao, D. Porter, F. Vollrath, *Soft Matter* **2016**, *12*, 5926.

[58] S. H. Tsao, D. Wan, Y. S. Lai, H. M. Chang, C. C. Yu, K. Te Lin, H. L. Chen, *ACS Nano* **2015**, *9*, 12045.

[59] C. Guo, G. N. Hall, J. B. Addison, J. L. Yarger, *RSC Adv.* **2015**, *5*, 1937.

[60] N. Kojic, E. M. Pritchard, H. Tao, M. A. Brenckle, J. P. Mondia, B. Panilaitis, F. Omenetto, D. L. Kaplan, *Adv. Funct. Mater.* **2012**, *22*, 3793.

[61] H. Chen, L. Shao, Q. Li, J. Wang, H. Misawa, P. van Dorpe, P. Nordlander, S. A. Maier, S. Wolff, M. Fischer, S. Gsell, M. Schreck, C. Becher, U. Sennhauser, B. Hecht, *Chem. Soc. Rev.* **2013**, *42*, 2679.

[62] A. M. Alkilany, A. Shatanawi, T. Kurtz, R. B. Caldwell, R. W. Caldwell, *Small* **2012**, *8*, 1270.

[63] S. C. Boca, S. Astilean, *Nanotechnology* **2010**, *21*, 235601.

[64] B. Nikoobakht, M. A. El-Sayed, *Chem. Mater.* **2003**, *15*, 1957.

[65] G. Perotto, Y. Zhang, D. Naskar, N. Patel, D. L. Kaplan, S. C. Kundu, F. G. Omenetto, *Appl. Phys. Lett.* **2017**, *111*, 103702.

[66] Q. Lu, X. Hu, X. Wang, J. A. Kluge, S. Lu, P. Cebe, D. L. Kaplan, *Acta Biomater.* **2010**, *6*, 1380.

[67] X. Hu, D. Kaplan, P. Cebe, *Macromolecules* **2008**, *41*, 3939.

[68] X. Hu, D. Kaplan, P. Cebe, *Thermochim. Acta* **2007**, *461*, 137.

[69] M. Tsukada, G. Freddi, P. Monti, A. Bertoluzza, *J. Polym. Sci. B* **1996**, *33*, 1995.

[70] H. Petrova, J. Perez Juste, I. Pastoriza-Santos, G. V Hartland, L. M. Liz-Marzán, P. Mulvaney, *Phys. Chem. Chem. Phys.* **2006**, *8*, 814.

[71] S. Link, C. Burda, B. Nikoobakht, M. A. El-Sayed, *J. Phys. Chem. B* **2000**, *104*, 6152.

Chapter 3.

Functionalization of Silk-TNSs nanocomposites via a simple cation exchange route

3.1. Introduction

The ion exchange between a solid material and a liquid (melt or solution) is a well-known and widely used process in many scientific and technologic fields, from water softening and chromatography to catalysis and strengthening glass. [1,2] In the material science, ion exchange is also used as a soft chemistry tools for preparing new materials. This process used since the Roman age, (just thinking of the famous example of the Lycurgus cup), is recently receiving a new interest in the nanotechnology field. Exchange on the nanoscale exhibits some unique attributes, like fast kinetics at room temperature, those open the possibility to synthesize compositionally novel or multicomponent materials and heterostructures. [3–8]

For definition, it is considered ion exchanger a solid material which carries exchangeable ions. When this material is in contact with an electrolyte solution, the ions can be exchangeable with a stoichiometrically equivalent number of different ions with the same charge. If the ions are positively charged, the material is considered a cation exchanger, while it is called anion exchanger if it carries negatively charged anions. [9] Because anions usually present a larger radius compared to cations, cation exchange is most diffused especially in the case of the post-synthetic chemical modifications of the materials.

The overall cation exchange reaction is:

$$M^{n+}(liquid) + CA(solid) \rightarrow C^{n+}(liquid) + MA(solid) \quad (3.1)$$

Where M is the ingoing ion, and C and A are the exchangeable cation and the counterion, respectively. The thermodynamics of the process is controlled by different steps of the exchange reaction:

$$CA \rightarrow C + A\ (dissociation) \quad (3.2)$$

$$M^{n+} \rightarrow M\ (desolvation) \quad (3.3)$$

$$M + A \rightarrow MA\ (association \quad (3.4)$$

$$C \rightarrow C^{n+}(solvation) \quad (3.5)$$

The ease with which the metal ion is dissociated and solvated, dictate the energy balance of cation exchange. The reaction is favorite if the exchangeable cation is more strongly solvated in the reaction solvent than the ingoing cation. [10] The propensity for selective ion binding in solution can be qualitatively understood considering the Pearson's hard soft acid base (HSAB) theory, which classifies Lewis acids and bases on the base of their polarizability in different grades of hardness. According to this theory, hard-hard and soft-soft interactions are favored compared to the soft-hard interactions.[11]

These considerations about thermodynamics can give information on the nature and on the feasibility of the ion exchange process. In the case of exchange at room temperature, the reaction is under thermodynamic equilibrium; therefore, the reaction is controlled by kinetic factors. Considering that, most of the ion exchange processes are diffusion phenomenon, two determining steps control the kinetics in most of the cases: diffusion of ions inside the material (referred as particle diffusion) or diffusion of the ions through the liquid film (a solution zone of a certain thickness closed to the interface with no convection). The particle diffusion-controlled phenomenon is favored by a high metal ion concentration, a relatively large particle size of the exchanger and vigorous shaking of the exchanging mixture.[12]

At the nanoscale, the kinetic mechanism is partially different because the limits on long-range ion diffusion are relaxed by the large surface-to-volume ratios of nanoscale crystallites. In this case, the process results accelerated, because of the short time scale and low activation energy.[6]

In **Figure 3.1** a schematic of all the possible reactions involved in a generic ion exchange process is reported.

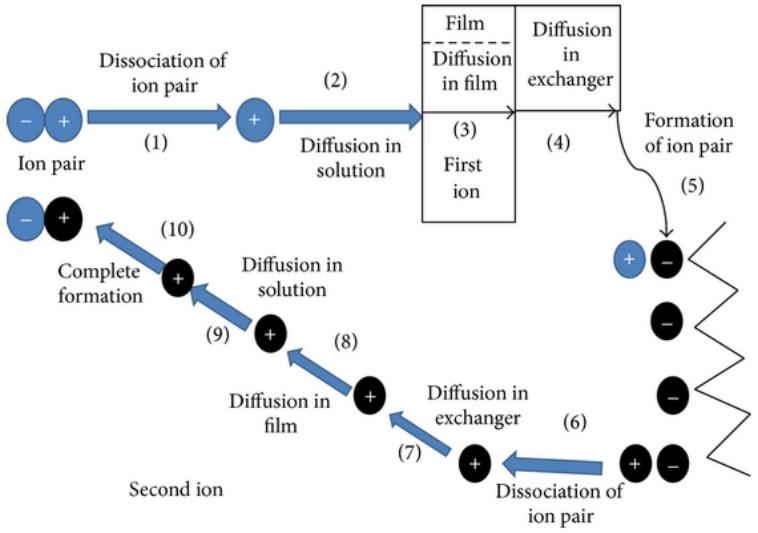

Figure 3.1. Schematic representation of the steps involved in an ion exchange process. The dissolved salt dissociates (step 1), followed by diffusion of the first ion from solution towards the interphase film (step 2). Then the ion diffuses out of the film (step 3) towards the material phase (step 4). The ion associates with the functional group (step 5) and then dissociation of second ion and the functional group occurs in step 6. The second ion diffuses inside the material phase towards the surface (step 7). The second ion diffuses inside the interphase film (step 8), followed by diffusion and random distribution in the solution (step 9). Thus the formation of second ion pair completes (step 10).[13]

A wide number of natural and synthetic materials presents ion exchange properties. Among the naturals, zeolites and clays are the main representatives of the inorganic compounds, while proteins and polysaccharides are examples of organic ion exchangers because of the presence of carboxyl groups (–CO_2H), and phenolic groups (–OH), that are weakly acidic and can exchange their hydrogen ions for other cations under neutral or alkaline conditions.[13] In the category of synthetic materials, the organic exchangers are phenolic, acrylic and polystyrene divinyl resins, while the

group of inorganics includes synthetic zeolites, titanates and transition metal hexacyanoferrate.[14]

Layered titanates are titanium oxide-based compounds, which have been produced in different shapes such as nanotubes, nanowires and nanoflowers and have been largely investigated because of their exchange capacity for application in adsorption of heavy metal ions from water,[15–18] generation of proton exchange membrane fuel cells [19,20] or for the synthesis of complex metal oxide structures.[21] Titanates nanosheets (TNSs), in particular, present good cation exchange properties at the nanoscale because of the high surface to volume ratio, the high concentration of hydroxylic groups and the interlayer distance adaptability. These nanoparticles have been investigated for the fabrication of thin films with intercalated protons or metal cations for optoelectronic applications,[22,23] but even in combination with a polymeric matrix for the generation of proton exchange membranes.[24]

As proposed in the previous chapter, TNSs can be easily combined with silk fibroin (SF) for the fabrication of nanocomposite thin films and membranes with tunable optical properties and processability at the micro and nano-scale range. In this chapter, the ion exchange properties of this novel nanocomposite will be investigated as a strategy for post-synthetic chemical modification of the material.
In the first part, a study on the exchange process will be proposed, focusing in particular on the kinetic of the process. Three main ions will be selected as a representative to evaluate the influence of the valence and ionic radius on the adsorption capacity of the nanocomposite. To determine the effect of the TNSs on the exchange properties, different SF-TNSs formulations will be considered in the study and compared with the behavior of the pure silk fibroin. As previously illustrated, the fibroin protein presents organic groups capable to act as exchange sites in neutral or alkaline solutions.
The structural and thermal properties of the nanocomposite after the exchange will be characterized in the second part of the chapter. X-ray diffraction analysis and transmission electron microscopy will be used to determine the change in the crystalline structure and the possible collapse of the layered arrangement.

Differential thermal analysis and thermogravimetric analysis will be selected to characterize the thermal stability of the material and verify the possible formation of complex metal oxides.

The last part of the chapter will be focused on the study of the new optical functionalities introduced in the material, such as plasmonic resonance and fluorescence.

As already reported in the literature, the exchange of the ammonium ions inside the interlayer of TNSs with metal cations like silver, gold and copper, allow synthesizing in situ plasmonic nanoparticles and nanoclusters.[25–27] The development of polymeric membranes with embedded metal nanoparticles with is of great interest in the nanotechnology field for example for biocide or photocatalytic applications.[28] The advantage of the nanocomposite ion exchange materials is the possibility to allocate the particles preferentially at the surface or to control the distribution by a selective reduction of the ions.[28] In addition, the *in situ* synthesis approach is highly tailorable because it allows for control of the amount of metal ions in the precursor films and thus the size of the resultant metal nanoparticles.[29,30]

Here, the possibility to synthesize silver nanoparticles inside the SF-TNSs nanocomposite by photoreduction mediated by the presence of TNSs will be demonstrated.

Finally, the luminescence of SF-TNSs incorporating europium ions will be presented. The preliminary results obtained suggests the possibility to use the ion exchange as a tool for the fabrication of luminescent polymer-based materials suitable for the fabrication of optical waveguides and sensors.

3.2. Synthesis

The SF-TNSs nanocomposite was synthesized according to the protocol reported in *Chapter 2*, by simple mixing of silk fibroin solution and TNSs water dispersion in the appropriate ratio and gently mixed to avoid the fibroin flocculation. For the study of the ion exchange kinetic and for the main characterizations, free standing samples were prepared by drop casting the solution on

polydimethylsiloxane (PDMS) flat substrate. Different formulations were prepared: 80:20 %wt, 50:50 %wt, 20:80 %wt SF-TNSs and 100 %wt SF (as reference), starting from a 5 %w/w SF solution and 20 %w/v TNSs solution. The volume of the solution was adjusted to obtain a final thickness of the sample of about 30 μm. The details of the formulations are reported **Table 3.1**, considering a total volume of the final solution equal to 1 ml.

Table 3.1. Formulations used for the preparation of the SF-TNSs samples. The values reported refer to a volume of the final solution equal to 1 ml.

SF-TNSs ratio (% w/v)	SF sol (μl)	TNSs sol (μl)
100:0	100	-
20:80	500	500
50:50	800	200
80:20	941	59

After drying (30-40 %RH, room T), samples were cut in small pieces and dip in methanol for 30 min and leave to dry under hood for 4 hours to crystallize the silk and make them water insoluble.[31]

For ellipsometric measurements, thin film samples were deposited on a quartz substrate by spin-coating at 3000 rpm for 60 s, using the SF-TNSs solutions as prepared without further dilutions.

3.3. Ion exchange study

To study the ion exchange process, the prepared samples (15 mg) were incubated in nitrate metal aqueous solutions (15 ml) with a concentration of 0.1 M at room temperature, under stirring (600 rpm). Considering that the diffusion of the ions in solution mainly affects the kinetic of the process, the study was conducted in ideal conditions of “endless flux” (high ratio between the volume of solution and the volume of the sample, high concentration of metal ions). All the experiments were

effectuated at room temperature (25° C), no temperature effects on the kinetic were studied.

After a given time, the samples were removed from the solution, rinsed with DI water and dried in air before the characterizations. Kinetic studies were developed by changing the ion exchange time.

Even if several metal cations (M^{n+} = Ag^{+}, Na^{+}, Cu^{2+}, Mg^{2+}, Fe^{3+}, Al^{3+}, Eu^{3+}) were considered at the beginning to verify the ion exchange capacity of the material, the main study was focused on three principles ions: Ag^{+}, Cu^{2+}, Eu^{3+}.

These are often considered as representative ions in ion exchange studies,[16] specifically Ag^{+} is a noble metal cation presenting the same valence of the TMA, Cu^{2+} is a common heavy metal contaminant, and Eu^{3+} is a trivalent lanthanide. Cu^{2+} was chosen as a model heavy metal ion because it is tinted with light blue color in aqueous solution which is easily observed by naked eye or spectrometer.[32] Silver was selected as possible precursors for the *in-situ* synthesis of Ag nanoparticles,[33] while Eu^{3+} was chosen because of its excellent photoluminescence (PL) properties.

3.3.1. UV-VIS spectroscopy on SF-TNSs/Cu

A preliminary study to qualitative characterize the kinetic of the ion exchange process on the material was conducted using Cu^{2+} ions. The $Cu(NO_3)$ water solution presents in fact a characteristic light blue color due to a strong absorption at 800 nm that can be easily detected using a UV-VIS spectrophotometer, as shown in **Figure 3.2**.

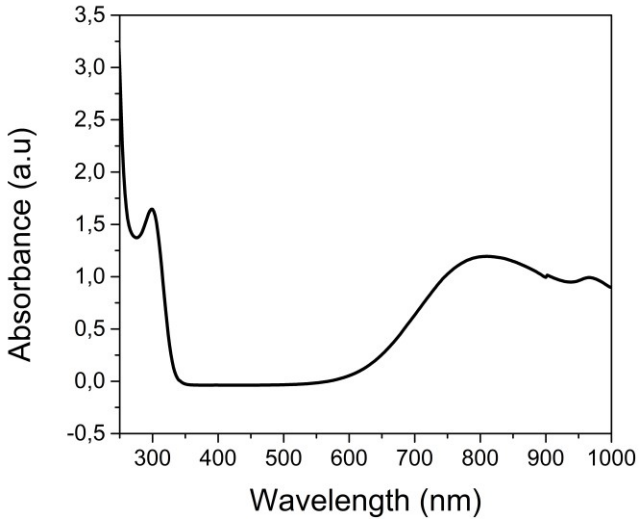

Figure 3.2. UV-VIS absorbance spectrum of 0.1M $Cu(NO_3)_2$ water solution.

The study was conducted on SF-TNSs free standing films with composition 50:50 and on sample SF films as reference. The absorbance of the samples was measured before and after the incubation in the 0.1 M $Cu(NO_3)_2$ water solution for different times.

The absorbance spectrum of SF-TNSs sample before and after the exchange process is reported in **Figure 3.3**(a). The effect of the copper cation intercalation is a red shift on the absorption edge relative to the starting material and the appearance of a broad absorption peak in the spectrum center at 800 nm, that corresponds to a visible green color. The absorbance intensity of the peak increases with the increase of the exchange time, because of the increase of the copper ions inside the materials. By monitoring the difference in absorbance at 800 nm, it was possible to qualitative determine the kinetic of the process. As reported in Figure 3.2(b), the exchange process is extremely fast in the first 10 minutes and the equilibrium is reached in about 1 h.

In the same figure is reported for comparison the profile of the copper absorption in the case of the pure SF. The trend is similar to the curve of the nanocomposite, but the total absorption is lower. This result confirms that the presence of TNSs in the material is fundamental for the adsorption of the metal ions and suggests that the predominant process involved is the exchange between the TMA^+ and the Cu^{2+} ions.

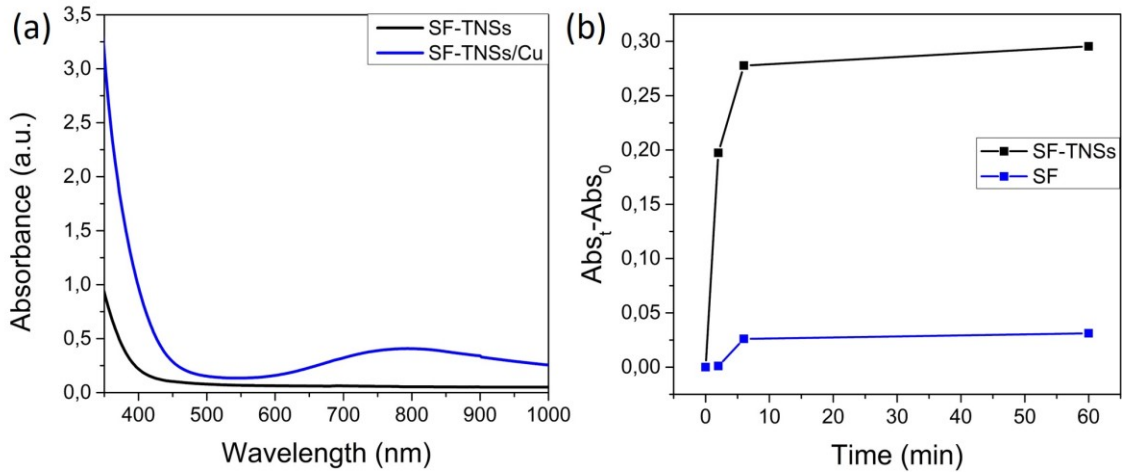

Figure 3.3. **(a)** UV-VIS spectra of the SF-TNSs before (black) and after (blue) Cu2+ exchange for 1 h. (b) Correlation between the difference in absorbance at 800 nm before and after the exchange for different time of incubation in 0.1 M $Cu(NO_3)_2$ solution.

This detection method is particularly simple and can provide a qualitative indication of the exchange process. Unfortunately, without knowing the extinction coefficient of the absorbing species, it was not possible to carry out quantitative analysis based on the Lambert-beer law.

3.3.2. ICP analysis

Elemental analysis was conducted to determine the amount of metal introduced into the nanocomposite. Small pieces (0.03 g) of the nanocomposite were treated with an acidic solution (6 ml of HNO_3, 2 ml of H_2O_2 and 1 ml of HF) to completely dissolve the samples. After cooling, HF was buffered with 1 ml of H_3BO_3 and the resulting clear solution was then diluted to 50 ml with high purity water, filtered and analyzed by inductively coupled plasma optical emission spectroscopy (ICP-OES) (see *Appendix A3.9*). The metal content was then correlated with the time of exchange to evaluate the kinetic profile and normalized to the amount of Ti detected to determine the effect of the %TNSs on the exchange properties of the nanocomposite.

The kinetic curves of M^{n+} on Silk-TNSs nanocomposite are reported in **Figure 3.4**(a). The exchange process is extremely fast in the case of Ag^{+} and Cu^{2+} and the equilibrium is reached out in about 10 minutes. In contrast, the nanocomposite presents a slower kinetic of exchange in the presence of Eu^{3+}.

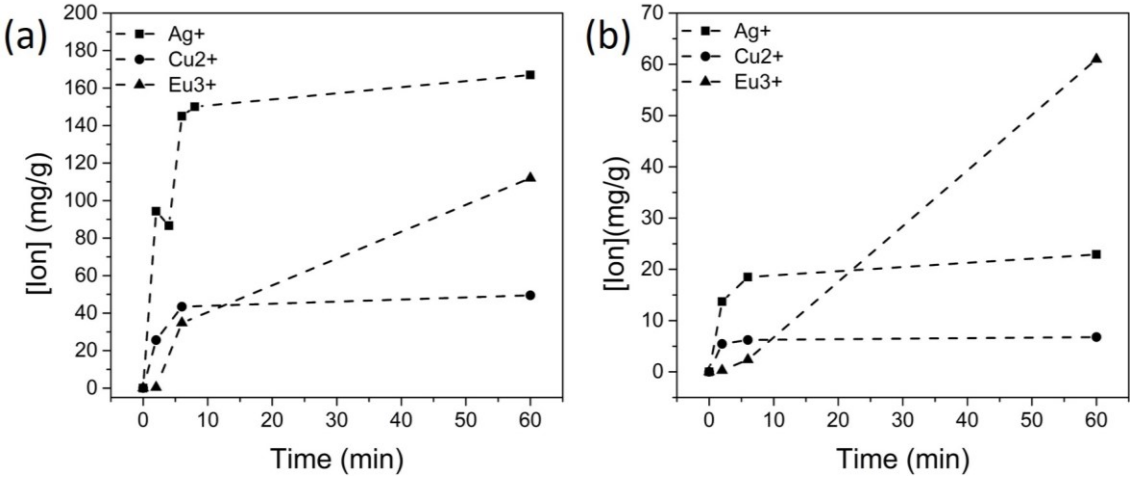

Figure 3.4. Ion loading as function of ion exchange time for Silk/TNSs nanocomposite (a) and for pure silk (b) in 0.1 M $[Ion]^{n+}$ aqueous solutions.

It is well established that the adsorption of metal ions by TNSs can be attributed to -OH and -O-TMA located in titanate interlaminations, and the adsorption mechanism is ion-exchange between H+/TMA+ and metal ions. [15,34,35] Specifically, hydrated metal ions in solution dissociate into free ions and then exchange with H+/TMA+. Hence, the affinity of metal ions to TNSs is closely related to the ion radius and hydration energy of metal ions. In general, ions with smaller ion radius can be expected to transfer more easily into the layers of TNSs and then exchange with H+/TMA+. In the present case, the hydrated ion radius of the three metals is ranked as Eu3+>Cu2+>Ag+, as reported in **Table 3.2**. This validated the hypothesis that the process is faster and easier in the case of Ag and Cu, compared to Eu.

Table 3.2. Characteristics of the ions considered in this study: valence, ionic radius, hydration shell (Δr), hydrated radius and Gibbs free energy of hydration.[36]

Ion	Valence	Ionic radius (nm)	Hydration shell Δr (nm)	Hydrated radius (nm)	Hydration energy (KJmol-1)
NH4+	1	0.148	0.065	0.213	-285
Ag+	1	0.115	0.097	0.212	-430
Cu2+	2	0.073	0.224	0.297	-2010
Eu3+	3	0.095	0.218	0.313	-3360

In **Figure 3.4**(b) the adsorption kinetic curves of the silk fibroin films are reported for comparison. The curves present the same profile found in the case of the nanocomposite, with an equilibrium at ~8 min for Ag and ~5 min for Cu. These results are in agreement with the literature, in fact is well-known that silk fibroin presents the capability to adsorb and bind both these metal ions with a higher affinity for Cu^{2+} in condition of a neutral pH. [37,38] As previously observed in the case of the nanocomposite, a different behavior is observed for the Eu ion. Even in the case of the simple fibroin matrix, the kinetic profile does not present an equilibrium in the first 10 minutes. In addition, the maximum metal content detected after 1 h is higher compared to the other two ions. This result suggests that the different behavior in the case of Eu^{3+} is related not only with the exchange process into the TNSs layers, but also with a different affinity for the silk fibroin matrix. Not comparable results are reported in literature, for this reason further experiments will be necessary to determine the mechanism of Eu^{3+} exchange.

Compared with the silk matrix, the nanocomposite presents a higher ion loading capacity. This suggests that the main mechanism involved is the exchange between TMA^+ and H_3O^+ cations with the M^{n+} to preserve the charged neutrality of the TNSs. A second mechanism is the chemical adsorption of cations on the silk matrix mediated by the presence of polar amino-acids such as glutamic acid, cysteine and histidine in its structure, which act as binding sites.[38,39]

The difference in the maximum exchange capacity between Ag and Cu is instead related mainly with the valence of the ions: due to the stoichiometric nature of the process, the replacement of monovalent TMA^+ by multivalent M^{n+} decreases the number of ions necessary to preserve the charge neutrality of the system.

To investigate the dependence of the TNSs amount in the nanocomposite on the ion exchange capacity, samples with three different compositions were dipped in 0.1 M Ag^+ solution for 6 minutes (considered as the time to equilibrium from the previous results). As reported in **Figure 3.5**, for the 80:20 SF-TNSs the maximum amount of metal ion adsorbed is 112 mg/g, and it increases to 145 mg/g for the 50:50, and to 155 for the 20:80. In the case of the pure silk fibroin the value is negligible (18 mg/g).

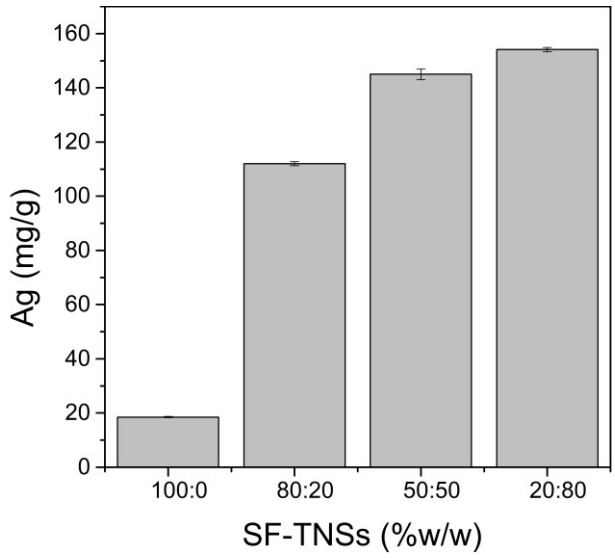

Figure 3.5. Istograms shows the influence of the TNSs concentration on the exchange capacity of the nanocomposite. For comparison the pure silk material is reported (100:0 SF-TNSs).

As expected, the presence of higher concentration of TNSs increases the ions uptake capacity. The relation is not linear, and this could mean that for the higher TNSs concentration it is necessary a longer time to achieve the saturation of the exchange sites. In addition, the process causes damaging for the structural stability of the nanocomposite material itself. In fact, after 1 h in contact with the ions solution, the samples with 80:20 TNSs/SF composition tend to swell losing their solid

appearance, whereas the film with a 50:50 composition retains a solid structure not affected by the aqueous environment. Nonetheless, for this composition, the ICP measurements carried out on the solutions after the adsorption process reveal a negligible titanium presence, so no TNSs are released in the liquid despite the samples swelling, indicating the stable retention of the nanostructures in the fibroin matrix. Taking into account these considerations, the 50:50 SF-TNSs composition is a good compromise between the ion exchange performance and the structural integrity of the solid material.

3.4. Characterization of the material

The structure and morphology of the materials after the exchange process was characterized by X-ray diffraction (XRD) and Transmission Electron Microscopy (TEM) analysis.

Figure 3.6(a) shows the XRD pattern of the TNSs powder as synthesized and of the 50:50 SF-TNSs nanocomposite. The pattern of the bare TNSs presents the main diffraction peak at 7.8°, which corresponds to an interlayer distance of 1.14 nm, as derived from the Bragg law.[40] When the TNSs are introduced in the silk matrix, the characteristic diffraction peak shifts to lower angles (5.2°), corresponding to an increase in the interlayer distance estimated equal to 1.88 nm. These results could indicate that SF has been intercalated into TNSs interlayers and expanded the distances between adjacent TNS sheets, as already observed for other composites made with polymers and layered materials [41] and in the case of silk fibroin combined with graphene oxide sheets [42] and montmorillonite. [43]

As already demonstrated with TEM analysis,[31] the TNSs lamellar nanostructure is maintained also after the embedding in the fibroin matrix. This validation is fundamental for assessing the stability of the system before the ion exchange tests with metal ions.

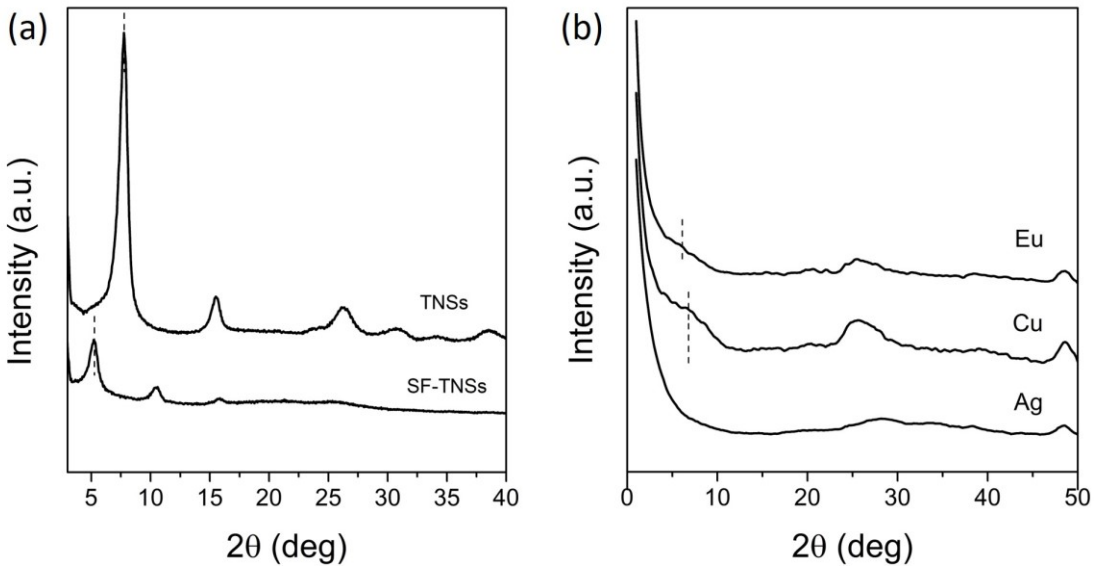

Figure 3.6. (a) XRD patterns of the bare TNSs and the nanocomposite (50:50 SF-TNSs). (b) XRD patterns of the nanocomposites after ion exchange with the three target ions (Ag^{+}, Cu^{2+}, Eu^{3+}).

The XRD patterns of the samples after the ion exchange process are shown in **Figure 3.6**(b). After ion exchange with Cu^{2+} and Eu^{3+} the XRD patterns show a broad shoulder in the low angles range of the diffractograms. The broad peaks (indicated with dashed line) are at 6.4° and 5.6° respectively for SF-TNSs/Cu and SF-TNSs/Eu, corresponding to an interlamellar distance of 1.38 nm and 1.58 nm (**Table 3.3**). In contrast, the XRD pattern of SF-TNSs/Ag nanocomposite shows no clear reflection peak in the 2θ range from 1.3° to 10°, indicating the possible loss of the stack structure. In all the samples in-plane reflection peak of the single sheet can still be detected at 48°, this suggests that the exchange process is not detrimental for the integrity of the crystalline structure of the single sheets. The modification in the crystalline pattern of the nanocomposite observed after the exchange could be explained in terms of hydration degree and size of the ions[44] or dehydration phenomena typical in the case of soft ions (such as Ag). According to Pearson's Hard-Soft Acid-Base (HSAB) theory, metal ions in solutions act as Lewis acids and they can be classified in hard (H+, Li+, Na+ and K+), soft (Ag+, Pd2+ and Au+) and borderline (Cu2+, Pb2+ and Ni2+).[11] As hard base, H_2O (H+) binds tightly to TMA+, so the exchange with a soft ion such as Ag+ is accompanied by dehydration.[16]

Table 3.3. Interlayer distance (d) derived from the Bragg law for XRD patterns reported in Figure 3.6.

Sample	2ϑ (°)	d (nm)
TNSs	7.8	1.14
SF-TNSs	5.2	1.88
Ag+ ex	/	/
Cu2+ ex	6.4	1.38
Eu3+ ex	5.6	1.58

To further investigate the structure of the TNSs inside the silk matrix after the exchange process with the ions, TEM measurements were applied. The samples were prepared by deposition of a diluted suspension (1% total weight, 30% w/v TNSs) by spin coating (1000 rpm x 60 s) on a copper-carbon coated grid, treated in methanol for 30 min and exchanged for 6 min in the salts solutions. As visible in **Figure 3.7**, the exchange with Cu and Eu doesn't affect the layered structure of the TNSs, although the existence of single TNSs-sheets cannot be ruled out. A similar result was found in the case of the silver (see the following section).

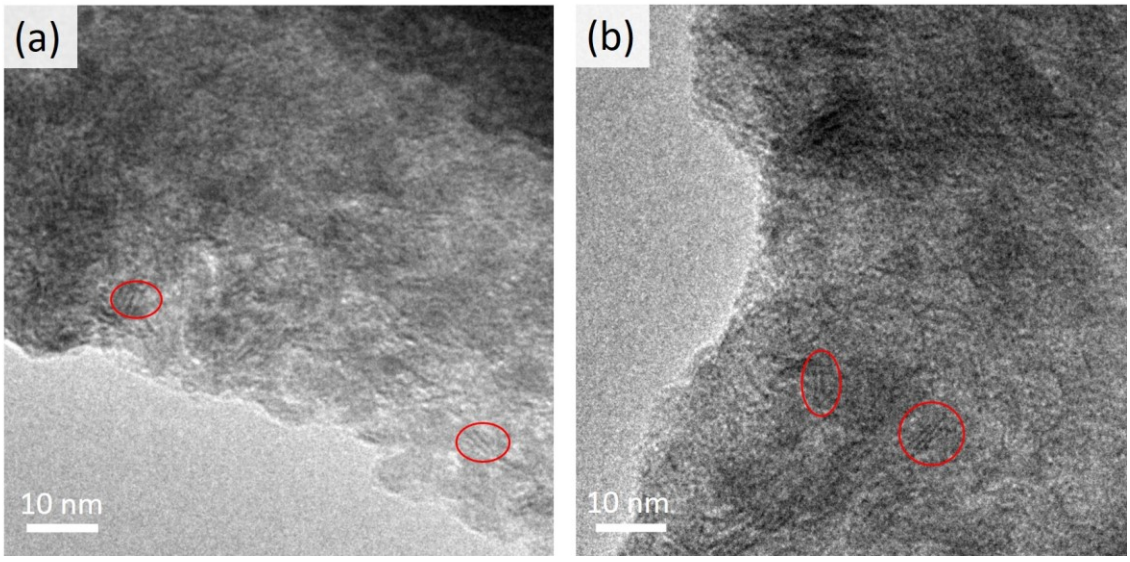

Figure 3.7. TEM images of the SF-TNSs after the exchange with Cu (a) and with Eu (b).

The effect of the exchange on the structure of the material and on the conformation of the silk fibroin were investigated with Fourier Transform Infrared

(FTIR) spectroscopy in ATR mode. **Figure 3.8** shows the FTIR spectra of SF-TNSs before and after ion exchange.

The main peaks of the TMAH at 949 cm^{-2} and 1487 cm^{-2}, related with the $-CH_2$ bending, are evident in the material before the exchange and disappear after the process, confirming the removal of the cation. After the ion exchange with the metal ions, the vibrational modes of TNSs [TiO] lattice experience some modifications, as evident in the region above 900 cm^{-2}. In particular, the peak at 881 cm^{-1}, assigned to the stretching vibration of short Ti-O bonds, disappears. This stretching is mainly affected by inter-layer ions and the result is consistent with the literature.[16]

For what concerns the conformation of the silk fibroin, not visible changes are detected after the exchange process in the region between 1700 and 1500 cm^{-2}, corresponding to the main bands of Amide I and Amide II. The peaks are situated at 1620 and 1520 cm^{-2} respectively for the Amide I and II and they are assigned to a β-sheets conformation induced in the material with the methanol treatment .[45]

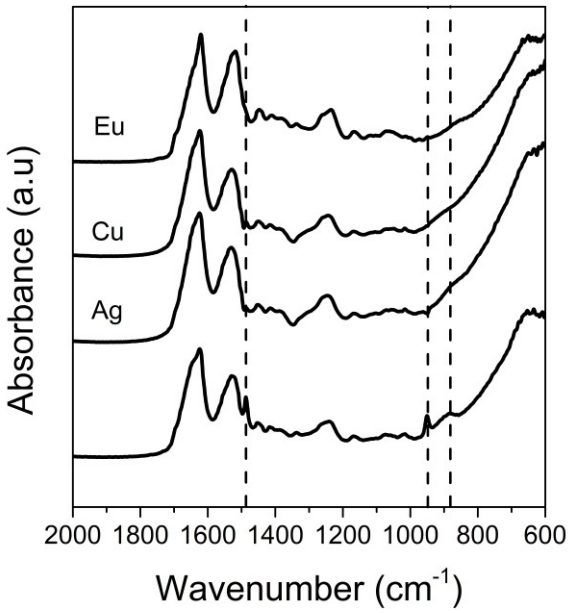

Figure 3.8. FTIR spectra of the silk/TNSs nanocomposite before and after the ion exchange with different ions. The dotted line indicates the wavenumber at 1487 $cm^{-1}$and 949 cm^{-1} related to the identifiable peaks of TMAH, and the peak of TiO at 881 cm^{-1}.

Thermal stability and weight loss of the free-standing films were investigated by Thermogravimetric (TG) and Differential Thermal Analysis (DTA) measurements from room temperature to 600° C with a heat rate of 5° C/min. The analysis was conducted in air, in order to detect possible formation of complex metal oxide between TNSs and the metal ions.

Figure 3.9 and **Table 3.4** present the TG and DTA traces and data for the SF-TNSs nanocomposite before and after the ion exchange with the three different ions and for the reference SF and the bare TNSs.

Silk fibroin film shows a loss of 10% in the first 100° C due to the evaporation of water and a second loss of 40% related to the degradation of the protein between 200° C and 400° C.[46] The final exothermic peak at 500° C is instead assignable to a combustion of the protein due to the oxidative atmosphere, as confirmed from the obtained total weight loss.

In agreement with previous results, [41,47,48] TNSs lose approximately 10 wt% from ambient temperature to 120° C and a further 15 wt % after heating to high temperature. The losses correspond to an endothermic event and two exothermic events at 320° C and 440° C, respectively, and have been ascribed to loss of physiosorbed water molecules, followed by lattice water and TMAH degradation to form a disordered product. A further exothermic peak at 500° C can be ascribable to the combustion of residual organic.

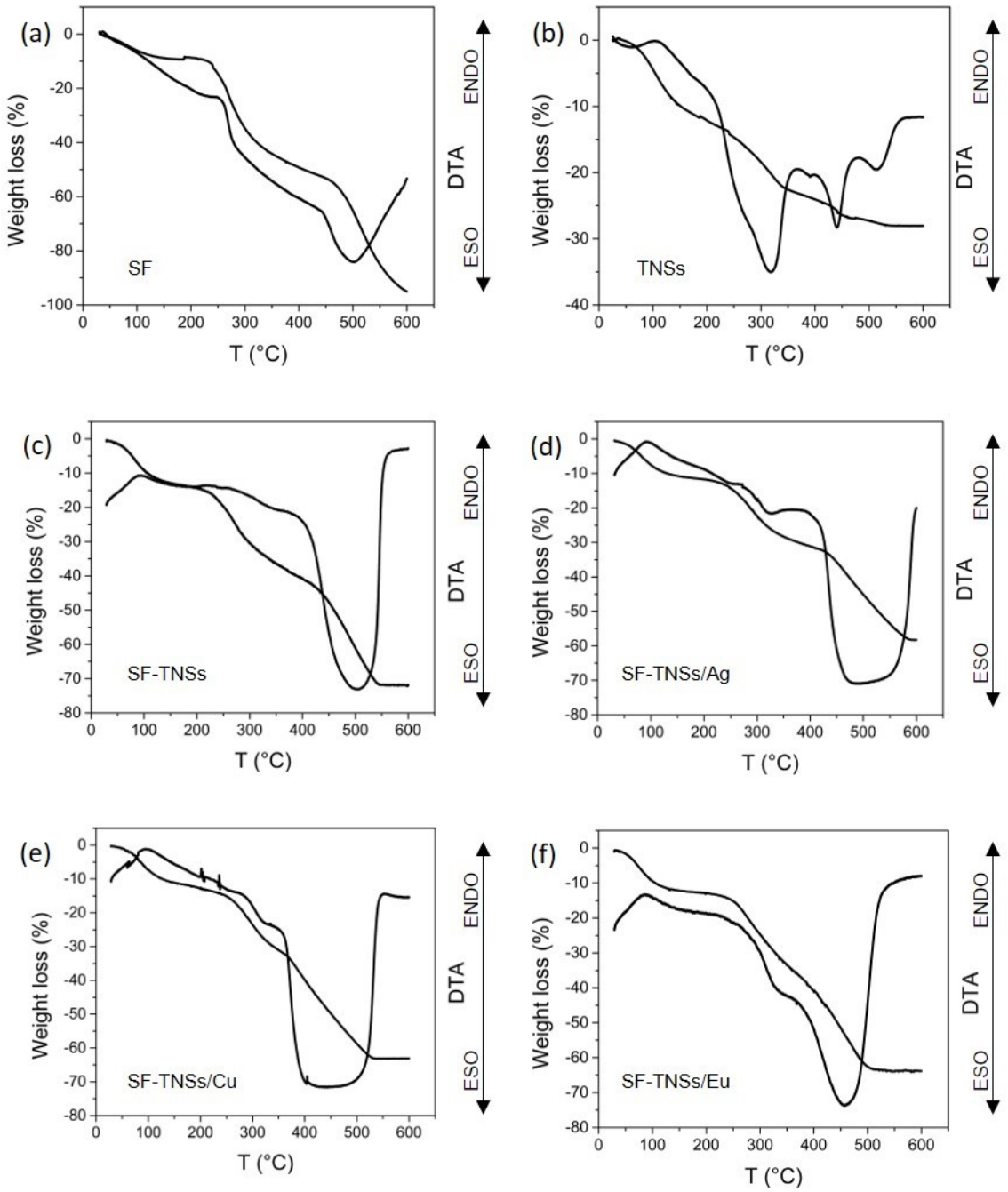

Figure 3.9. TGA and DTA curves for the SF (a), TNSs powder (b) and SF-TNSs nanocomposite (c) as prepared, and for the nanocomposite after the exchange with the three ions (d, e, f). The measurements were carried out in air.

The SF-TNSs nanocomposite shows an endothermic loss of approximately 10% around 120° C, again ascribed residual water. A strong mass loss between 250° C and 450° C is ascribed predominately to polymer decomposition, although the titania

sheets may also degrade in this range. The complete degradation and combustion of the organic part of the nanocomposite are instead relivable from the presence of a strong exothermic peak at 500° C. The total weight loss is around 70% and it is consistent with the loss of all the fibroin (50% in weight) and the residual water and TMAH still present in the material after the methanol annealing. No endothermic event related with crystallization of the anatase was detected from the DTA profile,[49] probably because of the simultaneous exothermic processes.

Table 3.4. TGA and DTA data obtained by the traces reported in Figure 3.9.

	Temperature (°C)	Weight loss (%)	DTA peak
SF	25-180	10	endo (100°C)
	240-460	44	endo (260°C)
	450-600	41	eso (500°C)
TNSs	25-120	7	endo (100°C)
	318	13	eso
	440	5	eso
	500	3	eso
SF-TNSs	25-120	10	endo (100°C)
	200-300	15	endo (270°C)
	300-400	15	eso (320°C)
	450-550	30	eso
SF-TNSs/Ag	25-120	10	endo (100°C)
	200-300	12	endo (270°C)
	300-400	9	eso (318°C)
	400-600	27	eso
SF-TNSs/Cu	25-120	10	endo (100°C)
	200-300	13	endo (270°C)
	300-400	17	eso (320°C)
	360-550	23	eso
SF-TNSs/Eu	25-120	11	endo (100°C)
	200-300	13	endo (280°C)
	300-400	16	eso (330°C)
	370-540	23	eso

After the ion exchange, the samples show a similar DTA profile, but different weight loss compared with the SF-TNSs as prepared. The SF-TNSs/Ag shows a total weight loss of 58%, while after the exchange with Cu and Eu the total loss detected is about

63%. One of the possible explanation is the formation of a second phase in the case of Ag (metallic or oxide). To investigate the phenomenon and verify the possible formation of AgO, a second TGA measurement was conducted on SF-TNSs and SF-TNSs/Ag in inert atmosphere (N_2). The weight loss profiles are reported in **Figure 3.10**.

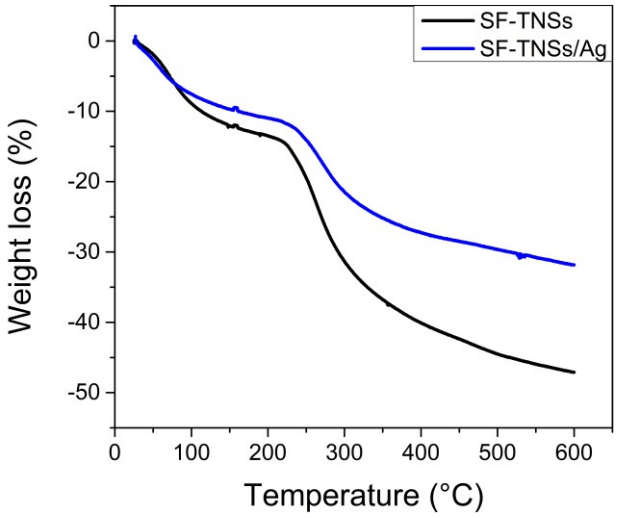

Figure 3.10. Weight loss profiles of SF-TNSs and SF-TNSs/Ag obtained by TGA measurements in N_2.

The total weight loss measured for the SF-TNSs nanocomposite is about 50%, while in the case of the exchanged material (SF-TNSs/Ag) is only 30%. In the case of the as prepared SF-TNSs, the total loss is due by the evaporation of water molecules and the degradation of the organics (SF and TMA^+). The difference in the loss is about 20%, that corresponded to the value reported in literature for the TNSs powder treated in the same condition.[48] These results suggest that all the organic TMA^+ ions are completely substituted by the inorganic Ag^+ that is still present as Ag or AgO after the thermal treatment.

To further confirm this hypothesis and verify the possible formation of complex oxides, the residual powders were analyzed by XRD. The crystalline phases presented were determined by using the software Match!. **Figure 3.11** shows the patterns obtained for the material after ion exchange with all the three different ions and for the SF-TNSs reference.

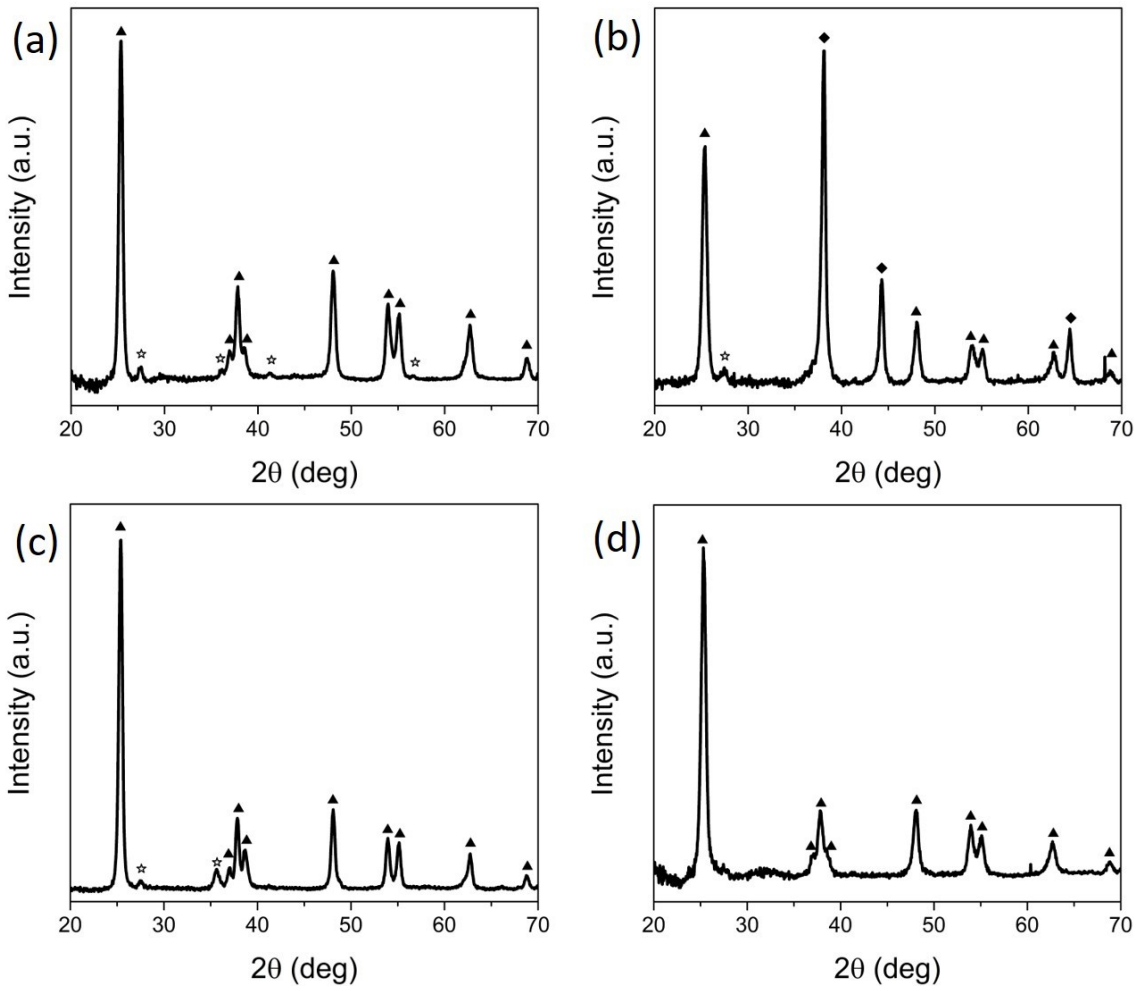

Figure 3.11. XRD pattern of the nanocomposites after TGA study: as prepared (a) and after ion exchange with Ag+ (b), Cu2+ (c) and Eu3+ (d). The characteristic diffraction peaks of anatase (triangle), rutile (star) and silver (rhombus) are reported.

The pattern of the nanocomposite presents the main peaks corresponded to anatase and few peaks of the rutile phase. After the exchange with the ions, the crystalline structure is still dominated by anatase and no other oxide phases are detected. Only in the case of the SF-TNSs/Ag, three characteristic peaks corresponded to the metallic silver are visible. This suggests an easier nucleation of silver compared with the other two ions, and confirm the hypothesis of a higher exchange capacity of the TMA^+ in the case of Ag^+. Probably, in the case of Cu and Eu, the exchange is not completed in only 6 minutes and partial organic ions are present. If we compare the data reported in **Table 3.4** in fact, the weight loss at 300-400° C (in the temperature range of the TMA^+

degradation) is about 16% for the Cu and Eu, and only 9% for the Ag. Other differences can be attributed to a different dehydration during the exchange process.[16]

This characterization suggests the possibility of growth in situ metallic nanoparticles starting from the Ag^+ ions as "precursor" by nucleation induced by thermal annealing. Instead, the synthesis of metallic copper or the formation of complex titanium based oxides are not promoted in the specific conditions investigated.

3.5. In situ synthesis of Ag nanoparticles by photoreduction

Silver nanoparticles were synthesized inside the SF-TNSs material by photoreduction with UV light, after the introduction of Ag^+ ions through the ion exchange process. The process was conducted both on free standing samples and thin films deposited by spin coating on quartz substrate. First the samples were dip in 0.1M $AgNO_3$ solution for 6 minutes, then washed with DI water, dried and finally illuminated for different times with an UV lamp (Hamamatsu LC5s Lightncure) to promote the reduction of Ag^+ and the formation of Ag^0 cluster. The distance between samples and the lamp's fiber was adjusted to achieve a light intensity of 50 mW/cm^2. A schematic representation of the process is presented in **Figure 3.12**(a).

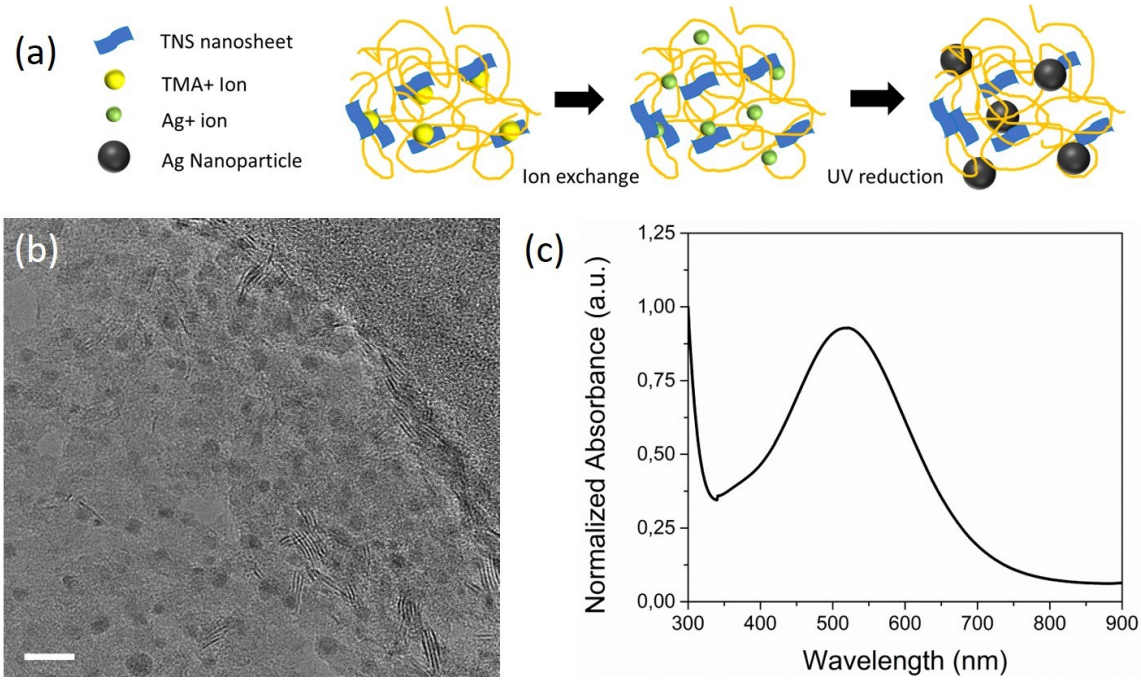

Figure 3.12. (a) a) Schematic rapresentation of the process to synthesis Ag Nanoparticles inside the SF-TNSs matrix. (b) TEM image of a silk/TNSs nanocomposite after reduction of Ag ions and formation of AgNPs. The scale bar is 10 nm. (c) UV-VIS spectrum of free standing film after the in situ formation of NPs.

Before irradiation the free-standing film has a light-yellow colour, as a result of the absorption of the Ag+ ions (owing to the ligand-to-metal charge transfer (LMCT)[50]) inside the matrix. The color gradually turned to brownish after just few seconds of irradiation, indicating the photoreduction transformation of Ag(I) to Ag element. It is likely that this reduction is accelerated by the TNSs, which shows high photocatalytic activities, but even by the reductive amino acid tyrosine of the silk.[51,52] The corresponding UV-vis absorption spectrum is presented in **Figure 3.12**(c).

The strong absorption peak at around 530 nm corresponded to the localized surface plasmon resonance (LSPR) of Ag nanoparticles. Compared to widely reported LSPR peak of Ag nanoparticles, which show absorption peak at around 400 nm ,[53] it is evident that the Ag nanoparticles formed in a complex matrix with TNS exhibits a large red shift. The red shift is attributed to the high refractive index of TNSs.[33,51]

The formation of Ag cluster was also confirmed by TEM images. As visible in **Figure 3.12**(b), the clusters are formed both between the TNSs sheets and in the

surrounding silk matrix. The polydispersity and the complex medium explain the broadening and the redshift of the LSPR peak.

To further investigate the effect of the refractive index of the SF-TNSs matrix, ellipsometry measurements were effectuated on thin films deposited on quartz before and after the photoreduction. The films were characterized using a VASE, VB-400, J. A. Woollam Co. ellipsometer at angles of incidence of 50–60 deg and within a spectral range of 300–1700 nm. The samples were modeled as a homogeneous effective material using a Cauchy dispersion layer for the as prepared sample and a GENOSC layer with Tauc-Lorentz and Lorentz oscillators for the samples after ion exchange and after the photoreduction (see *Appendix A3.11*).

The formation of the Ag clusters into the SF-TNSs thin films was confirmed by the appearance of an absorption peak at around 575 nm in the UV-VIS spectrum (**Figure 3.13**(a)) and by the color changes of the samples that gradually turned from colorless to bluish gray.

Figure 3.13(b) shows the refractive index (n) and the absorption coefficient (k) of the films in the visible and NIR range. The refractive index of the as prepared SF-TNSs is 1.68 at 630 nm and it is consistent with the value previously obtained for the nanocomposite with composition 50:50 after the methanol annealing.[31] After the exchange with Ag, the material shows an increase of n of about 5%, with a value of 1.77 at 630 nm. This is due to the replacement of the organic TMA+ ion with the metal Ag^+ and to the dehydration of the film, as confirmed by the reduction of the thickness (see **Table 3.5**). In both the cases, the extinction coefficient is very low.

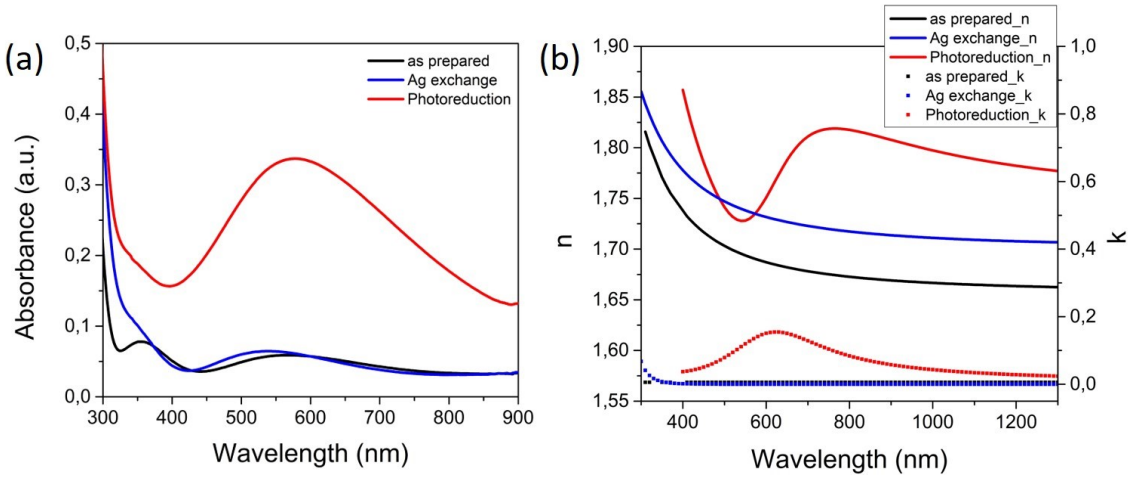

Figure 3.13.(a) UV-VIS absorbance spectra of silk-TNSs thin film on quartz slide as prepared (black), after ion exchange with Ag+ (blue) and after photoreduction of the silver with UV light (red). b) Refractive index (n) and absorption coefficient (k) of the film in the same condition reported in figure (a).

The refractive index (n) and the extinction coefficient (k) of the film after the photoreduction of the silver are shown in red in **Figure 3.13**(b). The extinction coefficient exhibits a similar profile as that of the absorption spectrum (**Figure 3.13**(a)) with a peak at 620 nm. The dispersion curve of n shows a decrease from 430 to 670 nm, with a minimum dip at 540 nm. The refractive index increases again for wavelength longer than the LSPR peak wavelength. This profile is consistent with the presence of a LSPR between 570-630 nm, redshifted compared to Ag nanoparticles embedded in lower refractive index matrix .[54]

Table 3.5. Optical constants and thickness of the SF-TNSs films from ellipsometer measurements as prepared, after ion exchange with UV and after the UV photoreduction.

Sample	Complex refractive index@ 630 nm		Complex refractive index @ 1000 nm		Thickness (nm)
	n	k	n	k	
As prepared	1.68	0.0058	1.67	0.0058	248
Ag ion exchange	1.73	0.0016	1.71	0.0008	229
Photoreduction	1.72	0.15434	1.80	0.0432	208

Finally, it was investigated the possibility to control the organization of the nanoparticles in the film by a selective photo irradiation through an appropriate

mask.[55] This strategy permits to generate a metallic pattern on the surface of the SF-TNS/Ag nanocomposite. **Figure 3.14**(a) shows two different patterns created on a free-standing film by a selective photoreduction of the silver ions using a lithographic mask, by irradiation with UV light for 15-30 sec. As visible from the optical microscopy images (**Figure 3.14**(d), (f) and (g)), it was possible to obtain a resolution in the order of 300 μm. In addition, the material preserves the flexibility typical of the silk films when hydrated.

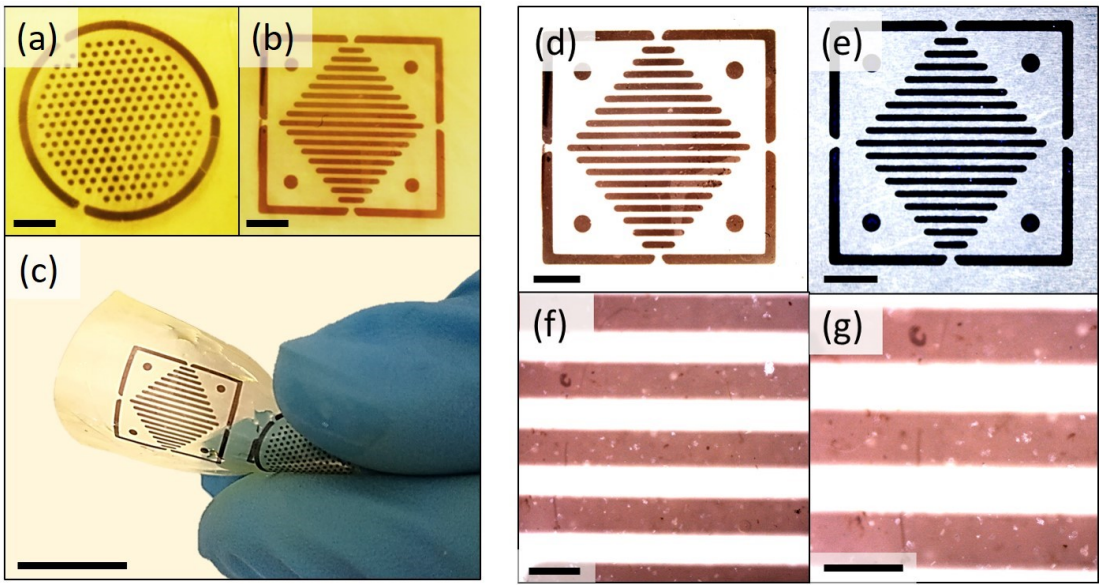

Figure 3.14. (a) & (b) Photographs of two different patterns created on a free standing film through photoreduction of silver ion using a mask at different times of exposition: 10s (a) and 5s (b). (c) Image showing the flexibility of the sample when hydrated. The scale bar is 1 cm. (d) Stereomicroscope images of a photopattern on the free standing film and (e) of the mask. (f) and (g) Particulars of the pattern at different magnifications. The scale bars are: 2 mm (a,b,d,e) and 500 μm (f,g).

It has to underline that the stability of the as-prepared pattern was found critical with the exposition to sunlight and oxygen atmosphere. After a month, the samples resulted completely metallic gray because of the total reduction of the silver ions and in some cases brownish because of the partial oxidation of the silver.

Despite the criticism observed in this specific case, the method can be applied to other metallic materials that are not affected by the same instability (for example gold) and can be extended to thin films deposited on a substrate. To preserve the patterns, a

second ion exchange with Na^+ can be effectuated to remove the residual metal ions. This simple strategy proposed for the preparation of patterned metal particles on polymeric substrates may open new potential applications for the fabrication of flexible sensors due to the advantages of polymer materials (plasticity, ease of processing, and light weight).

3.6. Luminescence of Silk-TNSs/Eu

The emission properties of Silk-TNSs/Eu were investigated through luminescence measurements on the free-standing samples (50:50 SF/TNSs and 100:0 SF compositions) after exchange in the Eu^{3+} solution for 6 min. The measurements were effectuated using a Jasko FP-6300 spectrofluorometer with a Xe light source.
The excitation wavelength was chosen starting from the absorbance spectrum of the $EuNO_3$ water solution. As visible in **Figure 3.15**(a), the absorbance spectrum of the solution shows strong absorbance at wavelength <300 nm related with the nitrate ions in water and a characteristic peak at 395 nm due to the intra-configurational ^4f-^4f transition of central Eu^{3+} ions.[56] The emission spectrum of the solution excited at 395 nm exhibits the main peaks at 592, 616, 653 and 693 nm characteristics of the Eu ions and ascribable to the $^5D_0 \rightarrow {}^7F_j$ (j =1–4d) transition, respectively (**Figure 3.15** (b)). In the same image (blue line), it is also reported the excitation spectrum of the solution obtained by monitoring the emission at 616 nm.

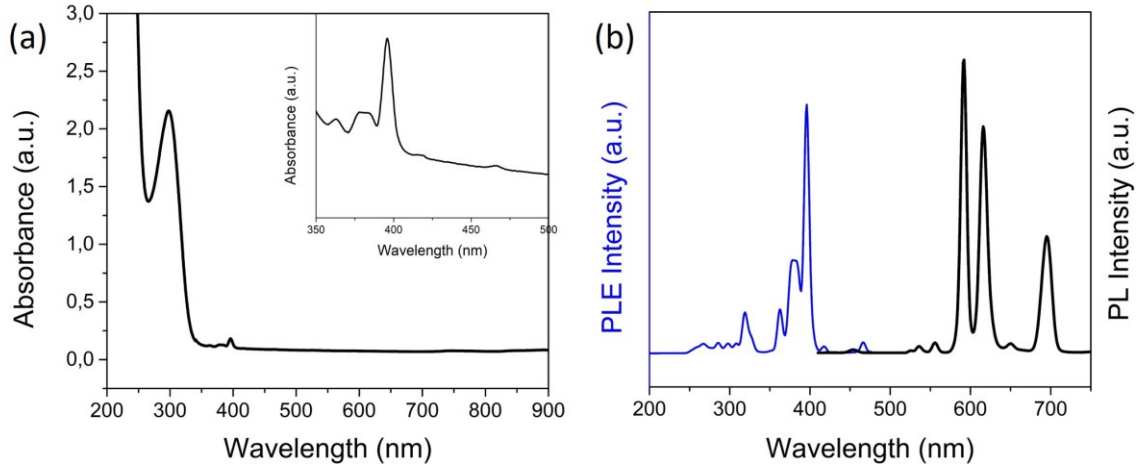

Figure 3.15. (a) UV-VIS spectrum of the 0.1M EuNO3 aqueous solution. The inset shows the 350-500 nm range where it is visible the peak at 395 nm (b) Emission spectrum (black) of the EuNO3 solution excited at a wavelength 395 nm and the excitation spectrum (blue) obtained by monitoring the emission at 616 nm.

Figure 3.16(a) shows the absorbance spectra of the SF, SF-TNSs and SF-TNSs/Eu films. In the case of the SF-TNSs/Eu film, the Eu^{3+} peak is not clear discernable because of the overlapping, in the 220–380 nm range, with the band-gap of the TNSs sheets in the matrix. The effect of the lanthanide cation intercalation is a red shift on the absorption edge relative to the starting material, which can be assigned to the host layer-guest ion interaction and resultant reduction in the quantum size effect of TNSs nanosheets.[57]

The emission spectrum of the SF-TNSs/Eu is reported in **Figure 3.16**(b), where excitation was carried out at 395 nm wavelength. The peaks at 593 and 616 nm were assigned to the $^5D_0 \rightarrow {}^7F_1$ and $^5D_0 \rightarrow {}^7F_2$ transitions, respectively.[58] The most intense peak was observed at 616 nm and it corresponds to a red emission, which also could be seen with the naked eye under illumination with a 400 nm led light.

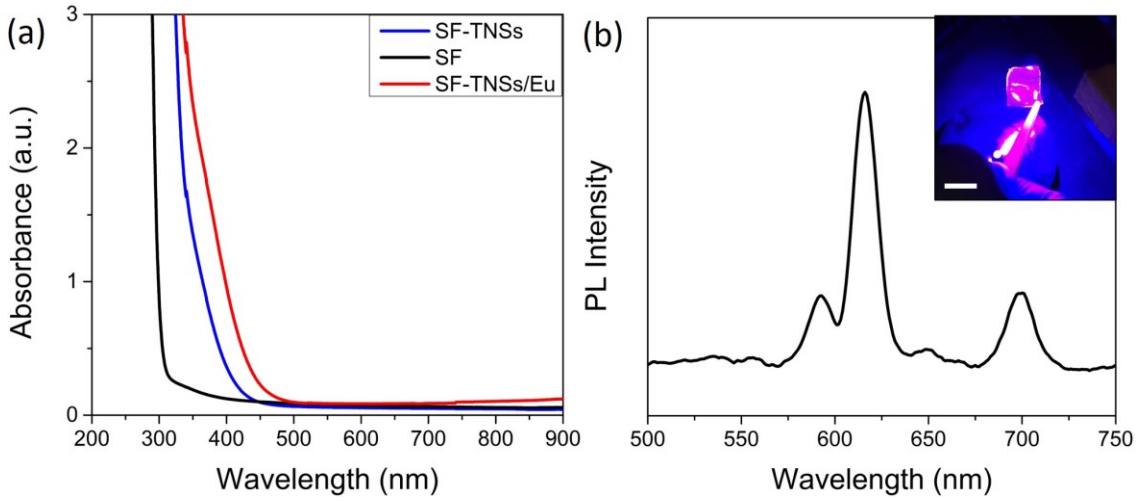

Figure 3.16. (a) Absorbance spectra of the SF and SF-TNSs as prepared and of the nanocomposite after the ion exchange with europium ions. (b) Emission spectrum of SF-TNSs/Eu excited at 395 nm. In the inset is reported an image of the sample illuminted with a 400 nm led showing a visible red emission (the scale bar is 2 cm).

To further investigate the luminescence behavior, the PL spectra of the as prepared material and of the pure SF were collected before and after the exchange with Eu^{3+}. The measurements were carried out exciting at two different wavelengths: 395 nm, corresponded to the absorption of the europium ion, and 280 nm (200-300 nm range), that corresponds to the region of the band-gap absorption of the TNSs nanosheets [59] and the absorption of the aminoacidic groups of the protein.[60]

As reported in **Figure 3.17**(a), the spectra of both SF and SF-TNSs materials are dominated by a broadband emission. After the exchange with the europium ions (**Figure 3.17**(b)), all the spectra show an emission peak centered at ~616 nm. The intensity is higher in the case of the SF-TNSs compared to the pure SF, and this can be explained considering the ion exchange capacity of the TNSs compared to the adsorption properties of the protein. What it is interesting to underline is that the emission is stronger when the material is excited at 280 nm compared to the excitation at 395 nm.

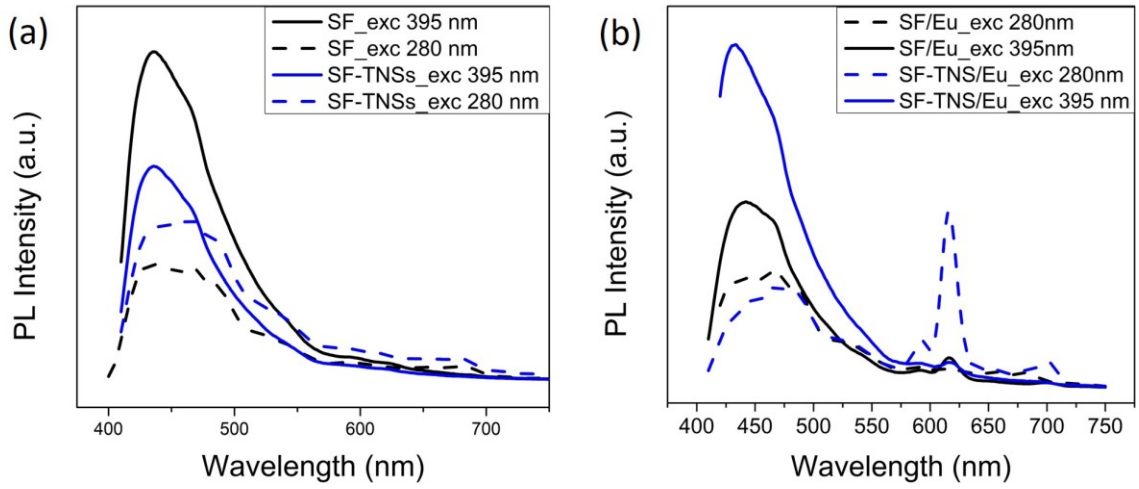

Figure 3.17. (a) Photoluminescence emission spectra of the SF and SF-TNSs as prepared and (b) after the exchange with Eu excited at two different wavelengths.

These results suggest a possible energy transfer mechanism between the host and the guest, as already reported for titanates materials intercalated with lanthanides ions. A possible mechanism for the emission is schematized in **Figure 3.18**: electrons and holes produced by the band-gap excitation migrate in the host layer and a possible transfer takes place through the coordinating water molecules to the interlayer lanthanide cations.[58,61,62]

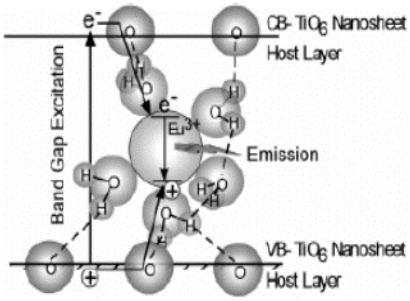

Figure 3.18. Model of photoluminescence of the water-coordinated Eu^{3+} in the interlayer of the TNSs.[63]

Considering that the emission of Eu strongly depends on the surrounding environment, these results provide a possible strategy for the preparation of fluorescent sensors (and biosensors),[64,65] but even for the fabrication of biopolymer-based optoelectronic devices.[66]

3.7. Conclusions

In summary, it was demonstrated the potentiality of the cation exchange process as a tool for post-synthesis functionalization of the SF-TNSs nanocomposites. A preliminary study to determine the capacity of the material to exchange ions with different valence and radius was presented. Thanks to the nanoscale dimension of the TNSs, it was found that the process can be conducted for a different number of ions, in short times (few minutes) at room temperature.

The structural integrity and the thermal behavior of the material after the exchange were characterized by different characterization techniques. In addition, the possibility to synthesize in situ metallic plasmonic particles through photoreduction with a control of the spatial distribution was demonstrated. Finally, it was also characterized the luminescence behavior of SF-TNSs/Eu nanocomposites, showing an interesting energy transfer mechanism between the TNSs and the Eu^{3+} ions.

These promising results suggests the possibility to develop sensing devices based on SF-TNSs, combining plasmonic and fluorescence properties, by a simple controlled exchange process.

Furthermore, the exchange behavior of the TNSs, combined with the specific properties of the silk matrix, offers opportunities in the development of membranes for water cleaning applications. Further studies in this direction are in course in collaboration with Dott. Giovanni Perotto and the Smart Materials group at IIT Genova.

References

[1] A. A. Zagorodni, *Ion exchange materials : properties and applications*; Elsevier, 2007.

[2] P. Mazzoldi, S. Carturan, A. Quaranta, C. Sada, V. M. Sglavo, *Riv. del Nuovo Cim.* **2013**, *36*, 397.

[3] J. B. Rivest, P. K. Jain, *Chem. Soc. Rev.* **2013**, *42*, 89.

[4] V. B. Nalbandyan, *J. Solid State Electrochem.* **2011**, *15*, 891.

[5] D. H. Son, S. M. Hughes, Y. Yin, A. Paul Alivisatos, *Science (80-.).* **2004**, *306*, 1009.

[6] B. J. Beberwyck, Y. Surendranath, A. P. Alivisatos, *J. Phys. Chem. C* **2013**, *117*, 19759.

[7] F. Zhang, Y. Shi, X. Sun, D. Zhao, G. D. Stucky, *Chem. Mater.* **2009**, *21*, 5237.

[8] M. Oh, C. A. Mirkin, *Angew. Chemie* **2006**, *118*, 5618.

[9] H. S. Sherry, *Engineering* **2003**, *24*, 382.

[10] C. E. (Clive E. . Harland, R. W. Grimshaw, *Ion exchange : theory and practice*; Royal Society of Chemistry, 1994.

[11] R. G. Pearson, *Inorg. Chem* **1988**, *27*, 734.

[12] Z. A. Al-Othman, Inamuddin, M. Naushad, *Chem. Eng. J.* **2011**, *166*, 639.

[13] S. Kumar, S. Jain, *J. Chem.* **2013**, *2013*, 1.

[14] A. A. Zagorodni, A. A. Zagorodni, In *Ion Exchange Materials*; Elsevier, 2007; pp. 9–54.

[15] D. Yang, Z. Zheng, H. Liu, H. Zhu, X. Ke, Y. Xu, D. Wu, Y. Sun, *J. Phys. Chem. C* **2008**, *112*, 16275.

[16] N. Li, L. Zhang, Y. Chen, M. Fang, J. Zhang, H. Wang, *Adv. Funct. Mater.* **2012**, *22*, 835.

[17] W. Liu, T. Wang, A. G. L. Borthwick, Y. Wang, X. Yin, X. Li, J. Ni, *Sci. Total Environ.* **2013**, *456*, 171.

[18] Y.-C. Chen, S.-L. Lo, J. Kuo, *Colloids Surfaces A Physicochem. Eng. Asp.* **2010**, *361*, 126.

[19] Y. Jun, H. Zarrin, M. Fowler, Z. Chen, *Int. J. Hydrogen Energy* **2011**, *36*, 6073.

[20] C. H. Rhee, Y. Kim, J. S. Lee, H. K. Kim, H. Chang, *J. Power Sources* **2006**, *159*, 1015.

[21] L. Wang, T. Sasaki, *Chem. Rev.* **2014**, *114*, 9455.

[22] H. Tian, X. L. Zhang, J. Scott, C. Ng, R. Amal, W. J. Shen, J. W. Geus, *J. Mater. Chem. A* **2014**, *2*, 6432.

[23] K. Sasaki, K. Matsubara, S. Kawamura, K. Saito, M. Yagi, W. Norimatsu, R. Sasai, T. Yui, *J. Mater. Chem. C* **2016**, *4*, 1476.

[24] D. Marani, A. D'Epifanio, E. Traversa, M. Miyayama, S. Licoccia, *Chem. Mater.* **2010**, *22*, 1126.

[25] Y. Zhou, R. Ma, Y. Ebina, K. Takada, T. Sasaki, *Chem. Mater.* **2006**, *18*, 1235.

[26] R. Shimizu, T. Kawakami, Y. Takashima, T. Tsuruoka, K. Akamatsu, *RSC Adv.* **2016**, *6*, 18895.

[27] K. Sasaki, K. Matsubara, S. Kawamura, K. Saito, *J. Mater.* **2016**.

[28] B. Domenech, J. Bastos-Arrieta, A. Alonso, J. Macanas, M. Munoz, D. N., In *Ion Exchange Technologies*; InTech, 2012.

[29] I. Toda, T. Tsuruoka, J. Matsui, T. Murashima, H. Nawafune, K. Akamatsu, *RSC Adv.* **2014**, *4*, 4723.

[30] K. P. Divya, M. Miroshnikov, D. Dutta, P. K. Vemula, P. M. Ajayan, G. John, *Acc. Chem. Res.* **2016**, *49*, 1671.

[31] G. Perotto, M. Cittadini, H. Tao, S. Kim, M. Yang, D. L. Kaplan, A. Martucci, F. G. Omenetto, *Adv. Mater.* **2015**, *27*, 6728.

[32] X.-H. Zong, Z.-Z. Shao, S.-M. Chen, X. Chen, B.-W. Hu, F. Deng, W.-H. Yao, *Biochemistry* **2004**, 11932.

[33] Q. Wang, H. Yu, L. Zhong, J. Liu, J. Sun, J. Shen, *Chem. Mater.* **2006**, *18*, 1988.

[34] L. Xiong, C. Chen, Q. Chen, J. Ni, *J. Hazard. Mater.* **2011**, *189*, 741.

[35] Y.-C. Chen, S.-L. Lo, J. Kuo, *Colloids Surfaces A Physicochem. Eng. Asp.* **2010**, *361*, 126.

[36] Y. Marcus, *J. CHEM. SOC. FARADAY TRANS* **1991**, *87*, 2995.

[37] C. S. Ki, E. H. Gang, I. C. Um, Y. H. Park, *J. Memb. Sci.* **2007**, *302*, 20.

[38] T. Arai, G. Freddi, G. M. Colonna, E. Scotti, A. Boschi, R. Murakami, M. Tsukada, *J. Appl. Polym. Sci.* **2001**, *80*, 297.

[39] P. Taddei, P. Monti, G. Freddi, T. Arai, M. Tsukada, In *Journal of Molecular Structure*;

Elsevier, 2003; Vol. 651–653, pp. 433–441.

[40] A. Antonello, M. Guglielmi, V. Bello, G. Mattei, A. Chiasera, M. Ferrari, A. Martucci, *J. Phys. Chem. C* **2010**, *114*, 18423.

[41] N. Sukpirom, M. M. Lerner, *Chem. Mater* **2001**, *13*, 2179.

[42] L. Huang, C. Li, W. Yuan, G. Shi, *Nanoscale* **2013**, *5*, 3780.

[43] Q. Dang, S. Lu, S. Yu, P. Sun, Z. Yuan, *Biomacromolecules* **2010**, *11*, 1796.

[44] R. Llavona, M. Subrez, J. R. Garza, J. Rodriguez, *Inorg. Chem* **1989**.

[45] X. Hu, K. Shmelev, L. Sun, E.-S. Gil, S.-H. Park, P. Cebe, D. L. Kaplan, *Biomacromolecules* **2011**, *12*, 1686.

[46] J. Ming, B. Zuo, *J. Appl. Polym. Sci.* **2012**, *125*, 2148.

[47] C. Airoldi, L. M. Nunes, R. F. de Farias, *Mater. Res. Bull.* **2000**, *35*, 2081.

[48] A. Antonello, **2009**, 1.

[49] G. Perotto, A. Antonello, D. Ferraro, G. Mattei, A. Martucci, *Mater. Chem. Phys.* **2013**, *142*, 712.

[50] Y. Chen, T. Yang, H. Pan, Y. Yuan, L. Chen, M. Liu, K. Zhang, S. Zhang, P. Wu, J. Xu, *J. Am. Chem. Soc.* **2014**, *136*, 1686.

[51] Y. Zhou, R. Ma, Y. Ebina, K. Takada, T. Sasaki, *Chem. Mater.* **2006**, *18*, 1235.

[52] Qun Dong, and Huilan Su, D. Zhang, *J. Phys. Chem. B* **2005**, *109*, 17429.

[53] D. D. Evanoff, G. Chumanov, *ChemPhysChem* **2005**, *6*, 1221.

[54] I. Yaremchuk, A. Tamulevičienė, T. Tamulevičius, K. Šlapikas, Z. Balevičius, S. Tamulevičius, *Phys. status solidi* **2014**, *211*, 329.

[55] Jongok Won, Kyo Jin Ihn and, Kang Yong Soo, *Langmuir* **2002**, *18*, 8246.

[56] A. Riss, M. J. Elser, J. Bernardi, O. Diwald, *J. Am. Chem. Soc.* **2009**, *131*, 6198.

[57] S. Ida, U. Unal, K. Izawa, O. Altuntasoglu, C. Ogata, T. Inoue, K. Shimogawa, Y. Matsumoto, *J. Phys. Chem. B* **2006**, *110*, 23881.

[58] S. Ida, U. Unal, K. Izawa, O. Altuntasoglu, C. Ogata, T. Inoue, K. Shimogawa, Y. Matsumoto, *J. Phys. Chem. B* **2006**, *110*, 23881.

[59] N. Sakai, Y. Ebina, K. Takada, T. Sasaki, *J. Am. Chem. Soc.* **2004**, *126*, 5851.

[60] I. Georgakoudi, I. Tsai, C. Greiner, C. Wong, J. DeFelice, D. Kaplan, *Opt. Express* **2007**, *15*, 1043.

[61] H. Xin, R. Ma, L. Wang, Y. Ebina, K. Takada, T. Sasaki, *Appl. Phys. Lett.* **2004**, *85*, 4187.

[62] S. Ida, C. Ogata, Y. Matsumoto, *IOP Conf. Ser. Mater. Sci. Eng.* **2009**, *1*, 12014.

[63] Y. Matsumoto, U. Unal, Y. Kimura, S. Ohashi, K. Izawa, *J. Phys. Chem. B* **2005**, *109*, 12748.

[64] M. L. Moraes, L. R. Lima, R. R. Silva, M. Cavicchioli, S. J. L. Ribeiro, *Langmuir* **2013**, *29*, 3829.

[65] Y. Zhang, D. Fang, R. Liu, S. Zhao, X. Xiao, C. Wang, Y. Cao, W. Xu, *Dye. Pigment.* **2016**, *130*, 129.

[66] M. P. Dandekar, S. B. Kondawar, S. G. Itankar, D. V Nandanwar, *Procedia Mater. Sci.* **2015**, *10*, 580.

Chapter 4.

Bioinspired stimuli-responsive multilayer film made of Silk-TNSs nanocomposite

4.1. Introduction

For centuries, the natural world has fascinated human beings with its palette of colors. As discovered by the scientists, vivid colors present in animals and plants are originated from the absorption of light by pigments or from the interaction of the incident light with a spatial structure. These so-called "structural colors" are the result of fundamental optical processes of diffraction and interference that occurs when the incident light interacts with a periodic nanostructure.[1–3]

Nature has perfect these structures to adapt the coloration to the needs of the living creatures, playing important roles such as communication and camouflage, or protection in critical environmental conditions.[4–6] For example, the night vision of some mammals is improved thanks to the *tapetum lucidum* structure in the eyes, a regular assembly of high refractive index rodlets that is being exploited to reflect light back.[7] Several species of insects and fishes show tunable structural color in response to variations of surrounding environment, such as humidity, temperature or stressful condition.[8,9]

Taking inspiration from the biological nanostructures, researchers have developed a wide range of tunable structural color materials for applications in colour displays, security and sensing.[10]

In the present chapter, a stimuli-responsive multilayer film inspired to the cuticle of *Hoplia coerulea* will be presented.[11] This beetle is able to modify its color in the presence of moisture, thanks to the variation of the thin films stack responsible for the interference color. In the same way the fabricated multilayer structure, which can be considered a Bragg reflector,[12] can sense the environmental humidity with a reversible mechanism and the presence of humidity can be recognized by a color change.

A Bragg reflector is a structure formed by multiple layers of alternating materials, which have two different refractive indices, with planar interfaces between each couple of bilayers. Each interface causes a partial reflection of an optical wave. For particular ranges of energies, there is a constructive interference of reflected light and very high reflectivity values can be observed. This diffraction phenomenon is described by the Bragg-Snell law, which predicts the wavelength position of the Bragg-diffraction maximum as a function of the thickness and the refractive index of the materials of the bilayers:

$$m\lambda_{MAX} = 2(n_L t_L + n_H t_H) \quad (4.1)$$

where m is the diffraction order, t_L and t_H are the thicknesses of the low- and high-refractive- index materials, and n_L and n_H are the respective refractive indices.[13]

Different humidity-responsive systems have been already proposed based on photonic structure,[14–16] and a wide range of materials have been investigated, including inorganic material (to increase the refractive index), polymers and hydrogel (for their swelling and de-swelling properties), or hybrid organic-inorganic systems.[17–19]

The materials proposed in this chapter are the regenerated silk fibroin and the titanate nanosheets (TNSs).

As extensively discussed in *Chapter 1*, silk fibroin is a good candidate for the realization of a new class of bio-photonic and optical interfaces and devices thanks to the high transparency in the visible spectrum and low surface roughness, coupled

with its biocompatibility and good mechanical properties. In addition, it presents cycling contraction property when exposed to different humidity conditions.[20]
Silk presents a refractive index of 1.54 at 633 nm,[21] so in order to obtained the refractive index contrast necessary to generate the constructive interference, pure silk will be interfaced with a high refractive index TNSs:silk nanocomposite. As reported in Chapter 2, this nanocomposite shows a high (up to almost 2 for high TNSs filling factor) and tunable refractive index, while preserving the processability of the pure silk materials.[22]

The present chapter is organized in three main sections. The first section is focused on the fabrication of the structure based on a layer by layer approach. The main parameters involved in the process are studied in order to propose a standard protocol for the fabrication of the designed structure. The structural and optical properties of the multilayers structured are presented in the second part and compared with theoretical simulations. Finally, the last section of the chapter is focused on the sensing behavior of the fabricated multilayer film. A mechanism for the sensing is proposed, validated by numerical simulations, and the principal figures of merit of the sensor will be characterized. The results are partially published in *Journal of Material Chemistry C* (2017).

4.2. Fabrication of the multilayer structure

The multilayer structure was prepared by a simple layer by layer deposition of aqueous solutions by spin coating method. A regenerated silk fibroin solution (Rsilk), extracted from the bombyx moori fibers, was used as low refractive index layer. The solution was prepared following the protocol previously reported,[23] starting from degummed fibers boiled 45 minutes in the sodium carbonate solution. For further details, see the *Appendix A1.1*. For the high refractive index layer, a silk-titanates nanocomposite (HRIsilk) was synthesized by gently mixing the stock TNSs dispersion with the silk solution in order to obtain a TNSs:silk ratio equal to 80:20 by weight. After each deposition, the sample was treated in methanol for 30 min to induce the crystallization of silk and make the film water insoluble. This was shown

to be an efficient way of curing both Rsilk and HRIsilk, because the treatment induces a crystallization of silk and a densification of the layered structure of the TNSs,[22] as explained in *Chapter 2*.

First, a standard protocol for the deposition of the thin layers was optimized acting on the main parameters involved in the spin coating process, such as rotational speed, deposition time and concentrations of the solutions. It was found that a rotational speed of 3000 rpm or above is necessary for the film homogeneity, and a TNS:silk ratio not higher than 80:20 is necessary for avoiding cracks formation. Taking into account these considerations and the data reported in literature, the film thickness of the Rsilk film was adjusted acting on the concentration of the solution. A thickness of ~180 and of ~80 nm was measured by ellipsometry for a concentration of 5% w/v and 2.5% w/v, respectively (3000 rpm x 60 s).

For what concern the HRIsilk layer, more experiments were conducted to determine the better parameters. **Figure 4.1** shows the relation between the thickness and the spin speed for two different concentration of solution (1.5% w/v and 3% w/v), for a TNSs:silk ratio 80:20. In all the chapter I will use the abbreviation HRIsilk to refer to this TNSs:silk ratio.

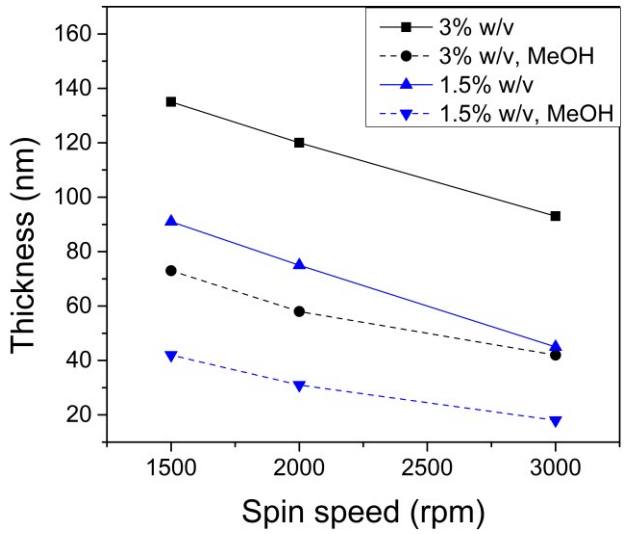

Figure 4.1. Relation between thickness and spin speed for two different concentration of HRIsilk (TNSs:silk 80:20)before and after the methanol annealing.

In the same graphs, it also possible to observe the value obtained after the methanol annealing for a fixed deposition protocol. Ellipsometry measurements were used to investigate the effect of the methanol annealing on the thickness and the refractive index of the thin films. A Cauchy dispersion was used to model the refractive index of both layers. In

Table 4.1 the results obtained for the Rsilk (2.5% w/v) and HRIsilk (3% w/v) are reported. It was determined an increase of the refractive index of 1.3% and of 12.3% for Rsilk and HRIsilk, respectively, while thickness decreases of about 2.5% and 55%, respectively. The high reduction in thickness for the HRIsilk layer is directly correlated with the mechanism of curing induced by methanol, that causes a dehydration of the nanocomposite resulting in the densification of the film (see *Chapter 2* for a more detailed description of the process).

Table 4.1. Effect of methanol annealing on the thickness and the refractive index of the film (at λ= 500 nm) deposited on a silicon substrate. The values reported are obtained from spectroscopic ellipsometry by fitting the experimentally obtained data to a Cauchy dispersion equation.

	Rsilk			**HRIsilk**		
	As deposited	*MeOH annealing*	*Variation (%)*	*As deposited*	*MeOH annealing*	*Variation (%)*
Thickness (nm)	82 ±2	80 ±2	-2.5	93 ±2	42 ±5	-55
Refractive index	1.54	1.56	1.3	1.62	1.82	12.3

To verify that both HRIsilk and Rsilk layers present suitable quality for the preparation of an optical multilayer structure, the surface roughness of films after methanol annealing was studied with atomic force microscopy (AFM). The surface micrographs of Rsilk and HRIsilk films are reported in **Figure 4.2**.

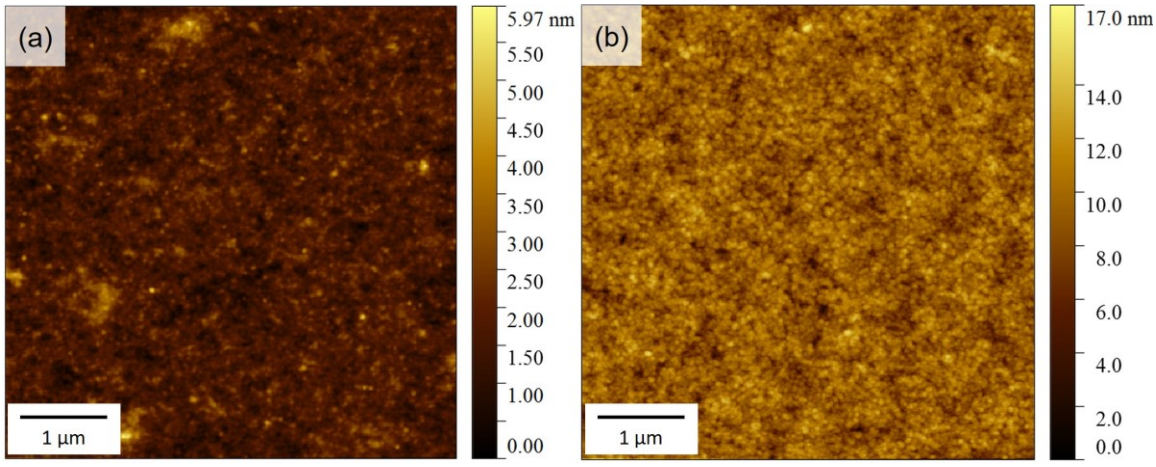

Figure 4.2. .AFM micrographs of Rsilk film (a) and HRIsilk film (b) deposited after methanol treatment.

In **Table 4.2** and **Table 4.3** the average roughness (R_a) and the root-mean-square roughness (rms) calculated for different profiles extracted from AFM micrographs are reported.

Table 4.2.Roughness average (Ra) and root-mean-square roughness (rms) of Rsilk film. The values reported are calculated on profiles extracted from 5x5μm AFM images.

Profile	Ra [nm]	rms [nm]
1	0.381	0.488
2	0.344	0.435
3	0.447	0.549
4	0.395	0.486
5	0.316	0.396
6	0.399	0.495
7	0.415	0.515
8	0.297	0.375
9	0.443	0.565

Table 4.3. Roughness average (Ra) and root-mean-square roughness (rms) of HRIsilk film. The values reported are calculated on profiles extracted from 5x5μm AFM images.

Profile	Ra [nm]	rms [nm]
1	1.501	1.891
2	1.012	1.319
3	1.179	1.505
4	1.075	1.370
5	1.156	1.443
6	1.222	1.558
7	1.141	1.462
8	1.079	1.354
9	1.215	1.535

Both Rsilk and HRIsilk films present a low roughness, with a R_a of ~0.4 nm and ~1.2 nm and rms of ~0.6 nm and ~1.9 nm for Rsilk and HRIsilk, respectively. These values are low enough for the fabrication of multilayer structures with good optical quality.

After the determination of the parameters for a single layer, it was optimized the deposition of the multilayer film. It has to report that the hydrophobicity of the silk films depends on the hydrophobicity of the substrate used to cast the films on. A study

reported in literature,[24] on films deposited on different substrates after methanol annealing, showed that films cast on hydrophilic glass substrates were more hydrophobic at the film-air surface in comparison to films cast on hydrophobic PS and PTFE substrates. On hydrophilic templates like glass, hydrophilic silk regions are oriented toward the substrate, and the hydrophobic polyalanine stretches are organized into micellar-like structures or oriented away from the hydrophilic bulk to the silk-air interface, inducing a hydrophobic film surface.[24,25] This hydrophobicity can affect the deposition of the n+1 layer. For this reason, different strategies were first investigated to improve the wettability, such as UV irradiation of the deposited layer or addition of an organic solvent in solution. No significant effects were observed for the UV irradiation, while an improvement was obtained with the addition of an organic solvent (like isopropanol, acetone, butanone). The problem in the case of this second strategy was the formation of particles in sol (for the faster sol-gel transition) with an increase of defects (e.g. comets) in the films. For this reason, at the end it was decided to carry out the process without the addition of solvents, only taking attention to cover completely the substrate with the solution before starting the spin process. In these conditions, it was possible to obtain the deposition of up to 12 layers. A different strategy to improve the wettability could be an oxygen plasma treatment of the surface of the deposited layer, but no experiments were effectuated because of the absence of the instrument.

A final multilayer films made of 4 couples of layers was deposited on a SiO_2 slide designed to achieve an interference reflectance peak in the spectrum around 400 nm, in order to satisfy the Bragg condition in the visible range also when the material swells in presence of moisture.[13] Since the refractive indexes of these layers after the methanol annealing were of 1.56 and 1.82 (at 500 nm), respectively, the spin-coating parameters were optimized for the deposition of 80 ± 2 nm thick Rsilk layer and of 40 ± 5 nm thick HRIsilk layer (all the details are summarized in the *Appendix A2.3*). The schematic of the overall process is reported in **Figure 4.3**.

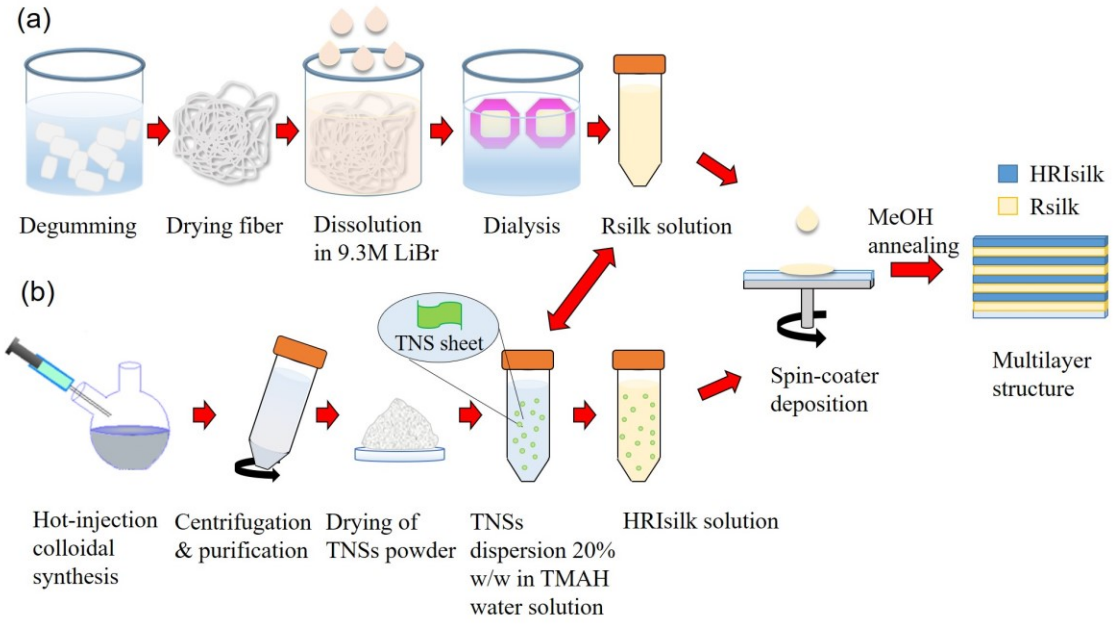

Figure 4.3. Schematic representation of the processing steps required to fabricate the multilayer structure on quartz substrate, based on layer by layer deposition of the water solution of Rsilk and HRIsilk by spin-coating.

4.3. Characterization of the multilayer film

The evolution of the optical properties with the number of layers (N) deposited is illustrated in **Figure 4.4**(a). An interference peak in the transmittance spectrum created by the periodic arrangements of the layers is evident for stacks made of six or more alternate layers, which is a direct consequence of the large refractive index contrast achieved using the TNS:silk nanocomposite. It is observed, as expected, that the peak becomes both narrower and more intense as the number of layers in the stack is increased.

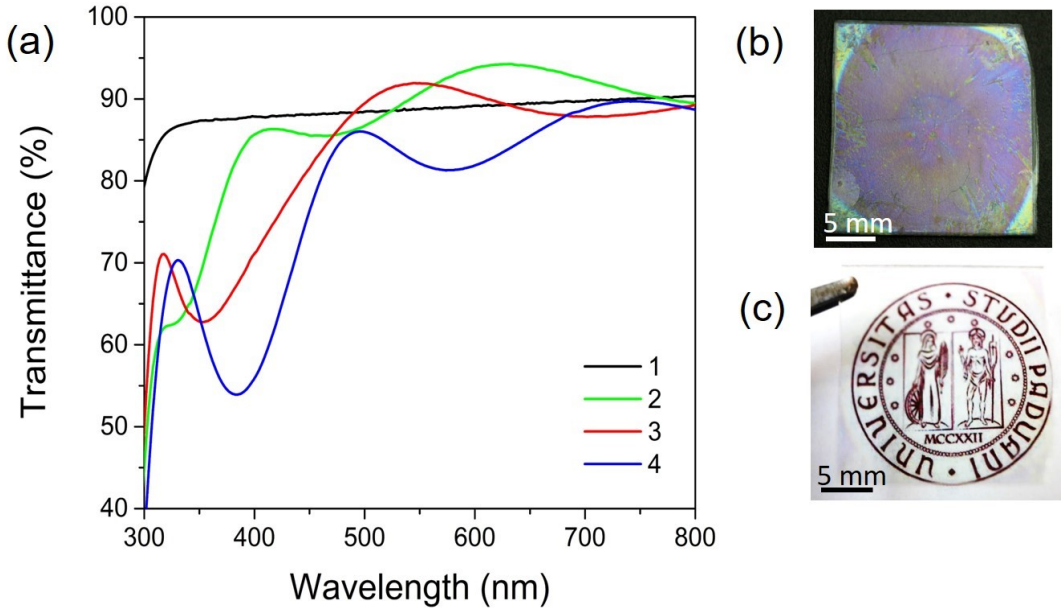

Figure 4.4. (a) Transmittance spectra of multilayers structure for 1, 2, 3 and 4 couples of bilayers. (b) Photographic image of a multilayer structure (N=4) in reflectance mode, showing a violet distinct color, and in transmittance mode (c).

In the case of a film made of 4 couples of layers, the minimum is centered at ~385 nm, close to the design target of 400 nm. Photographs showing the multilayer film are presented in **Figure 4.4** (b) and (c). The multilayer shows a bright violet reflection color when the angle of incidence of light is the same of the angle of reflection and high transparency under ambient light.

While this 8-layers structure shows a bright coloration that is clearly visible to the naked eye, it is important to note that a higher reflection is necessary to obtain a complete photonic band-gap. In that case, the approach presented can be extended to prepare a film with a larger number of layers (a 12-layers structure was fabricated with the same protocol).

Further confirmation of the quality of the optical structure was obtained by fitting the spectrum with numerical simulations. The simulations were performed based on the transfer matrix theory,[26] considered the structure as a Bragg reflector, using the WVASE32 software. 'Superlattice' function was used to create the model of the four-period repeated periodic structure, using two different Cauchy dispersion to model both Rsilk and HRIsilk layers. In **Figure 4.5**(a) the best-fit for the multilayer is

shown, overlapped with the experimental data. Good agreement between measured and simulated transmittance was observed in terms of wavelength position and shape of the peak. At shorter wavelength, the simulation is less accurate, probably due to absorption and scattering losses which were not considered in our simple models.

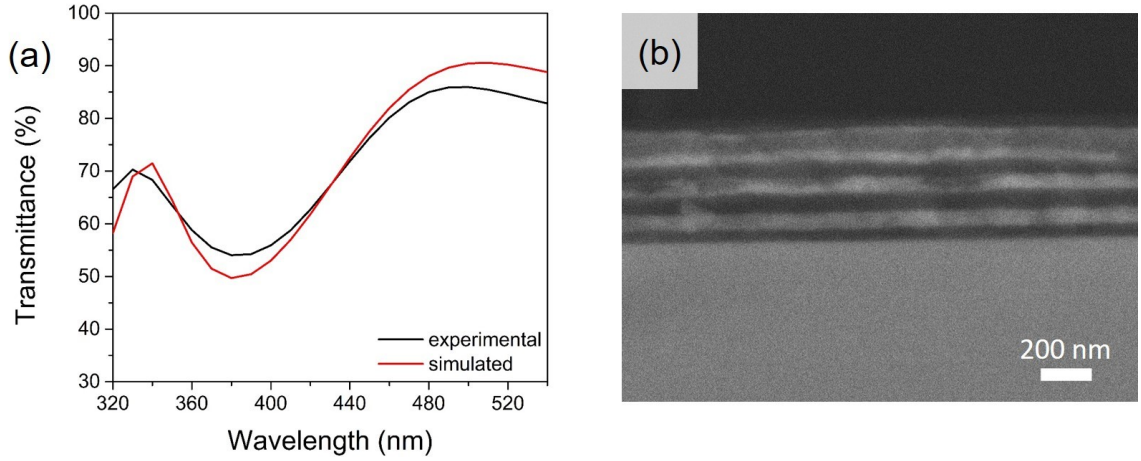

Figure 4.5. (a) Experimental (black) and simulated (red) transmittance spectrum of the fabricated multilayer structure made of 4 couples of layers. (b) Cross-section SEM image of a multilayers structure made of 4 couples of layers on quartz substrate.

Finally, the structure of the multilayer was investigated by Scanning Electron Microscopy (SEM) images. **Figure 4.5**(b) shows a cross-section of a multilayer structure made of 4-bilayers, from which it is possible to distinguish the Rsilk (darker) and the HRIsilk (clearer) layers. No significant interpenetration of the individual layers was observed.

4.4. Humidity-responsive behavior

Besides the structural and optical characterizations provided, the potential of the silk-TNSs multilayer film as base materials for optical vapor sensing devices was investigated.

As well-known, the diffraction properties of a Bragg-like structure are strictly correlated with the variation of the physical thickness of the layers composing the stack or of the effective refractive index of each layer.[13]

Many polymers, both natural and synthetic, have the property of swelling in presence of suitable molecular liquids, causing a variation of their volume. This swelling behavior is induced by the diffusion of vapor molecules inside the holes and micro-voids in the polymeric structure. After desorbing the molecules, the polymers shrink and return to its initial volume.[27]

In this specific case, we observed a visible and reversible color change of the multilayer when exposed to a variation of the relative humidity (RH) of the environment or at water vapor (**Figure 4.6**).

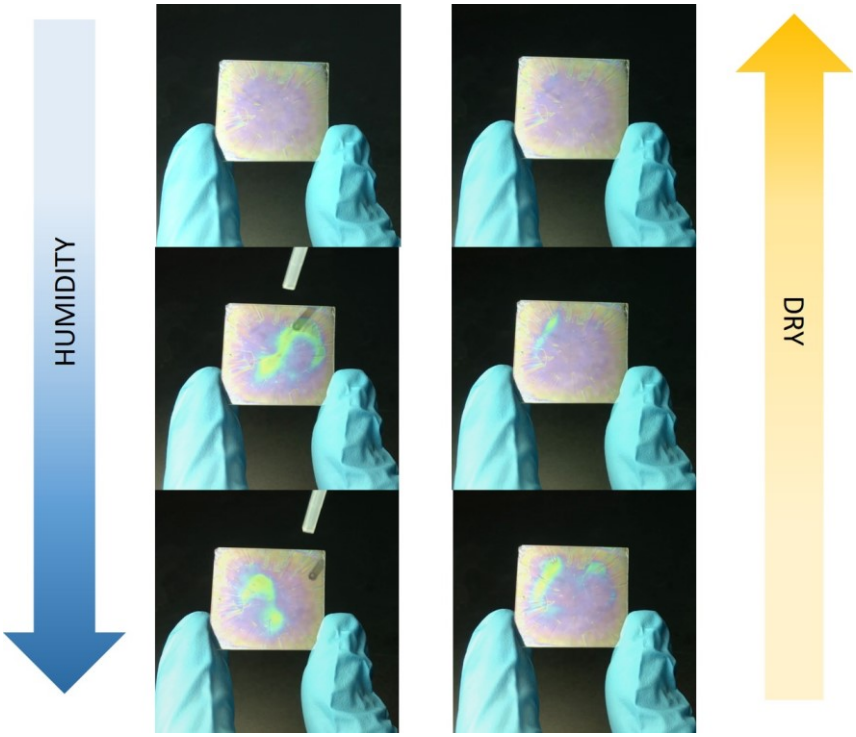

Figure 4.6. Digital photographs showing the reversible color changing of a multilayer sample when it is exposed to water vapor. The images were collected using a digital camera (Canon EOS Rebel T1i).

In order to verify the humidity-responsive behavior observed, the silk-TNSs multilayer was introduced into a closed chamber with two transparent windows, and the position of the reflection peak was measured as a function of %RH. Preliminary experiments were effectuated by controlling the humidity of the chamber trough the use of saturated salt solutions.[28,29] Because of the long times necessary to reach the

equilibrium condition inside the chamber, it was decided to use a different set-up based on a steel chamber with two quartz windows connected to a RH sensor and a bubbler system, used to generate moist (all the details are reported in *Appendix A3.16*). The transmittance spectra were collected with a portable spectrophotometer (Ocean Optics, HR4000). This set-up showed the advantage to permit a faster variation of the humidity of the chamber by simple controlling the flow rate of dry and moist air, allowing the possibility to make dynamic measurements and to determine the response time of the fabricated structure.

Figure 4.7 shows the transmittance spectra of the multilayer when the RH changes between 10% and 80%.

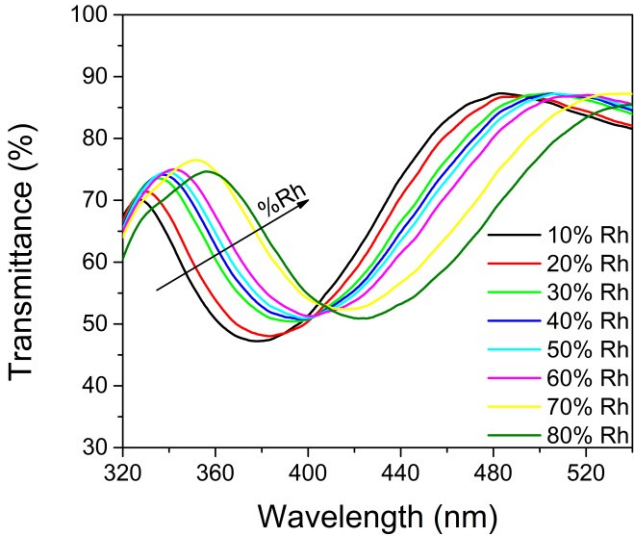

Figure 4.7. Transmittance spectra of multilayer when the humidity is increased from 10 to 80 % RH.

The peak position shifts to longer wavelengths, while the transmittance value and the bandwidth gradually increase with increasing RH. This behavior agrees with the Bragg reflector theory because the modification of the refractive index and the thickness of layers affect not only the position of the diffraction peak but also the spectral position and the bandwidth.

4.4.1. Proposed mechanism for sensing

As previously reported, both spider silk and silkworm silk show a cycling contraction property induced by humidity, due to infiltration of water molecules into fibers that induces a general swelling of the silk. This property is preserved also in regenerated silk: different studies demonstrated that silk can be used as humidity dependent sensing material thanks to its swelling/de-swelling behavior under varying RH conditions.[20] In addition, methanol annealing used to crystallize silk could improve the capacity to absorb water if compared with other treatments, increasing the sensing performance of the material.[20,30]

The mechanism underlying the optical response of the multilayer to the humidity variation is based on the following considerations : i) the thickness of the Rsilk layers is changing when the water molecules are absorbed/desorbed, in fact the moisture forms hydrogen bonds with the protein inducing an internal swelling [31]; ii) the refractive index of both layers changes because of the uptake/loss of water; iii) because of their negative charge (the TNSs formula is $(Ti_{(1-x)}O_2)^{4x-}$), the TNSs interact very strongly with water molecules, causing a bigger change in its properties (both thickness and refractive index) with changes in the RH, compared to the silk fibroin.[32]

Further numerical simulations were performed to verify the proposed mechanism. The simulated transmittance spectra in different humidity condition were numerically fit to the measured data using thickness and optical constants of the single films obtained from ellipsometry spectroscopy as starting parameters and then fitting them to the best values. In **Figure 4.8** the simulated transmittance spectra of the multilayer in two different humidity conditions are reported and compared with the experimental ones.

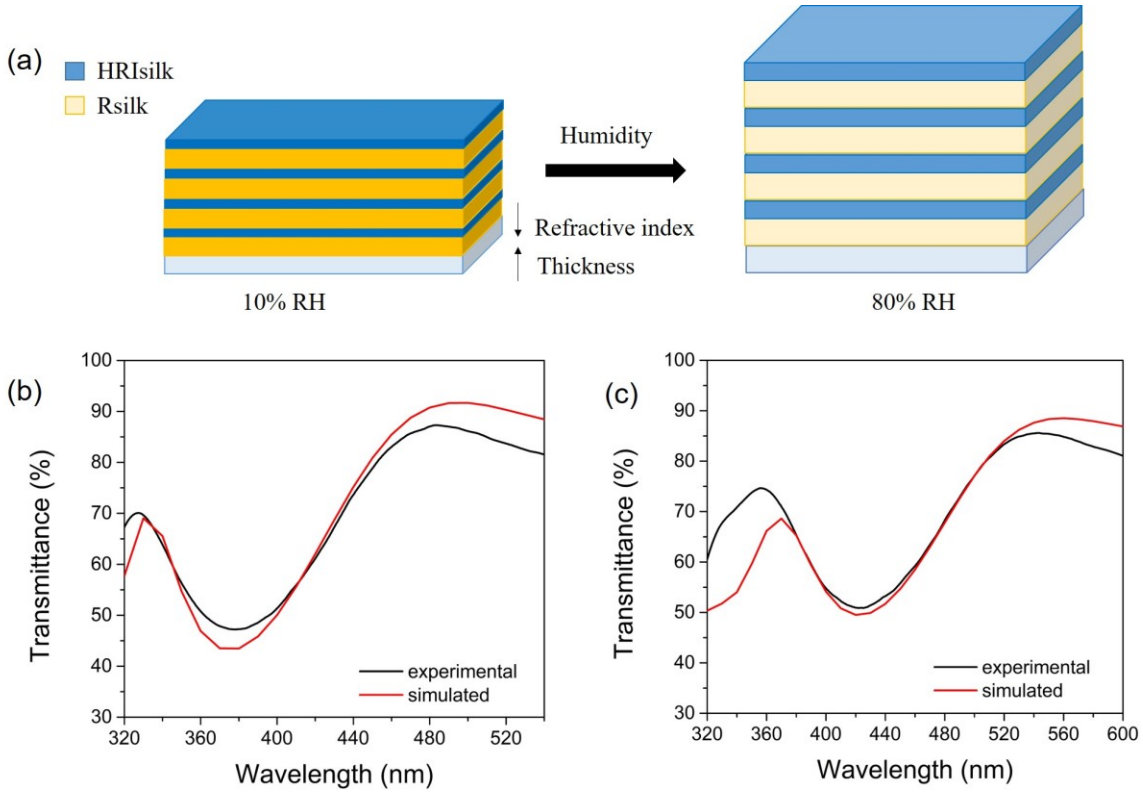

Figure 4.8. (a) Scheme of suggested humidity sensing mechanism. (b) Experimental (black) and simulated (red) transmittance spectrum of interference peak at 10% RH. (c) Experimental (black) and simulated (red) transmittance spectrum of multilayer structure at 80% RH.

For the modeling, it was assumed that when humidity decreases, the structure responds with a reduction of the thickness and a partial increase of refractive index of the layers due to the loss of water, as reported in a simple scheme in **Figure 4.8**(a). This behavior induces a blue-shift of diffraction wavelength and an increase of reflectivity compared to standard condition. On the other hand, when the humidity is increased from the 10% to 80% RH, water absorption causes a swelling of the layers and a reduction of refractive index. The best fitting of experimental data obtained from simulations estimates that the increase of thickness is about 15% for Rsilk and about 27% for HRIsilk, while the decrease of refractive index is about 2.5% and 4.5%, respectively for Rsilk and HRIsilk (**Table 4.4**).

Table 4.4. Thickness and refractive index of Rsilk and HRIsilk films of the best fitting of experimental data for different humidity conditions: 10% RH and 80% RH.

	Rsilk			**HRIsilk**		
	10%RH	*80%RH*	*Difference (%)*	*10%RH*	*80%RH*	*Difference (%)*
Thickness (nm)	78	90	15	37	47	27
Refractive index @500 nm	1.58	1.52	-3.8	1.83	1.75	-4.5

The good agreement between the simulations and the experimental confirm the validity of the aforementioned considerations.

4.4.2. Characterization of the sensor

The four important figures of merit of a sensor (sensitivity, hysteresis, stability and response time) were characterized for the fabricated structure.

The sensitivity of the silk-TNTs multilayer structure was investigated considering the effect of the RH both on the wavelength and on the transmittance value of the interference peak. **Figure 4.9**(a), in particular, depicts the dependence of the position of minimum in transmittance as RH changes. A non-perfect linear response of the sensor to the humidity variation was observed: the sensitivity (defined as $\Delta\lambda_{peak}/\Delta RH$) was higher for high and low RH, while the slope is lower in the range between 30% and 60% RH. From the best linear fit of the experimental a sensitivity of 0.54 was estimated.

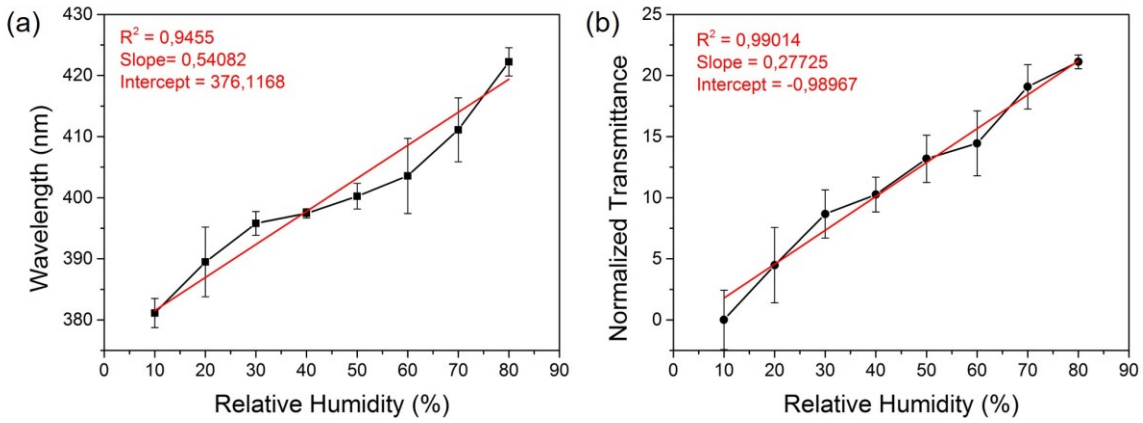

Figure 4.9. Dependence of peak position (a) and transmittance at 360 nm (b) of the multilayer structure with RH variations. Each point is a mean of 5 measurements (error bars correspond to standard deviation).

The sensitivity can be defined also as the variation in relative transmittance at certain wavelength in the interference peak ($\Delta T(\lambda)$ /ΔRH). As shown in **Figure 4.9**(b), the sensor presents an excellent linearity at 360 nm, with a sensitivity of 0.28.

Another important characteristic of the sensor is its hysteresis, defined as the non-coincidence between the loading and unloading curves when the sensor is subject to increasing/decreasing cycles of humidity. In order to investigate this behavior, three different optical properties have been monitored: wavelength position (**Figure 4.10**(a)), relative transmittance at 360 nm (**Figure 4.10**(b)) and band-with of the peak (**Figure 4.10**(c)).

The hysteresis of the system is less than1%, for the wavelength position and the band-with, and about 2% for the relative transmittance as reported in the table in **Figure 4.10**(d). These values are very good if compared with other optical systems that show hysteresis in the range 1 - 5%. [33,34]

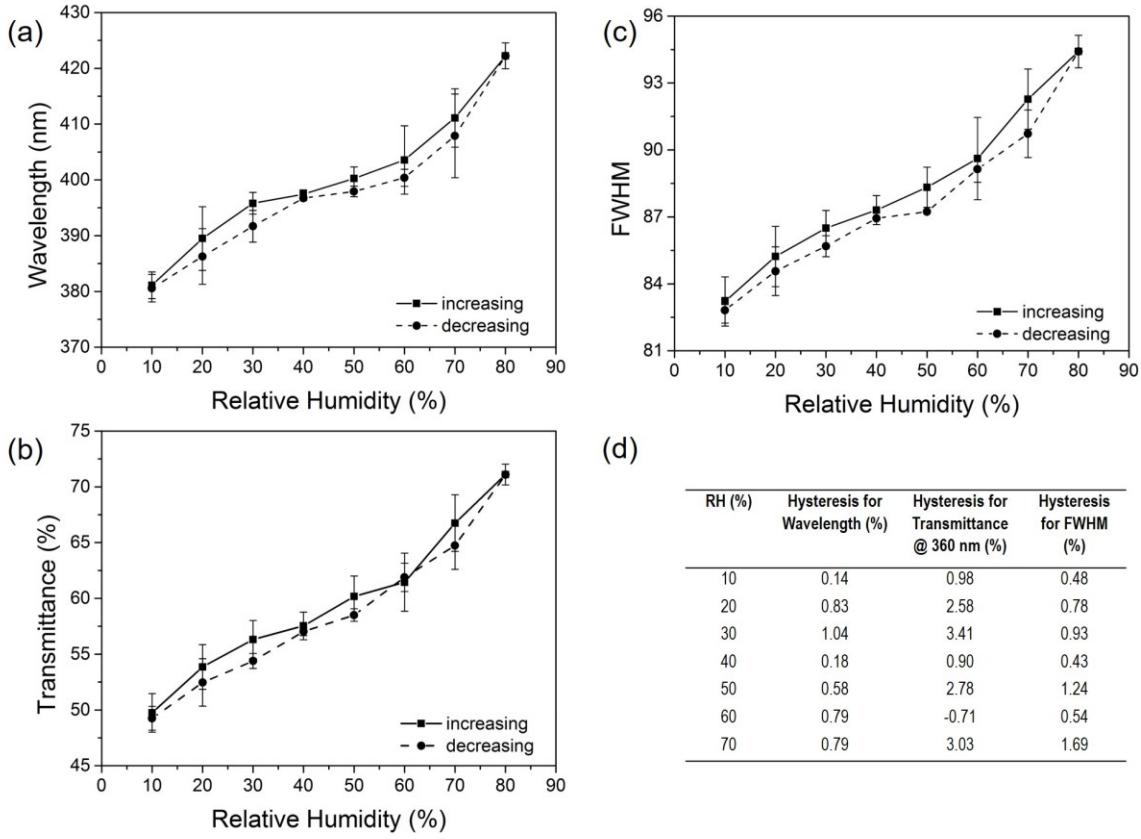

RH (%)	Hysteresis for Wavelength (%)	Hysteresis for Transmittance @ 360 nm (%)	Hysteresis for FWHM (%)
10	0.14	0.98	0.48
20	0.83	2.58	0.78
30	1.04	3.41	0.93
40	0.18	0.90	0.43
50	0.58	2.78	1.24
60	0.79	-0.71	0.54
70	0.79	3.03	1.69

Figure 4.10. Variation of the wavelength position of the minimum in transmittance (a), the relative transmittance at 360 nm (b) and the FWHM of the minimum (c) to RH increasing/decreasing cycle. The solid squares represent the adsorption (RH increasing) process, and the circles represent the desorption (RH decreasing) process. Each point is a mean of 5 measurements (error bars correspond to standard deviation). (d) Hysteresis values calculated from the curves

The stability and repeatability of the humidity sensor over a large RH range are demonstrated in a multi-cycle experiment. The multilayer structure was placed in a closed chamber where the humidity was alternately changed from 10% to 80% RH. Two different properties were examined: the variation of relative transmittance and the shift of wavelength position. The data were recorded at every 25 s interval. **Figure 4.11** shows that the transmittance increases of 25% (**Figure 4.11**(a)), while the wavelength shifts of about 50 nm (**Figure 4.11**(b)) when the RH changes from 10% to 80%.

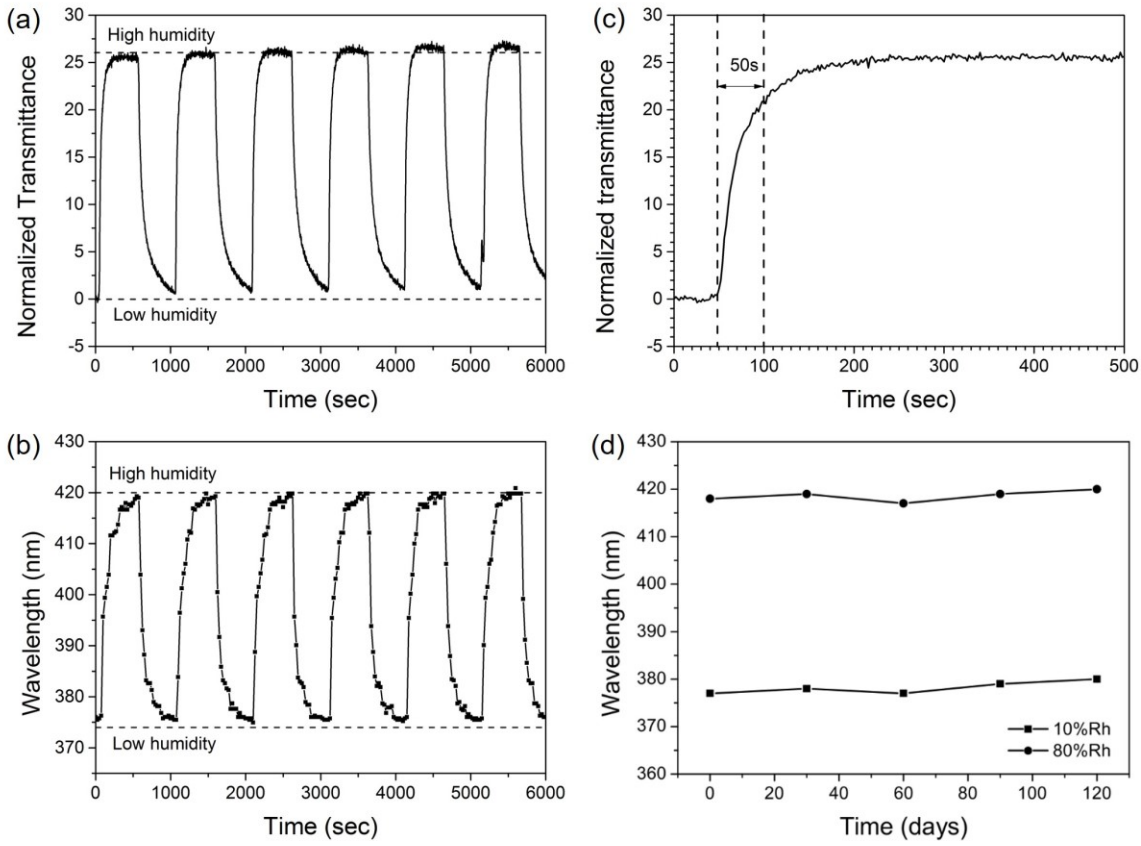

Figure 4.11. (a) Time-dependent transmittance (λ = 360 nm) for RH variation between 10% and 80% for multiple cycles. (b) Time-dependent wavelength position of the minimum of transmittance for RH variation between 10% and 80%. (c) Response time of the multilayer structure considering the variation of transmittance at 360 nm. (d) Long period stability of silk-based multilayer sensor.

This shift is lower compared with other photonic structures,[15] but it represents an improvement in the sensitivity with respect to previous device based on silk showing a wavelength shift limited to 20 nm when humidity increases from 30% to 80%. [35] No significant variations between several cycles are observed in both cases, which indicates good stability and reproducibility of the sensor.

To evaluate the response time of the structure, defined as the time for a sensor to achieve 90% of its final value, it was measured the variation of transmittance with time at 360 nm when the relative humidity was increased from 10% to 80%. As shown in **Figure 4.11**(c), the response time is ~50 s, a good value if it is compared with the response of natural nanostructures such as the chameleon skin and the

feathers of birds, presenting an answer to humidity variation respectively of about 360 s and 80 s. [36]

In addition, a good long-term stability was also demonstrated for the multilayer humidity sensor. The response of the structure (in terms of $\Delta\lambda_{peak}/\Delta RH$) was tested several times over a period of 120 days. After every test, the sensor was stored at room temperature in a drawer, with temperatures fluctuations between 19° C and 30° C and relative humidity between 30% to 60%. Only small fluctuations of the wavelength position of the interference peak (less than 1%) are observed over the 120 days (see **Figure 4.11**(d)), which indicates good stability of the sensor. The variation observed can be attributed to changes of the room condition during the storage, which slightly affect swelling behavior of the silk.

4.5. Conclusions

In this chapter, it is proposed a bioinspired multilayer film made of the silk-titanates nanocomposite material, showing a humidity-responsive behavior. The multilayer structure mimics the structure of the cuticle of *Hoplia coerulea* and is fabricated with a simple and low cost method, based on alternately deposition of regenerated silk and silk:TNSs nanocomposite films by spin coating. Thanks to the high refractive index contrast achieved with the TNSs, the structure presents a Bragg diffraction peak centered at ~400 nm with only 4-couples of layers, which responds to changes in environmental humidity. As the RH changes from 10% to 80%, the peak redshifts of 50 nm and the relative transmittance at 360 nm increases of 25%. Furthermore, the sensor presents a very stable and reproducible response and a long-term stability, important features for real-world application of the sensor device.

References

[1] P. Vukusic, J. R. Sambles, *Nature* **2003**, *424*, 852.

[2] S. Kinoshita, S. Yoshioka, *ChemPhysChem* **2005**, *6*, 1443.

[3] M. Srinivasarao, *Chem. Rev.* **1999**, *99*, 1935.

[4] L. M. Mathger, E. J. Denton, N. J. Marshall, R. T. Hanlon, *J. R. Soc. Interface* **2009**, *6*, S149.

[5] R. Montgomerie, In *Bird coloration*; Harvard University Press, 2006; Vol. 1, pp. 90–147.

[6] R. Hanlon, *Curr. Biol.* **2007**, *17*, R400.

[7] F. J. Ollivier, D. A. Samuelson, D. E. Brooks, P. A. Lewis, M. E. Kallberg, A. M. Komáromy, *Vet. Ophthalmol. 7*, 11.

[8] N. Oshima, R. Fujii, *Cell Motil. Cytoskeleton* **1987**, *8*, 85.

[9] A. E. Seago, P. Brady, J.-P. Vigneron, T. D. Schultz, *J. R. Soc. Interface* **2009**, *6*, S165.

[10] A. G. Dumanli, T. Savin, *Chem. Soc. Rev.* **2016**.

[11] M. Rassart, P. Simonis, A. Bay, O. Deparis, J. P. Vigneron, *Phys. Rev. E - Stat. Nonlinear, Soft Matter Phys.* **2009**, *80*, 1.

[12] S. Y. Choi, M. Mamak, G. Von Freymann, N. Chopra, G. A. Ozin, *Nano Lett.* **2006**, *6*, 2456.

[13] L. D. Bonifacio, B. V. Lotsch, D. P. Puzzo, F. Scotognella, G. A. Ozin, *Adv. Mater.* **2009**, *21*, 1641.

[14] Z. Wang, J. Zhang, J. Xie, C. Li, Y. Li, S. Liang, Z. Tian, T. Wang, H. Zhang, H. Li, W. Xu, B. Yang, *Adv. Funct. Mater.* **2010**, *20*, 3784.

[15] K. Szendrei, P. Ganter, O. S??nchez-Sobrado, R. Eger, A. Kuhn, B. V. Lotsch, *Adv. Mater.* **2015**, *27*, 6341.

[16] R. A. Barry, P. Wiltzius, *Langmuir* **2006**, *22*, 1369.

[17] M. Xiao, Y. Li, J. Zhao, Z. Wang, M. Gao, N. C. Gianneschi, A. Dhinojwala, M. D. Shawkey, *Chem. Mater.* **2016**, *28*, 5516.

[18] P. Ganter, K. Szendrei, B. V. Lotsch, *Adv. Mater.* **2016**, *28*, 7294.

[19] E. Tian, J. Wang, Y. Zheng, Y. Song, L. Jiang, D. Zhu, E. Vekris, S. Wong, V. Kitaev, I.

Manners, R. Z. Wang, S. John, D. Wiersma, G. A. Ozin, *J. Mater. Chem.* **2008**, *18*, 1116.

[20] B. D. Lawrence, S. Wharram, J. A. Kluge, G. G. Leisk, F. G. Omenetto, M. I. Rosenblatt, D. L. Kaplan, *Macromol. Biosci.* **2010**, *10*, 393.

[21] S. T. Parker, P. Domachuk, J. Amsden, J. Bressner, J. A. Lewis, D. L. Kaplan, F. C. Omenetto, *Adv. Mater.* **2009**, *21*, 2411.

[22] G. Perotto, M. Cittadini, H. Tao, S. Kim, M. Yang, D. L. Kaplan, A. Martucci, F. G. Omenetto, *Adv. Mater.* **2015**, *27*, 6728.

[23] D. N. Rockwood, R. C. Preda, T. Yücel, X. Wang, M. L. Lovett, D. L. Kaplan, *Nat. Protoc.* **2011**, *6*, 1612.

[24] S. Wohlrab, K. Spieß, T. Scheibel, *J. Mater. Chem.* **2012**, *22*, 22050.

[25] C. B. Borkner, M. B. Elsner, T. Scheibel, *ACS Appl. Mater. Interfaces* **2014**, *6*, 15611.

[26] J. Jasieniak, C. Sada, A. Chiasera, M. Ferrari, A. Martucci, P. Mulvaney, *Adv. Funct. Mater.* **2008**, *18*, 3772.

[27] A. Convertino, A. Capobianchi, A. Valentini, E. N. M. Cirillo, *Adv. Mater.* **2003**, *15*, 1103.

[28] P. W. Winston, D. H. Bates, *Ecology* **1960**, *41*, 232.

[29] L. Greenspan, *J. Res. Natl. Bur. Stand. Sect. A Phys. Chem.* **1977**, *81A*, 89.

[30] I. Agnarsson, A. Dhinojwala, V. Sahni, T. A. Blackledge, *J. Exp. Biol.* **2009**, *212*.

[31] E. Steven, V. Lebedev, E. Laukhina, C. Rovira, V. Laukhin, J. S. Brooks, J. Veciana, B. Panilaitis, S. M. Won, Y.-S. Kim, Y. M. Song, K. J. Yu, A. Ameen, R. Li, Y. Su, M. Yang, D. L. Kaplan, M. R. Zakin, M. J. Slepian, Y. Huang, F. G. Omenetto, J. A. Rogers, *Mater. Horiz.* **2014**, *1*, 522.

[32] T. Sasaki, M. Watanabe, *J. Am. Chem. Soc.* **1998**, *120*, 4682.

[33] A. Tripathy, S. Pramanik, J. Cho, J. Santhosh, N. A. zuan A. Osman, *Sensors (Basel).* **2014**, *14*, 16343.

[34] S. Kolpakov, N. Gordon, C. Mou, K. Zhou, *Sensors* **2014**, *14*, 3986.

[35] Y. Y. Diao, X. Y. Liu, G. W. Toh, L. Shi, J. Zi, *Adv. Funct. Mater.* **2013**, *23*, 5373.

[36] C. M. Eliason, M. D. Shawkey, *Opt. Express* **2010**, *18*, 21284.

Chapter 5.

Silk-based inverse opal structures

5.1. Introduction

Photonic crystals (PC) have been extensively investigated over the past few decades because of their ability to tailor and control the propagation of light. The first example was studied by Lord Rayleigh in 1887, who showed in a one-dimensional (1D) photonic crystal the existence of high reflectivity of light over a well-defined range of wavelengths known as stop-band. This ability to control photons is comparable to the way in which the semiconductors manage electrons. Recently, PC have moved from 1D into more complex 2D and 3D photonic lattices. In the case of the 3D structure, for high refractive index contrast, it is possible to develop an omni-directional photonic band-gap (PBG) offering complete control of the flow of light in all the three directions.[1,2] Among them, opals (and their inverse)[3–7] are attractive great attention as platform for application in sensing,[8,9] photocatalysis,[10] dynamic full color displays,[11] polymer lasers,[12] enhanced light harvesting for solar-cells.[13]

Opals are natural structures that present structural colors deriving from interference phenomena caused by the interaction of the light with the lattice structure. These natural stones are composed by silica particles arranged in a face-center cubic lattice. In analogy with natural opals, it is possible to fabricate artificial opal by assembly of colloidal monodisperse spheres, like silica and latex. In these materials, the stop band positions depend largely on three factors: i) refractive index contrast between the two periodic media (spheres and the surrounding medium), ii) the lattice constant (the spacing between spheres), iii) the filling factor (volume of the

spheres compared to the volume of surrounding phase).[7] A good approximation for modeling the PBG properties of a photonic crystal is obtained combining the law of reflection with the Bragg-Snell's law. For constructive interference, the wavelength of maximum reflection (λ) can be defined by the following equation:

$$m\lambda = 2d\sqrt{n^2 - n_0^2 sin^2\alpha} \tag{5.1}$$

where m is the order of refraction, d is the space between the planes, n and n_0 are the refractive index of the two media. For opals and inverse opals, the refractive index n can be expressed as an average of the refractive indices of the spheres and the interstitial space for opals or of spherical voids and solid walls for inverse opals:

$$n_{avg} = \varphi n_{spheres} + (1 - \varphi) n_{background} \tag{5.2}$$

Where φ is the filling fraction. The distance d is the spacing between the close-packed planes of voids and in the case of the [111] plane corresponded to

$$d_{hkl} = D\sqrt{\frac{2}{3}} \tag{5.3}$$

If n_0 is equal to 1, we obtain for the first order of diffraction (m=1):

$$\lambda = 1.633D\sqrt{n_{avg}^2 - sin^2\alpha} \tag{5.4}$$

Although this equation does not take into account other phenomena, such as strong scattering, it is considered a good approximation for the prediction of the reflection of opals and inverse opals.[7] In **Figure 5.1** it is represented the PBG calculation and the respective reflection spectrum in the case of a silica opal. In the same figure it is also reported the case of a silicon inverse opal. As shown, only in the case of index contrast higher than 2.8 it is possible to obtain a complete band-gap (full band-gap). Usually, for opaline and polymeric inverse opals, it is difficult to obtain a complete gap in all the three directions. In this case, the band gap is called *stop band* or even pseudo band gap (pPBG) to distinguish it from the complete one. In this chapter I will used both these terms.[6]

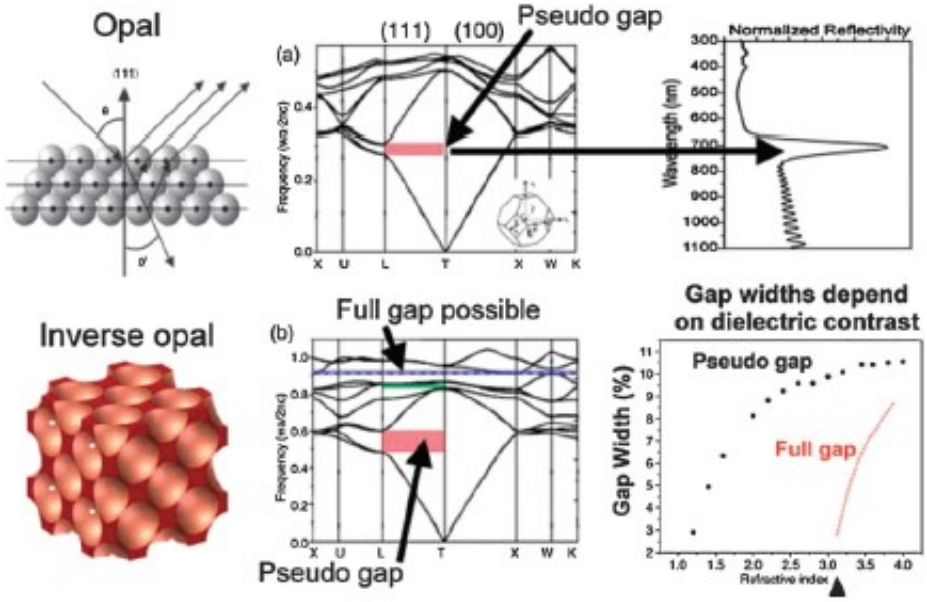

Figure 5.1. Top row from left to right: Opal structure; photonic band structure calculation for a silica opal, the stop band is marked in red; reflectance measurement along the 111-direction. Bottom row from left to right: Inverse opal structure; photonic band structure calculation for a silicon inverse opal, the stop band is marked in red. The complete photonic band gap is marked in blue; Gap widths plotted over index of refraction.[6]

PC can be fabricated using both top-down and bottom-up approaches. Top-down approaches produce smaller elements using precise tools such as photo-lithography, ion beam lithography, but they are very expensive and time-consuming. By comparison, bottom-up approaches involve assembly of small building-blocks into large area periodic structures. The most diffused chemical method employs the crystallization of spheres in colloidal crystals, opals, which can also be used as template for the fabrication of inverse opals. The assembly can be obtained by using different driving forces to induce the colloidal compaction, such as gravitational, capillary, electric and magnetic fields.[14]

In sedimentation process the assembly is controlled by Brownian motion and this limit the particle size to 100 nm. Centrifugation makes the compaction feasible for a wider range of dimension, but in both these processes, the drawback is a limited control over the crystal formation (thickness) and make difficult the integration into device.

Spin coating is another technique used for the assembly of colloidal crystal film, where the assembly is controlled by centripetal forces, gravitational forces, viscosity and even capillary forces during the evaporation of the solvent. This technique has the advantage to produce large-area uniform films and to be compatible with established technologies.[15]

Large-area colloidal crystal films can be prepared by using the Langmuir-Blodgett approach. This technique permits a good control of the crystallization of monolayer, but suffers of problem during the transfer step from the liquid interface to the substrate, limiting its use only for scientific studies.[16]

Evaporation of a dispersion droplet on a flat surface, dip coating and vertical sedimentation are other techniques largely diffused for the fabrication of opaline structures. In the first one, the main problem is related with the coffee ring effect that limit the size of opal. In the dip-coating the main limit is related with the maximum thickness achievable, while in the case of the sedimentation, the major limitation is the interruption of the film formation in proximity of the meniscus.[17–19]

Finally, electric or magnetic field can provide a versatile driving force to control the assembly process of opal, with some practical limitations (especially in the case of the magnetic one).[20,21]

It has to underline that all these methods present two main challenges: random stacking of hexagonal closed-packed planes and development of cracks during solvent evaporation.

For the inverse opals (IOs) the fabrication process involves 4 main steps: opal formation, infiltration, conversion and inversion. The infiltration proceeds by infilling the pores of the opal with a liquid. The most diffuse method is the impregnation with a polymer precursor or a sol-gel solution. Principal problems in this step arises from inhomogeneous infiltration of the interstitial. The inversion procedure is determined by the choice of the opal template. In the case of latex, it can be chemical etching or calcination. This step can modify or even disrupt the complex porous architecture, and therefore special care has to be taken during the replica of the template to avoid

cracking and volume shrinkage (the last one is widely diffuse especially in the case of polymeric IOs).[6]

Intrinsic defects in the opal and IOs lattices, for examples vacancies, interstitials, stacking fault and dislocations or impurities, are common imperfections that compromise the optical quality of the PC. On the contrary, extrinsic defects are introduced into the lattice intentionally to provide specific functionality, in the same way of the doping process in electronics. The creation of these defects in the PCs can induce the formation of optical states within the (complete or partial) photonic band gap, allowing to tune the material's optical properties and to increase the structure functionality.[15,22,23] Optical waveguides obtained in PCs by creating a line (1D) defect within a homogeneous photonic lattice are an example of this functional outcome. The challenges in the field of self-assembled PC is how to incorporate extrinsic defects into the lattice that perform at optical wavelength, how to understand their photonic properties through theory, simulation and experimentation and how to couple efficiently the light to create photonic devices. A portfolio of approaches has been developed to introduce extrinsic defects including both top-down and bottom-up techniques and a wide range of material have been investigated for the realization of functional PC embedded defects.[24]

A wide range of materials have been investigated for the realization of PC structures with specific functionality. It is possible to regroup all the materials in two main classes: (i) passive photonic crystals, with the ability to guide, diffract, localize and amplify light and (ii) active ones whose structural colors can be altered in response to an external stimulus. Among them, "soft" dielectric materials such as polymers and hydrogel are particularly promising for the realization of flexible, stimuli-responsive IOs that can find application in sensing, tunable color displays and anti-counterfeit devices.

Biologically compatible photonic devices are currently attracting an increasing interest, as they could enable optical transduction from living tissues for biomedical applications, and several PC structures made of biopolymers such as collagen,[25] keratin[26] and silk fibroin[27–31] were recently proposed as optically responsive

nanostructures for colorimetric sensing or as chemical-free implantable spectral labels. Silk based PC are in particular interesting because they combine biocompatibility with biodegradability and sustainability, with applications in biomedical and even environmental sensing, if properly functionalized.[32]

In the present chapter I will present the fabrication of Silk-based large inverse opals realized with both the nanocomposite materials presented in the *Chapter 2*. The first part will focus on the description of the fabrication method, based on a different approach compared to the previously reported in literature by Kim.[27] The potentiality of this method for the design of heterostructures embedding extrinsic optical defect will be explored in the *Section 5.3*. In the second part of the chapter, I will report about the fabrication of Silk-TNSs inverse opals and Silk-AuNRs inverse opals. A wide space will be reserved to the description of the fabrication protocol and the structural and optical characterization of the IOs. Finally, I will present the first results related to the stimuli-responsive behavior of the fabricated structures.

5.2. Assembly of large area silk inverse opals: the layer by layer approach

For the fabrication of the silk-based inverse opals it has been selected the bottom-up approach based on a two-step strategy: i) a sacrificial opal template is fabricated by assembly of polymeric beads; ii) a negative-replica of the opal structure is then obtained by infiltrating it with the silk-based solution and dissolving the beads after drying.

This method has been proposed by S. Kim to obtain free-standing silk inverse opal films.[27] In his work, S. Kim reported a fabrication of the opal template, based on a self-assembly of polymethylmethacrylate microparticles on a silicon substrate, using a drop casting method. This approach permits to obtain opal templates with a high number of layers, but with a small surface area because of coffee rings problems and the formation of defects during the self-assembly (see *Section 5.1*).

To avoid this limitation, it has been investigated a different approach for the fabrication of large inverse opals based on a layer by layer scooping transfer

technique. The method has been developed in collaboration with Y. Wang at SilkLab (Tufts University).[33] The protocol for the fabrication was first optimized focusing on the realization of silk inverse opals (SIO) and only after the optimization of the parameters, it was extended to the realization of silk-composite inverse opal structures.

The first step of the fabrication consists on the assembly of a hexagonally close-packed monolayer of polystyrene beads at the water-air interface that is then transferred onto another substrate. As previously reported,[34] the scooping technique makes very simple the fabrication of a multilayer with controllable layers and with good quality on large scale. This method is similar to the Langmuir-Blodgett technique,[16] the most studied approach for industrial-scale mass production. Both the approaches present the same ability to fabricate multilayers with a controllable number of crack-free layers over large area. The significant difference between them is the close-packing process. In the scooping transfer method, the packing of the beads is obtained by chemical interaction, using chemically-modified PS beads and surfactants. This permits to achieve crystallization of the monolayer at low temperatures and to avoid the use of expensive equipment.

Figure 5.2 shows a crystalline PS monolayer assembly at the water/air interface. The self-assembly process is influenced by different parameters: PS nanosphere size, PS concentration, presence of electrolytes and surfactants, water evaporation rate.[35] Experiments were conducted considering different sizes of PS nanospheres commercially available, 300 nm and 400 nm (Interfacial Dynamics Co.), modified with carboxylic acid groups. A few drops of the suspension were introduced on the water surface using a partially immersed silicon wafer. The self-assembly process was promoted by the addition of liquid medium and surfactant (sodium dodecyl sulfate, SDS).

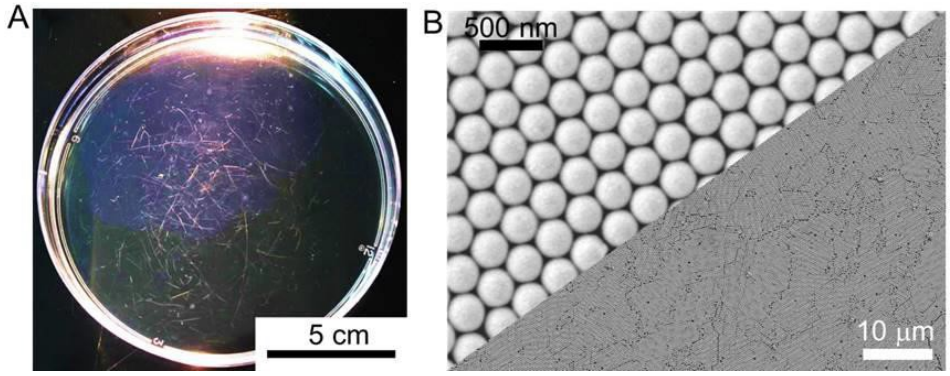

Figure 5.2. Crystalline PS nanosphere monolayer array. (a) Photograph of crystalline PS monolayer at the air/water interface. The colloidal crystals grow over a large scale with the assistance of SDS. (b) SEM images of PS nanosphere monolayer array on substrate. The nanospheres are stacked in a close-packed hexagon structure and such an arrangement is highly ordered on a large-scale. The diameter of the PS nanosphere is 300 nm.[33]

The dimension of the crystal layer depends both on the size of the substrate used to introduce the PS spheres suspension and the water container. Large opals can be obtained by using larger transferring substrate and water containers. In the specific case, the self-assembly processes were carried out inside a Petri dish of 12cm diameter. The rigid, hexagonally-close-packed PS sphere monolayer array was then transferred from the water surface to the surface of a silicon substrate and let to dry. The process was repeated several times to obtain a multilayer structure with desired number of layers. **Figure 5.2**(b) shows a SEM image of a surface of a PS monolayer deposited on a silicon substrate, where the hexagonally-close-pack arrangement is clearly visible.

The fabrication of the opal template was followed by the negative-replica of the nanostructure to obtain the final inverse opal. The voids in the opal template were infiltrated with a liquid silk-based solution and then the sample was dried to allow the formation of a free-standing film. The favorable material characteristics of the silk, mechanical robustness and ability to replicate structure at the nano-scale level, guarantee the complete replication of the template structure and the fabrication of high-quality inverse opals films. Finally, the PS template was removed by soaking the film in toluene.

It is important to underline that this step is crucial for preserving the integrity of the nanostructure in the case of the nanocomposite matrix. Two different problems were observed, one related with the impregnation and the second related with the dissolution. Concerning the impregnation, it is important that the nanoparticles embedded in the silk matrix present a dimension smaller than the pores as well as the viscosity of the solution is adequate to permit a homogeneous infiltration. The second factor to consider is the solvent used to dissolve the PS spheres. In his work, Kim dissolved the PMMA template using an acetone bath. During this process, the acetone induced a partial crystallization of the silk fibroin in the β-sheets conformation. Instead, the toluene used to dissolve the PS beads does not affect the structure of the fibroin, which preserves its random coil conformation. The final freestanding SIO is water-soluble and sensitive to post-processing treatments able to change secondary structure of the protein. In particular, it was demonstrated the possibility to modulate the photonic lattice through a control of the protein conformation by the use of UV light or water vapor.[33] On the other side, the amorphous conformation makes the structure sensible to the presence of moisture during the evaporation of the toluene after the dissolution of the template (in particular in the case of the SF-TNSs inverse opals). For this reason, the removal of the samples from the toluene bath was carried out under a hood at 30 %RH, to avoid possible collapsing of the structure and loss of the structural color due to capillary forces and swelling of the material.

In **Figure 5.3** is illustrated a schematic diagram of the fabrication process. Additional information is reported in *Appendix A2.5*.

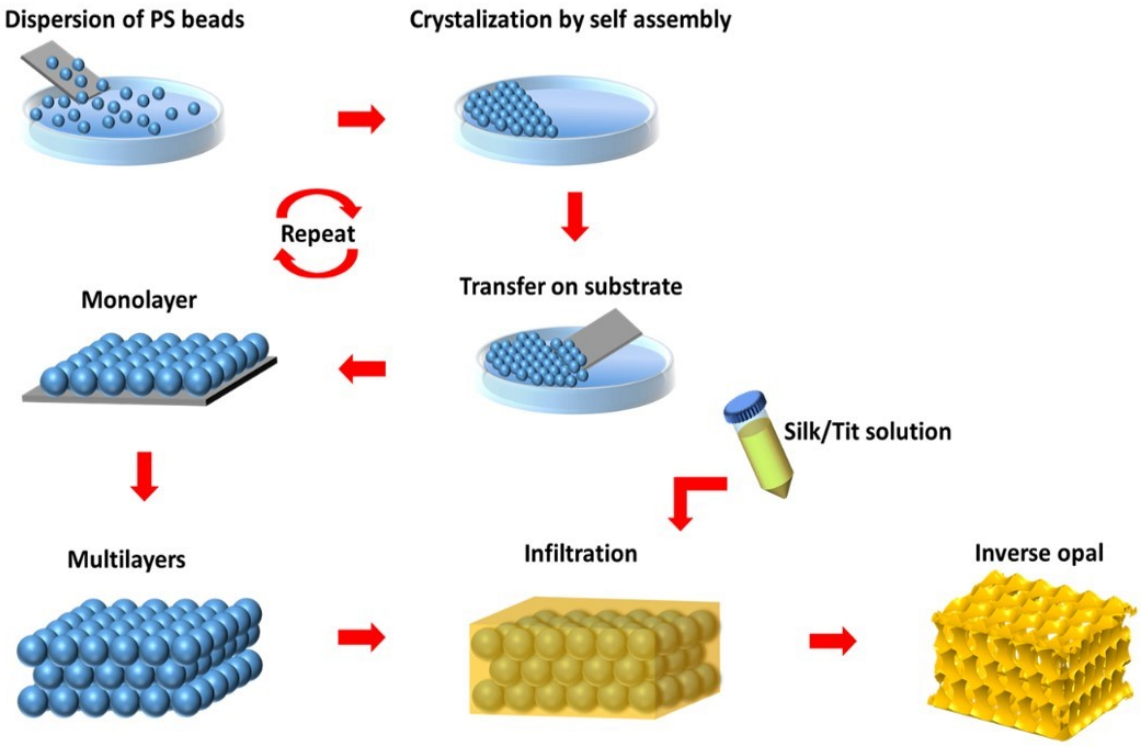

Figure 5.3.. Schematic illustration of the fabrication process of SIO. A monolayer of PS microspheres is realized by self-assembly at the water/air interface and transferred on a silicon substrate. The process is repeated until the final opal template is obtained. The opal template is then infiltrated with the silk-based solution. After drying, the PS beads are removed from the free-standing film by dissolution in toluene (further details are reported in the Appendix).

Different silk-based IO structures were fabricated using the developed protocol and characterized optically and structurally by reflection measurements and SEM analysis (*see Appendix A3.13 and A3.14*). Two different sizes of beads commercially available (300 nm and 400 nm) were used to tune the pseudo-photonic band-gap of the final photonic lattice. In addition, the effect of the number of the layers on the final reflectivity and the diffraction-angle dependent properties were characterized.

5.3. Introduction of a defect layer in silk inverse opals

One of the advantage of the presented LbL approach is the possibility to engineer the photonic band-gap by introducing controlled defects during the fabrication process and by the creation of complex heterostructures. Specifically, the method was explored for the fabrication of a sandwich-like inverse opal structure with a planar defect. The results here reported are published in *Journal of Material Chemistry C* (2017).

5.3.1. Structure design and modeling

The protocol presented in the *Section 5.2* was adapted to create a sandwich-like structure with a planar defect layer by changing the size of the PS spheres during the fabrication of the opal template. Given that one of the relevant features of silk is its biocompatibility, the SIO was designed to have a band-gap within the so-called biological window, centered at λ_c=800 nm. Once λ_c is selected, the optimal diameter of the holes (D) in the photonic lattice is also automatically defined in accordance to the Bragg law and in this case, it corresponded to the use of commercial polystyrene beads (Interfacial Dynamics Co.) having a 420 nm diameter.

As anticipated in the *Section 5.1*, the introduction of a defect in a periodic photonic structure creates localized states in the gap and thus a dip in the reflection peak.[36] The spectral position and the amplitude of the dip depends both on the refractive index and the thickness of the defect, as well on the characteristic of the surrounding photonic crystals.[37] Specifically, it is possible to control the spectral position of the dip by changing the diameter of the spheres (and, consequently, the pores in the inverse structure) used to realize the defect layer. In this case we choose to break the periodicity of the lattice inserting a layer of commercial PS beads with a diameter d = 210 nm.

The realization of a controlled defect in the structure was confirmed both by SEM imaging and by reflection-spectrum analysis. By taking into account the structure observed through the SEM images, a simplified model of the SIO lattice was proposed

to support theoretically the observed resonant properties of the designed bandgap. The spatial distribution of PS beads reported in **Figure 5.4** was used as an approximation of the real structure and numerical simulations were performed by using a commercial FDTD (Finite Difference Time Domain) Software package (Lumerical Solutions Inc.). The simulations were performed by Fabio De Ferrari at Tufts University.

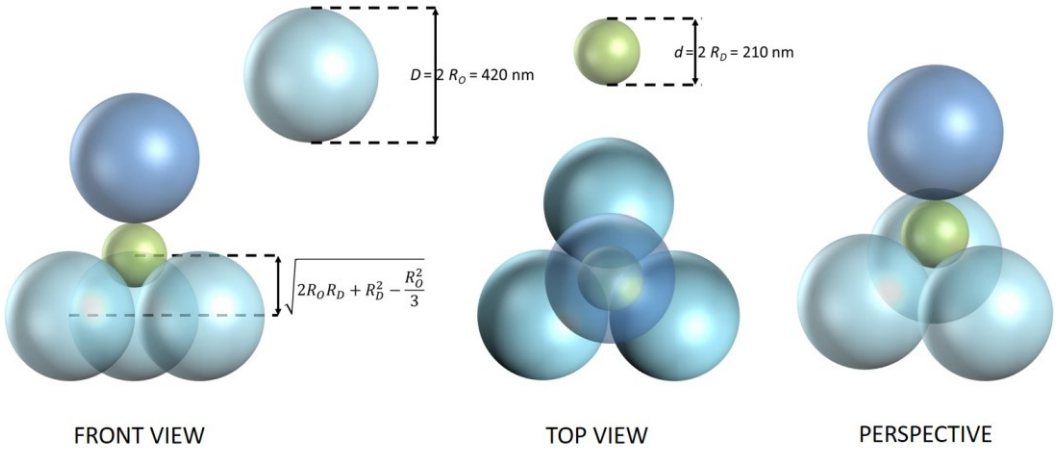

Figure 5.4. Schematic illustration of the spatial distribution of the PS beads used as model to determine the geometrical parameters for the FDTD simulations.

The simulated structure was composed by a stack of N layers, constituted by air holes (n=1.00) with diameter D in silk (n=1.54),[38] where each layer was designed with a hexagonally close packed pattern. The defect layer was represented by a homogeneous block of appropriate thickness (t_{def}) and effective refractive index given by the relation:

$$\sqrt{0.74n_{air}^2 + 0.26n_{silk}^2} \tag{5.5}$$

The distance between the centers of the beads above and below the defect layer (dCC) was set to:

$$D * \sqrt{\frac{2}{3}} + t_{def} \tag{5.6}$$

and the structure was defined give higher priority to the air holes, whenever they overlapped the defect layer.

The simulations were performed in the 0.4 μm to 1 μm wavelength range, and considering a disposition as shown in **Figure 5.5**: a plane-wave source was placed in close proximity of the opal surface (at 135 nm distance) and reflectance was measured 235 nm away from the opal surface.

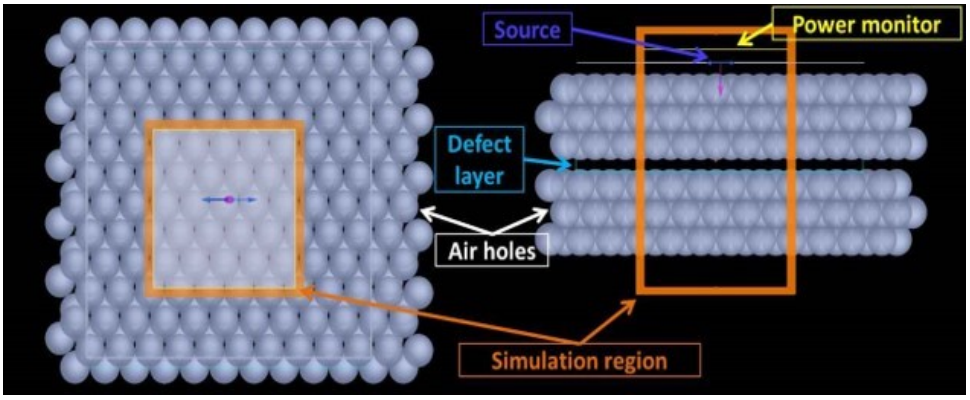

Figure 5.5. Schematic rapresentation of the structure used for the FDTD simulations.

It has to note that the simulated model is a simplification of the real structure that does not take into account the contribution of the silk/air interface of the film to the reflection. In addition, the model considers overlaps between the continuous defect layer and the pores of the sandwich structures, that in reality the geometry prevents.[39] Nevertheless, the good agreements obtained with the experimental results gave a qualitatively support for the design of the structure.

5.3.2. Structural and optical characterizations

Figure 5.6 shows the SEM cross section images of a colloidal crystal-template made of 6+1 layers of 420 nm spheres with a planar defect layer made of smaller beads (210 nm) and the resultant SIO film.

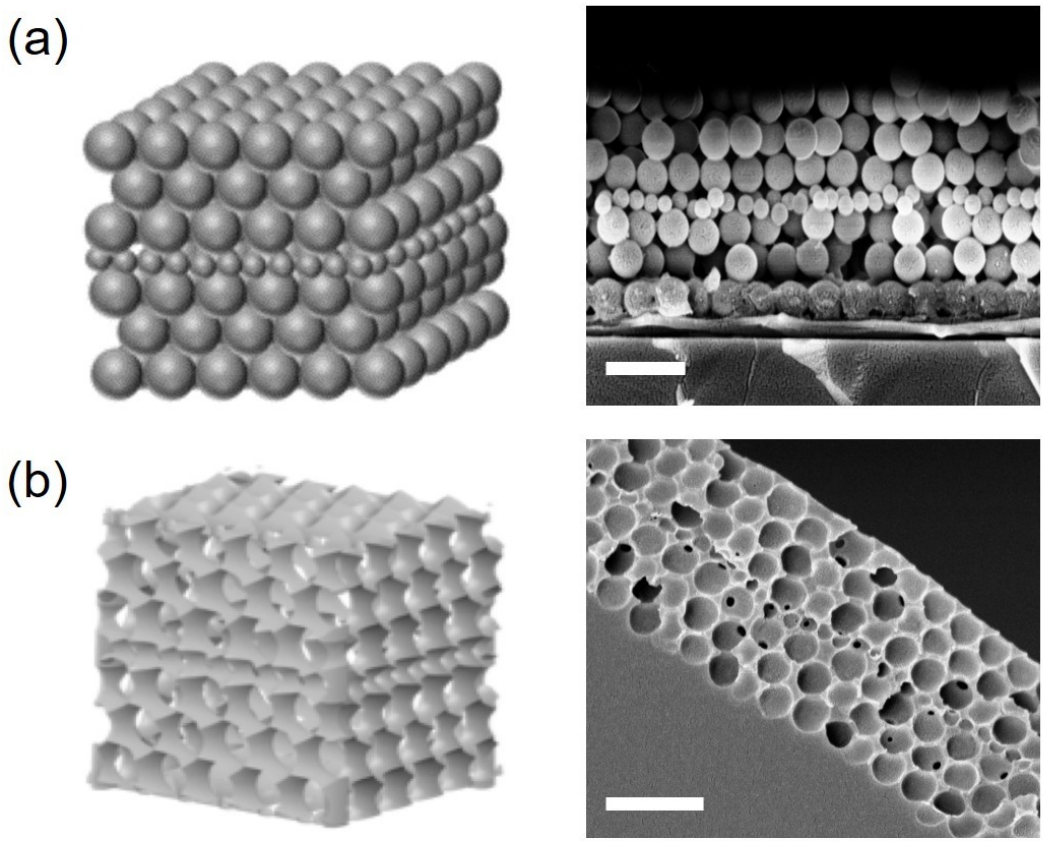

Figure 5.6. (a) Cross-sectional SEM images of the opal template structure made with the PS beads and (b) the resultant free-standing SIO film. The scale bar is 1 μm. Schematic representations of the structures are reported in the same image.

The SEM image of the SIO reveals a regular porous sandwich heterostructure made of larger pores with a single layer of smaller pores embedded in the middle (see the particular in **Figure 5.7**(d)). The closed-pack face-centered-cubic lattice of the opal template is converted to air spheres showing a hexagonal arrangement surrounded by the silk matrix, as confirmed by the SEM images of the surface of the SIOs (**Figure 5.7**). The observed order in the z direction suggests that the method permits a good assembly of the crystalline structure and avoids problems of collapse of the structure during the dissolution of the template. Slight distortions in the opal nanostructure are caused by the cleavage of the sample necessary for imaging.

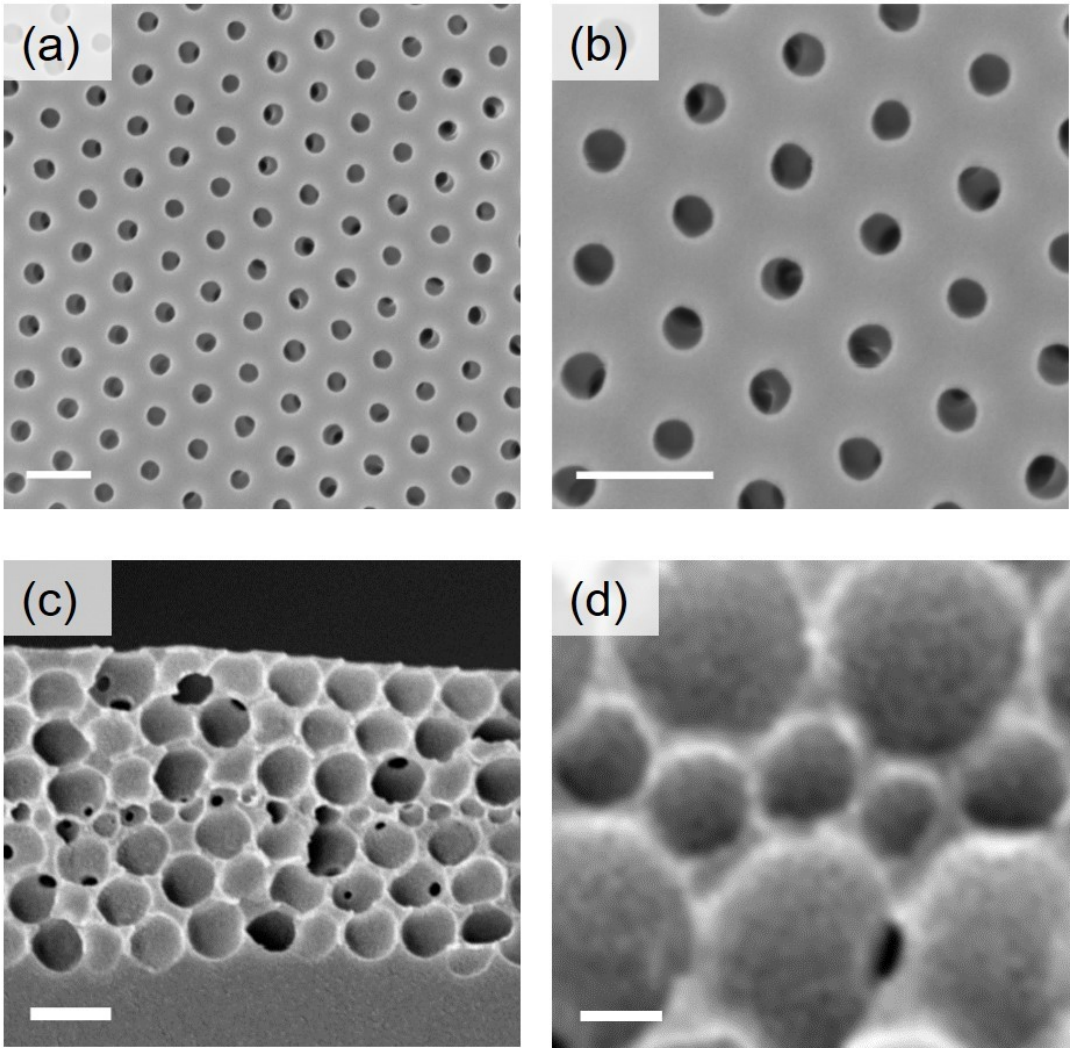

Figure 5.7. (a) and (b) SEM images of the surface of the inverse opal structure made with 420 nm beads. The scale bars are 500 nm. The nanopores are stacked in a hexagonally arrangement highly ordered on a large-scale.(c) and (d) High magnification SEM images of the cross-section of the SIO showing the disposition of the pores in the lattice. The scale bars correspond to 1 μm (c) and 125 nm (d).

The optical uniformity of the fabricated layered structure was examined trough reflection measurements. **Figure 5.8**(a) shows the reflectance spectrum of the defected-SIO. The expected resonance (pass band) appears as a dip within the stop-band at 800 nm, as a consequence of the presence of the planar defect.

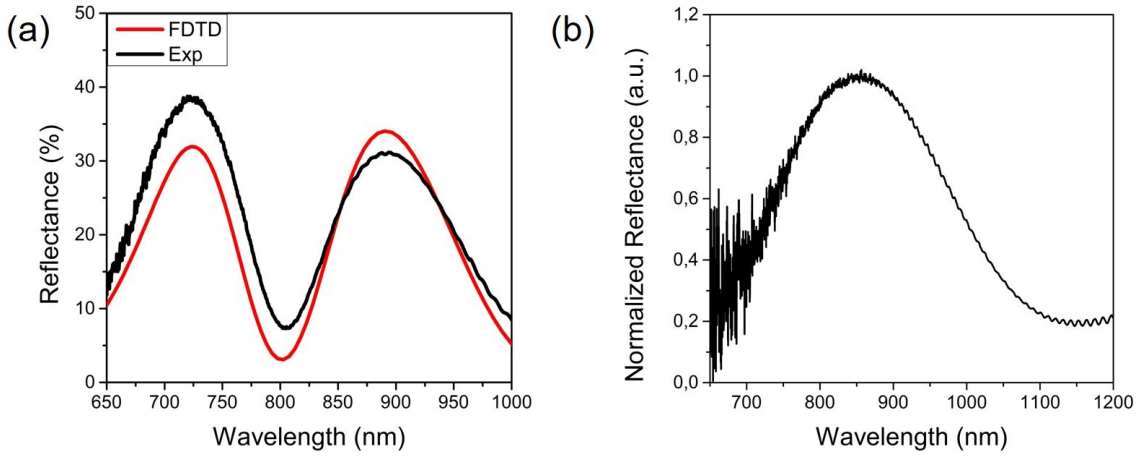

Figure 5.8. (a) Experimental (black) and simulated reflectance spectra of a SIO structure including a defect-layer realized by 210 nm PS beads. (b) Reflectance spectrum of a simple 3 layers silk inverse opal obtained by replica of an opal template made with 420 nm beads without a defect layer.

A comparison of the peak with the reflectance spectrum of a simple 3 layers silk inverse opal (**Figure 5.8**(b)) shows a broader spectral response. This behavior is consistent with the results previously reported in literature.[36] As expected,[33] increasing the number of layers of the slabs affects the width of the stop-band and the maximum value of reflectivity from the photonic lattice (**Figure 5.9**(a)). We also verified the effect of the size of the beads on the position of the dip by fabricating a SIO with a defect layer realized by 300 nm (instead of 210 nm) PS beads. The experimental reflectance spectrum (**Figure 5.9**(b)) shows that, as expected and previously reported for direct opal structures,[40,41] the position of the resonance moves to longer wavelength when the thickness of the defect increases.

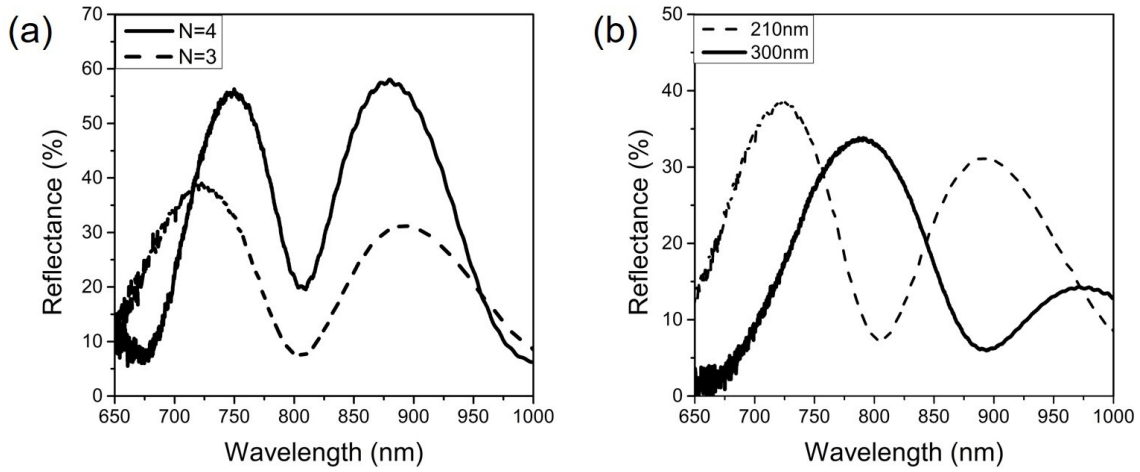

Figure 5.9. (a) Comparison between the experimental reflectance spectra of defected-SIO structures for $N = 3$ and $N = 4$. (b) Impact of the defect-beads size on the wavelength of the reflection-dip: we report in the same image both the spectrum obtained considering 210 nm defect beads and 300 nm defect.

These experimental results support the use of 210 nm beads to obtain a reflectance dip at 800 nm. From a theoretical point of view, the required defect size to create a resonant mode in the center of the reflection band of a 1D-grating (e.g. fiber gratings or waveguide gratings) should correspond to a π-radians phase-shift of the resonant wavelength, but the extension of this principle to the case of inverse opals is not straightforward for two reasons: reflections do not happen on planar interfaces, and when beads are considered, the packing effect has to be included in the model. For this reason, simulations were carried out considering a simplified structure with a continuous defect layer, as explained in the previous section. As reported in **Figure 5.8**(a), the simulated spectral positions and the depth of the defect mode are in qualitative agreement with the experimental results. The reflectivity asymmetry of the short-wavelength and long-wavelength red-line peaks (at about 730 and 900 nm) suggests that in the simulated system the band-gap is centered at a wavelength slightly longer than 800 nm. On the opposite, the central wavelength of the experimental opal seems to be slightly lower than 800 nm, probably because of the small structure contraction observed after that the PS beads are removed. Considering the absolute amplitude of the experimental and theoretical reflection curves, it is important to highlight that the observed difference could be explained

considering that the simplified model used for the FDTD simulations does not take into account the reflectivity contributions of the two silk-air interfaces present in the fabricated film.

In conclusion, an easy-to-implement method to engineer defect layers in a silk inverse opal was described. Thanks to the layer by layer approach, control of the crystal growth of the opal template and introduction of planar defects in an opal inverse structure was possible without the use of complex and expensive microfabrication techniques such as lithography. In addition, the simple model proposed for the FDTD simulations allowed us to qualitatively confirm the position of the passband in the reflection spectrum and assist in designing the lattice parameters of the structure. Furthermore, the method can be easily adapted for the fabrication of a multitude of biopolymer based inverse opal heterostructures, opening the possibility of application in filters, waveguides, laser sources and other optical components.

5.4. Silk-TNSs inverse opals

One of the limit factor to obtain a complete photonic band-gap in an opaline or an inverse opal structure is the refractive index. The condition to obtain an omni-directional photonic band-gap is that the refractive index (RI) contrast between the crystal and the surrounding medium exceeds a certain value, which is about three for three-dimensional lattices of high symmetry. In this case, light of certain wavebands cannot propagate in any direction inside the photonic crystal.[42] This condition is very difficult to obtain in opaline structures themselves, because they have too high dielectric filling fraction. Even in the case of the SIOs it was not possible to obtain a PBG, because of the low RI of the silk.[27] One of the strategy to increase the RI contrast is the infiltration with inorganic materials.[43] TiO_2 is one of the best candidate because of its high refractive index. Move from these consideration, we decided to improve the optical properties of the SIOs by increasing the refractive index of the SF matrix with the introduction of the TNSs. As illustrated in the previous chapters, it is possible to realize SF-TNSs nanocomposite with high TNSs filling factor and tunable

RI. In the following section, we will present the method studied for the realization of large area SF-TNSs IOs and the obtained results.

5.4.1. Fabrication

Silk-TNSs inverse opals were fabricated by infiltration and replica of a 3-layers PS opal template following the protocol presented in *Section 5.2*. Different formulations of Silk/TNS solution were investigated to optimize the fabrication protocol. Three different variables were considered: the concentration of titanates in solution (silk/TNS weight ratio), the total concentration of the solution and the concentration of tetramethylammonium (TMAH) in the starting dispersion of titanates in water.

The concentration of TNSs affects the final refractive index of the material and, as consequence, the reflection of the inverse opal. An increase of the refractive index (by increasing TNSs concentration) induces an increase of the reflectivity of the inverse opals and a redshift of the reflection peak.[44]

On the other end, the particles concentration affects the rheological properties of the solution (with consequence during the infiltration step) and the mechanical properties of the final free-standing films (it was observed that for TNSs ≥ 50% the SIOs resulted brittle and with optical inhomogeneity).

The total concentration of solution is relevant during the fabrication because affect the final thickness of the free-standing inverse opal, the viscosity of the solution and the sol-gel transition. High concentrations decrease the gelation time and increase the viscosity of the solution. If the gelation is to fast and the viscosity too high, the infiltration results critical for the final quality of the opals: inhomogeneity and incomplete filling of the template were observed. Dilution is a possible route to reduce the viscosity.

Finally, it was investigated also the effect of the tetramethylammonium hydroxide (TMAH). TMAH permits the dispersion of the titanates nanosheets in water due to electrostatic stabilization: high concentration of TMAH stabilizes better the titanates nanosheets in a colloidal solution.[45] At the same time, TMAH affects the sol-gel

transition of the silk solution by changing the pH (it is a strong base). For pH>9 both the basic and acidic groups of the fibroin protein are deprotonated and thus the effect of electrostatic interaction decreases or could become repulsive, significantly reducing the gelation process.[46] High concentration of TMAH in the final silk/TNS solution avoided a fast gelation of the silk making easier the infiltration step, but at the some time affected the formation of the inverse opal nanostructure during the final drying step, because of the high hygroscopic behavior of the TMAH (as already explained in *Section 5.2*).

The different formulations tested are reported in **Table 5.1**. The formulation that gave the best results in terms of optical quality and robustness of the inverse opals is named "I", that was selected for the following experiments.

Table 5.1. Formulations investigated during the development of the protocol for the SF-TNSs IOs.

	Titanates amount [%w/v]	Total concentration of solid in solution [%w/v]	Concentration of TMAH [M]	Fast sol-gel transition	Formation of inverse opal
A	50%	7%	1 M		
B	50%	10%	1 M		
C	50%	10%	0.2 M	x	
D	50%	8%	0.2 M	x	x
E	80%	10%	0.2 M		
F	80%	14%	0.2 M		
G	20%	7.6%	0.2 M	x	x
H	20%	7%	0.2 M	x	
I	20%	6%	0.2 M		x
J	20%	5%	0.2 M		
K	20%	5%	0.1 M	x	

As already illustrated, the as-prepared IOs are water-soluble since the fibroin is in the random coil-conformation. Considering that for some applications a water-stability is required, post-fabrication treatments were investigated to increase the population of β-sheets crystals and make them insoluble in water. Two different

annealing were considered: a methanol annealing and water vapor annealing. Both the treatments were reported in literature as efficient ways to crystallize the fibroin.[47] In addition, it was demonstrated that methanol is an efficient way of curing the silk-TNS nanocomposites as well. While pure TNSs are easily dispersed in methanol, the silk-TNS nanocomposites are methanol insoluble and methanol annealing induces an increase of the refractive index of the nanocomposite.[45]

The methanol annealing was effectuated by dipping the samples in methanol for 12 hours. After the treatments, the samples were removed from the bath and left to dry in controlled atmosphere to avoid a rapid evaporation of alcohol and reduce crack formations. For the water vapor annealing the samples were exposed to water vapor (relative humidity >90%) for 4 hours at room temperature. All the details are reported in *Appendix A2.6*.

Final, it was also studied the effect of UV irradiation. As recently demonstrated by Y. Wang, UV light can be used as efficient way to modulate the 3D photonic lattice of SIOs,[33] by acting on the protein conformation. A deep UV irradiation is able to induce peptide chain scission and photodegradation of the fibroin.[48] In addition, UV light affects the TNSs structure. As reported in literature, UV light can be used as post processing of the TNSs, increasing the refractive index by densification of the small cluster.[49] By this way it possible to create patterned inverse opals with potential application in sensing, gradient photonic band-gap and photonic paper.[50–52]

The opals were characterized optically and structurally by reflection measurements and SEM imaging. In addition, FTIR measurements were conducted to verify the effect of the treatments on the secondary structure of the protein, while ellipsometry spectroscopy was used to determine the refractive index of the material.

5.4.2. Structural and optical characterizations

In **Figure 5.10**(b) it is reported a SEM cross-section image of a standard sample, showing a 3-layers structure with open porosity. The lattice constant, defined as the center-to-center distance of the air cavities, is around 295 nm (see **Figure 5.10**(a)), closed to the diameter of the PS sphere used for the template. The

hexagonally closed-pack arrangement of the PS beads is preserved in the pore disposition of the inverse opal and no cracks or defects are visible, confirming the possibility to obtain structure with good optical quality.

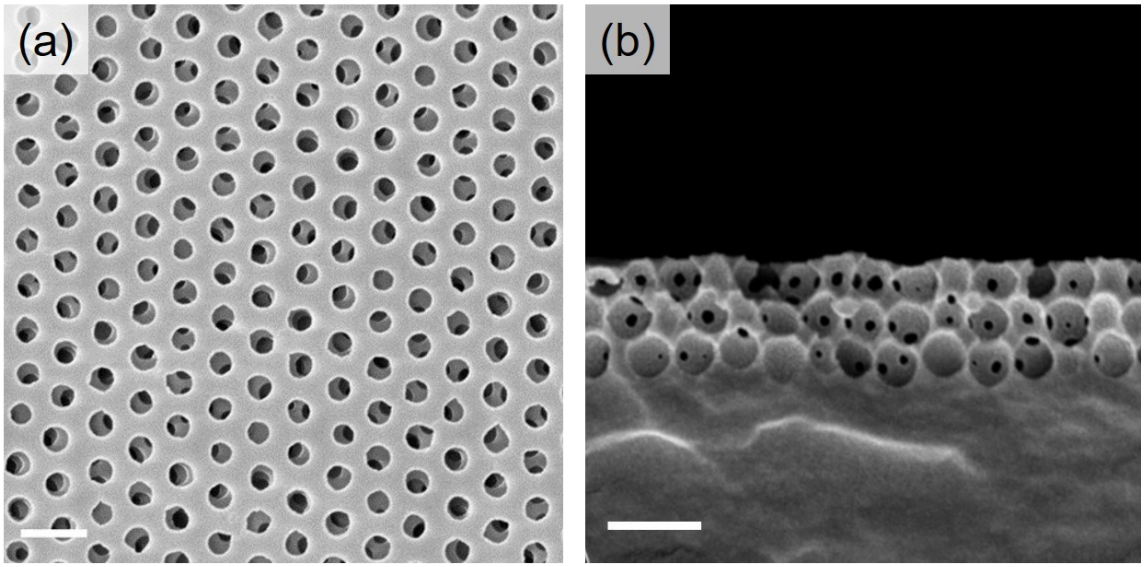

Figure 5.10. SEM images of the surface (a) and of the cross-section (b) of a 3-layers SF-TNSs IO. The scale bars are 500 nm.

The reflectance spectrum of the SF-TNSs IO shows a peak centered at 560 nm, with a maximum refection around 50% (**Figure 5.11**). Compared to a 3-layers SIO, the peak resulted blue-shift of about 10 nm, while the reflectance is comparable. The differences between the two spectra are imputable to a higher contraction of the SF-TNSs, with respect to SF, along the [111] direction during the dissolution of the template in toluene and the draying process due to the presence of the TNSs inside the SF matrix.

This effect was particularly evident during the development of the protocol in the case of the formulations with 50% and 80% of TNSs. The increase of the TNSs concentration caused not only a contraction of the structure, but also even the formation of cracks, compromising the structural integrity of the IOs. For this reason, the concentration of TNSs was set to 20% w/v.

It is interest to underline that the effect of the refractive index increase (due to the presence of the TNSs in the matrix) on the reflection properties of the IOs is negligible compared to the contraction effect.

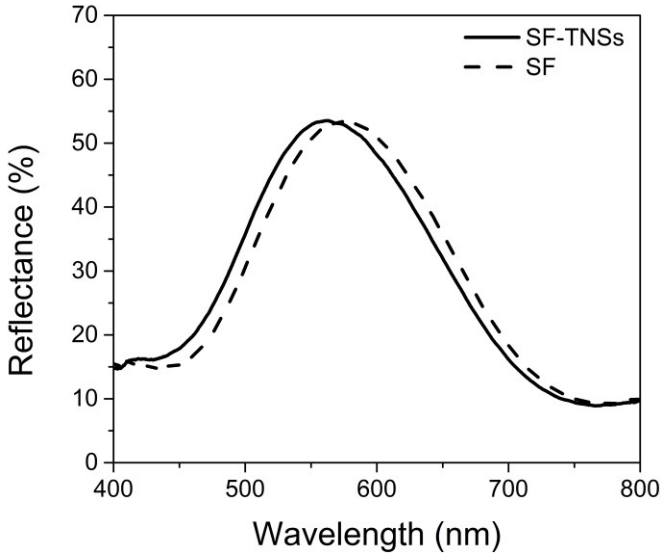

Figure 5.11. Reflectance spectra of the SF-TNSs inverse opal compared to the spectrum of a simple SIO fabrictaed by replica of a 3-layers opal template.

It was also evaluated the effect of treatments used to crystallize the SF on the optical properties of the IOs. **Figure 5.12** shows the reflectance spectra of the SF-TNSs IO after the methanol treatment and the water annealing, compared with the spectrum of an IO as prepared. Both the spectra present a significant blue shift of the reflection peak, of 20 nm in the case of methanol annealing and of about 100 nm for the water vapor treated structure. This effect can be explained considering a contraction of the structure with a consequent modification of the lattice constants of the crystal.

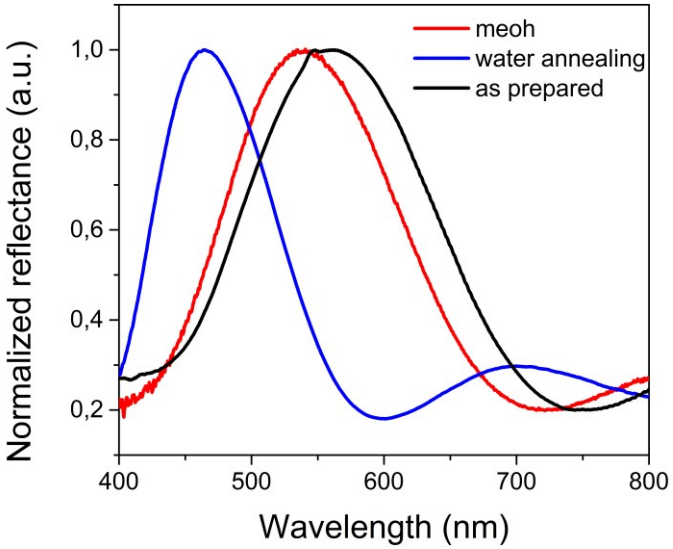

Figure 5.12. Normalized reflectance spectra of a SF-TNSs IO as prepared (black), methanol treated (red) and water annealed (blue).

From SEM images of the surface it was calculated a distance center-to-center of pores of about 285 nm after the methanol annealing and 260 nm after the water treatment (**Figure 5.13**). As already demonstrated in the case of the SIOs,[33] the water molecules can interact with the polar group of the silk fibroin chains inducing a conformational change of the secondary structure of the protein.[47] This process causes a change of the free volume of the polymer matrix and thus a compression of the lattice along the [111] direction. In addition, in the case of the SF-TNSs, the long treatment induced also a lateral shrinkage of the lattice as deductible from the calculated distance of the centers of the air cavities. Considering the hygroscopic behavior of the TNSs and the long times of the treatment, it has not to exclude a swelling during the annealing, with the introduction of residual stresses in the material.

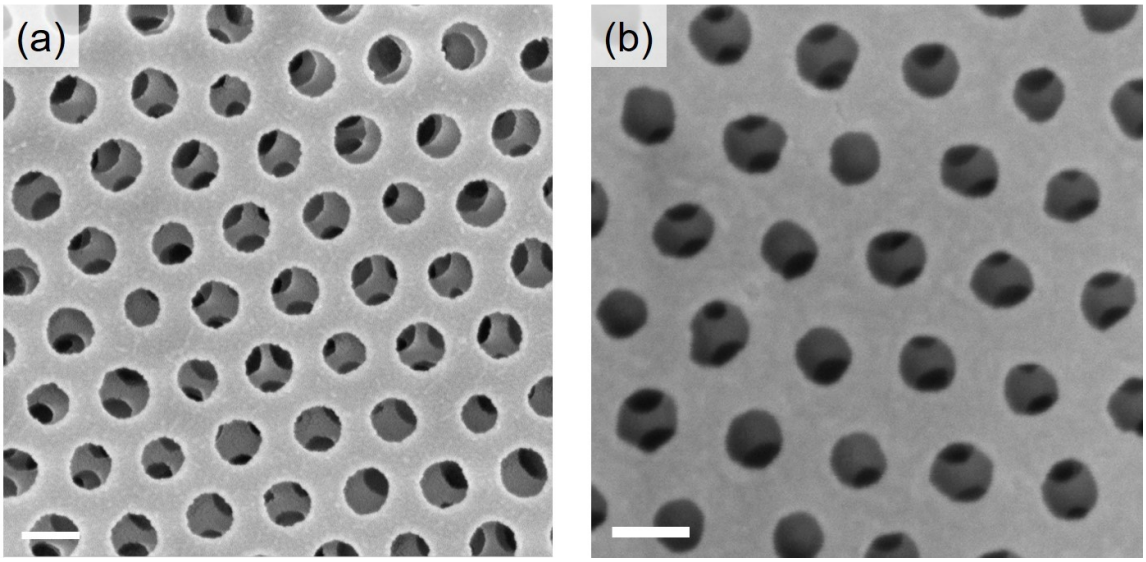

Figure 5.13. SEM images of the surface of SF-TNSs IOs after methanol annealing (a) and water annealing (b). The scale bars are 200 nm.

A same mechanism is ascribable for the methanol annealing. Methanol presents the same ability of the water to infiltrate the silk matrix and induce a reconfiguration of the protein chains through rearrangement of the inter/intramolecular hydrogen bonds.[53] Compare to other solvent (such as isopropanol, ethanol), the size of the methanol molecules is small enough to match the free volume of the silk and easily insinuate itself into the matrix.[54] In **Figure 5.14** the FTIR spectra of the SF-TNSs IOs after the treatments are reported. In the case of the methanol treated (MeOH), it is clearly visible from the absorbance of the Amide I the transition to the silk II structure, which presents a peak centered at 1626 cm^{-1} corresponded to the β-sheets.[47] In the case of the water annealing (WA) the transition to the insoluble form is not so clear and the structure still presents a strong absorbance related with the random coil conformation. We supposed that the presence of the TNSs inside the matrix influences the mechanism of crystallization, probably modifying the time necessary to obtain a complete transition to the silk II morphism. Further experiments would be necessary to better understand the effect of this treatment on the complex TNSs matrix.

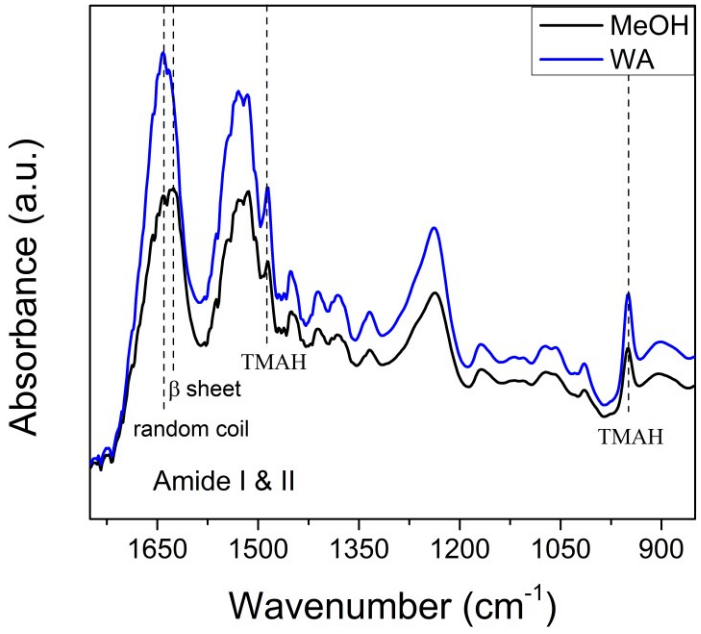

Figure 5.14. FTIR spectra of the SF-TNSs IOs after methanol annealing (MeOH,black) and water annealing (WA,blue).

It was also investigated the effect of both treatments on the refractive index of the material through ellipsometry spectroscopy (see *Appendix A3.11*). The measurements were effectuated on thin films deposited by spin coating on silicon substrate with the same formulation used for the IOs and treated following the same protocol. The values of the refractive index obtained from the best fitting of the experimental data are reported in **Table 5.2**.

Table 5.2. Complex refractive index of SF-TNSs samples as prepared, after MeOH ans WA. The values are obtained from the best fitting of the experimental data measured trough ellipsometry on thin films deposited on silicon substrates.

Sample	n @500nm	Thickness (nm)
As prep	1.562	185
MeOH	1.640	70
WA	1.574	175

Methanol annealing induced an increase of the refractive index which can be explained considering the effect on both the silk and the TNSs. In fact, compared to thermal annealing, methanol induces a dehydration and densification of the TNSs structure with a consequent increase of the refractive index. In the case of the WA, the increase of n is lower and can be probably correlated only with the crystallization of the silk. In the same table we also reported the thickness of the samples. As expected, both the treatments induce a decrease of the thickness related with the densification of the structure. The values are only indicative of the possible mechanism occurring because the conditions in the case of the thin films are different compared to the IO structures.

Considering the contraction of the films observed and the increase of fragility induced by the treatments, both the strategies investigated to make insoluble the material resulted not achievable if we want to preserve the flexibility of the IOs.

Finally, it was investigated the possibility to tune the position of the reflectance peak by irradiating the samples with a UV light. As already reported,[33] it is possible to tune the reflection of the SIOs along all the visible range by changing the time of radiation. This effect can be obtained by using a very low radiation dose and an exposition time in the order of the hours.

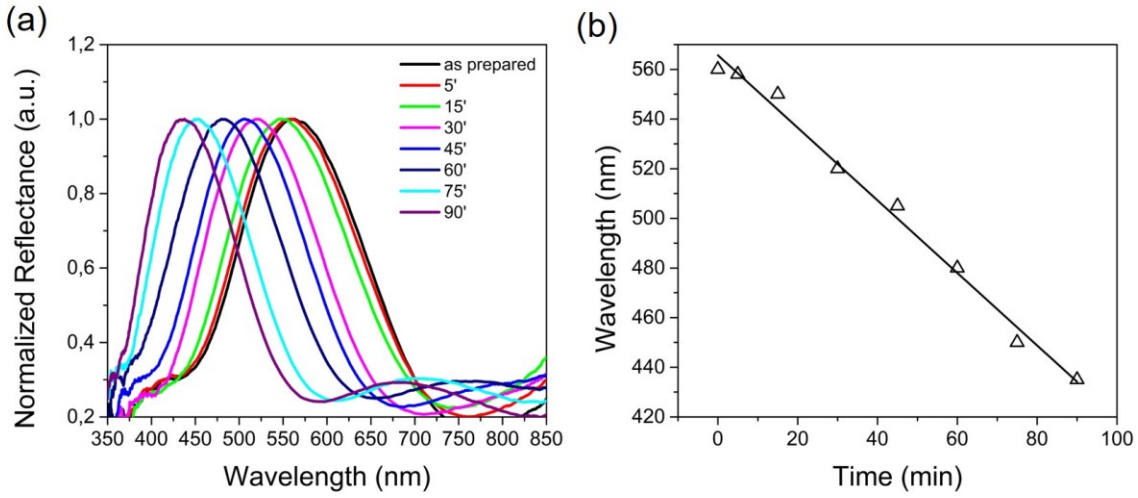

Figure 5.15. (a) Reflectance spectra collected from UV-irradiated SF-TNSs IOs. The reflectance peak is gradually blueshifted with the increase of irradiation time. (b) Time dependence of the stop-band position shift under UV irradiation.

In **Figure 5.15**(a), the normalized reflectance spectra for a SF-TNSs IO as a function of the irradiation time is reported. As already observed for the SIOs, the central wavelength of the stop-band decreases linearly with the irradiation time (see **Figure 5.15**(b)). In the case of the SF-TNSs, the blue-shift of the peak is obtained in the order of minutes using the same conditions reported for the SIOs.

To further investigate the mechanism of the UV curing, FTIR analysis was conducted on samples treated with different times of UV light. As visible in **Figure 5.16**, the UV irradiation causes a slight decrease of absorption peaks in the FTIR spectrum and does not induce a transition to silk II form, because typical bands of the β-sheet form in the amide bands did not appear. This is consistent with the results previously reported, which explain the effects of UV light as a weakening and/or breaking of the peptide bond in polypeptides.[55]

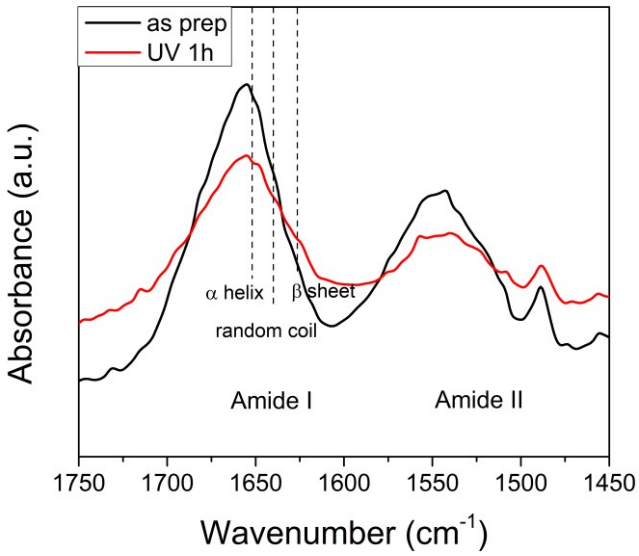

Figure 5.16. FTIR spectra of a SF-TNSs IOs before and after UV irradiation for 1h.

Compared to the results obtained by Y. Wang for the SIOs,[33] in this case the time necessary to tune the reflection of the photonic structure is significantly decreased. This is due to the presence of the TNSs, which present a photocatalytic behavior. As previously explained, the UV light is able to cure the TNSs inducing a densification of the structure and an increase of the refractive index. To evaluate this effect on the material, ellipsometry measurements were performed on thin films deposited on silicon substrates by spin coating, fabricated using the same formulation used for the SF-TNSs IOs and irradiated by UV light in the same conditions. As reported in **Table 5.3**, the UV radiation affects both the refractive index and the thickness of the material. Based on these results, we believe that the effect of the contraction of the structure on the optical properties of the IOs is more consistent compared to the increase of the refractive index.

Table 5.3. Refractive index and thickness of SF-TNSs films deposited on silicon substrates irradiated with UV light in the same conditions used for the SF-IOs.

Time of irradiation (min)	n @500 nm	Thickness (nm)
0	1.60	388
15	1.60	345
30	1.61	340
60	1.62	330

In addition, as demonstrated for the simple SIOs, the absorption of the UV irradiation light is more likely to happen in the layers closer to the irradiation source, inducing an increase of the surface roughness and changes in the morphology. This effect was confirmed by SEM images of the surface. As shown in **Figure 5.17** after 90min of irradiation, the shape of the voids significantly changes. Visible cracks were observed on the surface, not reported in the case of the SIOs.[33] Our hypothesis is that the presence of the TNSs in the matrix does not permit the relaxation of the residual stresses derived by the dehydration and the conformational changes, causing the formation of the cracks.

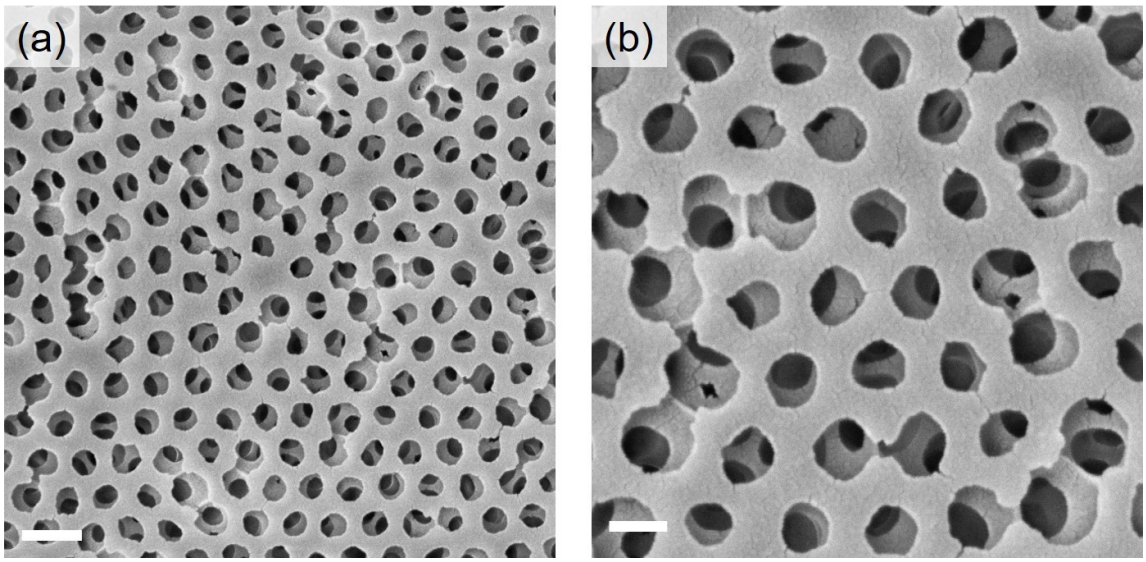

Figure 5.17. SEM images of the surface of SF-TNSs IOs after UV irradiation at 254nm for 90 min. The scale barse are 400nm (a) and 200nm (b).

Taking in account the results and all the critical issues presented, we can affirm that the introduction of the TNSs in the silk matrix does not represent a good strategy to obtain the RI contrast necessary to improve the optical properties of the silk-based IOs and guarantee the condition for a PBG. A different strategy to modify the refractive index could be the synthesis of a hybrid organic-inorganic silk-based sol-gel material or a chemical modification of the silk fibroin chains.[56,57] Another critical aspect to consider is the fragility of the material induced by the prolonged treatments (especially in the case of long time of UV irradiation). All these aspects would be considered in further studies to improve the quality of these structures. Nevertheless, the specific properties of the TNSs (ion exchange ability, structure modification) could be investigated for the post-fabrication functionalization of the opaline structures.

5.5. Silk-AuNRs inverse opals

Metallic nanoparticles combined with photonic crystals are promising structure as optical antenna for sensing application, or substrate for surface enhanced Raman scattering (SERS).[58–62] The localized surface plasmon resonance (LSPR) arising from noble metal nanoparticles enhances the absorption and emission of light, while a photonic crystal (PC) allows the control of light emission, flow and absorption and is also an efficient optical antenna. Here we report the first results concerning the fabrication and characterization of silk-based IOs incorporating AuNRs, with potential application as optical antenna for sensing or platform for laser-mediated heating applications.[27,30,59]

5.5.1. Fabrication

The Silk/AuNRs IOs (SANRIOs) were fabricated using the two-steps method presented in *Section 5.2*, by infiltration and replica of a multilayers PS opal template. Two different sizes of PS spheres with a diameter of 300 nm and 400 nm were used to assembly the opal template. The diameters were selected to have the stop-band respectively in the visible and in the NIR region.

The opal template was infiltrated with a Silk-AuNRs solution, with a nominal concentration of AuNRs equal to 0.05 wt%, using an adequate volume in order to have a final thickness of the film equal to 40 μm (as measured by SEM images). Compared to the Silk-TNSs opals, no problems related with fast gelation of the solution during the infiltration of the air voids were observed. For further details concerning the AuNRs synthesis and the SF-AuNRs composite solution, the reader can refer to the protocol reported in *Chapter 2* and *Appendix A1.3 and A1.5*.

As first step, the fabrication process was optimized to maximize the reflection of the opal at least of 60% with the minimum number of layers. The study was conducted using as proof of concept one size of beads (300 nm). Opal with 3, 5 and 7 layers were fabricated and characterized structurally and optically by SEM images and reflection measurements.

5.5.2. Structural and optical characterizations

Figure 5.18 shows the nanostructures of SANRIOs obtained from multilayer colloidal crystals composed of PS spheres with a diameter of 300 nm. As visible from the SEM cross-section images, the inverse structure presents the characteristics close-packed face-centered cubic lattice. A good arrangement along the [111] direction is obtained both for the 3 and 7-layers crystals. The SEM images of the surface show the highly ordered hexagonal array of air cavities with a distance center-to-center of about 300 nm. The crystalline quality obtained confirms the possibility to fabricate inverse opals made of the nanocomposite matrix with good optical quality.

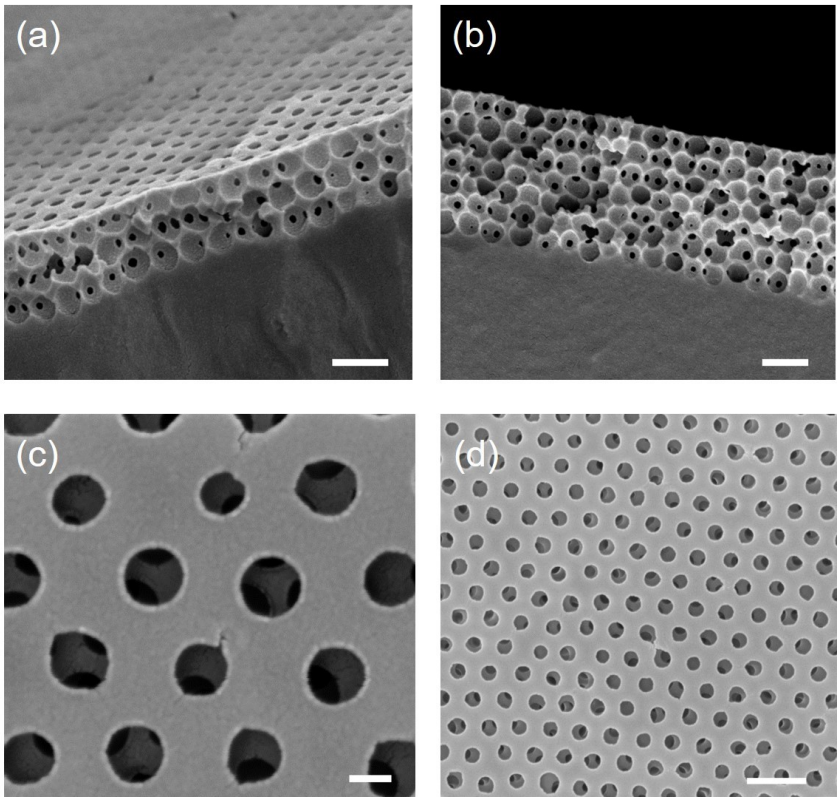

Figure 5.18. Cross-section SEM images of a 3-layers (a) and 7-layers (b) SANRIO templated from the colloidal crystals composed of PS spheres with diameter of 300nm (scale bars = 500 nm). (c) and (d) Surface SEM images of a 7-layers SANRIO at different magnifications. The scale bars are respectivetly 100 nm and 500 nm.

The opal presents a characteristic green color derived from the interaction of the light with the periodic nanostructure when observed from a normal direction to the surface, that blue shifts with the increase of angle of observation (**Figure 5.19**). In addition, the free-standing films preserved the mechanical properties typical of the silk with a good flexibility. The 7-layers SANRIO presents a very high mirror-like reflectivity, as it possible to observe in Figure 5.16(d).

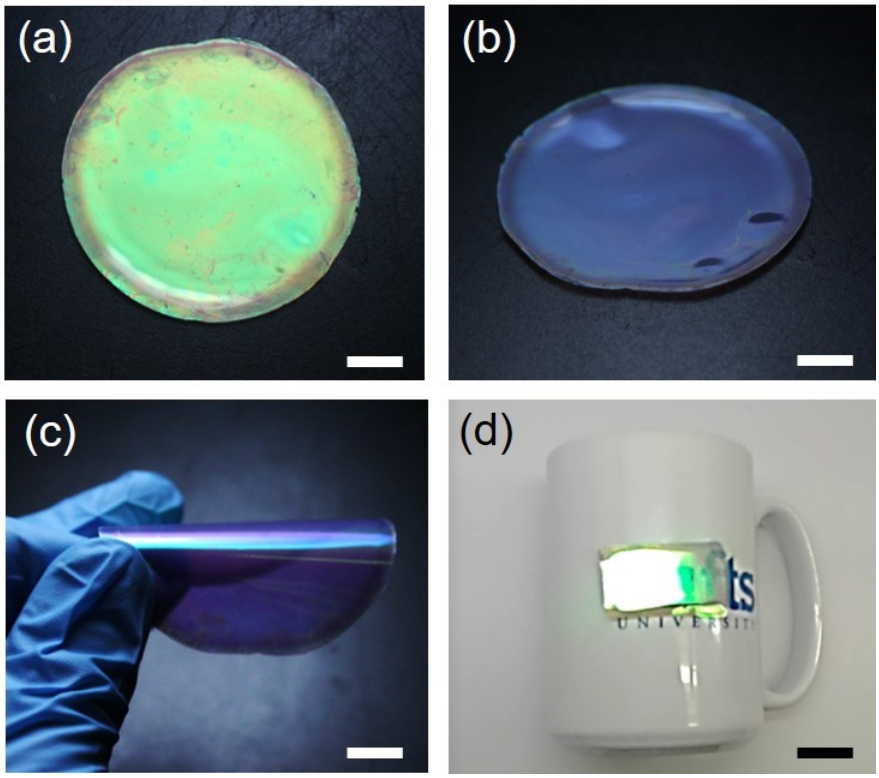

Figure 5.19. Photographs of a 7-layers obtained SF-AuNRs IO films (300nm PS spheres) under diffuse light at different angles of view (a) θ= 90°, (b) at θ= 45°.(c) A 50 µm thick bent IO film (300nm PS spheres) showing the flexible nature. (d) Photograph of a 7-layers IO showing the high reflectivity of the sample when exposed to a direct light source.

As previously explained, the maximum reflectance of the photonic structures is dependent by the number of layers and the refractive index contrast. The refractive index of the Silk-AuNRs composite at 633 nm is 1.54 (confirmed by measurements effectuated with Metricon on free standing films), the same value of the silk fibroin[63] To increase the reflectivity of the inverse opals it is possible to act on the number of layers. In **Figure 5.20** the reflectance spectra of SANRIOs made with a different

number of layers are reported. It is interest to underline that with only 7-layers it was possible to obtain a reflectivity of up to 65%.

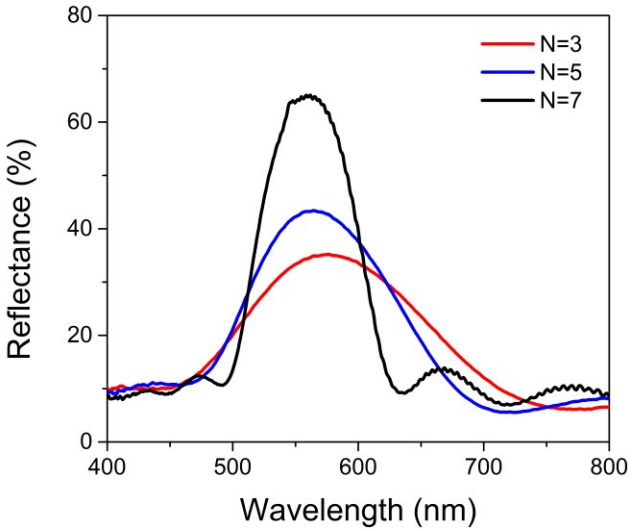

Figure 5.20. Reflectance spectra of SANRIOs with different number of layers.

As anticipated in the introduction of the chapter, the structural color properties of the opals and inverse opals are related to refraction and reflection phenomena that occurs when the incident light interact with the periodic nanostructures. The consequence of these interactions is the presence of a reflection peak in the visible spectrum. According to the Bragg-Snell theory, the wavelength position of the reflection peak depends on the refractive index, lattice constant and angle of incident light.[7]

In the case of the inverse structures, the lattice constant is related with the diameter of the air voids. In **Figure 5.21** it is possible to see the reflectance spectra of SANRIOs obtained using 300 nm and 400 nm PS opal crystals. The wavelength position of the reflection peaks is respectively 560 nm and 750 nm, corresponding to a green and violet color (as visible in the inset).

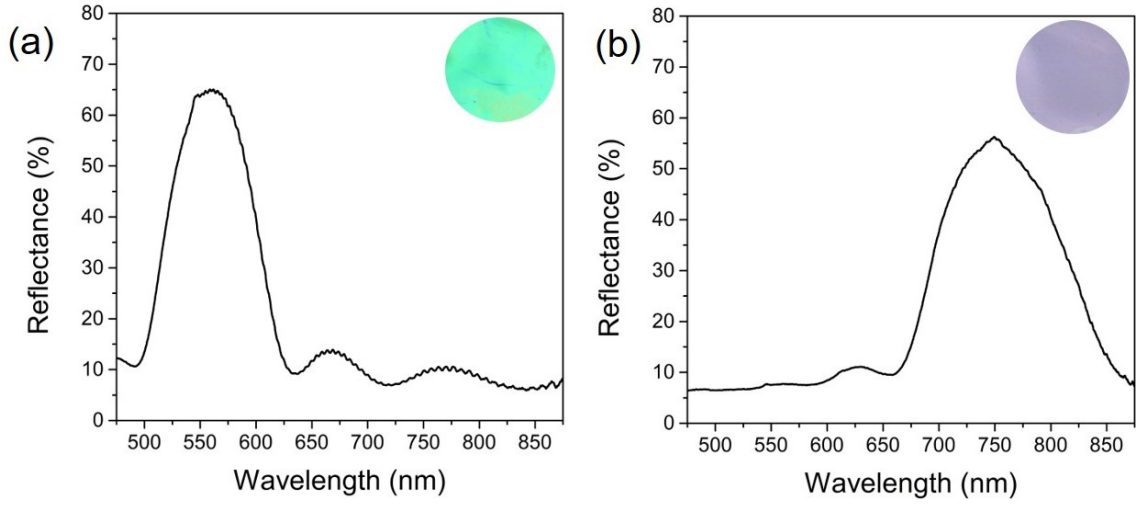

Figure 5.21. Normal reflectance spectra of a SF-AuNRs IO obtained from a 7-layers colloidal crystal formed by 300 nm (a) and 400 nm (b) PS spheres. The inset shows the color of the samples collected in the direction perpendicular to the films.

The second property that determines the position of the reflection peak, according to the Bragg law, is the angle of diffraction. The property of viewing angle dependence is at the origin of an interesting phenomenon typical in photonic nanostructured materials, which means that different structural colors will be observed when viewing at different orientations.[64] This intrinsic characteristic is disadvantageous for the construction of versatile colorimetric sensors and it has to take into account during the characterization of the sensing response.

Even in the case of the as fabricated SANRIOs we observed the angle dependence phenomenon, as shown in **Figure 5.22**. The images were taken with a camera (Canon EOS T3 rebel) in the same condition of light from two different angles of observation, as schematized in the figure.

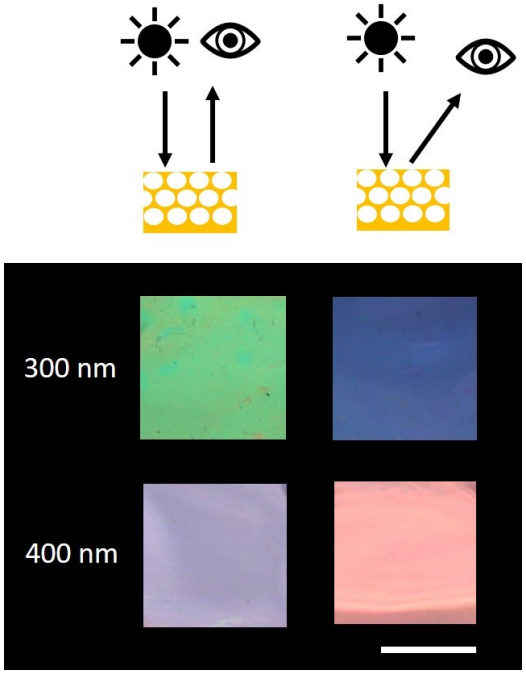

Figure 5.22. Photographs of the IOs at different viewing angles. The color is blue shift gradually with the increase of viewing angle, from green to blue for 300nm opal and from violet to red for 400 nm opal. The scale bar is 1 cm.

The angle-dependent behavior was further characterized by attenuation spectroscopy measurements (see *Appendix A3.15*).[62] As shown in **Figure 5.23**, the reflection peak of the inverse opals blue-shifts from 560 nm to 520 nm with the increase of the angle from 0° to 15° (respect to the normal), while the peak of the AuNRs plasmon centered at 775 nm (see *Chapter 2*) is independent from the angle. In the case of the IOs with the reflection peak centered at 750 nm, the Au NRs LSPR peak is not distinguishable because it overlaps with the pseudo-photonic band-gap of the inverse opal nanostructures.

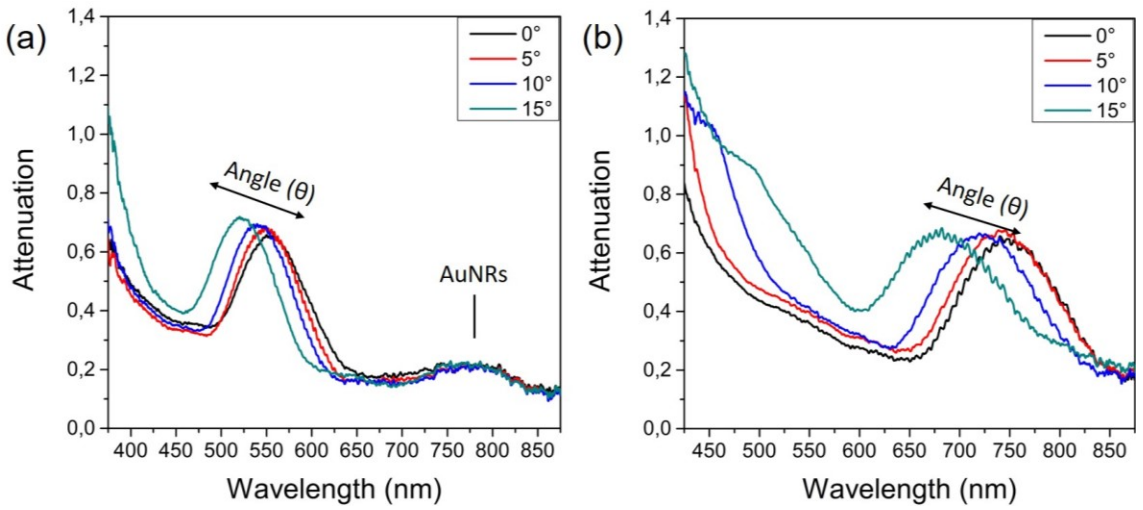

Figure 5.23. Attenuation spectra of Silk-AuNRs inverse opals made with 300nm (a) and 400nm PS sphere. SANRIOs combine the angle-depentent Bragg peak of inverse opals with the angle-indipendent longitudinal LSPR absoprtion peak of the gold nanorods.

Finally, we also evaluated the effect of the refractive index. As already reported for other IOs structures, and even for the SIOs,[33] the infiltration of the air voids with liquids induce a tuning of the stop band. To demonstrate this, we considered an as prepared SARNIO and exposing it to acetone vapor (n ~1.36). The experiment was conducted using the same set-up reported in *Chapter 4* for the humidity test, by using a bubbler system to generate the acetone vapor (see *Appendix A3.16*).

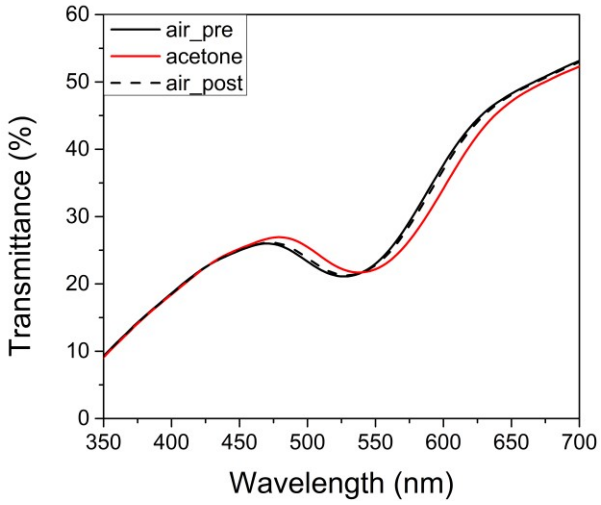

Figure 5.24. Transmittance spectra of SARNIO in air (black), acetone vapor (red) and in air after the exposition to the vapor (dot line).

As shown in **Figure 5.24**, the increase of refractive index inside the voids induced a red-shift of the peak. Compared to the results obtained by Kim and Wang,[27,33] the shift is only about 15 nm. This can be explained considering the low concentration of acetone in the saturated vapor atmosphere. Taking into account the reversible behavior and the low concentration detected, this preliminary result suggests the potentiality of this nanostructure as platform for sensing in gas/vapor phase.

5.5.3. Laser-heating experiments

The inclusion of gold nanorods was exploited to induce localized heating, thanks to the excitation of the nanoparticles LSPR, an effect that can be potentially used for photodynamic therapy application in medicine. As extensively explained in *Chapter 2*, the gold nanorods were selected because of the presence of a LSPR in the NIR region, the so-called "biological window". As already demonstrated, a gold nanoparticle photonic crystal would allow enhancement of the absorption, thereby reducing the amount of laser radiation needed to induce localized temperature

increases.[27] At the same time, the combination of the photonic properties of the opal with the plasmonic properties of the gold can open possibility for the realization of sensing devices.

To evaluate this potentiality, laser-heating experiments were conducted on both the two SANRIOs structure, the green one (Λ=300 nm) and the violet (Λ=400 nm). The experiments were effectuated by exciting the longitudinal LSPR peak of the AuNRs with 808 nm laser diode source. The increase of temperature was registered with a thermo-camera after 5 minutes of irradiation to permit the equilibrium (see *Appendix A3.17*).

Figure 5.25 shows the thermo-images collected from the two SANRIOs samples for different irradiance showing the temperature distribution obtained on the samples.

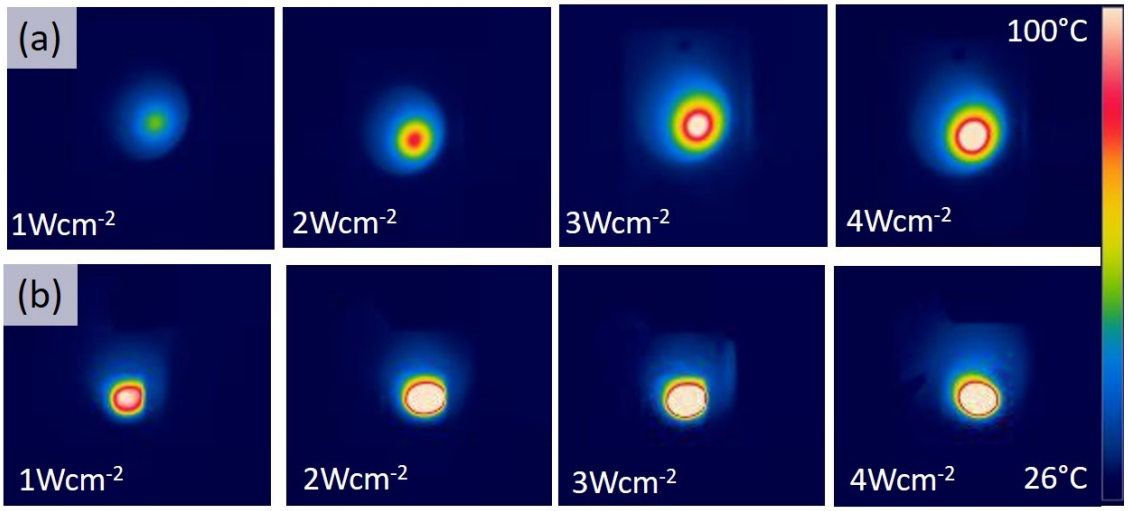

Figure 5.25. Thermo-images of the SANRIOs films, green (a) and violet (b), irradiated at different laser intensities.

The maximum temperature reached for different irradiance is plotted in **Figure 5.26**. As expected, the maximum increase of temperature in the case of the violet IO is higher compared to the green one, for the same SF-AuNRs composition. It is interest to note that the relation between T and I is linear below 100° C, while above this temperature there is a change of slope, as already observed and explained in the case of the simple films (see *Chapter 2*).

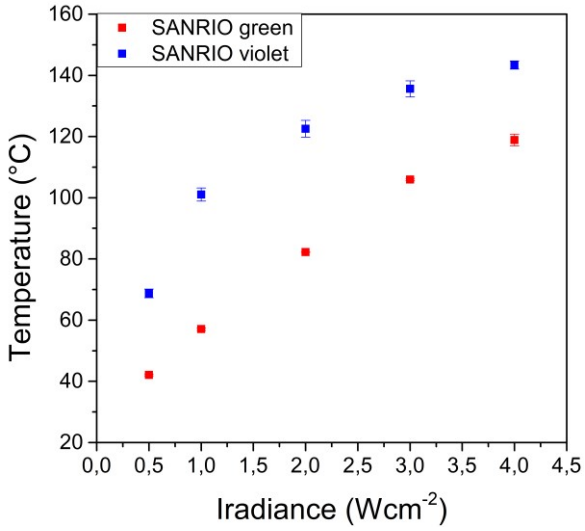

Figure 5.26. Temperature increase as a function of the laser intensity measured for the green and violet IOs.

In a second experiment, we evaluated the possibility to use the green IO as both passive and active device, by locally heating the area through light absorption and controlling the real temperature by checking the reflection band. The experiment was conducted using the IR laser source to excite the AuNRs LSPR and an optical fiber coupled to a portable spectrophotometer to measure the tuning of the reflection peak illuminated by a white source (further details are in *Appendix A3.17*).

When irradiated with the laser, the reflection peak of the IO blue-shifts, as reported in **Figure 5.27**, even if it is not linear. The same behavior was found for a different number of measurements (5) in the same conditions and on different samples (3), while it was observed a reduction of the shift after repeated measurements on the same sample.

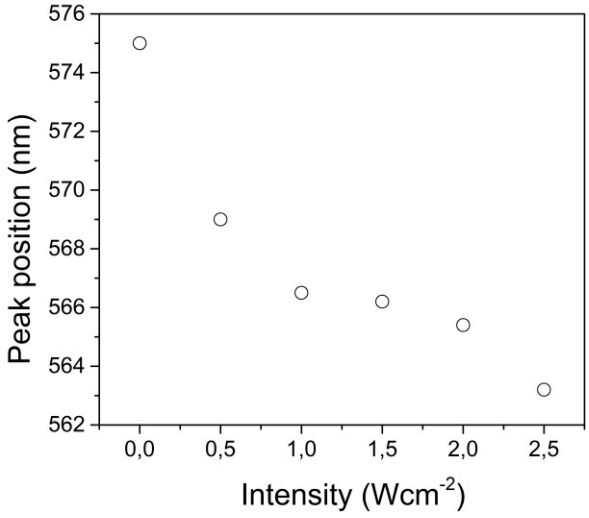

Figure 5.27. Position of the reflection peak of the SANRIO film as a fucntion of the laser intensity.

To better understand this behavior and verify the reproducibility and stability, we performed progressive experiments on the same sample following the scheme reported in **Figure 5.28**(a). The results are summarized in **Figure 5.28**(b). A consistent blue-shift of the peak wavelength was observed, but the IO presented a hysteresis behavior with the increase of the irradiation intensity and a reduction of the sensitivity after repeated cycles of irradiation. We tried to explain the observed blue shift by considering the thermal expansion behavior of the silk fibroin. As reported in literature, amorphous silk films have a negative thermal expansion coefficient before reaching their glass-transition temperature,[65] thereby shrinking their volume. This could explain the blue shift observed for the pPBG with the increase of temperature. The hysteresis phenomenon could be related with the amorphous state of the silk and the water present in the films. It is also to take in consideration possible mechanical variations of the film when irradiated that induce a change of the diffracted angle measured by the spectrophotometer.

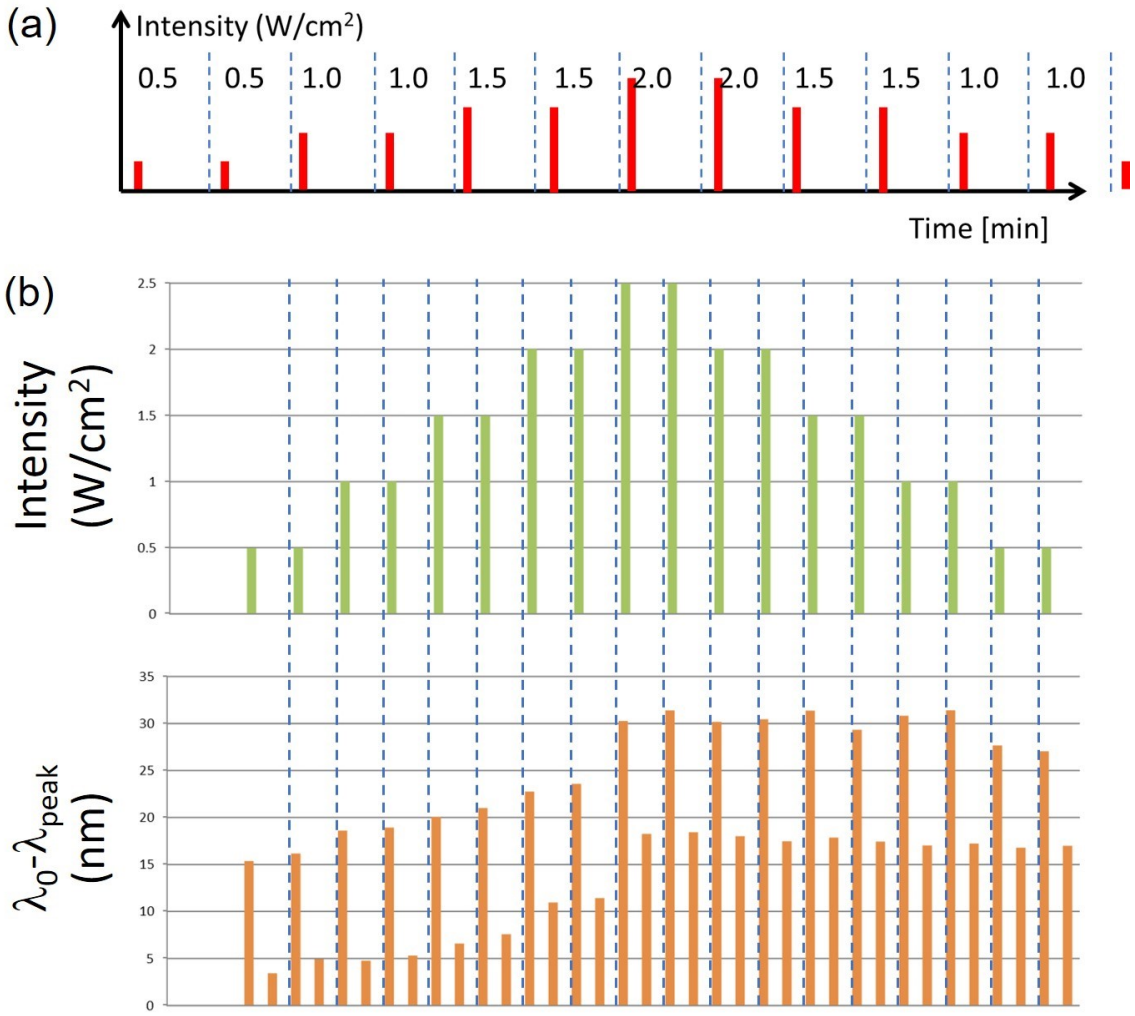

Figure 5.28. Schematic of the progressive experiments conducted on a SANRIO film to verify the consistent of the results and the stability of the response.

A further experiment was then conducted to investigate a real scenario by measuring the reflection of the IO film under a slice of ham, to simulate the absorbance and scattering of a real tissue, as schematized in **Figure 5.29** In this set-up the free-standing film resulted completely blocked between two microscope coverslip slides and possible mechanical contraction/dilatation of the film were avoided.

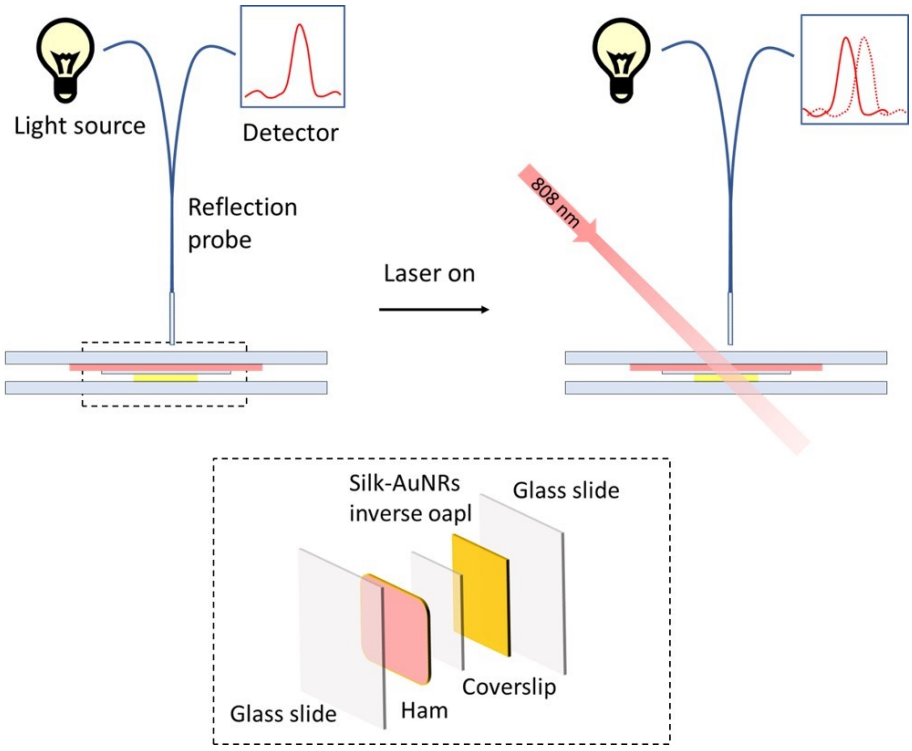

Figure 5.29. Schematic of the set-up used for the measurements "under tissue".

Thanks to the high reflectivity of the IOs, it was possible to measure a reflection peak even through a tissue (thickness 0.5 mm). Compared to the measurements obtained in air, the shift of the peak was difficult to be detected (lesser than 1 nm) and the maximum T reached was lower because of the absorption of the ham and the presence of the glass slides (**Figure 5.30**).

Further experiments are necessary to understand better the real mechanism and the potentiality of the IOs structure for this application, considering even the swelling behavior of the matrix in different humidity condition. Increasing the number of layers of the IOs and combining the SF matrix with another biopolymer, which presents a higher thermal coefficient, could represent two strategies to improve the properties of this structure.

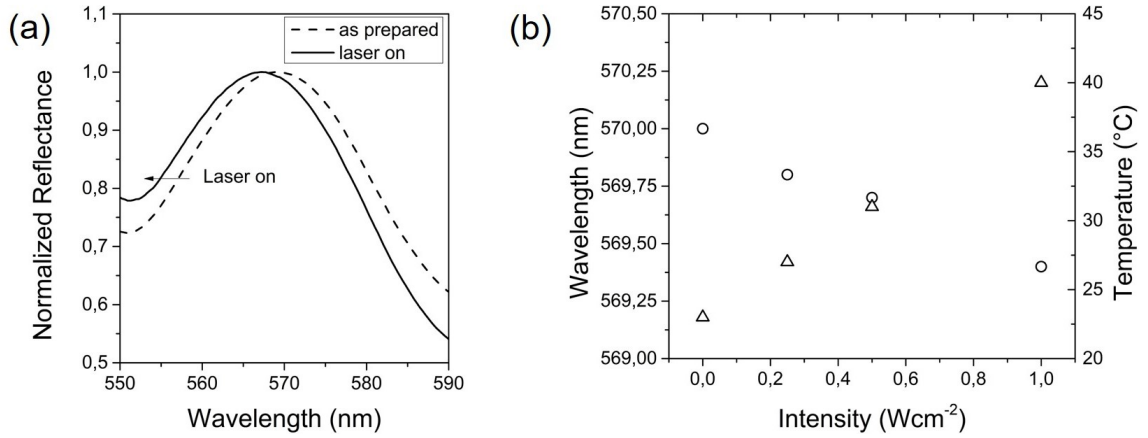

Figure 5.30. (a) Normalized reflectance spectrum of the SARNIO under ham before and after irradiation with the laser. (b) Wavelength position of the peak and increase of temperature as a function of the laser intensity measured in the condition schematized in **Figure 5.29**.

5.6. Conclusions

In this chapter a fabrication method to realize large area silk-based IOs was presented. The method is suitable for the fabrication of complex heterostructure and for the introduction of extrinsic optical defect inside the structure, as demonstrated in Section 5.3. The possibility to easy tune the optical properties by acting on the number of layers, the size of template beads and the refractive index was shown. In addition, it was demonstrated the possibility to fabricate IOs structure with silk-based nanocomposite materials.

The introduction of TNSs inside the SF matrix was explored as a strategy to increase the refractive index contrast and improve the optical properties of the SIOs. Unfortunately, the low concentration of particles achievable did not permit a real enhancement of the pPBG. The post-treatment investigated allowed to tune the reflection of the opal but at the same time affected the structural integrity and the flexibility of the freestanding. Nevertheless, the TNSs show interesting properties that can be explored for introducing new functionality in the IOs by using a different

fabrication approach to reduce the observed critical issues (for example, it is possible to realize a supported IO instead of a freestanding film).

For what concerns the AuNRs IOs, we obtained promising results in terms of fabrication, reflectivity and flexibility. Further experiments are necessary to determine the maximum concentration of AuNRs achievable and characterize the particles distribution inside the photonic lattice. Regarding the functional application of the SARNIO as platform for photodynamic therapy application and temperature-sensing probe, there are many unsolved questions about the mechanism of response and the applicability in a real scenario. Despite the criticisms observed, the combination of the porous structure with the photonic and plasmonic properties of the SARNIOs, considering the flexibility, biocompatibility and biodegradability of silk, open interesting opportunities for the generation of gas sensing optical platform or even SERS substrates.[66,67]

References

[1] E. Yablonovitch, Inhibited Spontaneous Emission in Solid State Physics and Electronics. *Phys. Rev. Lett.* **1987**, *58*, 2059.

[2] S. John, Strong Localization in Photons in Certain Disordered Dielectric Superlattices. *Phys. Rev. Lett.* **1987**, 2488–2489.

[3] G. I. N. Waterhouse, M. R. Waterland, *Polyhedron* **2007**, *26*, 356.

[4] R. C. Schroden, M. Al-Daous, C. F. Blanford, A. Stein, *Chem. Mater.* **2002**, *14*, 3305.

[5] V. L. Colvin, *MRS Bull.* **2001**, *26*, 637.

[6] G. von Freymann, V. Kitaev, B. V. Lotsch, G. A. Ozin, P. Spahn, T. Ruhl, G. A. Ozin, E. Vekris, I. Manners, S. Aitchison, D. Perovic, G. A. Ozin, H. M. van Driel, *Chem. Soc. Rev.* **2013**, *42*, 2528.

[7] C. I. Aguirre, E. Reguera, A. Stein, *Adv. Funct. Mater.* **2010**, *20*, 2565.

[8] C. Bourdillon, S. Gam Derouich, W. Daney De Marcillac, L. Coolen, A. Maître, C. Mangeney, C. Schwob, *Proc. SPIE - Int. Soc. Opt. Eng.* **2016**, *9756*, 1.

[9] H. Fudouzi, *Sci. Technol. Adv. Mater.* **2011**, *12*, 64704.

[10] M. Curti, J. Schneider, D. W. Bahnemann, C. B. Mendive, *J. Phys. Chem. Lett.* **2015**, *6*, 3903.

[11] D. P. Puzzo, A. C. Arsenault, I. Manners, G. A. Ozin, *Angew. Chemie* **2009**, *121*, 961.

[12] F. Jin, L.-T. Shi, M.-L. Zheng, X.-Z. Dong, S. Chen, Z.-S. Zhao, X.-M. Duan, *J. Phys. Chem. C* **2013**, *117*, 9463.

[13] D. M. Lebrun, **2014**, 83.

[14] D. J. Norris, E. G. Arlinghaus, L. Meng, R. Heiny, L. E. Scriven, *Adv. Mater.* **2004**, *16*, 1393.

[15] F. Fleischhaker, A. C. Arsenault, J. Schmidtke, R. Zentel, G. A. Ozin, *Chem. Mater.* **2006**, *18*, 5640.

[16] S. Reculusa, S. Ravaine, *Chem. Mater.* **2003**, *15*, 598.

[17] Z. Zhou, X. S. Zhao, *Langmuir* **2005**, *21*, 4717.

[18] E. Armstrong, W. Khunsin, M. Osiak, M. Bl??mker, C. M. S. Torres, C. O'Dwyer, *Small* **2014**, *10*, 1895.

[19] B. A. Grzybowski, C. E. Wilmer, J. Kim, K. P. Browne, K. J. M. Bishop, *Soft Matter* **2009**, *5*, 1110.

[20] K. S. Napolskii, N. A. Sapoletova, D. F. Gorozhankin, A. A. Eliseev, D. Y. Chernyshov, D. V. Byelov, N. A. Grigoryeva, A. A. Mistonov, W. G. Bouwman, K. O. Kvashnina, A. V. Lukashin, A. A. Snigirev, A. V. Vassilieva, S. V. Grigoriev, A. V. Petukhov, *Langmuir* **2010**, *26*, 2346.

[21] J. Ge, Y. Yin, *Angew. Chemie - Int. Ed.* **2011**, *50*, 1492.

[22] S. A. Rinne, F. García-Santamaría, P. V. Braun, *Nat. Photonics* **2008**, *2*, 52.

[23] K. Vahala, *Nature* **2004**, *424*, 839.

[24] A. Arsenault, F. Fleischhaker, G. von Freymann, V. Kitaev, H. Miguez, A. Mihi, N. Tétreault, E. Vekris, I. Manners, S. Aitchison, D. Perovic, G. A. Ozin, *Adv. Mater.* **2006**, *18*, 2779.

[25] S. Ahn, L. F. Deravi, S. J. Park, B. E. Dabiri, J. S. Kim, K. K. Parker, K. Shin, *Adv. Mater.* **2015**, *27*, 2838.

[26] B. Marelli, F. G. Omenetto, *J. Mater. Chem. C* **2015**, *3*, 2783.

[27] S. Kim, A. N. Mitropoulos, J. D. Spitzberg, H. Tao, D. L. Kaplan, F. G. Omenetto, *Nat. Photonics* **2012**, *6*, 818.

[28] P. Tseng, S. Zhao, A. Golding, M. B. Applegate, A. N. Mitropoulos, D. L. Kaplan, F. G. Omenetto, *ACS Omega* **2017**, *2*, 470.

[29] Y. Y. Diao, X. Y. Liu, G. W. Toh, L. Shi, J. Zi, *Adv. Funct. Mater.* **2013**, *23*, 5373.

[30] K. A. Burke, M. A. Brenckle, D. L. Kaplan, F. G. Omenetto, *ACS Appl. Mater. Interfaces* **2016**, *8*, 16218.

[31] E. Colusso, G. Perotto, Y. Wang, M. Sturaro, F. Omenetto, A. Martucci, *J. Mater. Chem. C* **2017**, *5*, 3924.

[32] J. MacLeod, F. Rosei, *Nat. Mater.* **2013**, *12*, 98.

[33] Y. Wang, D. Aurelio, W. Li, P. Tseng, Z. Zheng, M. Li, D. L. Kaplan, M. Liscidini, F. G. Omenetto, *Adv. Mater.* **2017**, 1702769.

[34] J. R. Oh, J. H. Moon, S. Yoon, C. R. Park, Y. R. Do, C. M. S. Torres, W. Kim, Y. R. Do, J. Perlich, A. Timmann, S. V. Roth, J. Keckes, G. A. Maier, *J. Mater. Chem.* **2011**, *21*, 14167.

[35] N. Denkov, O. Velev, P. Kralchevski, I. Ivanov, H. Yoshimura, K. Nagayama, *Langmuir* **1992**, *8*, 3183.

[36] R. Pradhan, I. Tarhan, G. Watson, *Phys. Rev. B* **1996**, *54*, 13721.

[37] E. Palacios-Lidón, J. F. Galisteo-López, B. H. Juárez, C. López, *Adv. Mater.* **2004**, *16*, 341.

[38] S. T. Parker, P. Domachuk, J. Amsden, J. Bressner, J. A. Lewis, D. L. Kaplan, F. C. Omenetto, *Adv. Mater.* **2009**, *21*, 2411.

[39] P. N. Hong, P. Bénalloul, Z. Guennouni-Assimi, R. Farha, · C Bourdillon, · M.-C Fauré, · M Goldmann, · W Marcillac, · L Coolen, A. Maître, · C Schwob, *Opt Quant Electron* **2015**, *47*, 55.

[40] J. F. Galisteo-López, F. García-Santamaría, D. Golmayo, B. H. Juárez, C. López, E. Palacios-Lidón, In *Photonics and Nanostructures - Fundamentals and Applications*; 2004; Vol. 2, pp. 117–125.

[41] P. Massé, S. Reculusa, K. Clays, S. Ravaine, *Chem. Phys. Lett.* **2006**, *422*, 251.

[42] M. Müller, R. Zentel, T. Maka, S. G. Romanov, C. M. S. Torres, *Adv. Mater.* **2010**, *12*, 1499.

[43] G. Subramanian, V. N. Manoharan, J. D. Thorne, D. J. Pine, *Adv. Mater.* **1999**, *11*, 1261.

[44] Z. Z. Gu, S. Kubo, W. Qian, Y. Einaga, D. A. Tryk, A. Fujishima, O. Sato, *Langmuir* **2001**, *17*, 6751.

[45] G. Perotto, M. Cittadini, H. Tao, S. Kim, M. Yang, D. L. Kaplan, A. Martucci, F. G. Omenetto, *Adv. Mater.* **2015**, *27*, 6728.

[46] A. Matsumoto, J. Chen, A. L. Collette, U. J. Kim, G. H. Altman, P. Cebe, D. L. Kaplan, *J. Phys. Chem. B* **2006**, *110*, 21630.

[47] X. Hu, K. Shmelev, L. Sun, E.-S. Gil, S.-H. Park, P. Cebe, D. L. Kaplan, *Biomacromolecules* **2011**, *12*, 1686.

[48] J. Shao, J. Zheng, J. Liu, C. M. Carr, *J. Appl. Polym. Sci.* **2005**, *96*, 1999.

[49] A. Antonello, M. Guglielmi, V. Bello, G. Mattei, A. Chiasera, M. Ferrari, A. Martucci, *J. Phys. Chem. C* **2010**, *114*, 18423.

[50] T. Tian, N. Gao, C. Gu, J. Li, H. Wang, Y. Lan, X. Yin, G. Li, *ACS Appl. Mater. Interfaces* **2015**, *7*, 19516.

[51] S. K. Lee, G. R. Yi, J. H. Moon, S. M. Yang, D. J. Pine, *Adv. Mater.* **2006**, *18*, 2111.

[52] H. Fudouzi, Y. Xia, *Adv. Mater.* **2003**, *15*, 892.

[53] M. Tsukada, G. Freddi, P. Monti, A. Bertoluzza, *J. Polym. Sci. B* **1996**, *33*, 1995.

[54] Y. Wang, D. Porter, Z. Shao, *Biomacromolecules* **2013**, *14*, 3936.

[55] A. Sionkowska, A. Planecka, *Polym. Degrad. Stab.* **2011**, *96*, 523.

[56] A. Hou, H. Chen, *Mater. Sci. Eng. B Solid-State Mater. Adv. Technol.* **2010**, *167*, 124.

[57] G. Palermo, L. Barberi, G. Perotto, R. Caputo, L. De Sio, C. Umeton, F. G. Omenetto, *ACS Appl. Mater. Interfaces* **2017**, *9*, 30951.

[58] S. G. Romanov, A. S. Susha, C. M. Sotomayor Torres, Z. Liang, F. Caruso, *J. Appl. Phys.* **2005**, *97*, 1.

[59] X. Zhao, J. Xue, Z. Mu, Y. Huang, M. Lu, Z. Gu, *Biosens. Bioelectron.* **2015**, *72*, 268.

[60] W. Shen, M. Li, B. Wang, J. Liu, Z. Li, L. Jiang, Y. Song, *J. Mater. Chem.* **2012**, *22*, 8127.

[61] V. Morandi, F. Marabelli, V. Amendola, M. Meneghetti, D. Comoretto, *Adv. Funct. Mater.* **2007**, *17*, 2779.

[62] Y. Vasquez, M. Kolle, L. Mishchenko, B. D. Hatton, J. Aizenberg, *ACS Photonics* **2014**, *1*, 53.

[63] G. Perotto, Y. Zhang, D. Naskar, N. Patel, D. L. Kaplan, S. C. Kundu, F. G. Omenetto, *Appl. Phys. Lett.* **2017**, *111*, 103702.

[64] Y. Zhao, Z. Xie, H. Gu, C. Zhu, Z. Gu, *Chem. Soc. Rev.* **2012**, *41*, 3297.

[65] Shigeo Nakamura, J. Magoshi, Y. Magoshi, In *Silk Polymers: Materials Science and Biotechnology*; American Chemical Society: Washington DC, 1994; pp. 211–221.

[66] C. Guo, G. N. Hall, J. B. Addison, J. L. Yarger, *RSC Adv.* **2015**, *5*, 1937.

[67] X. Zhao, J. Xue, Z. Mu, Y. Huang, M. Lu, Z. Gu, *Biosens. Bioelectron.* **2015**, *72*, 268.

Chapter 6.

Conclusion and Future Prospects

The main scope of this doctoral project was to develop silk-based nanocomposites for use in bio-photonic and optical devices. The purpose of this chapter is to summarize the main conclusions of the work and offer a prospect on future research.

In *Chapter 1* an overview on the silk materials and applications was offered. The structural characteristics of this natural polymer were described and correlated with the material properties. A particular section was dedicated to review the already published works on silk-based nanocomposites, with special attention for the materials combining the fibroin matrix with inorganic nanoparticles.

Two different nanocomposites were developed during the doctoral course. The synthesis and the main characterizations of the material properties were presented in *Chapter 2*. The principal nanocomposite studied was obtained by the combination of silk fibroin (SF) with titanate nanosheets (SF-TNSs), according to the synthesis proposed by Perotto at al.[1] The first part of the chapter reported the characterization of the material properties. In particular, the effect of the methanol annealing on the crystalline structure of the material was studied combining different characterizations techniques (CD, FTIR, TEM and XRD analysis). For the first time, the mechanical properties of SF-TNSs coatings were characterized trough nanoindentation tests. The results showed an improvement in the hardness and elastic modulus of the composite compared to SF films, especially in the case of combined post-process treatments.

In the second section, the synthesis of a nanocomposite obtained by introducing gold nanorods (AuNRs) into the silk fibroin (SF) matrix was discussed. The optical and thermal properties of the material were characterized and the effect on the secondary structure of the protein was evaluated. The inclusion of AuNRs was exploited to induce localized heating thanks to the excitation of their LSPR, an effect that can be potentially used in biomedical applications in the treatment of bacterial infections. [2] Specifically, the temperature increase induced by photoheating was characterized as a function of the particle concentration, irradiation time and intensity.

In *Chapter 3*, the ion exchange properties of this novel silk-TNSs nanocomposite were investigated as a strategy for post-synthetic chemical modification of the material. First, a preliminary study on the exchange process was conducted, focusing on the kinetic of the process. Three main ions (Ag+, Cu2+, Eu3+) were selected as representative to evaluate the influence of the valence and ionic radius on the adsorption capacity of the nanocomposite. In addition, the possibility to synthesize in situ metallic plasmonic particles through photoreduction and to introduce fluorescent ion (such as europium) was demonstrated. These promising results suggest the possibility to develop sensing devices based on SF-TNSs, combining plasmonic and fluorescence properties, by a simple controlled exchange process. In addition, the ion exchange properties can be exploited for the fabrication of membranes for water cleaning applications or environmental sensing of ions.

Realization of a simple optical device based on the SF-TNSs nanocomposite was discussed in *Chapter 4*. A structurally-colored multilayer film, which can be considered a Bragg reflector inspired to the cuticle of *Hoplia coerulea* beetle was fabricated by a layer-by-layer deposition technique by spin coating. SF was used as low refractive index layer and the SF-TNSs nanocomposite as high refractive index layer. Thanks to the high refractive index contrast achieved with the TNSs, it was possible to obtain a reflection peak with only four couples of layers, suitable to be used as optical antenna in sensing. In this contest, the silk-based multilayer reflector was explored as platform for humidity sensing. The stimuli-responsive properties of the film were characterized and a simple optical model for the sensing mechanism

was proposed. Specifically, the silk-based multilayer showed a reversible color change when exposed to different relative humidity, and good performances in terms of reproducibility and stability over time.[3] Other tuneable optical devices have been presented based on silk materials however, to the best of our knowledge this is the first realization of a multilayer structure. The simple and cheap fabrication by spin-coating, the possibility to tune the optical properties by acting on spin process, the low absorption coefficient showed, combined with the unique properties of the silk and the possibility to functionalize the material, suggest the possibility to integrate this structure in more complex device for lab-on-chip optical sensor.[4]

In *Chapter 5* the fabrication of large area inverse opals (IOs) made with both the two nanocomposites was discussed. In the first part an insight on the fabrication method was proposed, based on a layer-by-layer (LbL) scooping transfer technique.[5] A standard protocol for the fabrication was developed, considering different parameters involved. The optical properties of the fabricated opals were characterized by reflection and transmission measurements. In addition, the possibility to introduce controlled optical defects inside the structure was demonstrated. In the second part, the results obtain by the fabrication of SF-TNSs IOs were presented, with a particular attention on the possibility to tune the optical properties by using different treatments (such as UV light, water annealing and methanol). In the last part, SF-AuNRs IOs (SARNIOs) were exploited as platform for temperature sensing and photodynamic applications. Albeit some critical issues, in particular concerning the structural integrity of the SF-TNSs IOs and the effective applicability of the SARNIOs as temperature sensing probe, some interesting properties were observed. In particular, the combination of plasmonic (gold particles) and photonic properties (IOs), with the flexibility and biocompatibility of the silk, could be exploited for the fabrication of SERS devices or platform for optical biosensors.[6–8]

This thesis represents only a small contribution in the big field of the bionanocomposites, with specific attention to the silk-based one, but several interesting results have been presented, especially for what concern the SF-TNSs. A lot has still to be done, but the work presented here can be a valuable starting point for the implementation of the described nanocomposites inside optical and photonic devices, as demonstrated in the last two chapters.

References

[1] G. Perotto, M. Cittadini, H. Tao, S. Kim, M. Yang, D. L. Kaplan, A. Martucci, F. G. Omenetto, *Adv. Mater.* **2015**, *27*, 6728.

[2] Z. Zhang, J. Wang, C. Chen, *Theranostics* **2013**, *3*, 223.

[3] E. Colusso, G. Perotto, Y. Wang, M. Sturaro, F. Omenetto, A. Martucci, *J. Mater. Chem. C* **2017**, *5*, 3924.

[4] A. Ricciardi, A. Crescitelli, P. Vaiano, G. Quero, M. Consales, M. Pisco, E. Esposito, A. Cusano, *Analyst* **2015**, *140*, 8068.

[5] Y. Wang, D. Aurelio, W. Li, P. Tseng, Z. Zheng, M. Li, D. L. Kaplan, M. Liscidini, F. G. Omenetto, *Adv. Mater.* **2017**, 1702769.

[6] C. Guo, G. N. Hall, J. B. Addison, J. L. Yarger, *RSC Adv.* **2015**, *5*, 1937.

[7] C. Bourdillon, S. Gam Derouich, W. Daney De Marcillac, L. Coolen, A. Maître, C. Mangeney, C. Schwob, *Proc. SPIE - Int. Soc. Opt. Eng.* **2016**, *9756*, 1.

[8] K. A. Burke, M. A. Brenckle, D. L. Kaplan, F. G. Omenetto, *ACS Appl. Mater. Interfaces* **2016**, *8*, 16218.

Appendix

A1. Materials recipes

A1.1. Silk Fibroin extraction

Silk fibroin was extracted from the silk cocoons according with the protocol previously reported.[1] Bombyx mori cocoons were cut in small pieces and boiled in a 0.02 M Na_2CO_3 water solution for 30 or 45 min (depending on the required molecular weight) to remove sericin. After rinsing three times with milliQ water, dried silk fibers were dissolved in a 9.3 M LiBr solution at 60° C for 4 hours, followed by dialysis against DI water at room temperature for 3 days using Slide-a-Lyzer dialysis cassettes (MWCO 3500, Pierce Biotechnology, Rockford, IL). Remaining particulates were removed trough centrifugation (10000 rpm, 4°C, 20 min) obtaining a 50 mg/ml – 60 mg/ml silk fibroin solution in water.

A1.2. Titanates nanosheets synthesis

TNSs nanosheets were synthesized using a sol-gel process.[2,3] Initially, 12 mmol of titanium tetraisopropoxide $Ti(OPri)_4$ were added to 107 mmol of warm (110° C), dehydrated and degassed ethylene glycole (EG). Subsequently, 9 mmol of tetramethylammonium hydroxide (TMAH) dissolved in 300 mmol of water were injected in the solution, which became optically clear after few seconds. After four hours of reaction at 110 °C and after cooling the solution at room temperature (RT), flocculation was induced with excess of acetone. TNSs were then collected by centrifugation at 4000 rpm for 4 minutes. The precipitate was washed two times with acetone and two times with methanol and dried under vacuum. A stock dispersion of TNSs was obtained by dispersing 200 mg of TNSs in 1 ml of 1 M TMAH (Sigma-Aldrich) aqueous solution.

A1.3. Gold nanorods synthesis

Gold nanorods were prepared according to the seed-mediated method previous reported.[4] Briefly: the seed solution was prepared by mixing 0.12ml of HAuCl4 solution (15 mM) with an aqueous solution of hexadecyltrimethylammoniumbromide (CTAB) (2.5 ml, 0.20 M), 1 ml of deionized water, and 0.60 ml of ice-cold 0.010 M NaBH4. The growth solution was prepared by mixing CTAB solution (5.36 ml, 0.20 M), 4 ml deionized water, AgNO3 (0.4 ml, 4 mM), HAuCl4 (0.5 ml, 15 mM), ascorbic acid (0.124 ml, 0.0788 M), and 0.1 ml of the 30-min aged seed solution. The solution was left to react overnight at 27° C. The day after excess CTAB was removed by centrifugation at 14000 rpm for 30 min. Finally, the precipitate was redispersed in an aqueous solution of mPEG-thiol (MW∼5000, 0.5 ml, 0.2 mM, 1mg/ml) and kept overnight at room temperature to ensure the surface modification, then was submitted at another centrifugation step to remove the supernatant with unbound polymer. Finally, the solution was concentrated to a final concentration of 2 mg/ml by centrifugation. The final concentration in weight was estimated gravimetrically.

A1.4. SF-TNSs synthesis

Silk/TNSs films were prepared by gently mixing the SF solution with the TNSs solution according to different formulations, as reported in **Table A3.1**. The hybrid solution was cast onto a PDMS surface and dried under hood in condition of 30%RH at room temperature overnight. Alternatively, thin films were deposited on silicon or glass substrates by spin coating.

Table A3.1. Formulations used for the preparation of the SF-TNSs samples. The values reported refer to a volume of the final solution equal to 1 ml

SF-TNSs ratio (% w/v)	SF sol (µl)	TNSs sol (µl)
100:0	100	-
20:80	500	500
50:50	800	200
80:20	941	59

A1.5. SF-AuNRs synthesis

Silk/AuNRs films were prepared by gently mixing the SF solution with the PEG-AuNRs solution, ultimately resulting in 0.125-1 wt% (gold to polymer) Au in the final nanocomposite samples. The hybrid solution (1ml) was cast onto a PDMS surface or PMMA surface (2 x 2 cm^2). The samples were dried under hood in condition of 30%RH at room temperature overnight.

A2. Fabrication methods

A2.1. Substrates cleaning for thin film deposition

The substrates for the thin film deposition were cleaned according to the following protocol: first substrates were sonicated for 15 minutes in acetone to remove excess organic compounds, then they were washed thoroughly with deionized (DI) water and then immersed in hot (60 °C) basic piranha solution, a mixture of DI water, H_2O_2 (30% wt solution) and NH_3 (25% wt solution) according to 5:3:1 volume ratios, for 20 minutes in order to remove residual organic compounds and slightly etch the surface of the substrate creating –OH dangling bonds useful to improve their wettability and to allow sol-gel film anchorage. After a careful rinsing with DI water, substrates were stored under water, and dried in an air or nitrogen stream just before the deposition process.

A2.2. Thin films deposition

SF-TNSs thin films were deposited on different substrates (silicon, quartz and alumina) by spin coating (SCS G3P-8 spin coater, Cookson Electronics), at different speed to tune the final thickness of the samples (1000, 2000 or 3000 rpm) for 60 s. Where not specified in the text, for the deposition we adopted the formulations reported in Table A3.1.

A2.3. Bragg multilayer deposition

The Bragg multilayer structure was fabricated by sequential deposition of Rsilk and HRIsilk solution on a fused SiO_2 slide of 2 cm x 2 cm previously cleaned with piranha solution, rinsed with DI water and dried in a stream of nitrogen. Rsilk solution with a concentration of 2.5%w/v was obtained by diluting the silk fibroin solution with DI water. The high refractive index TNS:silk solution was prpeared by gently mixing the stock TNS dispersion with the silk solution in order to obtain a TNS : silk ratio equal to 80 : 20 in weight. The solution was diluted in order to obtain a total concentration of solid (fibroin and particles) of 30 mg ml^{-1}. Spin coating solutions were always made fresh and used within few hours to avoid the gelation of the silk fibroin that usually occurs after 6 hours. Both solutions were filtered using syringe filters (Millex® syringe filter, Durapore® PVDF, 0.22 μm) to remove aggregates and dusty. Thin layers of Rsilk and HRIsilk were produced by using the spin-coating technique (SCS G3P-8 spin coater, Cookson Electronics), at 3000 rpm for 60 sec. After each deposition, the sample was treated in methanol for 30 min to induce the crystallization of silk and make the film water insoluble.[5]

A2.4. Polydimethylsiloxane (PDMS) casting substrates fabrication

Flat PDMS substrates thickness were prepared by casting an appropriate amount of base and curing agent (9:1 ratio) from the Sylgard kit (Dow Corning) mixed together on petri dishes. The solution was then degassed for 2h and cured at 60° C for 12h. The PDMS substrates were then prepared for SF based solution casting by washing with

70% ethanol solution and rinsing three times deionized H_2O. PDMS surfaces were used for multiple casting.

A2.5. Inverse opals fabrication

The silk based inverse opals were prepared by using large-scale close-packed polystyrene (PS) spheres (modified by carboxylic acid group on the surface, Interfacial Dynamics Co.) arrays as template following the protocol previously reported.[6] A suspension of 4% (300 nm) or 6% (400 nm) aqueous PS spheres was prepared in a mixture with an equal volume of ethanol. A few drops of the suspension were introduced to the water surface in a petri dish using a partially immersed silicon wafer, which was pretreated by an O_2 plasma treatment to realize a hydrophilic surface. To help the direct crystallization process, a few drops of sodium hydroxide solution and sodium dodecyl sulfate (SDS, $NaC_{12}H_{25}SO_4$) were added to the water phase before introducing PS spheres to adjust the surface tension of water. The formation of a large crystal layer by self-assembly was promoted by the addition of liquid medium. To prevent the formation of cracks during the transfer step, few drops of SDS were introduced. A silicon substrate was immersed into the sub-phase and elevated under a shallow angle to transfer the monolayer from the water surface to the substrate (scooping transfer). To facilitate the final detachment of the SIO, a layer of polymethylmethacrylate was deposited on the wafer by spin-coating. After drying, the procedures were repeated for the fabrication of a multilayers colloidal crystals. The silk-based solution was added to the colloidal crystals to fill the air voids after immersing the template in water for a few minutes to remove SDS. The samples were set to dry for 24 h (25° C, 30% relative humidity) to form a free-standing silk/PS composite film. The PS spheres within the composite film were finally removed by immersing the film into toluene for 24 h.

A2.6. Inverse opals treatments

The free-standing opals fabricated were treated in order to increase the population of β-sheets crystals and make them insoluble in water. Two different annealing were investigated: a methanol annealing and water vapor annealing. Methanol annealing: samples were put in methanol for 12 hours and then remove and leave to dry in controlled atmosphere to avoid a rapid evaporation of alcohol and reduce crack formations. Water vapor annealing: samples were put in a vapor desiccator connected to a vacuum pump, filled with enough distilled water to generate water vapor to fill the volume of the desiccator during the evaporation (relative humidity >90%), but the water did not touch the sample holder. Then the vacuum pump was switch on for about 5 minutes. Once the desiccator was filled with vapor, the vacuum port was turn off to let the homogeneous water vapor annealed the samples for 4 hours.

UV irradiation were performed on the samples with a UV lamp, 254 nm with an intensity of 11 mW/cm^2.

A3. Characterizations

A3.1. Circular Dichroism (CD)spectroscopy

CD spectroscopy was used to determine the secondary structure of the silk fibroin in solid state in thin films deposited on a quartz substrate (Edmund Optics, window UV 26mm). The measurements were conducted using a spectropolarimeter Jasco J-710 in the wavelength range 185-255 nm, with a resolution of 0.2 nm, band with of 2 nm, scanning speed 20 nm/min, with 2 accumulations for sample. During the analysis of the results it was considered only the wavelength range without saturation of the signal (HT< 600 V). The spectra were corrected with a smoothing to reduce the signal to noise ratio.[7]

A3.2. Optical spectroscopy

Transmittance (or absorbance) spectra in the UV-VIS-NIR range were collected using a Jasko V-570 Spectrophotometer. Thin film deposited on quartz slide or free-standing samples were analyzing place them perpendicular to the light beam. Measurements were conducted with a scan speed of 400 nm/min with a data pitch of 2nm after baseline in air.

A3.3. Fourier Transform Infrared (FTIR) spectroscopy

Fourier transformed infrared measurements have been performed in the 4000-600 cm^{-1} range using a Jasco 6200 FTIR Spectrophotometer (JASCO, Tokyo, Japan). For each measurement 64 scans were coded at a resolution of 4 cm^{-1}. In the case of thin films deposited on silicon substrates, measurements were performed in transmition mode (background with a silicon substrate). Where not specified, measurements were effectuated in reflection mode on free standing samples, using a ATR equipment with a ZnSe crystal.

A3.4. X-ray diffraction (XRD)

XRD measurements on thin films deposited on glass slides were performed using a Philips PW1710 diffractometer equipped with grazing-incidence X-ray optics, using CuKα Ni-filtered radiation at 40 kV and 40 mA, at 2° of incidence. The measurements were performed from 3° to 70° 2θ with a 0.05° step size.
In the case of SF-TNSs samples after the ion exchange, the films were first reduced in powder using a mortar and pestle. XRD measurements were performed on a PANalytical Empyrean X-ray diffractometer using a Cu Kα anode (λ=1.5406 Å) operating at 45 kV and 40 mA. The diffraction patterns were collected in the range 3–70° 2θ with a 0.04° step size.

In the case of the residual powder obtained by DTA-TG, powders were deposited on a glass slide and measurements were performed using the same parameters for the thin films. The crystalline phases were then determined by analysis of the pattern

with the software Match!-Phase identification from Powder Diffraction (Crystal Impact).

A3.5. Transmition Electron Microscopy (TEM)

Transmission Electron Microscopy (TEM) analysis was carried out using a JEM 1400-Plus JEOL microscope operating at an acceleration voltage of 120 kV equipped with a LaB6 filament. Few drops of the SF-TNSs composite suspension were casted onto copper grids coated with an amorphous layer of carbon film and dried under air to allow solvent evaporation. For the characterization of the samples after ion exchange, a diluted suspension (1% total weight, 30% w/v TNSs) was deposited by spin coating (1000 rpm x 60 s) on a copper-carbon coated grid, treated in methanol for 30 min and exchanged for 6 min in the salts solutions.

A3.6. Nanoindentation test

These experiments were performed using an instrumented indentation system (Ultra Micro Indentation System, UMIS-2000, CSIRO, Australia) with a Berkovich diamond tip. Before the experiments, the indenter area function was established by making over 150 indents on a fused silica sample under loads from the range 1–250 mN.
Two different loads (100 μN and 50 μN) were used to test the coatings deposited on alumina substrate. On each flat surface specimen, one or two locations were chosen for indentation. At each location, 10 indentations were performed for assessing the variability of the measured mechanical properties and to determine the average values.[8] Following an indentation test, the hardness and the reduced elastic modulus were calculated as proposed by Oliver and Pharr.[9]

A3.7. Atomic Force Microscopy (AFM)

A Park Systems XE-70 atomic force microscopy (AFM) has been used to measure surface roughness of deposited thin films on silicon substrate. The measurements were conducted in non-contact mode to avoid modification of the surface of the films

(the contact of the tip with the sample can produce distort images and damages on a soft material as silk). A PPP-NCHR non-contact cantilever with a radius of less than 10 nm was used as scanning probe, with a vertical resolution of few Ångstrom. Measurements were conducted in a scanning area from less than 5 μm x 5 μm to 100 μm x 100 μm. The profiles and the average roughness were then calculated from the images by using the Gwyddion software. The experimental data were elaborated by subtracting the medium plane to correct distortion due to the non-perfect planarity of the sample during the measurements.

A3.8. Thermal gravimetric and Differential Scanning Calorimetry analysis (TG-DSC)

Thermal gravimetric analysis (TGA, TA Instruments Q500) was used to measure changes in weight of AuNRs-SF sample with increasing temperature. TGA curves were obtained under nitrogen atmosphere with a gas flow of 50 mL/min. The experiment was performed at heating rates 10° C/min.

The thermal properties of the silk films were measured in a TA Instrument Q100 DSC (TA Instruments, New Castle, DE) under a dry nitrogen gas flow of 50 ml min^{-1}. Measurements were performed using a TA instrument Q100 equipped with a refrigerated cooling system. The samples were heated at 2 C min^{-1} from 30 to 230° C.

A3.9. Ion Coupled Plasma (ICP) analysis

About 0.05 g of each sample was weighted with an analytical balance of nominal sensitivity 0.1 mg and digested by microwave digestion system (Ethos 1600, Microwave Labstation Milestone - 1 min 250 W, 1 min 0 W, 5 min 250 W, 3 min 400 W, 3 min 600 W, 120 min 0 W) with 6 ml of HNO_3, 2 ml of H2O2 and 1 ml of HF of analytical grade. After cooling, HF was buffered with 1 ml of H_3BO_3 and the resulting clear solution was then diluted to 50 ml with high purity water and filtered on PTFE syringe filters (porosity 0.45 μm). Ti, Ag, Cu and Eu concentration values for digested and properly diluted samples was performed by a Perkin Elmer ICP-OES 5300DV whose instrumental details and operating conditions are summarized in **Table A3.2**.

Commercially available 1000 mg/l standard solutions (Fluka TraceCERT®) of the analyzed elements were used to calibrate ICP-OES. Diluted working solutions were daily prepared by serial dilutions of the stock solutions. Two blank solutions not containing samples were carried through the same procedure to correct the elemental contributions of the reagent used for sample preparation. Precision measurements were performed by quadratic formula of error propagation as described in Valotto et al.[10] The sources of uncertainty considered were the sample weighing and the elemental characterization by ICP-OES. For these two processing steps, it was considered as uncertainty 0.1 mg and the standard deviation upon repeated concentration measurements, respectively.

Table A3.2. Instrumental characteristics and settings for ICP-OES Perkin Elmer Optima DV 5300.

Instrumental Characteristics	Parameter
RF power	1300 W
Frequency of RF generator	40 MHz
Plasma Ar flow	15 l min^{-1}
Auxiliary Ar flow	0.2 l min^{-1}
Nebulizer Ar flow	0.8 l min^{-1}
Sample flow rate	1.5 ml min^{-1}
Wash rate	1.5 ml min^{-1}
Wash time	30 sec
Points / peak	6
Peak algorithm	Peak area
Replicates	6

A3.10. Thermal gravimetric- Differential thermal analysis (TG-TDA)

Differential thermal analysis (DTA) and thermogravimetric analysis (TGA) were effectuated on SF-TNSs samples after ion exchanges and on TNSs powder. The measurements were conducted simultaneously with a TG-DTA Netzsch Geiàtebau instrument from room temperature to 600° C, with a heating speed of 5° C·min^{-1} in air or nitrogen. ~15 mg of sample was insert in an alumina melting pot and an equivalent of kaolin powder was used as reference.

A3.11. Ellipsometry spectroscopy

The complex refractive index of the sample was determined by Ellipsometry Spectroscopy. Transmittance at normal incidence and ellipsometry quantities Ψ and Δ have been measured using a J.A. Woollam V-VASE Spectroscopic Ellipsometer in vertical configuration, at various angles of incidence (usually three angles, 65°, 70°, 75°) in the wavelength range 300-1700 nm.

The technique measures the ratio between the two Fresnel reflection coefficient of the sample for p- and s- polarized light (ρ). The ratio is expressed in terms of the two real-valued ellipsometric parameters Ψ and Δ, following the equation:

$$\rho = \frac{R_p}{R_s} = \tan(\Psi)\, e^{i\Delta} \qquad \text{(A.1)}$$

where Ψ represents the magnitude of the ratio between R_p and R_s complex reflection coefficient, while Δ is the phase difference between them.

For data analysis a model of the measured sample was created using a layer of silicon or quartz (depending on the sample) as substrate. A second layer of dielectric with a Cauchy dispersion law for the refractive index and with Urbach absorption was used to model silk fibroins films.[11] The band edge for Urbach absorption was fixed at 270 nm, accordingly with the UV-Vis spectrum. In the case of the SF-TNSs nanocomposites, the material was modeled with another Cauchy dispersion for the refractive index and with an Urbach absorption fixed to 350 nm, accordingly with the UV-VIS spectra. The film thickness, the Cauchy parameters and the amplitude of the absorption were used as parameters to fit the experimental data. For the SF-TNSs samples after the ion exchange and the UV photoreduction of the silver, a GENOSC layer with Tauc-Lorentz and Lorentz oscillators was used to model the optical constant of the material, considered as an homogeneous layer.

A3.12. Photoluminescence spectroscopy (PL)

Luminescence measurements on the SF-TNSs samples exchanged with europium ions were performed using a Jasko FP-6300 spectrofluorometer with a Xe light source.

Emission spectra were collected in the 400-750 nm range, using two different excitation wavelengths 280 and 395 nm. Excitation spectrum was instead collected in the 200-500 nm range, by monitoring the emission at 616 nm. The *bandwidth* was fixed to 5 nm for the excitation and 10 nm for the emission. The measurements were performed using a scan speed of 1000 nm/min and 1 nm as data pitch.

A3.13. Scanning Electron Microscopy (SEM)

SEM observations of the multilayer film and of the IOs were performed with Zeiss Supra55VP microscope. For the cross-section images, samples were cleaved via cryofracture. The samples were sputtered with a 5 nm thick layer of gold using an EMS 300T D Dual Head Sputter Coater.[6]

A3.14. Specular reflection spectroscopy

The specular reflection spectra of the inverse opals were collected at normal incidence respect to the (111) crystallographic plane by using a portable spectrophotometer (USB 2000, Ocean Optics) in the wavelength range 400-850 nm and an optical spectrum analyzer (OSA, YokogawaAQ6370B, Yokogawa Corporation of America) in the wavelength range 650-1000 nm. The incident beam was provided by a white light source (LS450, Ocean Optics) connected to an optical fiber probe (R400-7-VIS-NIR, Ocean Optics) composed by 7 fibers with numerical aperture of 0.22 and core diameter of 400 μm. The 6 external cores of the probe were used to bring the while light illumination to the sample, while the central fiber was connected to the detector. Before measuring the prepared samples, the system was calibrated by using as a reference a metallic mirror (BB05-E02 Broadband Dielectric for the VIS andPF10-03-P01 Protected Silver Mirror for the NIR, Thorlabs Inc.) guaranteeing a reflectivity on the whole analyzed wavelength range higher than 99%. Additionally, micro translation stages and sample rotators were included in the measurement system to guarantee normal incidence and precise probe-sample positioning.

A3.15. Absorbance/Attenuation spectroscopy

Absorbance/attenuation spectra of Silk-AuNRs inverse opals films were collected at various angles of incidence using a variable-angle spectroscopy set-up. A collimated beam of white light (LS450, Ocean Optics) was sent through the sample, and the transmitted light as collected collinear to the light incidence direction in a solid angle of 1° and coupled into a fiber to a detector (R400-7-VIS-NIR, Ocean Optics). By rotating the sample using an appropriate stage, the transmition for varying angles light incidence was measured. For limits related with the set-up, it was possible to vary the angle only from 0° to 15°. From the measurements, it was calculated the attenuation (losses due to absorption and scattering), defined as $\log10(I_0/I)$, where I_0 is the incident light intensity and I is the transmitted light intensity.[12]

A3.16. Humidity sensing experiments

The Relative Humidity (RH) sensor response of the multilayer structure was measured using a custom-built closed chamber, consisting of a steel chamber with two quartz windows connected to a RH sensor and a bubbler system, used to generate moist air. The RH was varied between 10% and 80% by controlling flow rates of dry and wet gas. The RH of the test chamber was continuously monitored using a commercial RH sensor (Bel-Art, Scienceware digital hygrometer), previously calibrated with commercial calibration standards (Ambient Weather Field Calibration Kit). Optical transmittance measurements were recorded in situ using a home-made equipment consisting of a collimated beam of a fiber coupled UV-VIS-NIR light-source (DM-2000-BAL Micropack) and the spectra were obtained using a spectrometer (Ocean Optics, HR4000) from 300 to 1000 nm. The pictures showing the hygrochromic behavior of the sample when it is exposed to the vapor of human breath, are collected with a Canon EOS Rebel T1i digital camera.

A3.17. Laser heating experiments

A laser diode source (T808FUL5W laser 808 nm dpss 5A) was used for laser-heating experiments. To illuminate the SANRIO and the free-standing films, a convex lens with expanded the laser beam to a diameter of 8 mm. The beam-profile characteristics were evaluated by using the knife-edge technique: the measured beam power was plotted against the translation position of the knife-edge and the beam diameter was determined by a Gaussian-beam shape fit, obtained by differentiation of the power measurements.[13] For the investigation of individual IOs, the laser beam was directed onto the individual IOs. The temperature distribution of the samples was measured with a thermal camera (SC-600, FLIR).[14] All data were measured after 5 min so that the sample could reach a stable temperature. The laser power was measured using a laser power meter (S310C, ThorLab). For the experiments on the tuning of the reflection peak of the SARNIOs with irradiation, the laser beam was focused on the samples with an angle of incidence of 45° (horizontal radius of elliptic beam ~8.5 mm) and the normal reflection was collected by an optical fiber (R400-7-VIS-NIR, Ocean Optics) coupled to a portable spectrophotometer (USB 2000, Ocean Optics) illuminated by a white source (LS450, Ocean Optics). The set-up was built in order to avoid the collection of the laser radiation with the optical fiber.

References

[1] D. N. Rockwood, R. C. Preda, T. Yücel, X. Wang, M. L. Lovett, D. L. Kaplan, *Nat. Protoc.* **2011**, *6*, 1612.

[2] A. Antonello, M. Guglielmi, V. Bello, G. Mattei, A. Chiasera, M. Ferrari, A. Martucci, *J. Phys. Chem. C* **2010**, *114*, 18423.

[3] G. Perotto, A. Antonello, D. Ferraro, G. Mattei, A. Martucci, *Mater. Chem. Phys.* **2013**, *142*, 712.

[4] B. Nikoobakht, M. A. El-Sayed, *Chem. Mater.* **2003**, *15*, 1957.

[5] E. Colusso, G. Perotto, Y. Wang, M. Sturaro, F. Omenetto, A. Martucci, *J. Mater. Chem. C* **2017**, *5*, 3924.

[6] Y. Wang, D. Aurelio, W. Li, P. Tseng, Z. Zheng, M. Li, D. L. Kaplan, M. Liscidini, F. G. Omenetto, *Adv. Mater.* **2017**, 1702769.

[7] H. Y. Hu, Q. Li, H. C. Cheng, H. N. Du, *Biopolymers* **2001**, *62*, 15.

[8] J. A. Arsecularatne, M. Hoffman, *J. Phys. D. Appl. Phys.* **2014**, *47*, 315403.

[9] W. C. Oliver, G. M. Pharr, *J. Mater. Res.* **1992**, *7*, 1564.

[10] G. Valotto, G. Rampazzo, F. Visin, F. Gonella, E. Cattaruzza, A. Glisenti, G. Formenton, P. Tieppo, *Atmos. Environ.* **2015**, *122*, 596.

[11] G. Perotto, Y. Zhang, D. Naskar, N. Patel, D. L. Kaplan, S. C. Kundu, F. G. Omenetto, *Appl. Phys. Lett.* **2017**, *111*, 103702.

[12] Y. Vasquez, M. Kolle, L. Mishchenko, B. D. Hatton, J. Aizenberg, *ACS Photonics* **2014**, *1*, 53.

[13] M. A. de Araújo, R. Silva, E. de Lima, D. P. Pereira, P. C. de Oliveira, *Appl. Opt.* **2009**, *48*, 393.

[14] S. Kim, A. N. Mitropoulos, J. D. Spitzberg, H. Tao, D. L. Kaplan, F. G. Omenetto, *Nat. Photonics* **2012**, *6*, 818.